

**CONJUGATED POLYMER NANOFIBERS FOR ORGANIC
BIOELECTRONICS AND BIOACTUATORS**

by
Mohammadjavad Eslamian

A thesis submitted to the department of Biomedical Engineering,
Cullen College of Engineering
in partial fulfillment of the requirements for the degree of

DOCTOR OF PHILOSOPHY
in Biomedical Engineering

Chair of Committee: Dr. Mohammad Reza Abidian

Committee Member: Dr. Chandra Mohan

Committee Member: Dr. Mario I. Romero-Ortega

Committee Member: Dr. Sheereen Majd

Committee Member: Dr. Vijaykrishna Raghunathan

University of Houston

May 2021

Copyright 2021, Mohammadjavad Eslamian

DEDICATION

To all my beloved family

“My wife, my parents, and my parents-in-law”

Thank you for your endless love, sacrifices, and supports.

ACKNOWLEDGEMENTS

I would first and foremost like to express my gratitude to my advisor, Professor Mohammad Reza Abidian. Without his advice, guidance, and support, I would not have accomplished what I have achieved in my PhD study at University of Houston.

The interdisciplinary nature of my work has allowed me to have great collaborators. I would like to thank Prof. Vijay Krishna Raghunathan, Prof. Chandra Mohan, and Prof. Sheereen Majd. They have provided much guidance and assistance for my research.

I would like to thank to my PhD committee members, Prof. Mario I Romero-Ortega, Prof. Vijay Krishna Raghunathan, Prof. Mohammad Reza Abidian, Prof. Chandra Mohan, and Prof. Sheereen Majd, for their insightful comments and encouragements during my prospectus and final defense sessions.

I would like to thank to all my colleagues who collaborated on my PhD projects. It was a great experience working with all of them. I also would like to give my special thanks to Dr. Mohammad Khodadadi and Dr. Long Chang for providing me with technical support and training on microfabrication processes at UH Nanofabrication Facility.

I am deeply grateful to my parents and my parents-in-law who are always there for us. Finally, my deepest gratitude is to my wonderful wife, Fereshteh Mirab, who I am so lucky to be married to. Her support and encouragement are a constant source of power enabling me to face any challenge.

ABSTRACT

The emerging field of organic bioelectronics bridges the electronic world of organic-semiconductor-based devices with the soft, predominantly ionic world of biology. Conjugated polymers (CPs) are one of the most promising organic materials for biointerfaces owing to their biologically relevant mechanical characteristics, ability to be chemically modified, mixed electronic and ionic charge transport, and facile and versatile fabrication routes. CP nanofibers have been of great attention because of their extensive porosity and extremely high surface area to volume ratio that result in their high electronic/ionic conductivity and unique electro-chemo-mechanical properties. Thus far, CP nanofibers have been employed for biomedical applications such as biosensors, nerve tissue regeneration, controlled drug delivery devices, and surface modification of neural interfaces. This thesis is mainly focused on the state-of-the-art utilization of CP nanofibers for development of high performance organic bioactuators and for articulating flexible neural microelectrodes with movable recording sites. We first explored the ion transportation mechanisms in actuation of the two most versatile CPs, poly(pyrrole) and poly(3,4-ethylenedioxythiophene), in the form of randomly oriented nanofibers through direct mass measurement under cyclic voltammetry coupled with electrochemical quartz crystal microbalance. Understanding the actuation behavior of the CP nanofibers, we developed a high-performance bilayer beam actuator based on poly(pyrrole) nanofibers (PPy NFs) that efficiently operate in liquid and gel-polymer electrolytes. We studied the dynamics of the actuator using theoretical analysis and experimental measurements of motion and mass transport. The actuator demonstrated an impressive performance,

including low power consumption per strain percentage, large deformation, fast response, and excellent actuation stability. Ultimately, the concept of PPy NFs actuators was deployed for microfabrication of flexible neural microelectrodes with movable projections that enable to control the position of electrode recording sites in cerebral environment. We anticipate that the CP nanofiber-based actuators will be utilized for advancement of next generation actuators in the fields of soft robotics, artificial muscles, and biomedical devices.

TABLE OF CONTENTS

DEDICATION	iii
ACKNOWLEDGEMENTS	iv
ABSTRACT.....	v
LIST OF TABLES	xii
LIST OF FIGURES	xiii
I Introduction	1
Overview	1
Conjugated polymers.....	2
Fabrication of conductive nanofibers	4
Template fabrication of conducting polymer nanofibers	5
Hard template method.....	6
Soft template method.....	9
Conjugated polymer nanofibers for bioelectronics and bioactuators	14
Neural interfaces.....	14
Bioactuators	22
Artificial muscles	24
Controlled drug delivery	30
Research Objectives	34
II Electrospinning of Highly Aligned Fibers for Drug Delivery Applications	37
Abstract	37
Introduction	38
Methods.....	41
Materials	41
Electrospinning of aligned PLGA fibers	41
Size, alignment, and shape measurements.....	42
Surface roughness measurement	42
Compositional characterization	42
Physical characterization	43
Drug release	43

Statistical analysis.....	44
Results and discussion.....	45
Conclusions	64
III Coaxial Electrospinning of Aligned Core-Shell Nanofibers Encapsulated with Nerve Growth Factor: Process Optimization and Release Modeling	65
Abstract	65
Introduction	66
Methods	70
Materials	70
Fabrication of aligned core-shell nanofibers via coaxial electrospinning	70
Box–Behnken design for process optimization	72
Characterization of nanofibers.....	76
NGF enzyme-linked immunosorbent assay (ELISA).....	77
Results and Discussion.....	78
Nanofibers morphology and NGF encapsulation	78
Multivariable optimization	81
Effects of processing parameter	83
Model validation.....	91
NGF release assessment and release modeling	93
Conclusions	97
IV A Transdermal Patch Based on Biodegradable Fibers for Skin Drug Delivery..	99
Abstract	99
Introduction	99
Methods	102
Materials	102
Fabrication of the transdermal patch	102
Electrospinning of drug-loaded fibers	102
Patch Assembly.....	103
Fibers morphology characterization	104
In-vitro drug release assessment.....	104
In-vivo skin drug delivery	105

Results and discussion.....	106
Morphology of DEX-loaded PLGA fibers	106
In-vitro drug release and transport.....	107
In-vivo study of the transdermal patch	108
Conclusions	110
V Direct Measurement of Mass Transport in Actuation of Conducting Polymers	
Nanotubes	112
Abstract	112
Introduction	113
Methods	114
Materials	114
Electrospinning of template nanofibers	115
Electrochemical deposition of CPs.....	115
Cyclic voltammetry and EQCM measurements	116
Results and discussion.....	116
Conclusions	124
VI High-Performance Conducting Polymer Nanofiber-Based Actuators for Soft Robotics and Bioinspired Applications.....	126
Abstract	126
Introduction	127
Methods	129
Materials	129
Fabrication of Nanoscale Fiber Templates	130
Electrochemical Deposition of Conducting Polymer	130
Beam Actuation using Cyclic Voltammetry (CV)	131
Electrochemical Quartz Crystal Microbalance (EQCM) Measurements	131
Actuator Tip Kinematic Measurements.....	132
Mechanical characterization of the actuator	133
Rheological Characterization of Liquid and gel electrolytes	133
Structural Characterization of the Actuator.....	134
Statistical Analysis	134

Results and discussion.....	134
Conclusions	147
Supporting Information	148
Characterization of fiber dimensions.....	148
Electrode configurations for actuation experiment	149
Thickness measurement of the actuator layers	151
Calculation of charge storage density and specific capacitance	152
Elastic modulus of the actuator components	153
Calculation of effective modulus of the composite material	156
Viscosity measurement of the liquid and gel electrolytes	159
Calculation of actuation strain.....	161
Calculation of actuation force.....	161
Dynamic and kinematic measurements	165
Short-term response over CV cycling	170
VII Conjugated Polymer Nanofiber Actuators for Articulating Flexible Neural Microelectrodes	172
Abstract	172
Introduction	172
Methods.....	177
Materials	177
Device design and fabrication	177
Coating of device projections with conjugated polymer film	183
Coating of device projections with conjugated polymer nanofibers	183
Preparation of artificial cerebrospinal fluid (aCSF)	184
Projections actuation using cyclic voltammetry	184
Electrochemical impedance spectroscopy (EIS)	184
Projection deflection measurement	185
Structural characterization of the probe devices.....	185
Results and discussion.....	185
Structural design of probe devices.....	185
Morphology of conjugated polymer coatings.....	186

Electrochemical impedance measurements	188
Actuation performance of the probe devices	191
Conclusions	196
VIII Conclusions and future directions	197
Conclusions	197
Future directions.....	198
Insertion and actuation of neural probes in brain phantom gel	198
Neural probe projections with variable thickness ratio	199
Alternate probe projection geometries	199
Development of multifunctional neural probes devices	200
REFERENCES.....	201

LIST OF TABLES

Table III.1. Coded levels of the factors.....	74
Table III.2. BBD experimental design with comparison between actual and predicted values of the fiber diameter and fiber size distribution.....	75
Table III.3. The coefficients for quadratic models.	83
Table III.4. Analysis of variance for response surface quadratic models.	86
Table V.1. The potential (V) at the maximum Δm (Δm_{max}) for PEDOT and PPy samples at various scan rates obtained from the 20th cycle.	124
Table VI.1. Elastic modulus of the actuator components measured by AFM.	155
Table VI.2. Calculated β and γ values at various scan rates in liquid and gel electrolytes.	170

LIST OF FIGURES

Figure I.1. Schematic showing chemical (a, b, c, f) and electrochemical (a, d, e, f) synthesis of CPs using hard templates. In both cases, the templates are removed after deposition to yield CP nanostructures.....	7
Figure I.2. SEM micrographs of a polycarbonate template with 1 μm diameter holes (a) used to produce hollow PPy tubules (b) [29]. Electron micrographs of PANI nanotubes (c) and hollow octahedral (d) fabricated with Cu_2O templates [31].....	8
Figure I.3. Electron micrographs of polyaniline nanomaterials synthesized by emulsion polymerization [37].....	11
Figure I.4. Examples of CP micro and nanostructures fabricated with the soft template method: (a) PANI nanorods [40], (b) PANI nanofibers [41], (c) PANI/polyethylene fibers [43], and (d-g) hollow PEDOT nanotubes [13].	13
Figure I.5. a-c) Schematics of the reactive tissue responses resulting from inserting a neural probe into neural tissue: (b) acute and (c) chronic tissue responses. d) Immunoreactivity images in response to an implanted neural electrode [50].	17
Figure I.6. SEM images of PPy doped with a synthetic protein and coated with a total charge of a) 0 μC , b) 1 μC , c) 4 μC , and d) 10 μC . e) Impedance of PPy film (at 1 kHz) as a function of deposition charge. Cartoons illustrate the film morphology after deposition.....	19
Figure I.7. A) Fabrication of PEDOT nanotubes on neural microelectrodes: Illustrations of electrode sites before (a,e,f) and after PLLA electrospinning (b,g,h), PEDOT deposition and PLLA removal (c,d,i,j). B) SEMs of the PEDOT nanotubes [57].....	20
Figure I.8. a) Fabrication process for multifunctional polymer coatings on the neural microelectrodes. b) Optical micrographs (A: top view, B: side view) and SEM images (C,D) of deposited PEDOT (black color) on an electrode site [59].....	21
Figure I.9. Bilayer actuators: a) PPy/Au actuators curled in a liquid electrolyte [70], b-e) a microrobot arm with hinges comprised of PPy/Au bilayers [71], and f) a composite actuator composed of PPy (black) bonded to silk fibroin (clear) [72].....	25
Figure I.10. a,b) A PANI-gel electrolyte solid-in-hollow fiber linear actuator [74]. c-f) PU/PANI fibers: aligned PU nanofibers (c), aligned PU/PANI fibers (d), cross-section of PU/PANI fibers (e), and PANI coating around PU fibers [75].....	27
Figure I.11. a-b) SEM of PT gel crosslinked with BTH and its volume change during doping/undoping. c-e) PPy(DBS)/PT/PPy(ClO_4) actuator bends freely (c) or with a 10 mg (d) or 25mg (e) object. f) PEDOT/MWCNT/myotubes actuator.....	29
Figure I.12. a, b) SEM of a PPy/pTS polymer film loaded with NT-3 before (a) and after (b) electrical stimulation. c, d) Charts showing NT-3 release versus deposition time and stimulation regime for 3.6 μm (c) and 26 μm (d) PPy films [83].....	31
Figure I.13. a) Release of DEX from PPy matrix as a function of CV cycles. b-d) Optical images of stained astrocytes for control (b), DEX added to the media (c), and DEX released from PPy (d). e) Normalized astrocyte counts after 3 days [84].	31

Figure I.14. a-b) PPy(DBS)/Au bilayer valve in the closed (a) and open (b) position [85]. c) Reverse opal PPy films made by PMMA colloidal crystals template [86]. d-e) An electroactive pump operates with PPy doped with PCTC [87].	33
Figure I.15. Controlled drug release: Drug release from a degradable fiber (a,b) and CP- coated degradable fibers with restricted release avenues (c,d). Controlled drug release from nanotubes via electrical stimulation (e,f) [13].	33
Figure I.16. Flowchart summarizes the research objectives studied in this thesis. Schematic illustrates a CP nanofiber fabricated using a template biodegradable nanofiber.	36
Figure II.1. A) Electrospinning setup for production of aligned fibers: (a) syringe pump, (b) rotating wheel, and (c) power supply. B-D) SEM and optical images of highly aligned PLGA fibers. E) Optical image of relatively less aligned fibers.	46
Figure II.2. Effect of electrospinning processing parameters on the diameter of aligned PLGA fibers. The symbols ** and *** indicate the significance level of $p < 0.01$ and $p <$ 0.001 , respectively. Data is shown in mean \pm SEM ($n = 100$).	49
Figure II.3. Effect of processing parameters on the alignment of PLGA fibers. The symbols ** and *** indicate the significance level of $p < 0.01$ and $p < 0.001$, respectively. Data is shown in mean \pm SEM ($n = 100$).	52
Figure II.4. A) 3D confocal image of aligned PLGA fibers. B) Height profile obtained from the surface of a single aligned fiber to measure RMS roughness. C) Schematic illustrates the conical shape of aligned fibers.	54
Figure II.5. A-D) SEM images of aligned (A,C) and randomly oriented (B,D) DEX- loaded PLGA fibers at different magnifications. E) FTIR spectrum of DEX, PLGA and DEX-loaded PLGA in the wavelength range of $850\text{--}3250\text{ cm}^{-1}$.	56
Figure II.6. XRD patterns of DEX (A), random PLGA fibers (B), DEX-loaded PLGA random fibers (C) and DEX-loaded PLGA aligned fibers (D).	58
Figure II.7. DSC thermograms of DEX (A, blue), random PLGA fibers (B, red), and DEX loaded random PLGA fibers (C, black) and DEX-loaded aligned PLGA fibers (D, green).	60
Figure II.8. A) DEX release profile from PLGA aligned fibers and random fibers. B-D) SEM images of aligned (B,D) and random (C,E) fibers after 25 days incubation. F-G) Degradation modes of aligned and random fibers.	63
Figure III.1. Schematic illustrates the coaxial electrospinning setup.	72
Figure III.2. Flowchart illustrates the overall optimization process.	76
Figure III.3. A-B) Core-shell Taylor cones and jets form at the needle tip. C-D) SEMs of aligned core-shell nanofibers. E) Fluorescent image of the nanofibers loaded with FITC- BSA. F) SEM indicates cross-section of a core-shell nanofiber.	80
Figure III.4. 3D surface response plots for fiber diameter.	89
Figure III.5. 3D surface response plots for fiber size distribution.	90

Figure III.6. A-B) Scatter plots of experimental vs predicted responses for fiber diameter and size distribution. C-D) Studentized residual plots of the fiber diameter and size distribution. Studentized residuals with 95% limits (Bonferroni).	92
Figure III.7. A) NGF cumulative release profile during incubation in PBS at 37°C for two weeks. B) Release fraction profile associated with a curve fit (red line) based on Michaelis-Menten kinetics equation.	94
Figure III.8. SEM images of the aligned core-shell nanofibers after incubation in PBS at 37°C for different periods of time: A) 5 min, B) 8 hrs, C) 2 days, D) 3 days, E) 4 days, and F) 2 weeks. All scale bars represent 2 μm	96
Figure IV.1 Patch assembly: A) An adhesive bandage with an opening at the center, B) Placing a fibrous mat on the bandage, and C) making a hydrogel layer on top of the fibrous mat.	104
Figure IV.2. Circular shape patch (A and B) prepared for in-vitro drug transport assessment using Transwell plate system (C).	105
Figure IV.3. Scanning electron micrographs of the PLGA fibers encapsulated with DEX at various magnifications.	107
Figure IV.4. A) DEX release profile through Transwell plate membrane into PBS. B) DEX release percentage from PLGA fibers with a third order polynomial curve fit. Data is shown in mean \pm S.E. (n = 3, error bars are masked by data points).	108
Figure IV.5. A-B) Photographs of the patch applied on the mice skin. C) The patch peeled off from the mice skin at day 4.	110
Figure V.1. A) Electrospinning setup for formation of PLLA nanofibers on the gold coated quartz crystal. B) SEM of the random PLLA nanofibers. C-D) SEM images of PEDOT (C) and PPy (D) nanotubes after dissolving the PLLA template.	117
Figure V.2. Mass change (Δm) as a function of time during cycling of the PEDOT and PPy nanotubes at different scan rates (20 cycles).	119
Figure V.3. The maximum Δm values related to the 20th cycle for PPy and PEDOT nanotubes at different scan rates (n = 3).	120
Figure V.4. SEM images of CP nanotubes before and after CV at 100 mV/s for 20 cycles: A) PEDOT (before), B) PEDOT (after), C) PPy (before), and D) PPy (after). Arrows point to the cracks appeared after cycling. Scale bars equal to 2 μm	121
Figure V.5. Plots of measured current (blue) and Δm (red) as a function of potential for PEDOT nanotubes at different CV scan rates: A) 10 mV/s, B) 50 mV/s, C) 100 mV/s, and D) 200 mV/s. The arrows indicate the cycling direction.	123
Figure V.6. Plots of measured current (blue) and Δm (black) as a function of potential for PPy nanotubes at different CV scan rates: A) 10 mV/s, B) 50 mV/s, C) 100 mV/s, and D) 200 mV/s. The arrows show the cycling direction.	123
Figure VI.1. A-B) Design of PPy NFs actuator and step-by-step fabrication process. C) Photographs of the actuator beams during fabrication process. D-G) SEMs of template PLLA NFs (D), PPy NFs (E), and cross-section of PPy NFs (F, G).	136

Figure VI.2. A-C) Schematic and composite photographs represent ions transportation and bending motion of the actuator under redox processes. D-I) Cyclic voltammograms, mass flux, and displacement at various CV scan rates.	139
Figure VI.3. A-B) Maximum deflection of actuator at various CV scan rates in liquid (A) and gel (B) electrolytes. C-I) The electro-chemo-mechanical responses of actuator as a function of scan rate. J-K) Actuation force-displacement plots.	144
Figure VI.4. A) Power consumption/strain of the PPy NFs actuator compared to other actuators. B) Bending stability of the actuator. C-D) SEM of PPy NFs before (C) and after actuation (D). E-F) Cross-section of the actuator after actuation.	147
Figure VI.5. Histograms demonstrate the diameter of PLLA and PPy NFs obtained from 100 measurements. The diameter of PLLA and PPy NFs are 140 ± 4 nm and 626 ± 16 nm, respectively ($n = 100$).	149
Figure VI.6. Photographs of the actuation setup at different view angles. Images show the three-electrode configuration was used for CV. In these photos, the electrolyte is in hydrogel.	150
Figure VI.7. Schematic of the actuator deflection upon transportation of solvated cations into/out of the PPy NFs during CV. The actuator deflects counterclockwise upon reduction, and it deflects clockwise upon subsequent oxidation.	151
Figure VI.8. A-C) Step-height for the Au layer (A), PPy NFs constructed on EQCM crystal (B), and PPy NFs constructed on the actuator beam (C). D) 3D reconstructed confocal image represents the surface topography of the PPy NFs layer.	152
Figure VI.9. Specific capacitance of the PPy NFs actuator as a function of CV scan rate during cycling in liquid (black color) and gel (red color) electrolytes.	153
Figure VI.10. Force-separation curves for the actuator components, including PP film, Au, PLLA NFs, and PPy (reduced and oxidized states). The presented data were obtained using AFM in fluid in either contact mode and/or peak force mode.	155
Figure VI.11. Schematic illustrates the dimensions of a core-shell fiber. As indicated, r_c and r_s correspond to the core radius and shell radius, and l represents the fiber length.	156
Figure VI.12. Schematics illustrate the cross-section of the beam actuator before and after transformation.	157
Figure VI.13. Apparent viscosity of liquid and gel electrolytes containing 0.1 M NaPSS as a function of shear rate measured by 40 mm parallel plates with a gap of 0.5 mm at room temperature.	160
Figure VI.14. Free body-diagram and kinetic diagram of the actuator.	163
Figure VI.15. Applied linear potential waveforms (A,B), mass change $\Delta m(t)$ (C,D), the rate of mass change (dm/dt) (E,F), deflection (δ) (G, H), velocity (v) (I,J), and tangential acceleration $a(t)$ (K,L) of the actuator as a function of time.	168
Figure VI.16. Applied linear potential waveforms (A,B), drag force $F_d(t)$ (C,D), and actuation force (F_{act}) (E,F) of as a function of time at various CV scan rates in liquid (A,C,E) and gel (B,D,F) electrolytes.	169

Figure VI.17. Charge storage capacity (Q) (A,B), maximum mass exchange (Δm_{max}) (C,D), and maximum tip deflection (δ_{max}) (E,F) of the PPy NFs actuator as a function of cycle number in liquid (A,C,E) and gel (B,D,F) electrolytes.	171
Figure VII.1. Schematics represent probe designs with two and three movable projection sites.	179
Figure VII.2. Overview of the fabrication process of the probe devices.	182
Figure VII.3. Optical micrographs of the fabricated neural probes with two and three projection sites.	186
Figure VII.4. Scanning electron micrographs of probe projections coated with an electroactive layer of PPy film (A-C) and PPy NFs (D-F).	187
Figure VII.5. Coating of probe projections with PPy NFs: A) gold projection, B) electrospinning of template PLLA NFs, and C) electrodeposition of PPy around template NFs and removing of the uncoated template nanofibers.	188
Figure VII.6. Electrochemical impedance, phase angle, and Nyquist ($Z'-Z''$) plots of the probes with two (A,C,E) and three (B,D,F) projections before (black squares) and after coating with PPy film (red circle) and PPy NFs (blue triangle).	190
Figure VII.7. CV of the probe projections coated with PPy NFs at various scan rates. The black curves corresponding to the probes with two 1 mm projections and the red curves are attributed to the probes with three 0.5 mm projections.	192
Figure VII.8. Bending movement of the probe projections under cyclic voltammetry in aCSF electrolyte.	193
Figure VII.9. Charge storage density (A) and displacements (B) of actuating projection sites (1 mm and 0.5 mm projections) under various CV scan rates in aCSF. The data is obtained from a single probe actuated at various scan rates.	195
Figure VII.10. Electrochemical induced calcium phosphate (CaP) precipitation on the projection sites during CV actuation.	196

I Introduction

Overview

Fibrous conductive materials are of particular interest in electroactive composites. Metallic nanoparticles, carbon fibers, and carbon nanotubes have been efficiently dispersed in an insulating polymer matrix in order to improve both electrical and mechanical properties. Combination of improved electrical properties and mechanical performances has been of great interest in electroactive polymeric technology [1]. Electrospinning is a versatile technique employed for production of thin continuous fibers from a variety of materials including blends and composites.

Conjugated polymers (aka conducting polymers or electroactive polymers) are materials which simultaneously possess the physical and chemical properties of organic polymers and the electronic characteristics of metals. Conductive polymers in fibrillar form may be advantageous compared to films due to their inherent structural properties such as anisotropy and high surface area to volume ratio. Micro/nano-structures of conjugated polymers such as polypyrrole, polyaniline, and poly(3,4-ethylenedioxythiophene) have attracted great attention owing to their ease of polymerization, high conductivity, chemical stability, and biocompatibility. Conjugated polymer composites as a nanofiber mat can be utilized in electronics industry, sensors, batteries, and biomedical applications such as neural interfaces for electrical stimulation to enhance nerve regeneration and for the construction of scaffolds for nerve tissue engineering.

Conjugated polymers

Conjugated polymers (CPs) were discovered in 1976 by Alan Heeger, Alan MacDiarmid, and Hideki Shirakawa who initially synthesized n-doped and p-doped polyacetylene. These three scientists received the 2000 Nobel Prize in Chemistry for the discovery and development of conducting polymers. Since their initial discovery, development in the field of CPs has rapidly accelerated and many other conducting polymers and derivatives have been discovered. Intrinsic conducting polymers typically exhibit conductivity values in the range 10^{-10} - 10^{-5} S/cm, placing CPs between insulators and semiconductors. By undergoing a doping process, conductivity can be enhanced by several orders of magnitude (1 - 10^4 S/cm), rivalling that of metals.

Like other common polymers, CPs also enjoy ease of synthesis and processing compared to metallic and inorganic materials. The outstanding electrical properties of CPs originate from their conjugated π -electron backbone which can be readily synthesized through an electropolymerization process. Moreover, doping CPs with counter-ions provides them with ionic conductivity in addition to electrical conductivity. Up to now, CPs have been widely utilized in the microelectronics industry, including photovoltaic devices, supercapacitors, battery technology, light emitting diodes, and electrochromic displays [2]. Meanwhile, some CPs have attracted extensive attention for application in biomedical fields due their mixed ionic and electronic conductivity, biocompatibility, chemical stability, biomolecule functionalization, and intelligent response to electrical potentials from various types of tissues such as connective tissue, muscle, epithelium, and nervous tissues [3]. Hence, CPs have been explored for a wide range of biomedical

applications including bioelectronics and biosensors [4], regenerative medicine (nerve regeneration) [5], neural interfaces [6], artificial muscles [7], and controlled drug delivery systems [8]. Implantable bioelectrodes for neural stimulation or recording are extensively used in the area of brain-machine interfaces (BMIs). Early metallic implants suffered from lack of biocompatibility and integration with surrounding tissue, but modifying these implants with biocompatible CPs not only resolved this issue but led to development of neural probes with higher signal-to-noise ratio [6].

Developing high-performance biosensors is of great interest especially for measurement of vital analytes relevant to clinical diagnosis. Numerous studies have been conducted on utilization of carbon-based nanomaterials, such as graphene, carbon fibers, and carbon nanotubes for developing a new generation of biosensors, but intrinsic shortcomings still remain due to their inert surfaces [9]. As an alternative, CP-based biosensors have been introduced as sensing elements with immense potential to integrate into micro/nano scale devices for in-vivo sensing and monitoring of bio-analytes [10]. These miniaturized biosensors enable a cost-effective, portable, and high-density design. In particular, functionalized CP biosensors have exhibited great improvements in sensing performance via immobilization processes achieved by grafting functional groups onto the polymer backbone [11].

Development of materials that can securely and efficiently interface with living tissues and guide their behaviors is a long-sought goal of medical science. Some areas of tissue engineering have met with success already, for example, with the use of bioactive ceramics for orthopedic applications and synthetic extra-cellular matrix (ECM) for lab-grown

organs. Regarding the manipulation of neural tissue, CPs are promising bioactive scaffolds for use in nerve regeneration due to their conductive nature that allows the electrical stimulation of the cultured cells or tissue. In fact, CPs can provide a biocompatible platform for essential cellular activities at the polymer-tissue interface, including cell adhesion, migration, proliferation, differentiation, and protein secretion [5].

In realization of systems with biomimetic movements, researchers have tried to develop new artificial muscle-like actuators over the past three decades. Among various materials proposed for artificial muscles, CPs are unique in the sense that they can mimic biological muscles through the electrochemical reaction taking place in their porous structure. In fact, their composition (reactive chains, ions and water) mimics the intracellular matrix from functional cells. As artificial muscles, CPs are employed for the direct conversion of electrical energy to mechanical energy appearing as remarkable changes in their bulk volume [12]. CP-based bioactuators have also opened up new doors in development of devices with controlled drug release. The electrical stimulation of drug-encapsulated bioactuators can induce and trigger drug release by applying the contractive/expansive forces generated through the redox (reduction/oxidation) states of the CPs [13].

Fabrication of conductive nanofibers

There are various approaches to synthesize polymer nanostructures, such as template synthesis, chiral reactions, self-assembly, interfacial polymerization and electrospinning. Recent advances in CP nanotubes and nanofibers were reviewed by Long et al [14]. They discussed various preparation methods, physical properties, and potential applications of one-dimensional nanostructures of conjugated polyaniline (PANI), polypyrrole (PPy) and

poly(3,4-ethylenedioxythiophene) (PEDOT). The synthesis approaches include hard template method, soft template method, and electrospinning. Generally, CPs cannot be simply electrospun due to their low molecular weights, poor solubility and rigid backbone structure. To solve the processability problems of CPs, different techniques such as introducing side chains, controlling main-chain architecture, synthesizing new monomers, using functional dopants, and introducing alkyl groups into monomer have been applied [1].

Blending with other polymers and coating insulating polymer with CPs are the most familiar techniques. Blending with a spinnable polymer is a common way to compensate poor spinnability [15]. However, the presence of an insulating carrier polymer introduces a conductivity percolation threshold, which limits their usage in the applications where high conductivities are required. The polymerization of a conductive monomer associated a doping agent on the surface of a template fiber made with a common polymer is another approach which is reviewed in detail hereunder.

Template fabrication of conducting polymer nanofibers

For many electronic applications including transistors, supercapacitors, and increasingly in bioelectronics, it is highly desirable to fabricate complex micro and nanoscale structures [16-18]. CP nanostructures in particular have gained significant attention owing to the unique properties at the nanometer scale, which can lead to superior device performance [14]. In order to reproducibly fabricate CP micro- and nano-structures, a variety of fabrication methods have been developed, most of which fall into two major categories: hard templates and soft templates.

Hard template method

Hard template fabrication of conducting polymer nanostructures was proposed by C.R. Martin et al. in the late 1990s, and generally involves synthesis of CPs within the pores or channels of hard membranes in order to produce 1D nanomaterials [19]. The nanoscale pores and channels in the hard templates provide nanoreactor sites when dipped into an appropriate solution. CP nanostructures may be chemically synthesized through immersion of the template into monomer solution and subsequently adding an oxidizing agent (Figure I.1(a-c)). In chemical deposition, a porous hard template is immersed in monomer solution, after which the oxidizing or reducing agent is added to initiate polymerization of CPs on the template walls. This method has been used extensively for CPs such as PPy and PANI [20-23]. Alternately, the monomer solution and oxidizing agent may be separated by a template membrane, which allows both solutions to diffuse through the membrane towards one another and react in the pores [24, 25]. In electrochemical polymerization, the template is simply coated with a conductive metal such as gold or platinum and used as the working electrode when dipped into the appropriate monomer/dopant solution (Figure I.1(d-f)) [26]. In this process, the porous hard template is immersed in a monomer/dopant electrolyte after which the addition of current or potential initiates polymerization. Vapor deposition techniques may also be used with hard templates. In this method monomers are first deposited and subsequently polymerized through photochemical or thermal processes in a high vacuum [27, 28].

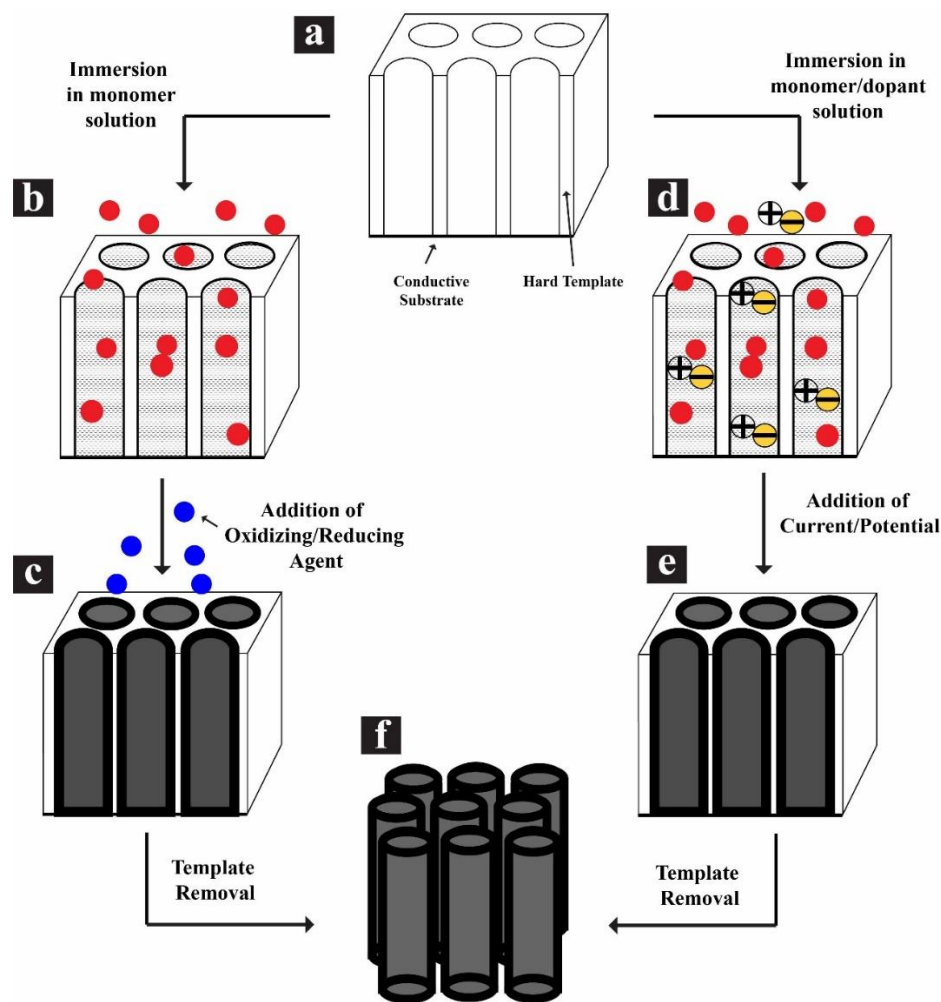


Figure I.1. Schematic showing chemical (a, b, c, f) and electrochemical (a, d, e, f) synthesis of CPs using hard templates. In both cases, the templates are removed after deposition to yield CP nanostructures.

Typical hard membranes include anodic aluminum oxide and track-etched polycarbonate or polyester [29, 30]. Martin and Charles [29] used both track-etched polycarbonate and porous alumina membranes to fabricate PPy nano-tubules and nano-fibrils (Figure I.2(a-b)). They found that both electrochemical synthesis and chemical oxidation techniques could be used to create 100 - 400 nm diameter tubules from PPy and PANI, and that the deposition time determined the thickness of the tubule walls.

Furthermore, they showed that by combination of electrochemical and chemical template synthesis, the capped version of the tubules (capsules) could be loaded with enzymes to make an enzymatic bioreactor. Zhang et al. [31] utilized octahedral copper oxide particles as templates for the subsequent chemical deposition of PANI (Figure I.2(c-d)). By changing the mass ratio of copper oxide to aniline before synthesis, they could form either 200 nm diameter nanotubes on copper oxide crystals or create octahedral geometries that could then be further treated to create hollow PANI octahedral structures.

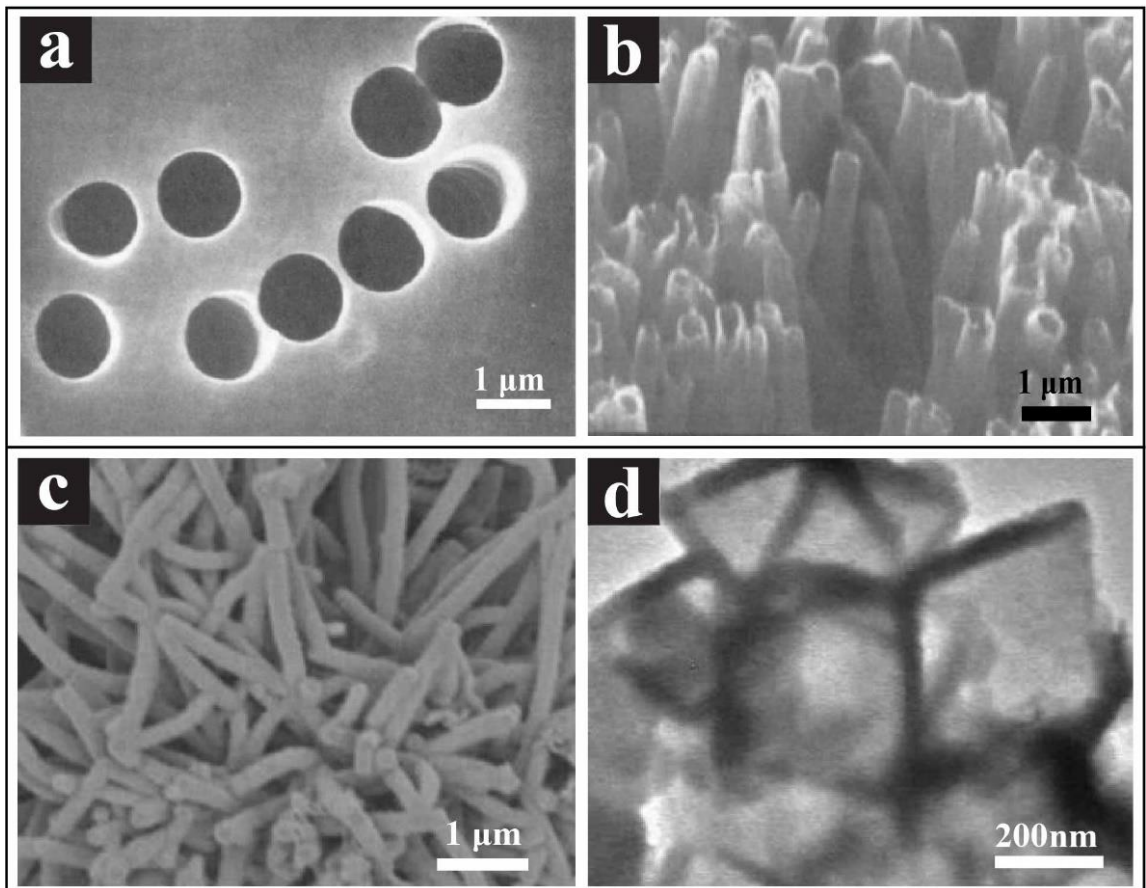


Figure I.2. SEM micrographs of a polycarbonate template with 1 μm diameter holes (a) used to produce hollow PPy tubules (b) [29]. Electron micrographs of PANI nanotubes (c) and hollow octahedral (d) fabricated with Cu₂O templates [31].

Overall, hard templating offers exceptional control over the morphology and geometry of CP micro and nanostructures, but the shape and size of structures are limited by the availability of the templates. In addition, the harsh treatments required to remove the hard template may damage the micro and nano-structures of CPs, and any residues are generally incompatible with biological systems, possibly resulting in adverse biological reactions [19, 32]. The use of hard templates for biomedical applications have therefore been limited, with most works focusing non-biological systems such as photovoltaics [33].

Soft template method

Soft templates in general are structure-directing molecules that are easily removable, thus requiring fewer post-fabrication steps, which makes this method more cost-effective. Some examples of soft template methods for CP fabrication include but are not limited to, emulsion, electrochemical polymerization, electrospinning, chemical polymerization, interfacial polymerization, and dispersion polymerization [14, 32, 34].

Surfactants are some of the most employed soft templates and are key components of emulsion polymerization techniques such as conventional emulsions (macroemulsions) and more controlled variants such as microemulsions [35, 36]. In general, emulsions are combinations of oil, water, and a surfactant, all of which are carefully chosen based on the monomer being polymerized. The use of surfactants in micelle formation can lead to the formation of myriad shapes including CP spheres, rods, ellipses, hexagons, and layered assemblies. Anilkumar and Jayakannan [37] created CP nanofibers and nanotubes via chemical emulsion polymerization of aniline using ammonium persulfate. Aniline itself

acted as an emulsifying agent, and self-organized into micelles, which would then grow into nanotubes and nanorods during polymerization. The resulting structures were 1-2 μm in length and 150 - 250 nm in diameter. The nanotubes were ~ 50 nm thick with a pore diameter of 50 – 70 nm (Figure I.3). While effective at creating a variety of CP structures, the technique offers poor control over the morphology and orientation of the resultant nanofibers [34]. Emulsion-based fabrication of CPs have seen limited use in bioelectronics applications, although this technique has been utilized extensively for drug delivery applications [38, 39].

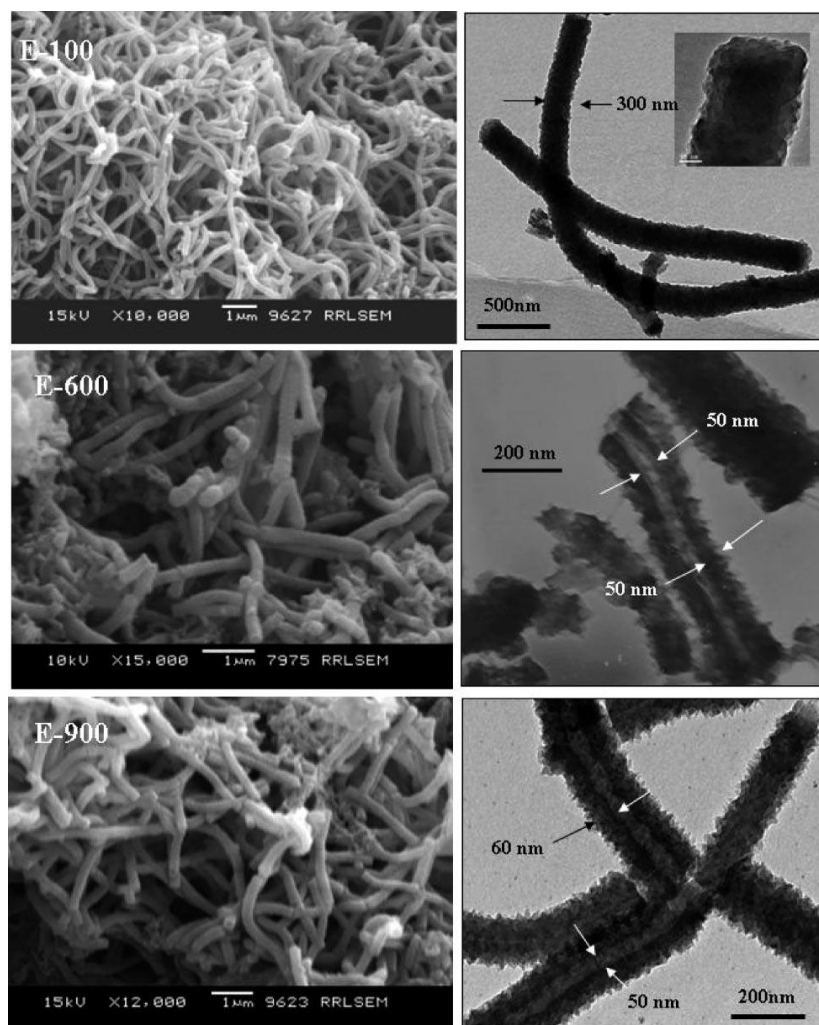


Figure I.3. Electron micrographs of polyaniline nanomaterials synthesized by emulsion polymerization [37].

Other soft templating techniques were inspired by early studies conducted by J. J. Langer. He found that micro-rods of PANI could be reproducibly fabricated in HCl solution through electrochemical oxidation of aniline on iridium or platinum needles (Figure I.4(a)) [40]. The resulting micro-rods were 2-3 μm in length, were organized in a non-periodic lattice, and were uniform in shape and size. Since then, other unique soft templates that do not use micelle-based approaches have been developed. Another

approach is aqueous organic/inorganic interfacial polymerization. Huang et al. [41] performed interfacial polymerization of aniline in chloroform, brought into contact with aqueous ammonium peroxydisulfate and camphorsulfonic acid. After 24 hours of interfacial contact and fiber purification, the technique was shown to have generated fibers up to several microns in length and with diameters between 30 – 50 nm (Figure I.4 (b)).

Electrospinning has been widely utilized in production of CP micro and nanofibers. This process involves the application of high voltage to a CP solution droplet eluted from a conductive spinneret, which builds electrostatic charge and is subsequently ejected from the spinneret in the direction of the electrostatic field [42]. Norris et al. [43] generated PANI microfibers via electrospinning of PANI (0.5 - 2 wt%) and polyethylene oxide (2 -4 wt%) blends. The resulting fibers were $\sim 1.6 \mu\text{m}$ diameter (Figure I.4(c)). Abidian et al. [13] employed randomly oriented poly(lactic-co-glycolic acid) (PLGA) nanofibers as templates ($\sim 100 - 200 \text{ nm}$ diameters) via electrospinning on neural electrodes. The templates were coated with PEDOT via electrochemical polymerization and then dissolved to produce PEDOT nanotubes. These nanotubes were 100 - 600 nm in diameter with wall thickness ranging between 50 - 100 nm (Figure I.4(d-g)).

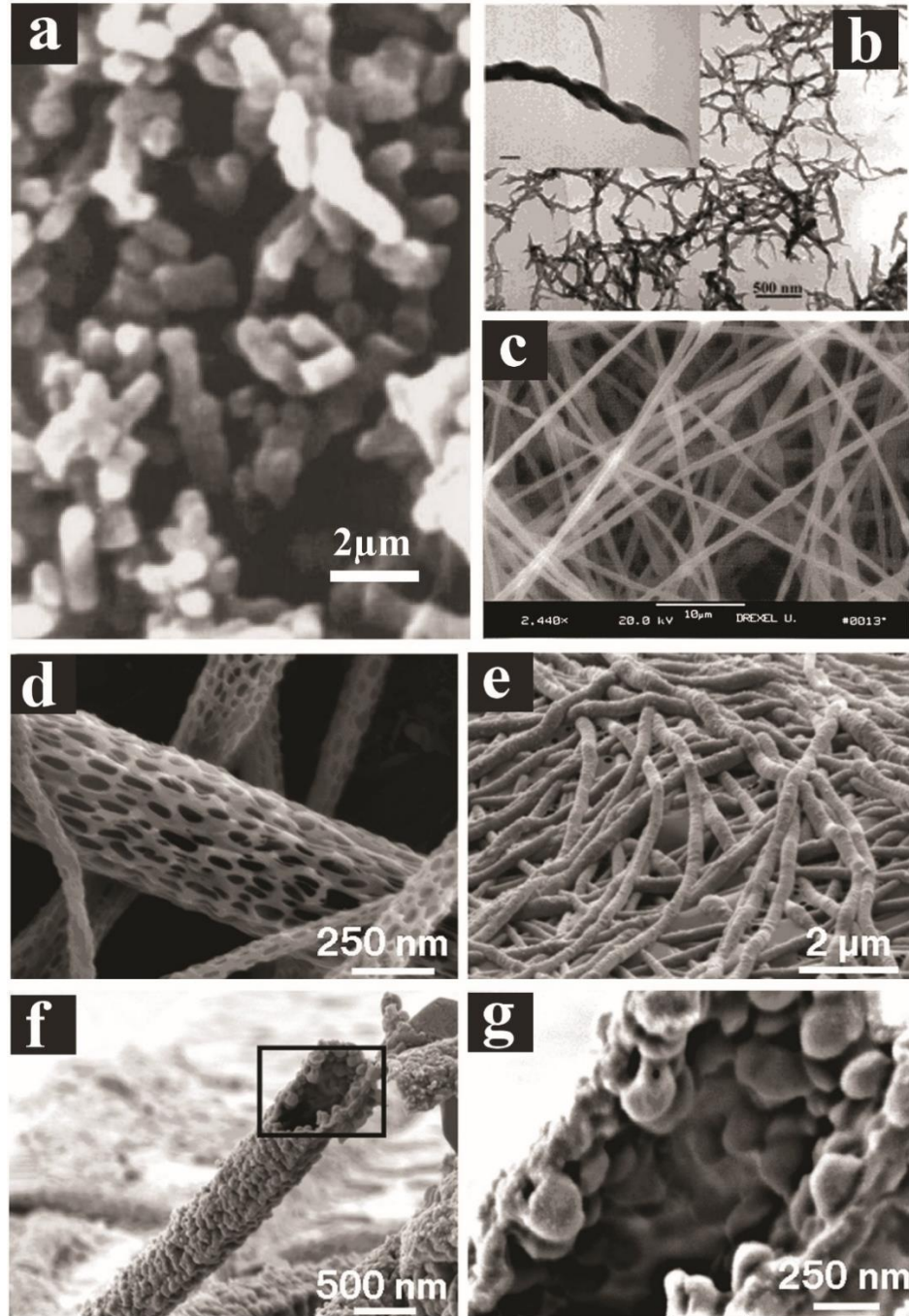


Figure I.4. Examples of CP micro and nanostructures fabricated with the soft template method: (a) PANI nanorods [40], (b) PANI nanofibers [41], (c) PANI/polyethylene fibers [43], and (d-g) hollow PEDOT nanotubes [13].

The flexibility of soft template methods has resulted in the development of a vast amount of unique CP structures, only a few examples of which are highlighted here. The ease of synthesis provided by these techniques combined with the ability to avoid harsh chemical post-processing steps makes them one of the most popular templating methods for biomedical applications. However, there is often a degree of variance in the dimensions of the resulting CP structures, which remains a significant challenge.

Conjugated polymer nanofibers for bioelectronics and bioactuators

CPs have several applications in biomedical engineering including tissue engineering, bioelectronics, neural interfaces, bioactuators, drug delivery systems, and biosensors [4-8]. CPs are considered attractive biomaterials due to their combination of conductivity, biocompatibility, stability in vitro and in vivo, suitability as cell culture substrates, ability to entrap and controllably release biological molecules, and tunability of their properties to suit the intended application. Here, we review prior works utilized CP micro/nanofibers for bioelectronic and bioactuator applications.

Neural interfaces

Over the last two decades, advances in micro and nanoscale technologies have sparked interest in the creation of a robust interface between synthetic devices and neural tissue. Such interfaces hold tremendous potential to overcome some of mankind's most debilitating disorders including physical injury to the nervous system, deafness, blindness, and neural degradation at the hands of degenerative diseases such as Parkinson's disease [44]. As detailed in the previous section, CPs are promising materials for the healing and

replacement of damaged peripheral nerves. However, damaged axons in the CNS do not readily regenerate. Therefore, studies involving CPs have focused largely on the creation of stable brain-machine interfaces. For over 50 years, brain-machine interfaces have been unitized to stimulate or record from the neural tissues of humans and animals [45]. Incredible advances have been made in the development of neural interface technologies. Micro- and macroscale implantable electrodes have been used to treat a wide variety of neurological disorders. For example, deep brain stimulation electrodes have been found to restore significant voluntary muscle control through electrical stimulation of the basal ganglia [46]. These electrodes have also been used to record and study neural activity [47]. A prominent application for this technology has been the translation of neural signals into commands that control robotic arms to assist patients with tetraplegia [48]. The key to these devices is the implantation of electrodes capable of translating bioelectronic signals into electronic signals. These electrodes must be able to communicate with as many discrete neurons as possible with excellent signal quality (signal-to-noise ratio) over variable time frames ranging from a few days to several years [48, 49]. In addition, the electrodes should ideally be biocompatible and integrate smoothly with neural tissue [50]. Furthermore, signals transduced through metals are electronic, while neurons conduct ionic biosignals, thus an ideal electrode would efficiently transduce ionic signals to electronic signals and vice versa [50]. A recent review has detailed neural interface technologies in-depth and discussed several material-based approaches to enhance the long-term performance of neural interfaces [44]. The following covers significant challenges in neural interfacing as

well as some of the most significant and recent developments in neural stimulation and recording.

Perhaps the greatest challenge facing neural interface technologies is the acute and chronic reactive tissue response that arises from implantation of electrodes into the neural tissue. Upon insertion of a neural probe into the CNS, neurons are torn or completely transected, resulting in local swelling that pushes neighboring neurons away from the electrode (Figure I.5(a-c)) [44]. Furthermore, conventional commercially-available neural devices are typically based on materials like gold, platinum, or silicon [51-53]. These electrodes are mechanically hard, principally two-dimensional, and electronically conductive; thus, they are not intrinsically compatible with neural tissue which is mechanically soft, highly three-dimensional, and functions by ionic conductivity. The mechanical mismatch between the electrode and the neural tissue exacerbates the inflammatory response that can be characterized by presence of activated microglia and reactive astrocytes [50], which are leading to encapsulation of the electrode by gliosis and severely limiting the performance of the electrode *in vivo*. Figure I.5(d) shows immunoreactivity images of the activated microglia (ED1), reactive astrocyte phenotypes (GFAP), neural bodies (NeuN), and neurofilaments (NF) in response to an implanted neural electrode (orange disk) after 4 weeks. It is evident that reactive astrocytes and activated microglia dominate the immediate vicinity of the neural probe, and release neurotoxins [50]. The size and geometry of the neural electrodes have a significant impact on the reactive tissue response. Seymore and Kipke [54] studied the response of rat neural tissue to the implantation of parylene-based shanks with four distinct geometries over a

four week period. They found that chronic encapsulation of the shanks and neural loss was significantly lower when the geometry of the shank was small ($\sim 5 \mu\text{m}$). It is plausible that glial cells could not attach and spread out on such a small surface, and that the thinner shanks were more flexible and better able to match the constant pulsing of brain tissue.

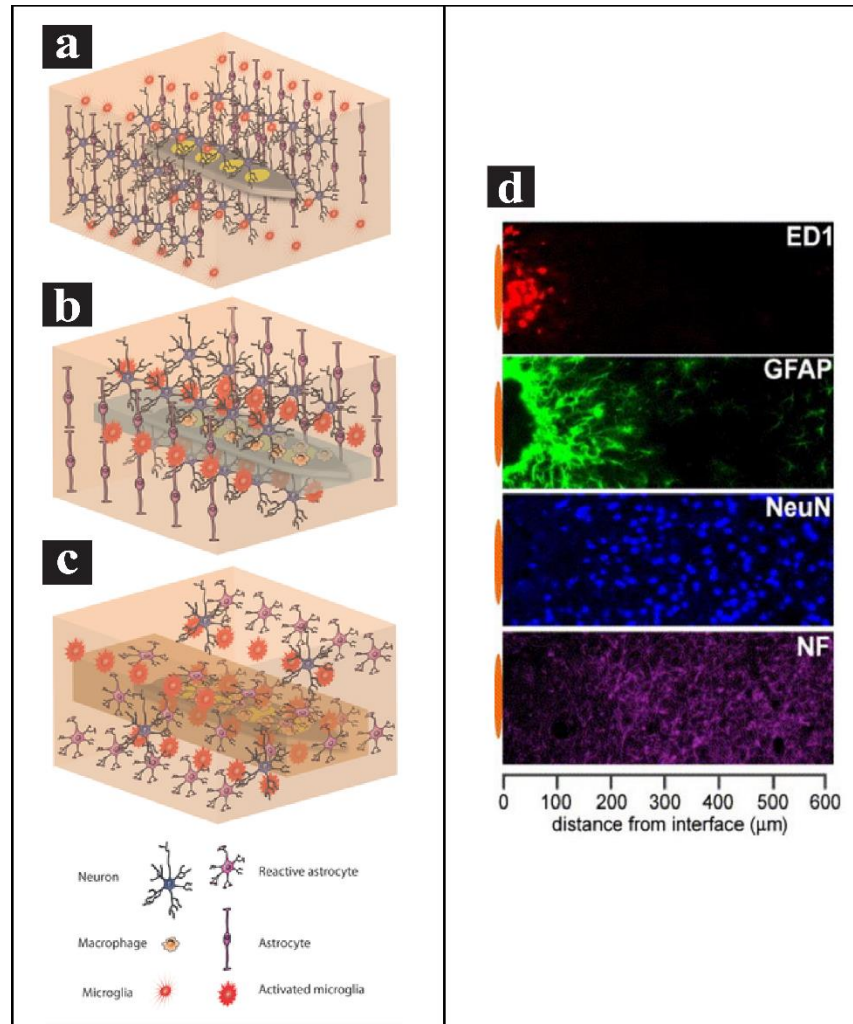


Figure I.5. a-c) Schematics of the reactive tissue responses resulting from inserting a neural probe into neural tissue: (b) acute and (c) chronic tissue responses. d) Immunoreactivity images in response to an implanted neural electrode [50].

Over the past two decades, CPs have been increasingly utilized to improve the electrical properties of neural electrodes including impedance and charge storage capacity while reducing reactive tissue responses. These electrical properties depend heavily on the effective surface area of the neural electrode. Cui and Martin demonstrated that by controlling the amount of charge passing through the working electrode during electrochemical polymerization, the surface area of PPy doped with a synthetic protein (SLPF) could be increased (Figure I.6(a-d)) [55]. As shown in Figure I.6, when the PPy film starts to grow, it forms a very smooth thin layer on the electrode. As the film grows further, the surface roughness of the film increases and a hairy morphology forms which results in a dramatic decrease in impedance of the electrode. However, when the film gets too thick, the impedance starts to increase as a result of the decrease in surface area and detachment of PPy film from the electrode. It is been reported that the film detachment can be reduced by depositing the PPy film on pre-roughened gold substrates. In fact, the roughening pretreatment improves the adhesion of PPy to the gold substrate while simultaneously reducing impedance [56].

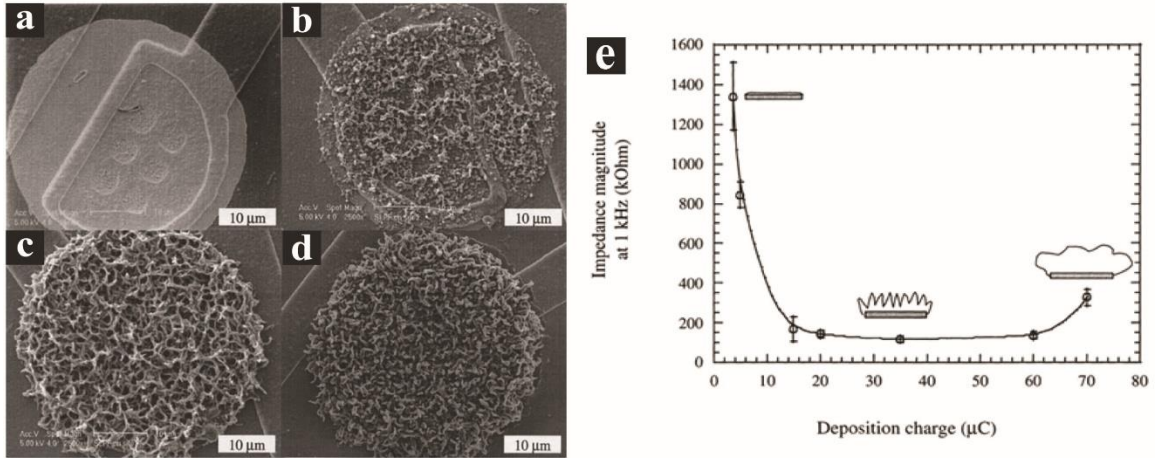


Figure I.6. SEM images of PPy doped with a synthetic protein and coated with a total charge of a) 0 μC , b) 1 μC , c) 4 μC , and d) 10 μC . e) Impedance of PPy film (at 1 kHz) as a function of deposition charge. Cartoons illustrate the film morphology after deposition.

Building on the foundation of flat film studies, several works have aimed to further improve the electrical properties and functionality of neural probes. Abidian et al. developed PEDOT nanotubes that were deposited on neural probe electrodes (Figure I.7) [57]. PEDOT Nanotubes with the diameter ranged from 50 to 140 nm were fabricated after electrochemical deposition of PEDOT on the poly-L-lactic acid (PLLA) template fibers followed by dissolving the template in dichloromethane. PEDOT nanotubes both improved the electrical impedance of the coated neural probes. Compared to PEDOT films, it was found that PEDOT nanotubes improved neural attachment and outgrowth of DRG cells in vitro, and as a result, produce longer neurites [58]. In-vivo experiments showed that the implantation of modified electrodes with PEDOT nanotubes into the barrel cortex of rats improved the impedance and signal to noise ratio (SNR) versus controls and caused significantly higher percentages of sites with high quality recordings (SNR > 4, 65% for PEDOT nanotubes versus 35% for control) on a day-to-day basis [57].

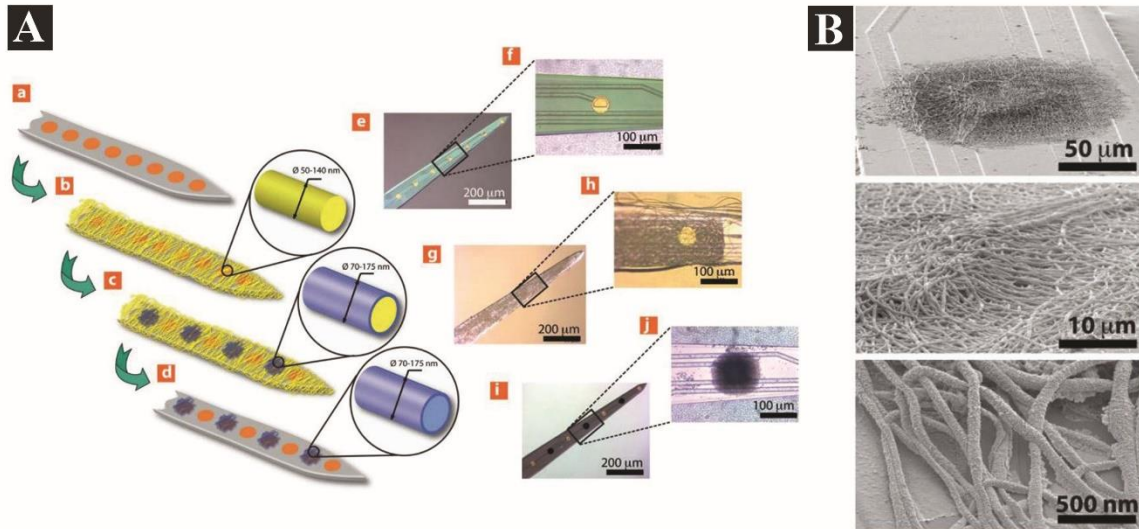


Figure I.7. A) Fabrication of PEDOT nanotubes on neural microelectrodes: Illustrations of electrode sites before (a,e,f) and after PLLA electrospinning (b,g,h), PEDOT deposition and PLLA removal (c,d,i,j). B) SEMs of the PEDOT nanotubes [57].

Other neural recording and stimulation probes were developed to mitigate the mechanical mismatch between hard electrodes and soft neural tissue using hybrid CPs with soft materials such as hydrogel, thereby reducing the reactive tissue responses in vivo. Abidian et al. [59] established a method for fabrication of 3D multifunctional hybrid coatings on neural microelectrode arrays. As illustrated in Figure I.8(a), this process includes electrospinning of drug-loaded biodegradable nanofibers (B), encapsulation of nanofibers by an alginate hydrogel layer (C), and then electrochemical polymerization of PEDOT on the electrode site, around the nanofibers, and within the hydrogel network (D). Optical micrographs of deposited PEDOT (black color) on electrode site are presented in Figure I.8(b) (A: top view, B: side view), which demonstrate vertical growth of PEDOT from an electrode site and through the alginate hydrogel scaffold. In addition, Figure I.8(b) shows SEM images (C, D) of the electrode site after dissolving the alginate coating. These

images reveal that PEDOT was grown around the electrospun nanofibers to form PEDOT nanofibers. They showed that electrical properties of neural microelectrodes significantly improved with these hybrid coatings. For instance, the impedance of the electrode sites significantly decreased from $783 \pm 15.7 \text{ k}\Omega$ to $2.5 \pm 0.5 \text{ k}\Omega$ (about two orders of magnitude) at the frequency of 1 kHz, and the charge capacity density significantly increased from $1.28 \pm 0.6 \text{ mC/cm}$ to $223.8 \pm 6.4 \text{ mC/cm}$.

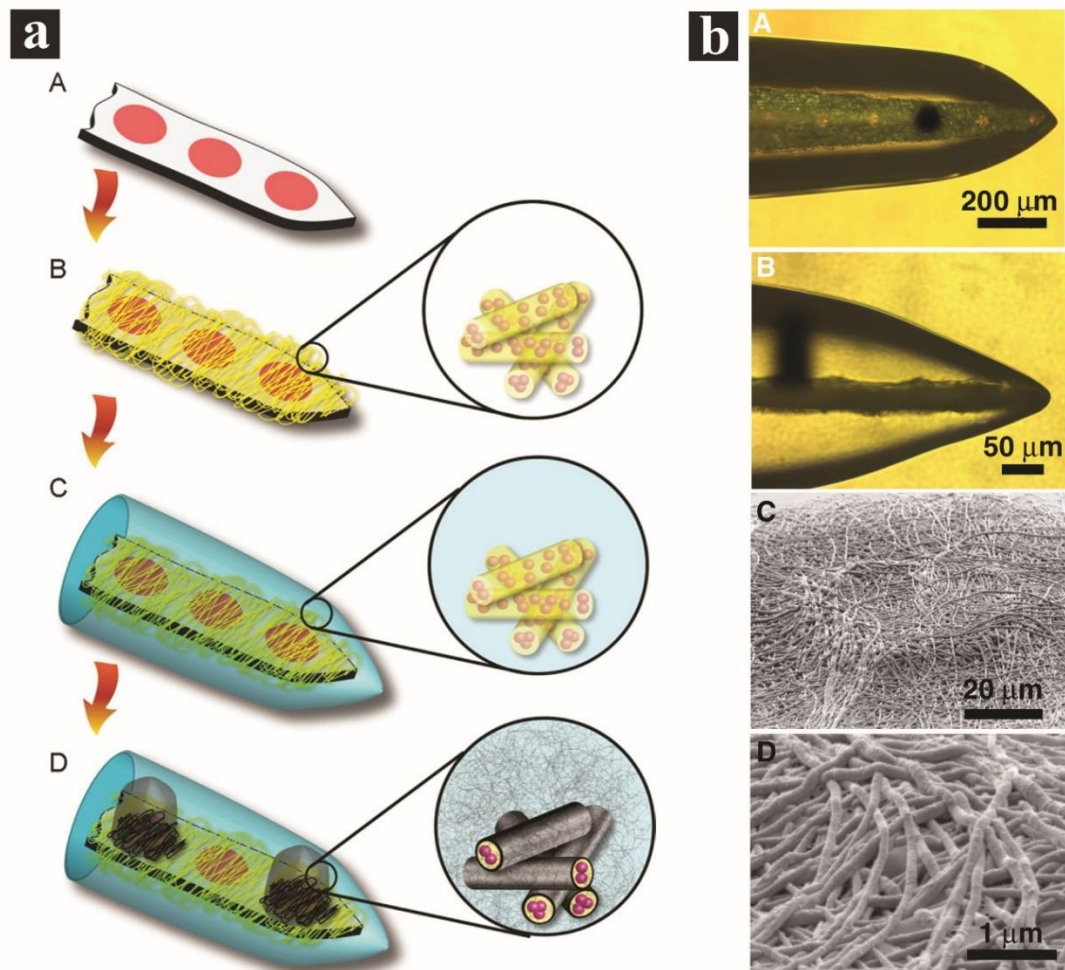


Figure I.8. a) Fabrication process for multifunctional polymer coatings on the neural microelectrodes. b) Optical micrographs (A: top view, B: side view) and SEM images (C,D) of deposited PEDOT (black color) on an electrode site [59].

The development of soft and flexible neural electrodes can significantly reduce reactive tissue responses; however, these electrodes mostly record signals from the surface of the brain, thus greatly reducing signal quality versus implantable neural probes. As demonstrated by Abidian et al. [57-59], future works should focus on the fabrication of implantable neural probes that better match the mechanical properties of neural tissue while providing intimate contact with individual neurons.

Bioactuators

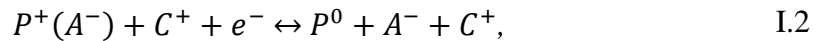
The realization of artificial muscle-like actuators capable of life-like motion has been of increasing interest over the past few decades. Conventional artificial actuators are typically motor-based, and thus face significant challenges when attempting to achieve biomimetic motions. Chief among them is the inherent complexity involved in performing discontinuous and non-repeating tasks [60]. A great deal of materials have been studied to overcome these challenges, including shape-memory alloys [61], ionic polymer-metal composites, piezoelectronic polymers and dielectric elastomers [62, 63], and carbon nanotubes [64]. CPs are attractive alternatives because their actuation mechanism relies on ion and solvent transport in response to electrical oxidation and reduction [65]. Following early studies with CPs that found a volumetric change upon the addition of a dopant, CP actuators emerged in the early 90s and have since been dubbed artificial muscles [66]. CP actuators are well suited to biomedical applications owing to their facile and customizable fabrication routes, established biocompatibility, high strain tolerance (>30%), mechanical strength, low activation voltage, light weight, operability in liquid electrolytes such as

physiological systems, and ability to hold position for long durations and repeatedly cycle between extreme positions [65-67].

The actuation of a CP is initiated by a change in its oxidation/reduction level, causing ions and solvent to enter or leave the polymer matrix in order to maintain equilibrium [68]. This process may be described by



and



where P^+ is the doped (oxidized) state of the polymer, A^- is the anion (dopant), C^+ is the cation, and P^0 is the polymer in its neutral state. When the dopant anion is large, e.g., dodecylbenzenesulfonate (DBS) or polystyrenesulphonate (PSS), it becomes entrapped within the CP matrix and is unable to transport in response to redox processes. Thus, only the mobile cation may migrate to balance the charge neutrality of the system as expressed in Equation I.1. However, for the CP doped with a small anion, both the dopant and the cation may move in response to redox of the system as shown in Equation I.2. In the former case, a reduction of the CP results in volume expansion as cations migrate into the matrix. In the latter scenario, reducing the CP results in mixed transportation of both cations and anions move simultaneously in opposite directions. Continuous actuation will eventually lead to a loss of both species from the CP matrix and thus reduce the longevity of the actuator. More details on CP actuation mechanisms and early works on CP actuators are

detailed in a series of reviews [3, 69]. In the following sections, we will focus on recent developments in CP artificial muscles and highlight controlled drug delivery as an application of CP bioactuators.

Artificial muscles

Most of the initial research on CP artificial muscles focused on PPy. Actuators in liquid electrolytes received the most attention in early studies [3], and are still prevalent in literature. Smela et al. [70] exhibited the controlled curling of $30 \times 1000 \mu\text{m}$ strips, and the folding of a gold cube from $300 \times 300 \mu\text{m}$ panels using controllable hinges. These strips and hinges were comprised of a bilayer of PPy doped with DBS on a thin gold layer, and could be reversibly curled/folded and uncurled/unfolded by applying a 0.35 V and -1.0 V bias respectively (Figure I.9(a)). A subsequent study took the concept of these hinges and constructed a microscale “robot” arm [71]. Each joint, comprised of bilayer PPy:DBS and gold, was individually controlled by applying voltages between 0.2 and -1.0 V, and allowed for the picking up and placement of a $100 \mu\text{m}$ diameter glass bead over a range of $250 \mu\text{m}$ (Figure I.9(b-e)). The PPy/Au micromuscles can operate in biological fluids such as salt solutions, blood plasma, urine, and cell culture medium; therefore, these microrobots could be utilized as a medical tool for minimal invasive surgery. A recent work aimed to create a fully biocompatible actuation platform without the use of metal substrates for in vivo applications [72]. In this work, chemical polymerization of PPy-doped with sodium allyl sulfonate was patterned on silk fibroin (Figure I.9(f)). This method of preparation avoided the common issue of delamination in actuation of PPy films constructed on metal substrates. In fact, the interpenetrating networks formed between silk and PPy prevented

the delamination. The composite material actuated and generated forces comparable with natural muscle (>0.1 MPa).

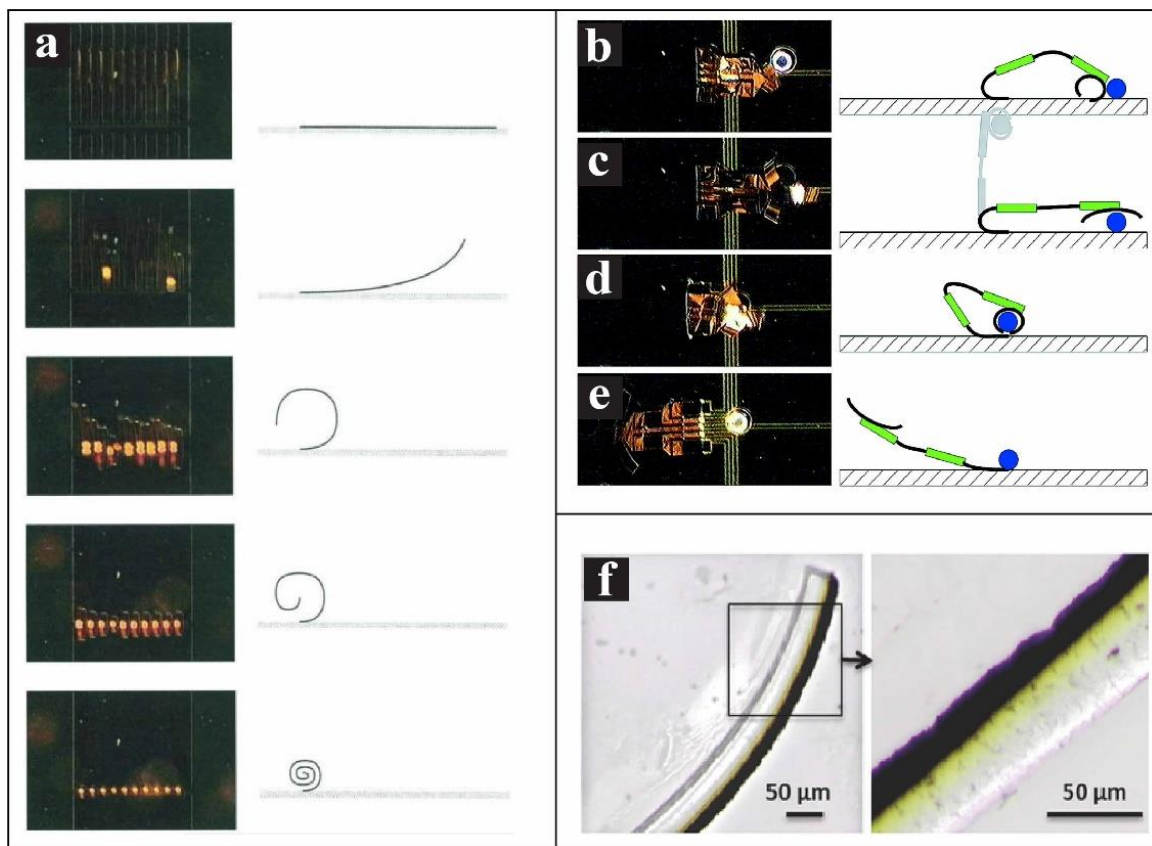


Figure I.9. Bilayer actuators: a) PPy/Au actuators curled in a liquid electrolyte [70], b-e) a microrobot arm with hinges comprised of PPy/Au bilayers [71], and f) a composite actuator composed of PPy (black) bonded to silk fibroin (clear) [72].

Research involving PANI has primarily focused on linear actuators comprised of various fiber composites. An early work sought to create steerable catheters comprised of a hollow tube of polypropylene carbonate, within which PANI fibers were surrounded by a solid polymer electrolyte [73]. The fibers were able to operate in air for a short time. A similar work constructed 2-acrylamido-2-methyl-1-propanesulfonic (AMPSA)-doped

PANI fibers with the diameter of $\sim 80 \mu\text{m}$ and electrical conductivity of $\sim 1000 \text{ S/cm}$ [74]. This composite fiber, when encapsulated by a PMMA/PC/EC/LiClO₄ gel electrolyte and polymer (AMPSA-doped PANI) sheath (with outer diameter of 1.5 mm, inner diameter of 1mm, and wall thickness of $250 \mu\text{m}$, and electrical conductivity of $\sim 400 \text{ S/cm}$) as counter electrode, was able to actuate in air for far longer than its prior works (Figure I.10(a-b)). This actuator can lift an object more than 4500x its own weight, which is a higher strength-to-weight ratio than human skeletal muscles. Another work used aligned polyurethane (PU) fibers coated with PANI to create artificial muscles (Figure I.10(c-f)) [75]. The coated fibers had $\sim 900 \text{ nm}$ diameter with high surface areas imparting a 0.5 S/cm conductivity and achieving a linear actuation strain of 1.65%. The hybrid fibers were also mechanically stable (without significant creep) during actuation and showed the work per cycle efficiency of 75% even beyond 100 actuation cycles. In order to apply these actuation capabilities to biocompatible systems, many works have focused on creating composites of PANI with biocompatible materials. One study incorporated PANI into and surrounding chitosan spun microfibers [76]. These fibers were able to retain a conductivity of 0.029 S/cm while simultaneously showing linear actuation strains up to 0.39%. A recent study created conductive nanofibrous sheets of PLA and PANI in order to enhance the growth of rat cardiomyocytes [77]. The resulting composite nanofiber mats were able to support the attachment of the cardiomyocytes and encourage synchronized spontaneous beating as high as 115 beats/min. The formation of a tube from the PLA/PANI composite combined with the synchronized beating of the cardiomyocytes created a 3D biological actuator with an actuation rate of $\sim 1.6 \text{ Hz}$.

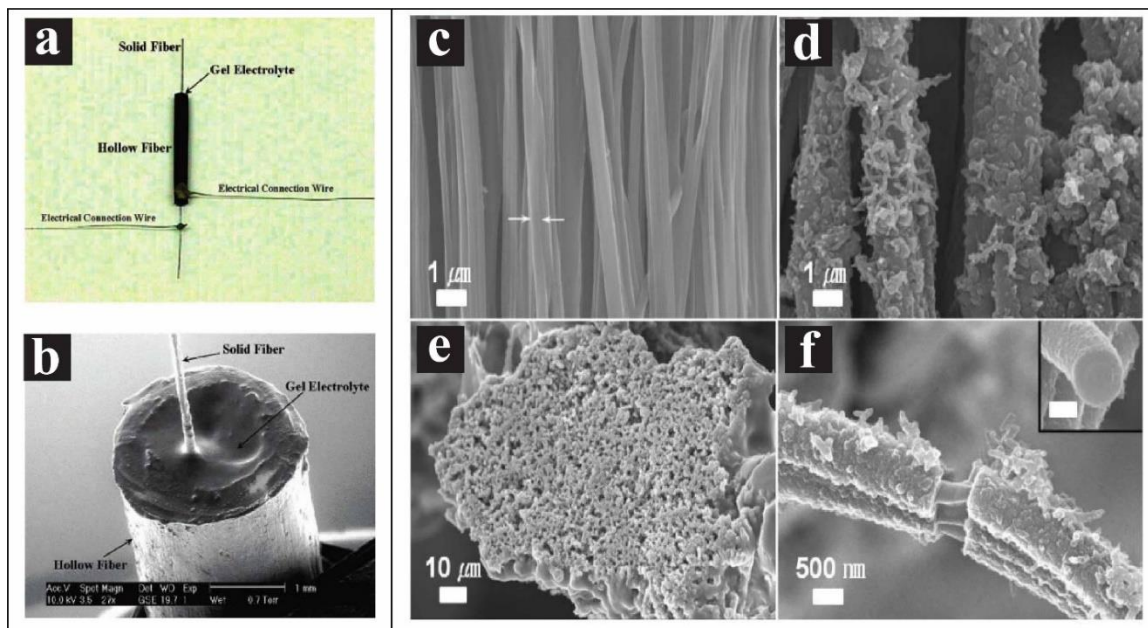


Figure I.10. a,b) A PANI-gel electrolyte solid-in-hollow fiber linear actuator [74]. c-f) PU/PANI fibers: aligned PU nanofibers (c), aligned PU/PANI fibers (d), cross-section of PU/PANI fibers (e), and PANI coating around PU fibers [75].

The actuation capabilities of polythiophene (PT) and its derivatives have also been demonstrated. Early works focused primarily on the actuation of PT conductive gels (Figure I.11(a)) [78]. It has been shown that doping/undoping of PT gels crosslinked by 1,6-(β,β')-bisthieryl-hexane (BTH) under step potentials could cause a significant change in volume [79]. Figure I.11(b) depicts the volume changes associated with doping (at 1.8 V) and undoping (at -0.5 V) of PT-BTH gels in ACN solution containing 0.1 M LiClO₄. A more recent work created tri-layer composites consisting of a PT support layer surrounded by a layer of PPy on either side. One PPy layer was doped with a large anion of DBS (PPy/DBS) and the other was doped with a small anion of perchlorate (PPy/ClO₄) [80]. The variance in doping caused bending of the composite, which was stronger than PPy controls (bi-ionic films PPy (DBS)/PPy (ClO₄)) owing to the PT backbone (Figure I.11(c-

e)). As shown in Figure I.11(d), a 0.4 mg tri-layer composite film can reversibly lift a 10 mg object from position 0° to the position of $+90^\circ$ and -90° at a voltage $+1.0$ V and -1.0 V, respectively. Most of the recent advances in PT actuators have focused on the use of PEDOT due to the chemical stability, conductivity, and biocompatibility of PEDOT. Early works demonstrated PEDOT capability to change the volume in response to electrochemical stimuli. Some of the most recent developments for PEDOT as artificial muscles are highlighted here. A study developed a soft biomolecule actuator comprised of a bacterial cellulose that contained an ionic liquid, and was dip-coated in PEDOT:PSS layers [81]. The resulting actuator was capable of repeatable bending actuation when ± 3 V were applied. It was also flexible and stretchable ($\sim 21\%$ elongation) indicating potential applications for wearable bioelectronics. Another group developed a biocompatible artificial muscle using a combination of multi-walled carbon nanotubes sheets coated with PEDOT/pTS and myoblasts were seeded on the tube surfaces [82]. A PTFE “window-frame” pattern was employed to separate the PEDOT-MWCNT sheet into two regions with and without proliferating myoblasts. They found that the myoblasts could differentiate to form align myotubes, and direct stimulation of myotubes was found to generate contractile forces where cells were seeded. The regions covered with myotubes acted as a power-generating component, and the myotube-free regions acted as a flexible hinge or joint. This combination allowed the device to undergo horizontal length change in aqueous solutions and thus simulate the undulations of a hornworm (Figure I.11(f)). Further developments for CP biological actuators will likely focus on creating faster response times with higher

mechanical strain capabilities that will enable commercial adaptation of these materials for artificial muscles.

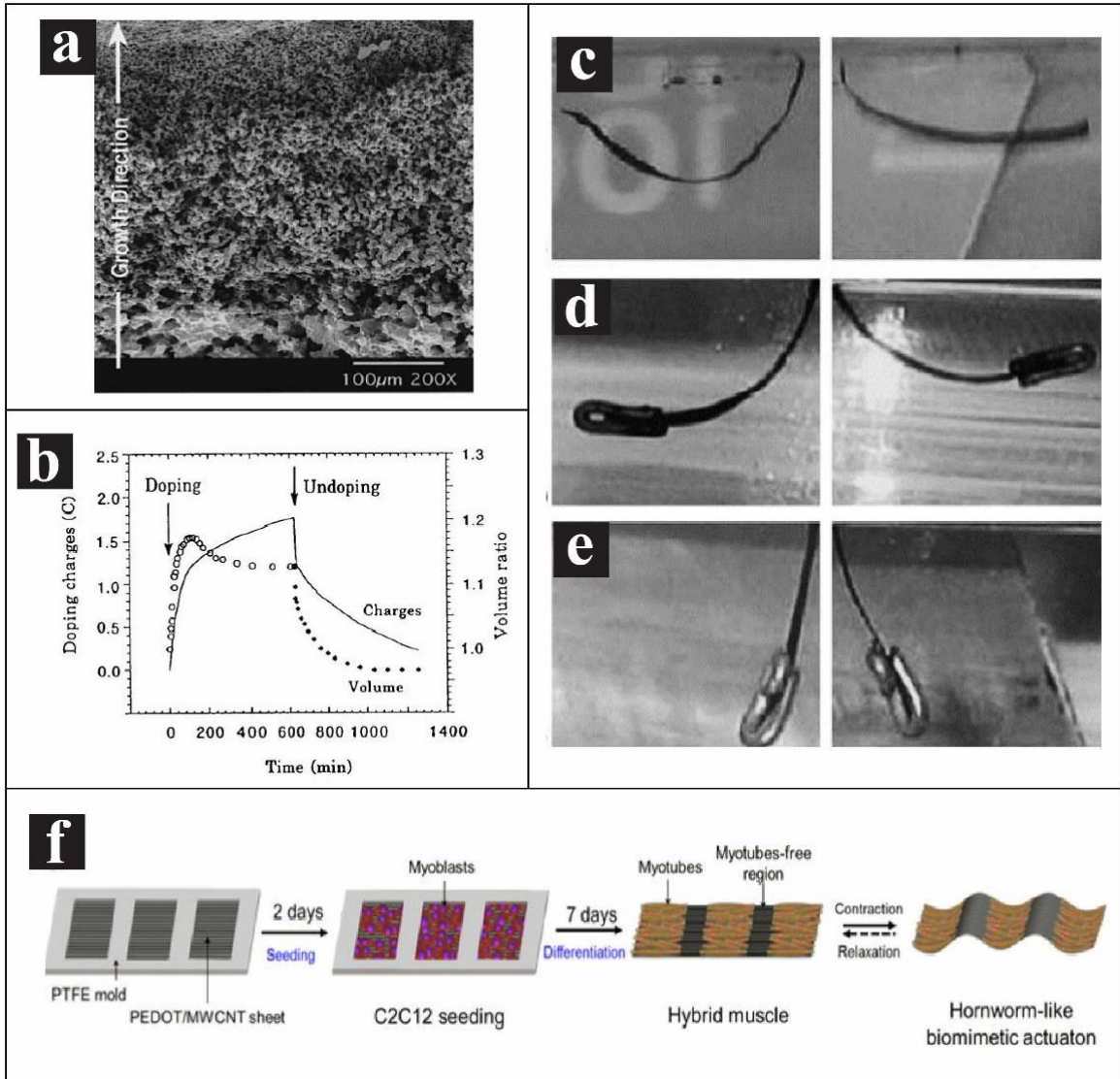


Figure I.11. a-b) SEM of PT gel crosslinked with BTH and its volume change during doping/undoping. c-e) PPy(DBS)/PT/PPy(ClO₄) actuator bends freely (c) or with a 10 mg (d) or 25mg (e) object. f) PEDOT/MWCNT/myotubes actuator.

Controlled drug delivery

The actuation capabilities of CPs have also been promising for drug delivery applications. As mentioned, early works in tissue engineering discovered that the electrical stimulation of PPy could release bioactive compounds that were incorporated into its matrix during electrochemical deposition. More recent works have further developed this methodology through the use of bioactive compounds as co-dopants for controlled release directly from the CP matrix. For example, one group integrated neurotrophin-3 (NT-3) into the PPy matrix as a co-dopant with pTS Figure I.12(c-d) [83]. The amount of NT-3 loaded into the PPy film could be increased with increasing deposition time, up to 130 ng for a 60 min deposition. The NT-3 was then released using three different electrical stimulations for 12 min and 60 min (Figure I.12(c-d)). The electrical stimulations were cyclic voltammetry (+0.8 V to -1 V at 50 mV/s), pulsed potential (± 0.6 V at 5 Hz), and pulsed current (± 0.5 mA and ± 20 mA at 5 Hz), all at 12 and 60 min release times. All these methods were able to increase the rate of drug release over unstimulated diffusion. Another group incorporated dexamethasone (DEX) modified with a negatively charged phosphate group into PPy as a dopant with [84]. The resulting films were stimulated using cyclic voltammetry (-0.8 to +1.4V at 100 mV/s). As the number of cycles increased, the amount of released DEX linearly increased, while it was significantly more than that of unstimulated controls (Figure I.13(a)). The DEX was incorporated with the intent to reduce astrocyte populations near the electrode surface, and in vitro testing showed a significant reduction of astrocyte count on the third day of implantation (Figure I.13(b-e)).

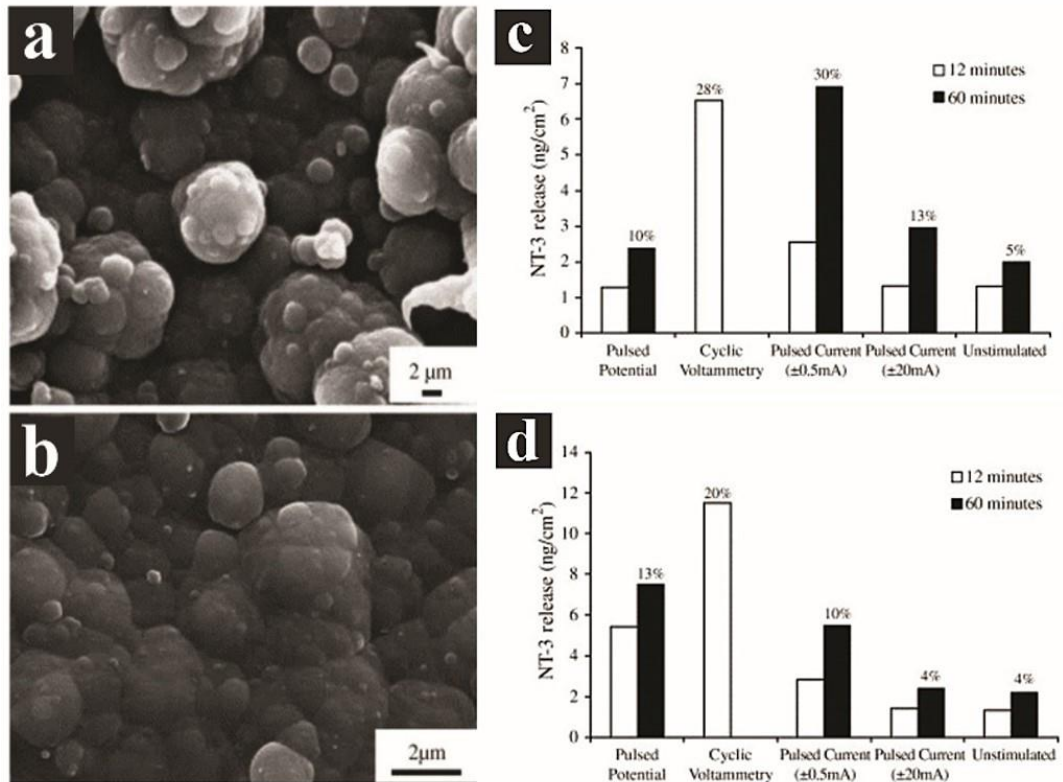


Figure I.12. a, b) SEM of a PPy/pTS polymer film loaded with NT-3 before (a) and after (b) electrical stimulation. c, d) Charts showing NT-3 release versus deposition time and stimulation regime for 3.6 µm (c) and 26 µm (d) PPy films [83].

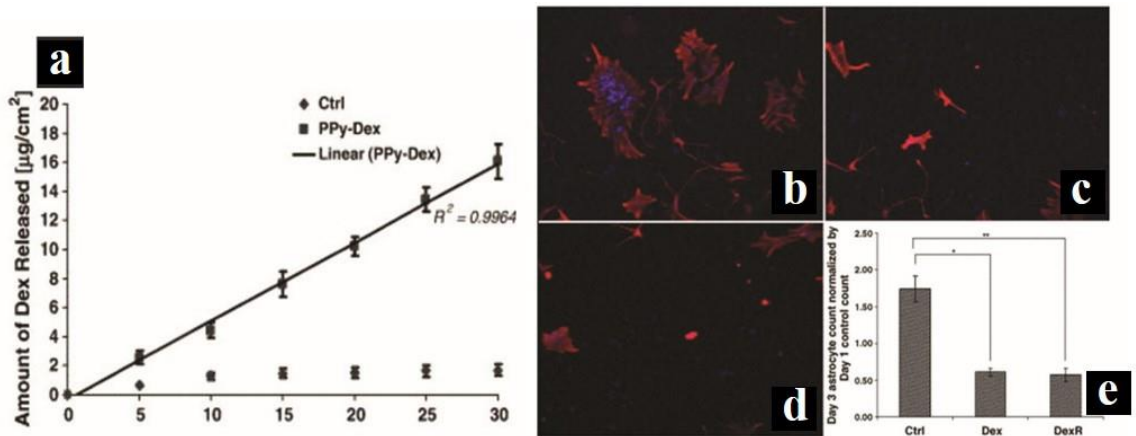


Figure I.13. a) Release of DEX from PPy matrix as a function of CV cycles. b-d) Optical images of stained astrocytes for control (b), DEX added to the media (c), and DEX released from PPy (d). e) Normalized astrocyte counts after 3 days [84].

New strategies have focused on the creation of controllable drug delivery systems through CP actuators. One approach was to create PPy:DBS valves capable of capping a drug reservoir, and controlling drug release from those reservoirs by opening the valves at specific time intervals through the application of a cyclic voltage between 0.5 V and -1V (Figure I.14(a-b))[85]. A more recent work created highly porous reverse opal scaffolds from poly(methyl methacrylate) sub-micron sized colloids as templates, and PPy doped with DBS (Figure I.14(c)) [86]. When loaded with the model drug risperidone and sealed with a layer of PPy:pTS, the application of a cyclic sweeping potential (± 0.6 V at 0.5 Hz) was able to increase the release rate versus unstimulated controls. Another recent work utilized PPy actuators to create an implantable pump [87]. The group doped PPy with a triblock macromolecule comprised of polycaprolactone-block-polytetrahydrofuran-block-polycaprolactone (PCTC). The structure of the pump is shown in Figure I.14(d-e), where PPy/triblock strips were secured to the walls with double sided tape, and actuated with electrical stimulation. In vitro testing showed that the pump was able to output 0.35 $\mu\text{L/s}$ over 20 actuation cycles using a driving current density of 1.0 mA/cm^2 . Another study templated PEDOT nanotubes using PLGA nanofibers loaded with DEX [13]. In Figure I.15(a-d), the drug release from uncoated and PEDOT-coated electrospun PLGA fibers were compared. The PEDOT coatings restricted drug release avenues, and by applying +1 V potential for 10 s at specified time intervals, mechanical force imparted by PEDOT during oxidation forced the controlled release of DEX from the coated PLGA fibers (Figure I.15(e-f)). The above works represent some of the most recent developments in the field of artificial muscles and drug delivery via CP actuation.

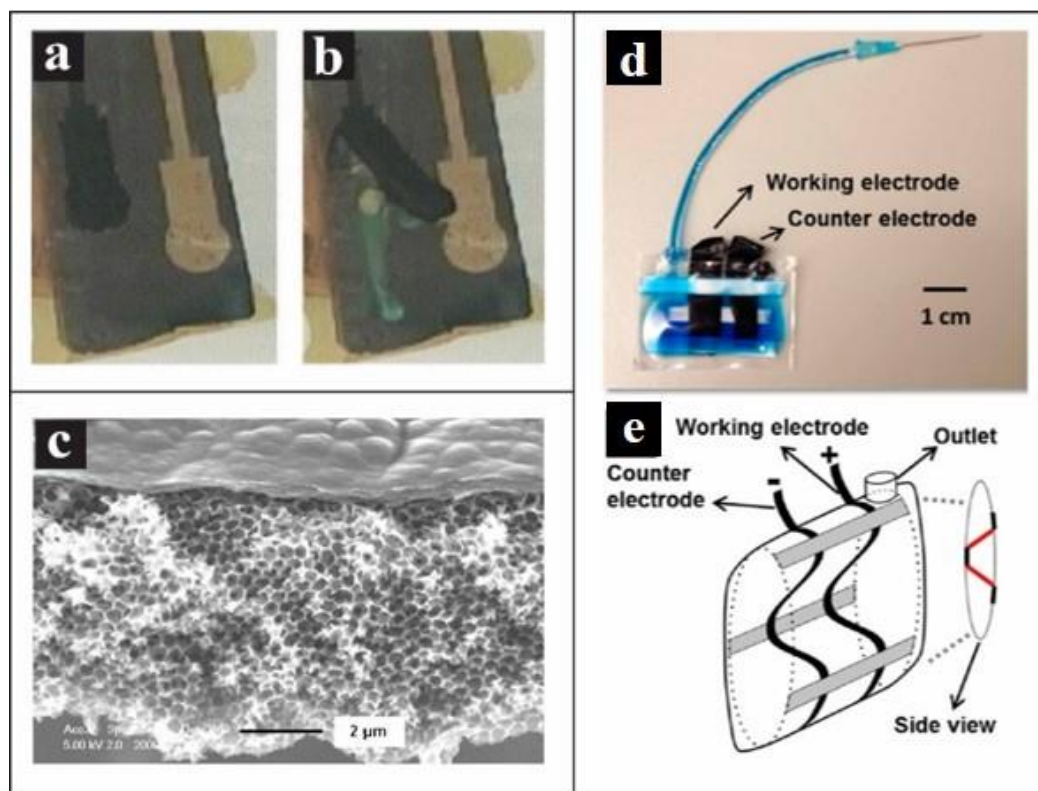


Figure I.14. a-b) PPy(DBS)/Au bilayer valve in the closed (a) and open (b) position [85].
 c) Reverse opal PPy films made by PMMA colloidal crystals template [86].
 d-e) An electroactive pump operates with PPy doped with PCTC [87].

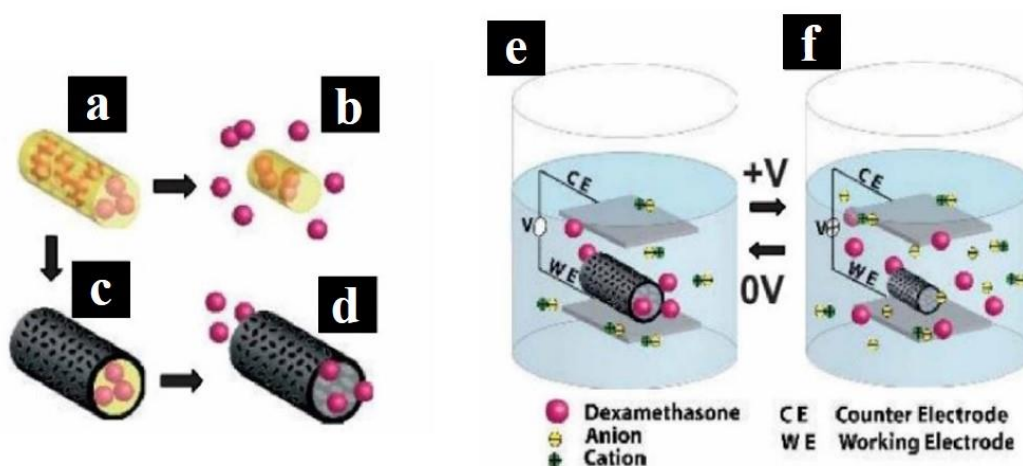


Figure I.15. Controlled drug release: Drug release from a degradable fiber (a,b) and CP-coated degradable fibers with restricted release avenues (c,d). Controlled drug release from nanotubes via electrical stimulation (e,f) [13].

Research Objectives

In summary, the primary objective of this thesis is to demonstrate the state-of-the-art utilization of CP nanofibers, which are created through templated electropolymerization, for development of organic bioactuators and bioelectronics. As schemed in Figure I.16, templated CP nanofibers are composed of a core biodegradable nanofiber covered by a CP layer. Accordingly, in this thesis, we first focus on creation and development of the nanofiber template made of biodegradable polymers which can also be loaded with various drugs or proteins for on-demand and controlled drug/protein delivery. This phase of research was conducted in three different projects (Project 1 to Project 3) as illustrated in the flowchart in Figure I.16. In Project 1, we investigated the effect of spatial orientation of drug-loaded biodegradable nanofibers (highly aligned vs. randomly-oriented nanofibers made by electrospinning method) on their drug release profile (Chapter II). In project 2 (Chapter III), we utilized coaxial electrospinning for encapsulation of fragile proteins (nerve growth factors) into core-shell nanofibers. In this project, we systematically studied the effect of coaxial electrospinning parameters on the size and size distribution of the core-shell nanofibers using design of experiment (DOE) approach, and also mathematically modeled their protein release profile based on experimental data. In project 3 (Chapter IV), we demonstrated the application of drug-loaded biodegradable fibers for skin drug delivery. In this project, we presented a novel transdermal patch made of biodegradable fibers encapsulated with an anti-inflammatory drug (dexamethasone) and assessed its drug delivery efficacy both in-vitro and in-vivo.

In the second and main phase of this thesis, templated CP nanofibers are introduced for development of bioactuator and bioelectronic devices. This phase of research includes three projects (Project 4 to Project 6) as shown in the flowchart in Figure I.16. In Project 4 (Chapter V), we studied ions transportation in actuation of CP nanofibers through direct mass measurement via electrochemical quartz crystal microbalance technique. Understanding the actuation behavior of CP nanofibers, in Project 5 we utilized them for development of high performance organic electronic actuators for soft robotics and bioinspired applications (Chapter VI). In this project, we developed a novel bilayer bending actuator based on CP nanofibers that efficiently operate in liquid and gel-polymer electrolytes. In Project 6 (Chapter VII), we demonstrated the utilization of CP nanofiber-based bioactuators for articulating movable neural probes. In this project, we first microfabricated flexible neural probes with two projection designs using standard photolithography. Then, we constructed an active layer of CP nanofibers on the probe projections to create movable projections. We ultimately demonstrated the functionality of the fabricated movable neural probes in cerebral environment.

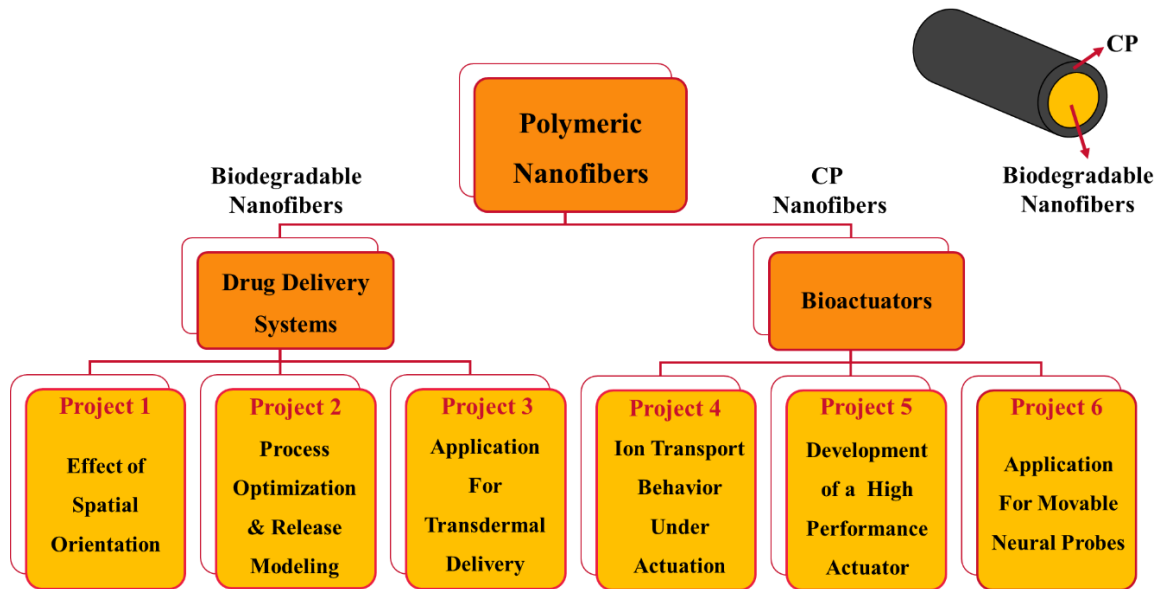


Figure I.16. Flowchart summarizes the research objectives studied in this thesis. Schematic illustrates a CP nanofiber fabricated using a template biodegradable nanofiber.

II Electrospinning of Highly Aligned Fibers for Drug Delivery Applications

This chapter is published as is in the journal of *Materials Chemistry B* 7.2 (2019): 224-232.

Abstract

Electrospinning is a straightforward, cost-effective, and versatile technique for fabrication of polymeric micro/nanofibers with tunable structural properties. Controlling the size, shape, and spatial orientation of the electrospun fibers is crucial for utilization in drug delivery and tissue engineering applications. In this study, for the first time, we systematically investigate the effect of processing parameters, including voltage, syringe needle gauge, angular velocity of rotating wheel, syringe-collector distance, and flow rate on the size and alignment of electrospun PLGA fibers. Optimizing these parameters enabled us to produce highly aligned and monodisperse PLGA fibers (spatial orientation >99% and coefficient of variation <0.5). To assess the effect of fiber alignment on the release of encapsulated drugs from these fibers, we incorporated dexamethasone, an anti-inflammatory drug, within highly aligned and randomly oriented fibers with comparable diameters (~0.87 μm) and compared their release profiles. In-vitro release studies revealed that the aligned fibers had less burst release (~10.8% in 24 hr) and more sustained release (~8.8% average rate of change for 24 days) compared to the random fibers. Finally, the degradation modes of the aligned and random fibers after 25 days incubation were characterized and compared. The findings of this study can be applied for the development

of 3D degradable aligned fibers for controlled drug release and tissue engineering applications.

Introduction

Generation of electrospun fibers with controlled size, surface morphology, and alignment is crucial for the development of electronic, photonic, and biomedical devices [88]. The electrospinning process utilizes electrohydrodynamic phenomena to draw fibers from a solution [89]. This technique is relatively cost-effective and simple for fabrication of ultrathin fibers from organic and organic/inorganic solutions [90, 91]. The electrospun fibers have been widely used in electronics and photonics [92, 93] (e.g., organic light emitting diodes [94], photovoltaics [95], and field effective transistors [96]), and bioengineering [97] (e.g., tissue engineering [98], drug delivery [59], neural interfaces [57, 99], biosensors [100, 101], and wound dressing [102]). High molecular weight polymers, such as poly(vinyl pyrrolidone), poly(ϵ -caprolactone), poly(methyl methacrylate), and poly(ethylene oxide) have been mixed with conducting polymers such as poly(3-hexylthiophene) [103] and polyaniline to generate electrospun conductive fibers for electronic devices [104, 105]. In Biomedical applications, a wide variety of natural and synthetic polymeric fibers have been produced using electrospinning process [106, 107]. Among these polymers, poly(lactic-co-glycolic acid) (PLGA), a FDA-approved biodegradable polymer, has become particularly popular for drug delivery purposes [108-110] due to its excellent biocompatibility, biodegradability, and high encapsulation efficiency for a broad range of compounds, including small hydrophobic drugs [111-113].

Moreover, the degradation of PLGA can be tuned by changing the lactic to glycolic acid ratio and thus, the rate of drug release can be precisely tailored [113-115].

The traditional electrospinning set up on a stationary substrate generates a nonwoven mat of randomly oriented fibers due to the bending instability of the highly charged jet [89, 116]. This nonwoven fiber mat provides a three-dimensional (3D) porous structures that can support cellular attachment and growth and is thus, of interest for wound dressing and tissue engineering [102, 117]. In contrast, uniaxially aligned fibers can be produced on a rotating drum [118], edge of a rotating wheel [119], or between a pair of split parallel substrates [120]. The control of spatial orientation of fibers can enhance their electrical and optical properties and ultimately improve the performance of electronic and photonic devices [121, 122], whereas the nonwoven fiber mat morphology interrupts a charge transport process by limited fiber-to-fiber contacts and scattered transport directions along unaligned fibers.

Although the electrospinning process is quite straightforward, several parameters must be carefully adjusted to achieve spinnable regime and, at the same time, control size, alignment, and morphology of fibers. These parameters can be categorized into processing parameters (including electrical field, flow rate, and syringe needle gauge), material parameters (including viscosity, ionic conductivity, molecular weight) and ambient parameters (including humidity and temperature) [123, 124]. Although the material and ambient parameters are considered as more decisive factors for spinnability and uniform shape of the fibers, processing parameters can also significantly influence the size and alignment of the produced fibers [125]. For instance, we previously demonstrated that the

polymer solution concentration and flow rate could alter the shape and size of the randomly oriented fibers, respectively [126, 127]. Zhou *et al.* reported that the needle gauge and electrical field had a drastic impact on the size of fibers. These authors found that the thinner fibers were formed as the size of needle and electrical field increased [128]. In another study, Zhao *et al.* showed that increasing the flow rate led to generation of thicker fibers [129].

While previous studies have reported on the effect of electrospinning parameters on size and alignment of the resulting fibers [128, 129], a comprehensive investigation to: (1) identify the effect of processing parameters on physical properties of fibers and (2) determine the optimized processing parameters that enhance the alignment of fibers; with identical materials parameters and ambient conditions is essential for reducing the cost of fabrication of large-area arrays of fibers and enhancement of device performance [130]. In particular, for the drug delivery applications the release profile may be affected by the orientation of the fibers.

Here we report, for the first time, a systematic study on processing parameters influencing the morphology of electrospun aligned PLGA fibers. Through optimization of these factors, we were able to generate highly aligned monodisperse fibers (with spatial orientation of >99% and coefficient of variation of <0.5%). We hypothesized that the alignment of the fibers has an impact on the release of encapsulated drug from these fibers. To test this hypothesis, dexamethasone (DEX), an anti-inflammatory drug, was incorporated within randomly oriented and highly aligned PLGA fibers with comparable size and fiber density, and the DEX release profiles were compared. One attractive feature

of electrospinning is its ability to generate fibers with nearly uniform size [131]. Moreover, this method can be utilized to create a uniform dispersion of drugs within a polymeric matrix, with high loading capacity and drug encapsulation efficiency [132, 133].

Methods

Materials

Poly(lactide-*co*-glycolide) (PLGA) (75 : 25 8.5E) was purchased from Lakeshore Biomaterials. Dichloromethane (DCM) and chloroform were purchased from Sigma Aldrich. Chloroform (99.8%) was obtained from Acros-Organics. Organic soluble dexamethasone (DEX) was purchased from Enzo Company. Phosphate buffered saline (PBS) tablets was purchased from Fisher Scientific. N-type Si wafers insolated with SiO₂ were obtained from University Wafers company. Si wafers were coated with chromium and gold for thickness of 20 nm and 100 nm, respectively.

Electrospinning of aligned PLGA fibers

A homogeneous solution of 14 wt% PLGA was prepared by dissolving 2.17 g PLGA in 10 ml DCM at room temperature. A typical electrospinning setup consisting of a syringe pump (Logato 100, KD Scientific, Figure II.1(A-a), a rotating wheel (diameter 25 cm, Figure II.1(A-b) connected to a motor (Caframo BDC6015), and a high voltage power supply (PS/ER40P07, Glassman High Voltage, Inc., Figure II.1(A-c) were used to produce aligned PLGA fibers. Electrospinning was performed at room temperature (25 °C) and humidity of 30%. PLGA fibers were collected on 5×20 mm plastic coverslip substrates, which were coated with 100 nm of gold layer (sputter coater Quorum EMS 150R S) and

attached to the edge of the wheel (Figure II.1(A-b)). The inner diameters of the syringe tip were 0.69 mm, 0.60 mm, 0.51 mm, 0.41 mm, and 0.34 mm for needle gauge numbers of 19, 20, 21, 22 and 23, respectively.

Size, alignment, and shape measurements

Optical images (Carl Zeiss Imager Z1, Germany) were used for qualitative assessment of fibers. Scanning electron micrographs (SEM) (Hitachi SU8230) were used for quantitative assessments. The diameter, alignment, and shape of electrospun fibers (n = 100) were characterized using Image J software (NIH) as previously reported [134, 135]. The cylindrical shape of fibers was evaluated by measuring the change of diameter along the length of 150 μm (conical ratio).

Surface roughness measurement

Materials confocal microscopy (LSM800 Zeiss, Germany) and ConfoMap software (Zeiss, Germany) were used to generate 3D surface topography and measure the root mean square of surface roughness of PLGA fibers.

Compositional characterization

The infrared spectra of the samples were measured by Fourier Transform Infrared (FTIR) spectrometry (Cary670 spectrometer, Agilent Technologies) in the range of 850-3250 cm^{-1} at room temperature in reflection mode (n = 64 scans per sample).

Physical characterization

X-ray diffraction (XRD) pattern of samples were recorded over a wide range of Bragg angles ($2\theta = 5^\circ - 90^\circ$) with a scan rate of $0.03^\circ \text{ s}^{-1}$ using an X-ray diffractometer (Pan Analytical) with Cu $K\alpha$ radiation generated at 40 kV and 40 mA. Differential scanning calorimetry (DSC) thermograms of the samples were obtained using a calorimeter (Mettler-Toledo, DSC1) in the temperature range of $0 - 400^\circ\text{C}$ at the heating rate of $10^\circ\text{C}/\text{min}$ under nitrogen atmosphere.

Drug release

The release profile of DEX from aligned and randomly oriented PLGA fibers was investigated in 1X PBS solution. To prepare DEX-loaded PLGA solution, 993 mg PLGA (10 wt.%) and 75 mg DEX were dissolved in 6 ml chloroform by stirring over night at room temperature. Then, the prepared solution was electrospun (at room temperature 25°C and 30% humidity) on rectangular shaped ($1 \text{ cm} \times 0.5 \text{ cm}$) gold-coated Si wafers ($n = 80$). To generate aligned and randomly oriented fibers with comparable diameter ($0.87 \pm 0.21 \mu\text{m}$) the processing parameters were accordingly adjusted. For aligned fibers, Si substrates were attached to the edge of rotating wheel and fibers were collected for 30 min using a syringe needle gauge 22, voltage (V) = 10 kV, flow rate (Q) = $400 \mu\text{l}/\text{hr}$, collector distance (L) = 10 cm, and the collector angular velocity (w) = 1000 rpm.

Random fibers were electrospun on the Si substrates for 45 s using a syringe needle gauge 23 at voltage (V) = 10 kV, flow rate (Q) = $100 \mu\text{l}/\text{hr}$, and collector distance (L) = 11 cm. The electrospinning time was selected 30 min for aligned fibers and 45 s for randomly

oriented fibers in order to collect approximately the same amount of electrospun fibers. To test whether the amount of aligned and random fibers on Si substrates were comparable, DEX-loaded PLGA fibers were dissolved in chloroform and then the amount of the DEX was detected at 240 nm using a UV-vis spectrophotometer (Molecular Devices SpectaMax) and compared. All samples were UV sterilized for 2 hrs, then they were placed in plastic Petri dishes (two same samples per Petri dish) containing 6 ml PBS solution (1x, pH 7.4) and sealed by parafilm. Samples were then kept in incubator (Eppendorf 170S) at 37 °C for different time periods. Since DEX is not water soluble, to quantify the amount of DEX released from the fibers, an inverse approach was employed. To this end, first, the samples were removed from PBS at different time points and immersed in chloroform, and the unreleased DEX was detected and measured. The amount of DEX released from PLGA fibers was then calculated based on a calibration curve and by subtraction of the measured amount of unreleased DEX from the total amount of DEX loaded into PLGA fibers. To maintain the sink condition during the drug release measurements, the amount of DEX for drug encapsulation was selected according to the maximum solubility of DEX 12.5 mg/ml in chloroform.

Statistical analysis

Statistical analysis of data was performed by one-way ANOVA and *post hoc* test (Tukey's test) to find significances between sample groups (Origin Pro, Northampton, MA). Data are presented as mean \pm standard deviation (SD) ($n = 5$) in Figure II.8 and as mean \pm standard error of mean (SEM) ($n = 100$) in Figure II.2 and Figure II.3.

Results and discussion

A set of preliminary experiments was performed to determine the spinnable range of processing parameters, including voltage (V), flow rate (Q), needle-collector distance (L), syringe needle gauge (G), and angular velocity of rotating wheel (w), by which uniform fibers can be produced (summarized in Table III.1). First, we found that a PLGA solution concentration in the range of 10-14 wt.% was required to obtain uniform fibers. The concentrations lower than 10 wt.% produced beaded fibers while higher than 14 wt.% did not generate fibers. This finding was in agreement with the PLGA concentration range previously reported by others in the literature [136]. Here, we used the solution of 14 wt.% PLGA to investigate the effect of processing parameters on the size and the alignment of electrospun fibers. Figure II.1(B-C) show the SEM images of aligned PLGA fibers that were produced using the processing parameters of $V = 12$ kV, $Q = 400$ μ l/hr, $w = 1000$ rpm, $G = 22$, and $L = 14$ cm. The diameter of PLGA fibers was 2.82 ± 0.7 μ m. SEM images in Figure II.1(B-C) illustrate the surface morphology of highly aligned PLGA fibers (spatial orientation = $99.3 \pm 0.5\%$). Figure II.1(D-E) show the optical images of highly aligned ($99.3 \pm 0.5\%$) and relatively less aligned ($94.7 \pm 2.9\%$) PLGA fibers, respectively.

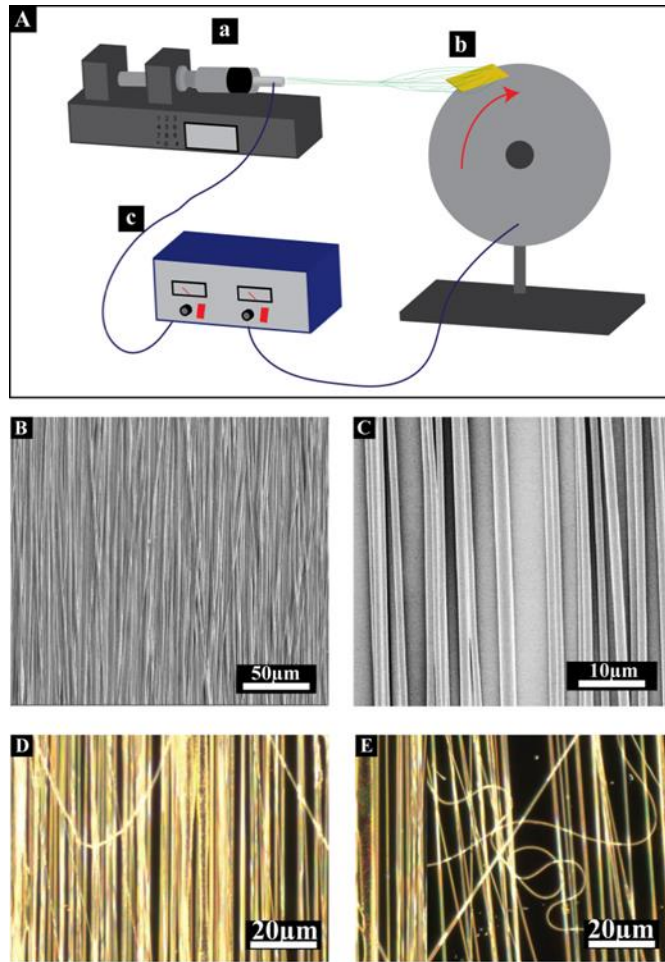


Figure II.1. A) Electrospinning setup for production of aligned fibers: (a) syringe pump, (b) rotating wheel, and (c) power supply. B-D) SEM and optical images of highly aligned PLGA fibers. E) Optical image of relatively less aligned fibers.

The effect of processing parameters on the diameter of aligned PLGA fibers is presented in Figure II.2. As shown in Figure II.2(A), the diameter of fibers varied from $1.37 \pm 0.02 \mu\text{m}$ to $1.30 \pm 0.02 \mu\text{m}$, $1.33 \pm 0.02 \mu\text{m}$, and $1.31 \pm 0.02 \mu\text{m}$ as the voltage (V) increased from 6 kV to 8 kV, 10 kV, and 12 kV, respectively. Although not significant, the observed trend of decreased diameter with increasing the voltage is in agreement with the prior reports. For instance, Gu *et al.* reported that the average diameter of randomly

oriented polyester fibers decreased as the applied voltage increased [137]. According to Figure II.2(B), the diameter of fibers significantly decreased ($p < 0.001$ and $p < 0.01$) as the syringe needle gauge number increased from 19 to 23. The resultant fiber diameters at various angular velocities of 100, 200, 400, 600 and 1000 rpm were $1.61 \pm 0.07 \mu\text{m}$, $1.42 \pm 0.03 \mu\text{m}$, $1.35 \pm 0.03 \mu\text{m}$, $1.23 \pm 0.03 \mu\text{m}$ and $1.3 \pm 0.02 \mu\text{m}$, respectively (Figure II.2(C)). This decrease in diameter can be attributed to viscoelastic properties of PLGA, resulting in formation of thinner fibers. There was statistically significant difference in diameter of fibers between angular velocities 100 rpm and 400 rpm, 100 rpm and 600 rpm, 100 rpm and 1000 rpm ($p < 0.001$), and 200 rpm and 600 rpm ($p < 0.01$). In addition, the coefficient of variation (CV) of the fiber diameters ($CV = \sigma / \langle d \rangle$, where $\langle d \rangle$ and σ denote the mean and standard deviation, respectively) decreased from 43% to 24%, 22%, 20%, and 15% when the angular velocity increased from 100 rpm to 200 rpm, 400 rpm, 600 rpm and 1000 rpm, respectively. These results suggested that fibers with significantly narrower size distributions can be produced at higher angular velocities.

The effect of needle tip-collector distance (L) on the size of fibers is shown in Figure II.2(D). The diameter of fibers was $1.36 \pm 0.02 \mu\text{m}$, $1.52 \pm 0.02 \mu\text{m}$, $1.47 \pm 0.03 \mu\text{m}$, $1.42 \pm 0.02 \mu\text{m}$ and $1.46 \pm 0.02 \mu\text{m}$ for the distances of 8 cm, 10 cm, 12 cm, 14 cm, and 16 cm, respectively. While in this case no trend was observed for the diameter of fibers, the size of fibers obtained at the collector distance of 8 cm was significantly less than all the other groups ($p < 0.001$ and $p < 0.01$) except collector distance 14 cm. The effect of flow rate (Q) on the size of fibers is illustrated in Figure II.2(E). The diameters of $1.28 \pm 0.02 \mu\text{m}$, $1.26 \pm 0.02 \mu\text{m}$, $1.3 \pm 0.03 \mu\text{m}$, and $1.26 \pm 0.02 \mu\text{m}$ were obtained using the flow rates of

250 $\mu\text{l/hr}$, 300 $\mu\text{l/hr}$, 350 $\mu\text{l/hr}$ and 400 $\mu\text{l/hr}$, respectively. There was no significant difference between the examined groups. The flow rate range of 250–400 $\mu\text{l/hr}$ was selected because we did not observe formation of fibers below and above this range. In fact, when the flow rates were lower than 250 $\mu\text{l/hr}$, the conical meniscus formed at the syringe tip rapidly solidified. The flow rate higher than 400 $\mu\text{l/hr}$ produced larger droplets at the syringe tip, resulting in less charge density for required electrostatic repulsive forces to overcome the surface tension of the solution and form fibers [138].

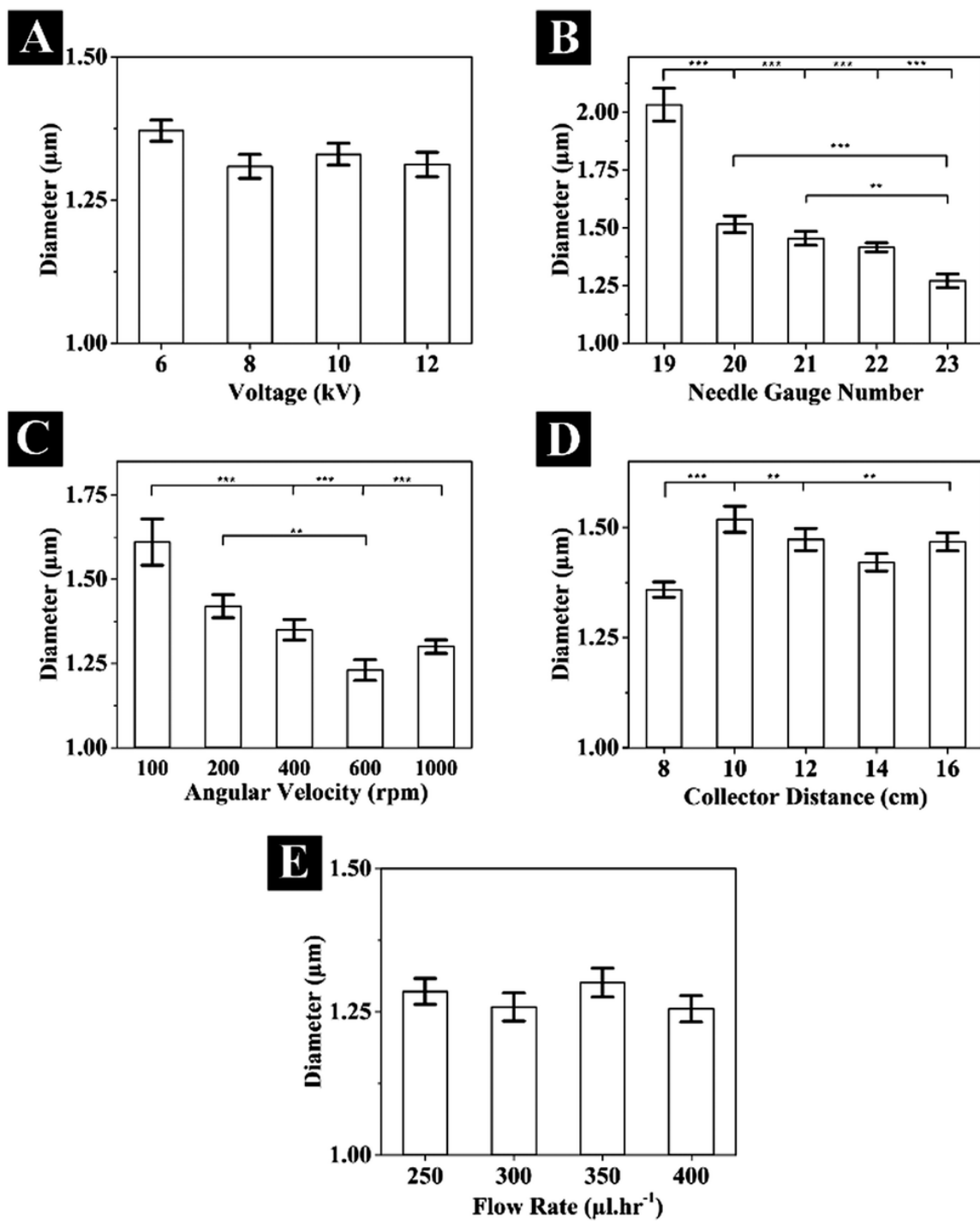


Figure II.2. Effect of electrospinning processing parameters on the diameter of aligned PLGA fibers. The symbols ** and *** indicate the significance level of $p < 0.01$ and $p < 0.001$, respectively. Data is shown in mean \pm SEM ($n = 100$).

The effect of the examined process parameters on the alignment of PLGA fibers is shown in Figure II.3. As the voltage increased from 6 kV to 8 kV, 6 kV to 12 kV, 8 kV to 12 kV, and 10 kV to 12 kV, the fibers alignment significantly decreased from $99.4 \pm 0.04\%$ to $99 \pm 0.07\%$, $99.4 \pm 0.04\%$ to 98.2 ± 0.11 , $99 \pm 0.07\%$ to $98.2 \pm 0.11\%$, and $99.1 \pm 0.08\%$ to $98.2 \pm 0.11\%$, respectively ($p < 0.001$) (Figure II.3(A)). The calculated CV showed monodispersity in alignment [139] for all the groups (i.e., CV of 0.43%, 0.65%, 0.77% and 1.11%, for voltages 6 kV, 8 kV, 10 kV, and 12 kV, respectively). However, it should be noted that the CV increased about 160% when the voltage increased from 6 kV to 12 kV. This result might be attributed to attraction of fibers toward other metallic parts of the wheel, resulting in reduced alignment.

Figure II.3(B) demonstrates the effect of needle gauge number on the alignment of fibers. As depicted, by increasing the needle gauge number, alignment (i.e., spatial orientation) of uniaxial fibers was enhanced. The alignment of fibers was increased from $97.77 \pm 1.0.14\%$ to $98.9 \pm 0.0.08\%$, $98.84 \pm 1.0.11\%$, $99.19 \pm 0.0.07\%$ and $99.35 \pm 0.0.07\%$ as the needle gauge number increased from 19 to 20, 21, 22 and 23, respectively. A statistically significant difference was found between all groups ($p < 0.001$) except between gauge numbers 20 and 21, 20 and 22, and 21 and 22. The wheel angular velocity (w) also had a significant influence on the fiber alignment. As shown in Figure II.3(C), the alignment of fibers was significantly enhanced from $96.04 \pm 0.45\%$ to $97.59 \pm 0.29\%$, $98.68\% \pm 1.0.12\%$, $98.27\% \pm 0.17\%$ and $99.59\% \pm 0.03\%$ by increasing the angular velocity from 100 rpm to 200 rpm, 400 rpm, 600 rpm and 1000 rpm, respectively ($p < 0.01$ and $p < 0.001$). However, no significant different was observed between the angular

velocities 200 rpm and 400 rpm, 200 rpm and 600 rpm, and 600 rpm and 1000 rpm. The calculated CV showed narrow alignment distribution was achieved at higher angular velocity (CV<5%) [139, 140]. The CV of alignment was 3.33%, 1.95%, 1.17%, 1.7% and 0.34% for angular velocities of 100 rpm, 200 rpm, 400 rpm, 600 rpm and 1000 rpm, respectively.

The effect of needle tip-collector distance (L) on the alignment of PLGA fibers is presented in Figure II.3(D). The fiber alignments $97.69 \pm 0.17\%$, $97.04 \pm 0.11\%$, $98.94 \pm 0.07\%$, $98.77 \pm 0.06\%$ and $96.9 \pm 0.12\%$ were obtained for the collector distances 8 cm, 10 cm, 12 cm, 14 cm and 16 cm, respectively. Although there was not any specific trend, the narrowest alignment distribution was found for the collector distance of 12 cm (CV = 0.65%). There was statistically significant difference between all groups ($p < 0.001$) except between the collector distances 10 cm and 16 cm. The fiber alignments $99.23 \pm 0.05\%$, 98.84 ± 0.09 , $99.32 \pm 0.05\%$ and $99.2 \pm 0.07\%$ were achieved for the flow rates 250 $\mu\text{l/hr}$, 300 $\mu\text{l/hr}$, 350 $\mu\text{l/hr}$ and 400 $\mu\text{l/hr}$, respectively (Figure II.3(E)). While no specific trend was observed, there was statistically significant difference between the flow rates 250 $\mu\text{l/hr}$ and 300 $\mu\text{l/hr}$, and between the flow rates 300 $\mu\text{l/hr}$, 350 $\mu\text{l/hr}$ and 400 $\mu\text{l/hr}$ ($p < 0.001$).

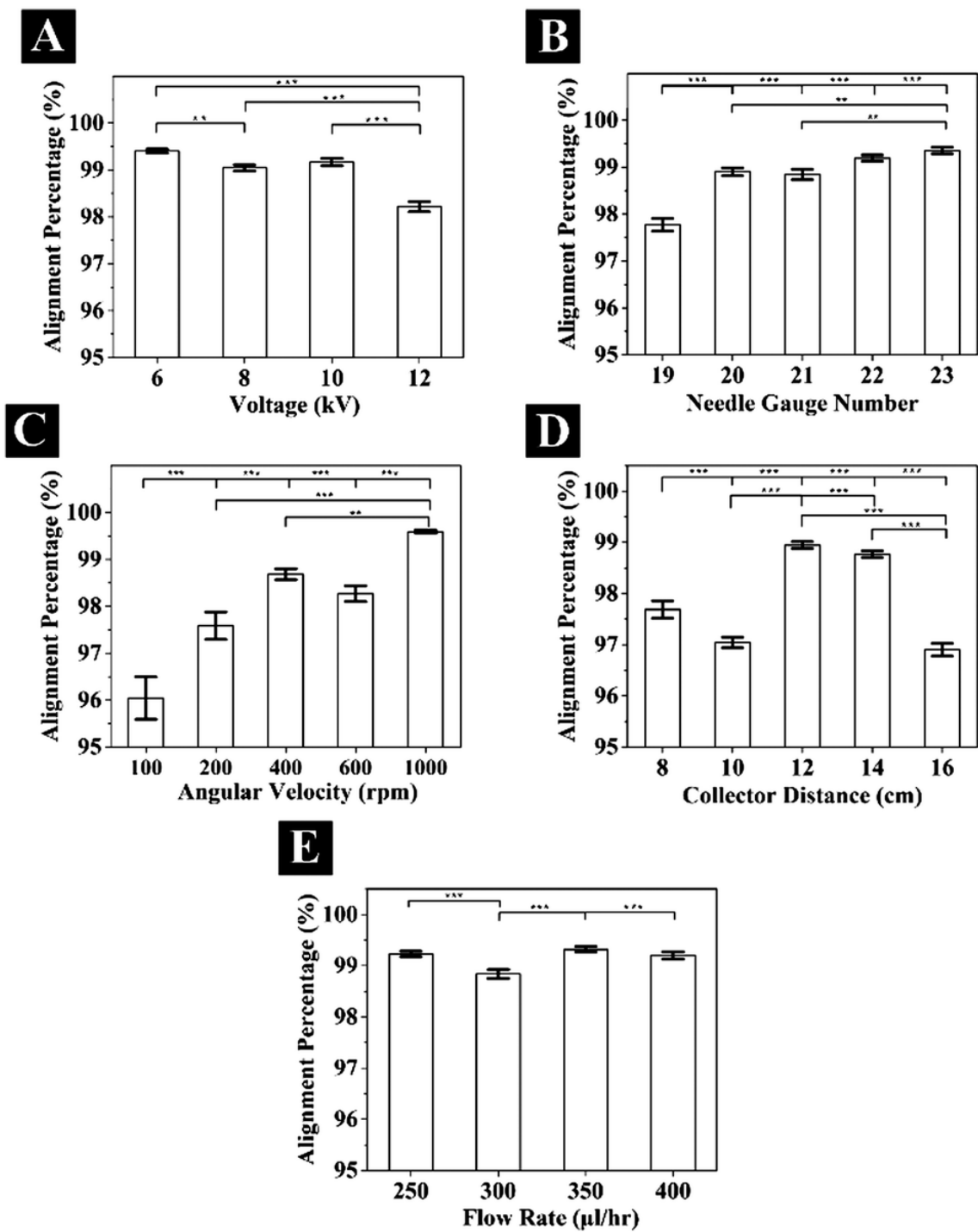


Figure II.3. Effect of processing parameters on the alignment of PLGA fibers. The symbols ** and *** indicate the significance level of $p < 0.01$ and $p < 0.001$, respectively. Data is shown in mean \pm SEM ($n = 100$).

Confocal materials microscopy was utilized to reconstruct 3D height map (Figure II.4) and measure the root mean square (RMS) roughness of the PLGA fibers (Figure II.4(B)). The color map in Figure II.4(A) indicates the variation in size of the electrospun fibers. The diameter of fibers was calculated $2.68 \pm 0.49 \mu\text{m}$, indicating 5% difference between the size of electrospun fiber measured by confocal materials microscopy and scanning electron microscopy. Figure II.4(B) illustrates the oscillation of RMS roughness along the length of fiber for a single PLGA fiber. The RMS roughness of $35.75 \pm 18.41 \text{ nm}$ and $4.99 \pm 0.11 \text{ nm}$ was obtained for PLGA fibers and bare gold (control), respectively. To evaluate the cylindrical shape of aligned PLGA fibers, the conical ratio (D_2/D_1) was calculated by measuring fiber diameters D_1 and D_2 for a fiber length (L) of $150 \mu\text{m}$ (Figure II.4(C)). The results showed that the conical ratio of the fibers was 1.09 ± 0.21 over a length of $150 \mu\text{m}$, indicating a good level of consistency in cylindrical shape of fibers (93%).

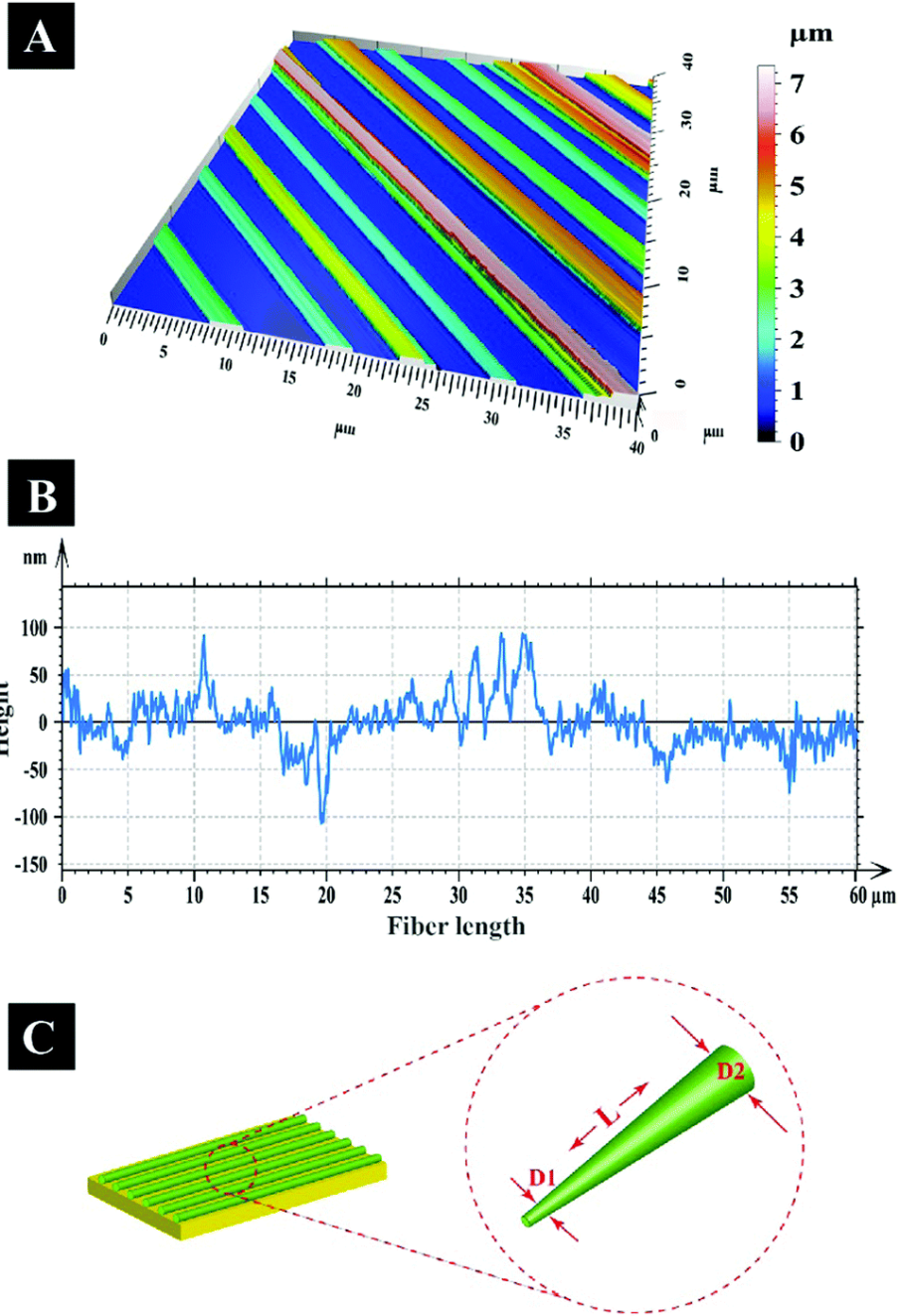


Figure II.4. A) 3D confocal image of aligned PLGA fibers. B) Height profile obtained from the surface of a single aligned fiber to measure RMS roughness. C) Schematic illustrates the conical shape of aligned fibers.

To investigate the effect of spatial orientation of PLGA fibers on drug release profile, DEX was incorporated within the aligned and the randomly oriented PLGA fibers (drug to polymer ratio of 1 : 13.2) with comparable sizes (diameter = $\sim 0.87 \mu\text{m}$). We first calculated DEX encapsulation efficiency in PLGA fibers. The drug encapsulation efficiency was found to be $\sim 85\%$. As anticipated, the high drug encapsulation efficiency in electrospun fibers may be attributed to solubility of both drug and polymer in organic solvent and minimum drug loss during encapsulation process [140]. The SEM images of the DEX-loaded randomly oriented and aligned fibers are shown in Figure II.5(A-D). The diameter of aligned and random fibers was $0.87 \pm 0.21 \mu\text{m}$. FTIR spectroscopy was utilized to validate the presence of DEX within PLGA fibers. Figure II.5(E) shows the FTIR spectrum of DEX, PLGA fibers, and DEX-loaded PLGA fibers. As depicted, the characteristic absorbance peaks of DEX are positioned around 2946 cm^{-1} (C-H), 1747 cm^{-1} (C=O), 1666 cm^{-1} (C=C), 1450 cm^{-1} (C-H) bending of alkanes, 1380 cm^{-1} (C-H and O-H bending) and 1083 cm^{-1} (C-F). The FTIR spectrum of PLGA fibers indicates the absorbance peaks at 2946 cm^{-1} (C-H), 1747 cm^{-1} (C=O), 1450 cm^{-1} (C-H) bending alkanes, 1380 cm^{-1} (C-H and O-H bending). In the case of DEX-loaded PLGA fibers, the absorbance peaks of C=C (1666 cm^{-1}) and C-F (1083 cm^{-1}), which are attributed to the characteristic peaks of DEX, revealed the presence of DEX in the PLGA fibers. The characteristic absorbance wavelengths obtained for DEX, PLGA fibers and DEX-loaded PLGA fibers are in good agreement with those previously reported in literature [141-143].

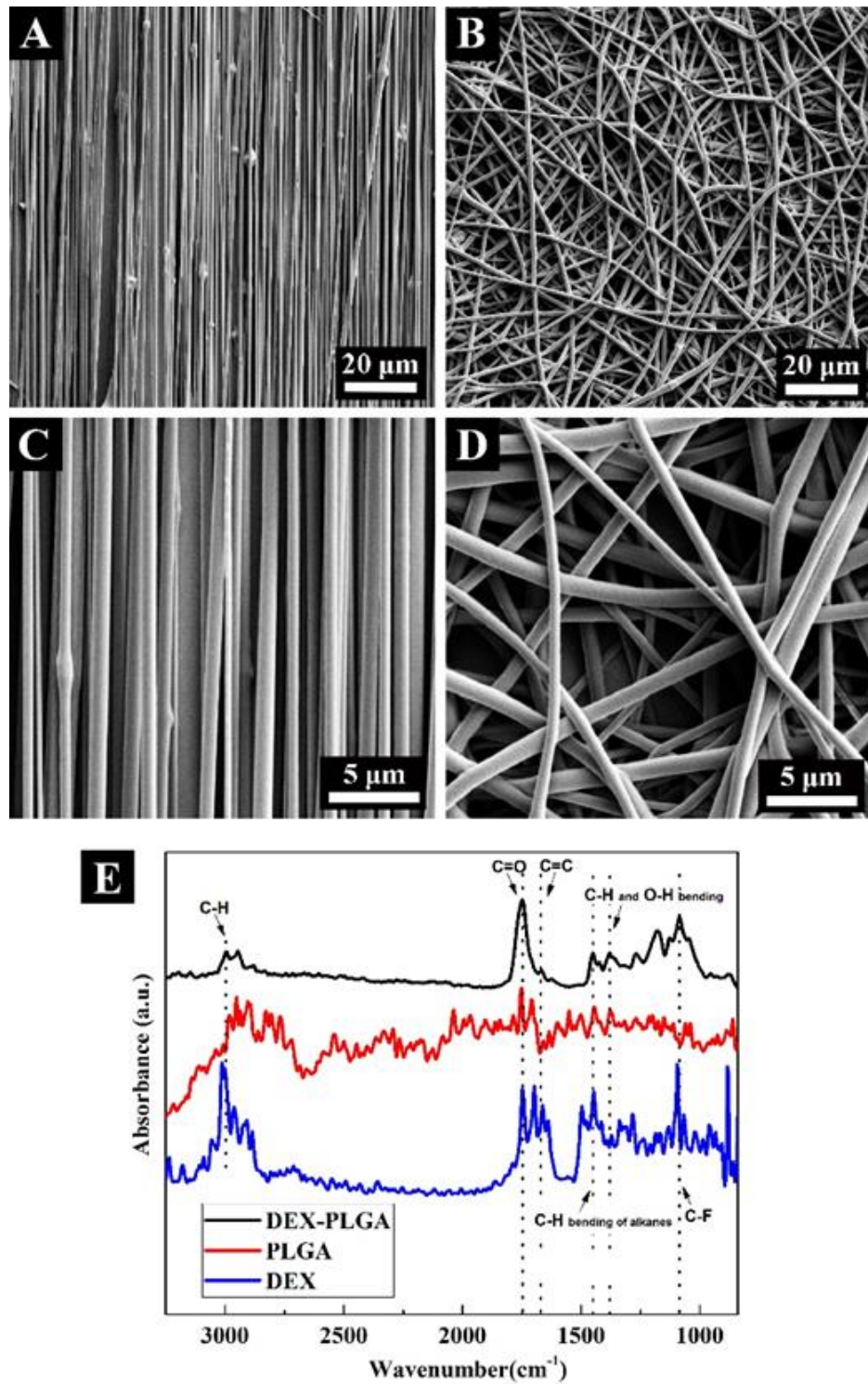


Figure II.5. A-D) SEM images of aligned (A,C) and randomly oriented (B,D) DEX-loaded PLGA fibers at different magnifications. E) FTIR spectrum of DEX, PLGA and DEX-loaded PLGA in the wavelength range of 850–3250 cm⁻¹.

We hypothesized that the alignment of the fibers would have an effect on the release of encapsulated DEX. To assess this hypothesis, first the structural and thermal properties of both random and aligned fibers were analyzed using XRD and DSC techniques, respectively. The XRD patterns of DEX powder, random PLGA fibers, and DEX-loaded PLGA fibers (random and aligned) are shown in Figure II.6. As shown in Figure II.6 (A), the three main characteristic peaks of crystalline DEX were positioned at $2\theta = 14.2^\circ$, 15.2° , and 16.9° . The XRD spectrum of random PLGA fibers showed a broad hump in the range of 12° – 25° , which is indicative of the amorphous polymeric matrix, and represented also two crystalline peaks at $2\theta = 27.1^\circ$ and 27.8° (Figure II.6(B)). The observation of these two crystalline peaks suggests that some ordered domains (fibrils) may exist within the amorphous matrix. These fibrillar/ordered domains were created as a result of arrangement of polymer chains induced by the elongation force applied on the polymer jet by the electric field during electrospinning [144]. As indicated in Figure II.6(C), by incorporation of DEX into the random PLGA fibers three small peaks, which are attributed to the main characteristic peaks of DEX, were appeared on the broad hump of PLGA spectrum. These results confirm the presence of DEX in the electrospun PLGA fibers. In the case of DEX-loaded aligned fibers (Figure II.6(D)), the XRD pattern indicates more crystalline peaks than that of their random counterparts (Figure II.6(C)). As shown in Figure II.6(D), the excess peaks are located at $2\theta = 38.5^\circ$, 43.4° , and 44.7° . The presence of excess crystalline peaks in aligned fibers is due to the formation of more ordered chain domains resulted from extra stretching forces as the fibers are collected on the rotating wheel. Thus in the case of aligned fibers, the ordered domains (fibrils) are organized along the fiber length [145, 146].

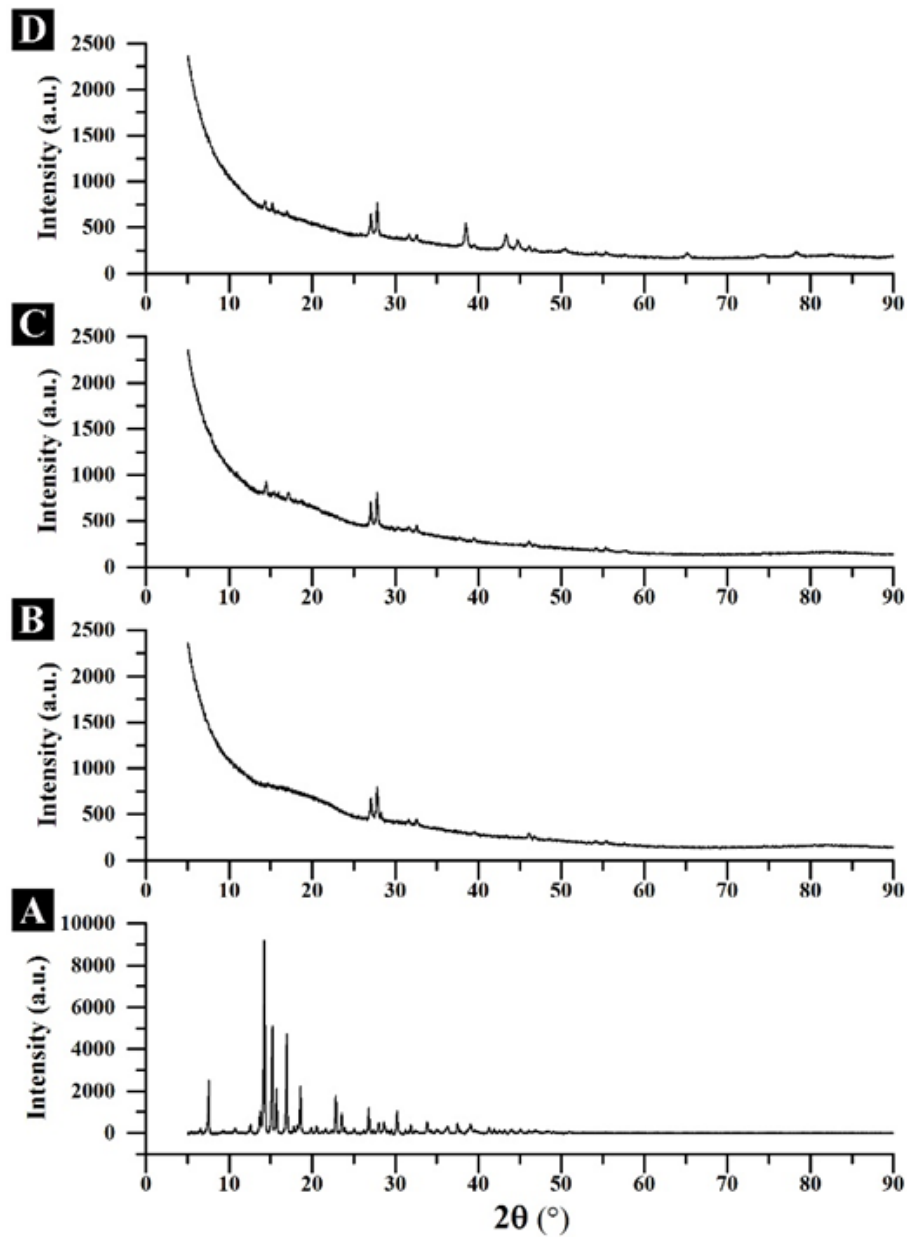


Figure II.6. XRD patterns of DEX (A), random PLGA fibers (B), DEX-loaded PLGA random fibers (C) and DEX-loaded PLGA aligned fibers (D).

The DSC thermograms of DEX, PLGA random fibers, and DEX-loaded random and aligned PLGA fibers are presented in Figure II.7. As indicated, the melting peak of

crystalline DEX was located at 257 °C (blue curve A). The DSC thermogram of PLGA random fibers (red curve B) showed a glass transition at $T_g \approx 47$ °C and also a decomposition peak over 300 °C. In the case of DEX-loaded PLGA fibers, the DSC thermograms of both random (black curve C) and aligned fibers (green curve D) indicated the same glass transition and decomposition peak of PLGA, but no melting peak for DEX. This implies that DEX was molecularly dispersed in the polymer matrix [147]. In addition, these results were verified by very low intensity of the main diffraction peaks of DEX in Figure II.6(C-D), which suggests that low quantity of the incorporated DEX was in the crystalline form. Furthermore, the DSC thermograms of random and aligned fibers demonstrated a small peak at ~57 °C which is likely attributed to the melting of fibrils form during electrospinning (see inset in Figure II.7). As observed, the melting peak for aligned fibers (green curve D) with more ordered domains (fibrils) was more pronounced than random fibers (black curve C).

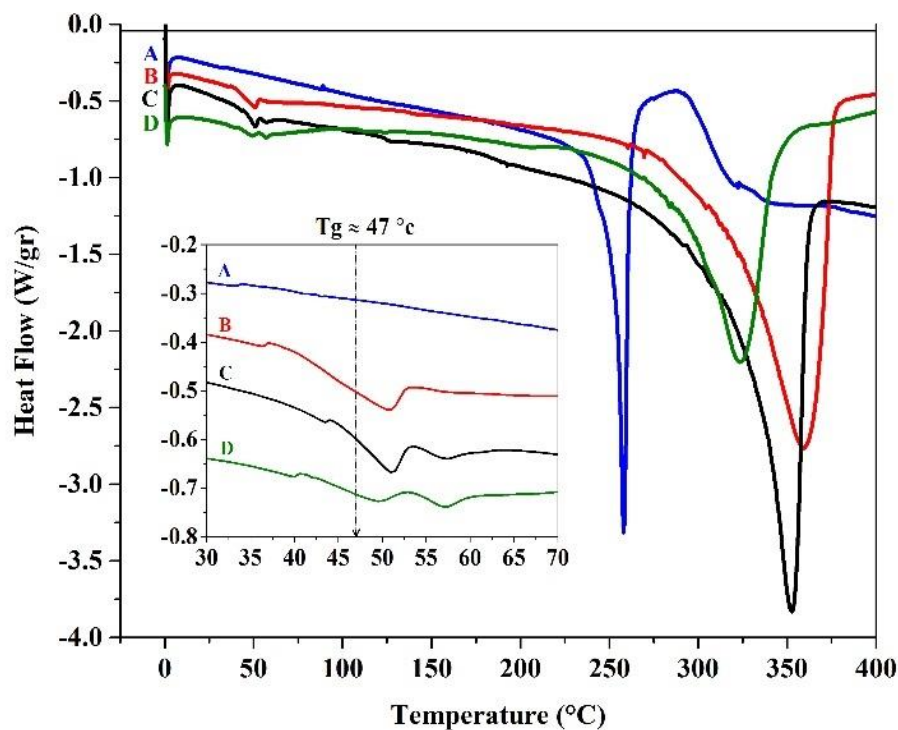
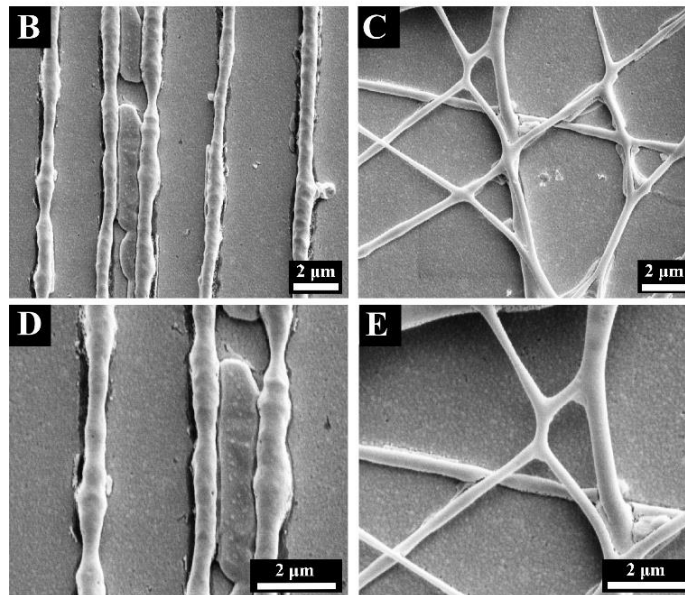
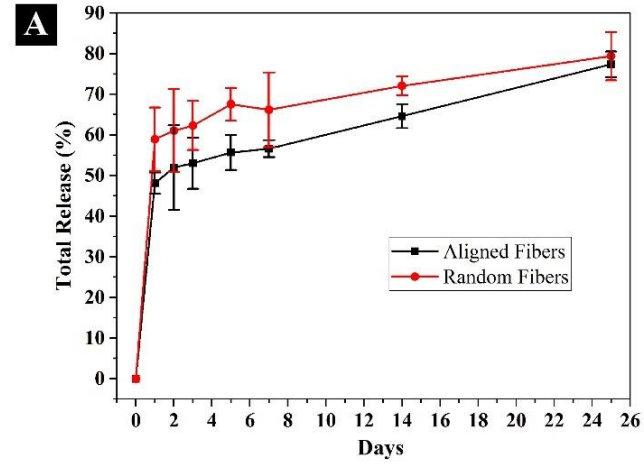


Figure II.7. DSC thermograms of DEX (A, blue), random PLGA fibers (B, red), and DEX loaded random PLGA fibers (C, black) and DEX-loaded aligned PLGA fibers (D, green).

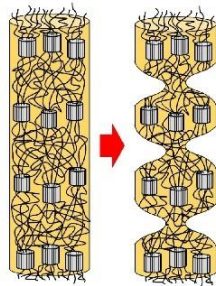
The *in-vitro* release profile of DEX from aligned and randomly oriented PLGA fibers was investigated in PBS at 37°C [119]. As illustrated in Figure II.8(A), both DEX release profiles exhibited an initial burst release during 24 hrs followed by a sustained release for the next 24 days. The burst release can be attributed to the tendency of accumulation of DEX molecules near the surface of fibers during electrospinning process, resulting in fast release of DEX due to the initial surface erosion of PLGA fibers [59, 126]. The subsequent prolonged release can be explained by bulk degradation of fibers and diffusion of drug [148].

There was statistically significant difference ($p < 0.05$) for initial burst release between randomly oriented fibers ($58.9 \pm 7.8\%$) and aligned fibers ($48.1 \pm 2.6\%$). The higher initial release of random fibers ($\sim 10.8\%$) is presumably due to the creation of pores between fibers of electrospun nonwoven mat that facilitate initial surface degradation of the randomly oriented fibers in comparison with aligned fibers that are packed together (SEM images in Figure II.5(A-D)). In contrast, over 24 days aligned fibers exhibited significantly $\sim 8.8\%$ higher rate of sustained release than their randomly oriented counterparts ($29.2 \pm 4.1\%$ for aligned fibers and $20.4 \pm 9.8\%$ for random fibers). As a consequence of higher rate of sustained release of aligned fiber, in day 25 there was no statistically significant difference for DEX release between randomly oriented fibers and aligned fibers ($77.4 \pm 3.1\%$ for aligned fibers and $79.4 \pm 5.9\%$ for random fibers). To further investigate this behavior, we characterized the surface morphology of the degraded fibers after 25 days. In contrast to randomly oriented fibers, aligned fibers exhibited in a non-uniform surface morphology (as shown in SEM micrographs in Figure II.8(B-E) and schematics illustrated in Figure II.8(F-G)). This interesting observation can be interpreted based on the different conformation of polymer chain developed during electrospinning [145, 146]. In Figure II.8(F-G), the cylindrical blocks are indicative of fibrils form during electrospinning of aligned fibers. As discussed earlier, random fibers almost hold an amorphous structure with less fibrils (Figure II.8G) [59]. However in the case of aligned fibers, more fibrillar domains are formed and oriented along the fiber length as a result of the excess stretching forces to the fiber stream during collection of fibers on the rotating wheel (Figure II.8(F)) [145, 146]. The favorable hydrolysis of amorphous regions compared to the fibrillar

domains in aligned fibers may contribute to anisotropic degradation of the aligned fibers (shown in Figure II.8(B,D) and illustrated in Figure II.8(F)) [148]. On the other hand, randomly oriented fibers demonstrated an isotropic surface degradation due to their predominant amorphous structure associated with the random dispersion of some fibrillar domains (shown in Figure II.8(C,E) and illustrated in Figure II.8(G)) [148]. In comparison to random fibers, the higher sustained release (i.e., average rate of change) of drug from aligned fibers might be explained by the anisotropic degradation of the aligned fibers. Overall, these findings revealed the effect of fiber alignment on their drug release profile and demonstrated that aligned fibers exhibited less initial burst release and more sustained release compared to the random fibers.



F Anisotropic Degradation of Aligned Fibers



G Isotropic Degradation of Random Fibers

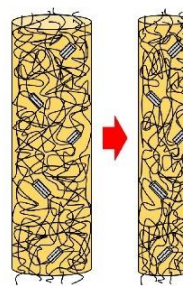


Figure II.8. A) DEX release profile from PLGA aligned fibers and random fibers. B-D) SEM images of aligned (B,D) and random (C,E) fibers after 25 days incubation. F-G) Degradation modes of aligned and random fibers.

Conclusions

In summary, we comprehensively investigated the effect of electrospinning processing parameters on the diameter and alignment of electrospun PLGA fibers. The experimental results revealed that needle gauge number, angular velocity of wheel, and collector distance have significant influence on the diameter of the produced fibers. The spatial orientation of fibers was predominantly affected by needle gauge number, voltage, and angular velocity of wheel. Highly aligned (with spatial orientation >99%) and monodisperse (CV < 0.5%) fibers were produced using the optimized electrospinning parameters. Moreover, the effect of spatial orientation of fibers on their drug release behavior was assessed using DEX. The release studies revealed that aligned fibers had less burst release and more sustained release than the random fibers, presumably due to the higher porosity of random fibers and anisotropic degradation of aligned fibers, respectively. The results of this study can be utilized for the development of highly aligned polymeric fibers for electronics and biomedical applications.

III Coaxial Electrospinning of Aligned Core-Shell Nanofibers Encapsulated with Nerve Growth Factor: Process Optimization and Release Modeling

Abstract

Oriented continuous nanofibers embedded with proteins may synergistically present topographical and biochemical signals to cells for tissue engineering. Coaxial electrospinning is a versatile technique for one-step encapsulation of delicate proteins such as nerve growth factors (NGF) into nanofibers with a core-shell structure. In this study, utilizing design of experiment (DOE) approach, we systematically investigated the effects of operational parameters of coaxial electrospinning on the diameter and size distribution (response variables) of aligned polyethylene oxide/poly(l-lactide-co-glycolide) (core/shell) nanofibers encapsulated with bioactive NGF. We minimized the response variables by optimizing the controllable factors including inner and outer flow rates, applied voltage, needle-collector distance, and rotating collector speed, and established predictive regression expressions for both responses using Box-Behnken Design (BBD). The ANOVA test results revealed that inner flow rate, collector distance, and voltage are the significant factors for the nanofibers diameter, while the collector speed was the only significant factor for the fibers size distribution. Diagnostic tests indicated that the quadratic regression model for the fiber diameter ($R^2 = 0.8$) provides a good prediction, whereas that of the fiber size distribution was not an accurate fit ($R^2 = 0.5$). Further, we assessed the NGF release profile from the aligned core-shell nanofibers over two weeks of

incubation in PBS, and then mathematically modeled the release fraction using Michaelis-Menten kinetics function. The NGF release profile indicated a short burst release (81% in ~8 hr) associated with a sustained and nearly zero-order release (~13%) over two weeks of incubation in PBS. Interestingly, mathematical modeling of the release fraction based on Michaelis–Menten function provided an excellent curve-fit to the experimental data ($R^2 = 0.993$).

Introduction

Over the past two decades, nanostructured fibrous materials have been widely utilized in the field of tissue engineering as controlled drug release systems with improved therapeutic effect, reduced toxicity, and sustained drug administration [149, 150]. Electrospinning is a low-cost and versatile technique that enables fabrication of meshed nanofibers with high surface to volume ratio and high porosity that resemble the structure of native extracellular matrix. In this technique, nanofibers are formed by a charged liquid jet which is drawn from spinneret towards collector under a high electric field. While fibers of a rich variety of materials including polymers [151-153], composites [154-156] and ceramics [157-159] have been created thus far, polymeric fibers have been of great attention for tissue regeneration owing to their potential biodegradability and ease of fabrication without the need for any post-treatment processing. Polymeric fiber delivery systems are technically produced based on two structural concepts: (1) matrix-type structure, where drug particles are dissolved/dispersed into the polymeric solution and blended nanofibers are made by mono-axial electrospinning, and (2) reservoir-type structure, where the drug is enclosed within polymeric nanofibers, forming so-called

“core-shell” structure which is generated via coaxial electrospinning [160]. Coaxial electrospinning is an innovative modification of electrospinning technique which employs two concentrically aligned capillaries to enforce the formation of fibers with a core-shell structure. Practically, coaxial electrospinning has been of great attraction for one-step encapsulation of delicate and water-soluble bioactive agents [161], such as growth factors [162], DNA [163], and even living cells [164], into core-shell fibers. Compared with single component fibers, coaxial fibers have several advantages on encapsulation of bioactive drugs and/or proteins: (1) the fiber shell serves as a barrier that prevents the premature release while promotes a sustained and controlled release; (2) bioactive agents can remain secured by the shell barrier from harsh environments; (3) one-step co-encapsulation of multiple drugs with different solubility characteristics can be achieved; and (4) even non-electrospinnable reagents can be embedded as the core material [165].

In tissue engineering, aside from cells and scaffolds, soluble signaling proteins are another indispensable and essential element that should be delivered into the cell microenvironment in a controlled and sustained manner without loss of bioactivity [166]. In the past decade, fiber delivery of neurotrophic factors such as nerve growth factor (NGF) has been of great focus for development of nerve autografts and conduits for nerve regeneration [167-169]. NGF plays critical roles in neuronal survival and axonal outgrowth and promotes axonal regeneration in the central and peripheral nervous systems after injury [170, 171]. Several researchers have reported successful encapsulation and sustained release of bioactive NGF using core-shell nanofibers made by coaxial electrospinning [162, 167, 172, 173]. For example, coaxial electrospun nanofibers composed of poly(lactic acid)

as the shell material and silk fibroin/NGF as the core material could preserve the bioactivity of encapsulated NGF and provide a sustained NGF release that supports differentiation of neuronal stem cells [173]. Liu et al. demonstrated establishment of nerve conduits made of coaxial poly(L-lactide-co-caprolactone)/NGF nanofibers which effectively promoted sciatic nerve regeneration in rats [167]. Further, Wang and coworkers incorporated NGF into aligned poly(DL-lactide-co-glycolide) nanofibers using coaxial electrospinning with a rotating drum collector [169]. By replacing the stationary collector with a rotating drum collector, aligned coaxial fibers are generated that provide physical guidance cues for directional neuronal growth and migration [168, 169]. It is been shown that alignment of NGF encapsulated coaxial fibers composed of poly(L-lactide-co-caprolactone), collagen type I and collagen type III induces directional neurite outgrowth along the fibers length [174].

Despite all aforementioned achievements in utilization of coaxial electrospinning for encapsulation and controlled release of bioactive NGF, optimization of effective processing parameters on the morphology of coaxial nanofibers requires to be explored yet. The diameter of nanofibers has a great impact on their functional performance, and so far downsizing the fibers diameter has been of major interest of many researchers for achieving nanofibers with high surface to volume ratio [175, 176]. Prior works on core-shell fibers, mostly focused on the application aspect and only a few articles [177-180] discussed the influence of the processing variables on the diameter of the core-shell fibers. In general, experimental variables include: i) operational parameters, such as applied voltage, fluid flow rate, collector distance, collector speed, and diameter of spinneret, ii)

properties of working fluids, such as polymer concentration, viscosity, surface tension, and conductivity, and iii) environmental conditions, such as temperature and humidity [175]. In an experiment, one or more process variables are deliberately changed to observe the effect on one or more response variables. Statistical design of experiments (DOE) is an efficient procedure for planning experiments and analyzing the results such that objective conclusions can be drawn [181, 182]. Determining the goal of an experiment is the first step of an experimental design, and selecting the process factors and responses to be analyzed is the second step in optimizing the important variables in a process [183]. Developing an experimental design is the most effective means of process optimization for achieving maximum production with minimum costs [182].

In this study, for the first time, we utilized DOE approach to systematically investigate the interaction effects of coaxial electrospinning parameters (operational variables including inner and outer flow rates, applied voltage, needle-collector distance, and collector speed) on the size (diameter) and size distribution of aligned core-shell nanofibers encapsulated with NGF. We synthesized aligned core-shell nanofibers composed of poly(L-lactide-co-glycolide) (PLGA) as the shell material and NGF loaded-polyethylene oxide (PEO) as the core. PLGA and PEO are two biocompatible synthetic polymers commonly used for electrospinning of core-shell nanofibers [160, 161, 165, 169, 184-187]. Here, PLGA is a biodegradable polymer which serves as the shell material that controls the degradation of coaxial fibers, and PEO is a water-soluble polymer which is employed as carrier material for encapsulation of NGF in the core. Further, we optimized the processing parameters based on Box-Behnken Design (BBD), which is widely used in

bioengineering processes as it decreases the number of experimental runs [182, 188], in order to minimize the nanofibers diameter and their size distribution. Ultimately, we assessed the NGF release from the optimized nanofibers, and mathematically modeled the obtained release profile using Michaelis–Menten kinetics model which is applicable to hydrolytically degradable PLGA matrices [189, 190].

Methods

Materials

Poly (DL-lactide-co-glycolide) (50:50 DL-PLG, ester terminated) with the inherent viscosity of 1.15 dL/g was purchased from Lactel Absorbable Polymers. Benzyl triethylammonium chloride and polyethylene oxide (PEO, $M_w = 300,000$ g/mol) were purchased from Fisher Scientific. Chloroform (99.8%) was supplied from Acros-Organics. Fluorescein isothiocyanate conjugate bovine serum albumin (FITC–BSA) was obtained from Sigma Aldrich. Recombinant rat β -NGF, DuoSet ELISA kit for rat β -NGF, and 10% BSA solution were purchased from R&D Systems. A prebuilt coaxial needle (inside needle: gauge 23, inner diameter = 0.33 mm, outer diameter = 0.64 mm; outside needle: gauge 18, inner diameter = 0.84 mm, outer diameter = 1.24 mm), PTFE tubing kit and components for the coaxial needle were purchased from ramé-hart instrument co.

Fabrication of aligned core-shell nanofibers via coaxial electrospinning

The setup for coaxial electrospinning is shown in Figure III.1. The shell solution was prepared by dissolving 661 mg PLGA (10 wt.%) in 4 ml chloroform. A small amount (13 mg) of benzyl triethylammonium chloride (an organosoluble salt) (was then added to the

PLGA solution to enhance the solution spinnability. For NGF encapsulation, the core solution was prepared by adding 1 ml of NGF solution (22 μ g NGF reconstituted with 1 ml of diluted (0.22%) BSA solution) into 3 ml of PEO solution containing 225 mg (7 wt.%) PEO in deionized water. To characterize encapsulated proteins after coaxial electrospinning, FITC-BSA was used as model protein. For this purpose, the core solution was prepared by adding 1 ml of 1% (w/v) FITC-BSA solution in deionized water into 3 ml of the PEO solution. To achieve homogenous core and shell solutions, each mixture was stirred for an hour at room temperature. The prepared solutions were then delivered to the outer and inner coaxial orifices using two programmable syringe pumps (Logato 100, KD Scientific) at various inner (Q_{in}) and outer (Q_{out}) flow rates. A high voltage power supply (PS/ER40P07, Glassman High Voltage Inc.) was used to generate a high electric field between the coaxial needle and collector. Aligned nanofibers were electrospun and collected on plastic coverslips (1 cm \times 0.5 cm) placed on the edge of a grounded rotating disk (disk diameter = 25 cm). The disk was located at a distance (λ) from the coaxial needle tip, and the disk speed (ω) was controlled by a stepping motor. The electrospinning process was carried out at room temperature (25°C) and relative humidity of 30%.

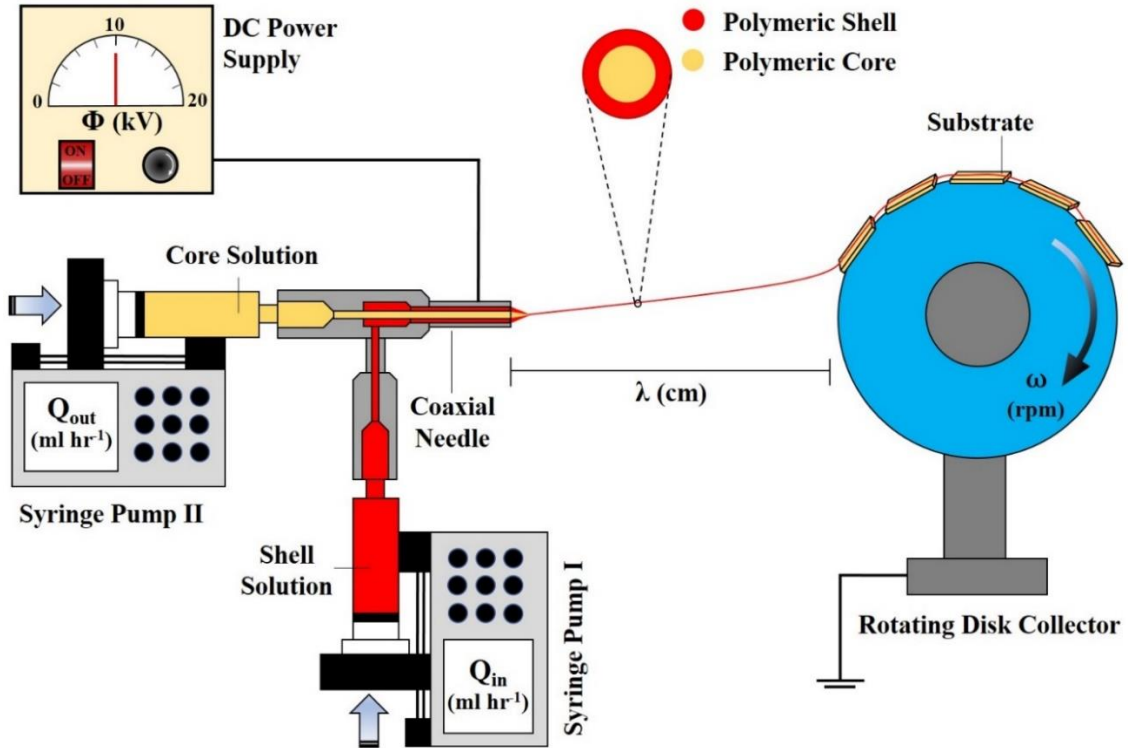


Figure III.1. Schematic illustrates the coaxial electrospinning setup.

Box–Behnken design for process optimization

The goal of process optimization was to minimize the fiber diameter and fiber size distribution, which are defined as response variables here. The effective processing parameters including inner flow rate (Q_{in}), outer flow rate (Q_{out}), collector speed (ω), applied voltage (Φ), and horizontal distance between the coaxial needle and the collector (λ) were considered as variable factors. The appropriate range for each factor was determined based on our preliminary results on formation of bead-free continuous nanofibers ($Q_{in} = 0.33 - 1$ ml/hr, $Q_{out} = 1 - 3$ ml/hr, $\omega = 500 - 1000$ rpm, $\Phi = 11 - 17$ kV, and $\lambda = 7 - 13$ cm). Design of experiment (DOE) was conducted using JMP Pro software

developed by the SAS institute. The Box-Behnken design (BBD), which is based on a three-level incomplete factorial design, was chosen for its higher efficiency compared to other response surface methods such as three level full factorial design and central composite design (CCD) [188]. The model efficiency is defined as the ratio of number of coefficients to the number of experimental runs. Another advantage of the BBD is that it does not include combinations at the extreme levels of all factors thereby reducing the number of experimental runs and avoiding unsatisfactory results [191]. According to BBD, the number of experimental runs required for optimization is achieved by

$$N = 2K(K - 1) + C, \quad \text{III.1}$$

where N , K , and C are the number of runs, factors, and center points, respectively. Here, $K = 5$ and $C = 5$; therefore, the total number of runs is $N = 45$. Each factor in BBD is coded to reflect three levels; the lowest value in the range is coded as “-1”, the center-point value is coded as “0”, and the highest value in the range is coded as “+1” (Table III.1). The experimental design generated by the software is given in Table III.2. Accordingly, we fabricated 45 sets of samples using various processing parameters specified for each run, and then measured the mean fiber diameter and size distribution for each set of samples. Using the measured values, the software generated prediction expressions and 3D surface response plots for both response variables, i.e., fiber diameter and size distribution, and also determined the optimal value for each parameter. The relationship between variable factors and responses is determined using a second-order polynomial equation expressed as

$$Y = \beta_0 + \sum_{i=1}^k \beta_i X_i + \sum_{i=1}^k \beta_{ii} X_i^2 + \sum_{i=1}^{k-1} \sum_{j=i+1}^k \beta_{ij} X_i X_j + \varepsilon, \quad \text{III.2}$$

where Y is the predicted response variable; X_i and X_j are the independent variables, β_0 , β_i , β_{ii} , and β_{ij} are the constant regression coefficients obtained by the least-square method, and ε is a random error. The optimal parameter values were used to prepare “optimized sample” for NGF release assessment. The overall optimization process is depicted as a flowchart in Figure III.2.

Table III.1. Coded levels of the factors.

Variable	Symbol	Coded Variable Level		
		Low (-1)	Center (0)	High (+1)
Inner Flow Rate (ml/hr)	Q_{in}	0.33	0.665	1
Outer Flow Rate (ml/hr)	Q_{out}	1	2	3
Rotating Disk Speed (rpm)	ω	500	750	1000
Applied Voltage (kV)	Φ	11	14	17
Needle-Disk Distance (cm)	λ	7	10	13

Table III.2. BBD experimental design with comparison between actual and predicted values of the fiber diameter and fiber size distribution.

Run No.	Q_{in}	Q_{out}	ω	Φ	λ	Experimental Fiber Dia.* (nm)	Predicted Fiber Dia. (nm)	Experimental Size Dist. (%)	Predicted Size Dist. (%)
1	-1	0	-1	0	0	416	297	3.57	3.83
2	-1	-1	0	0	0	674	480	4.32	4.39
3	0	0	0	-1	+1	1566	1357	4.42	3.85
4	-1	0	0	0	+1	469	539	4.31	3.96
5	0	-1	0	0	+1	588	675	5.50	5.43
6	0	0	0	0	0	477	497	2.92	3.92
7	0	0	0	0	0	487	497	5.31	3.92
8	0	0	+1	+1	0	551	569	4.42	4.68
9	0	0	0	0	0	657	497	3.79	3.92
10	0	0	0	-1	-1	494	655	3.99	4.18
11	0	-1	0	-1	0	968	960	4.75	5.30
12	0	-1	+1	0	0	670	645	6.80	6.05
13	0	0	-1	0	+1	512	526	4.77	5.58
14	0	+1	0	0	-1	675	549	4.44	3.82
15	+	0	+	0	0	593	607	4.59	4.38
16	0	+1	0	0	+1	596	738	4.21	4.60
17	-1	0	+1	0	0	463	510	3.41	4.31
18	+1	0	0	0	+1	503	659	3.88	4.00
19	0	0	-1	+1	0	318	310	3.87	4.28
20	-1	+1	0	0	0	491	449	2.45	3.15
21	+1	0	0	-1	0	1114	1124	3.69	3.31
22	0	0	0	0	0	435	497	4.45	3.92
23	0	+1	0	-1	0	1358	1145	2.85	3.77
24	+1	0	-1	0	0	708	555	5.85	4.99
25	0	-1	-1	0	0	376	497	5.68	5.55
26	0	0	0	+1	-1	476	621	3.16	2.66
27	-1	0	0	-1	0	519	766	4.24	3.69
28	-1	0	0	0	-1	350	297	2.95	2.54
29	-1	0	0	+1	0	350	394	2.95	2.35
30	+	0	0	+	0	583	391	4.39	3.95
31	0	-1	0	0	-1	677	496	5.61	4.53
32	0	+1	-1	0	0	451	570	6.94	5.34
33	0	0	0	+1	+1	511	287	5.93	4.67
34	0	0	+1	0	+1	800	766	4.12	5.05
35	0	+1	+1	0	0	714	688	6.93	4.71
36	0	+1	0	+1	0	460	466	2.93	4.18
37	+	+	0	0	0	575	716	3.05	4.23
38	0	0	-1	-1	0	995	988	5.11	5.10
39	0	-1	0	+1	0	325	535	3.31	4.19
40	0	0	0	0	0	431	497	3.11	3.92
41	+1	0	0	0	-1	499	533	3.69	3.74
42	+1	-1	0	0	0	579	568	3.99	4.54
43	0	0	+1	-1	0	976	995	4.72	4.57
44	0	0	-1	0	-1	414	449	3.14	4.27
45	0	0	+1	0	-1	488	475	3.42	4.67
Optimum	-1	0	-1	+1	0	323	245	2.37	2.63

* The fiber diameter value for each run is the mean of 100 measurements.

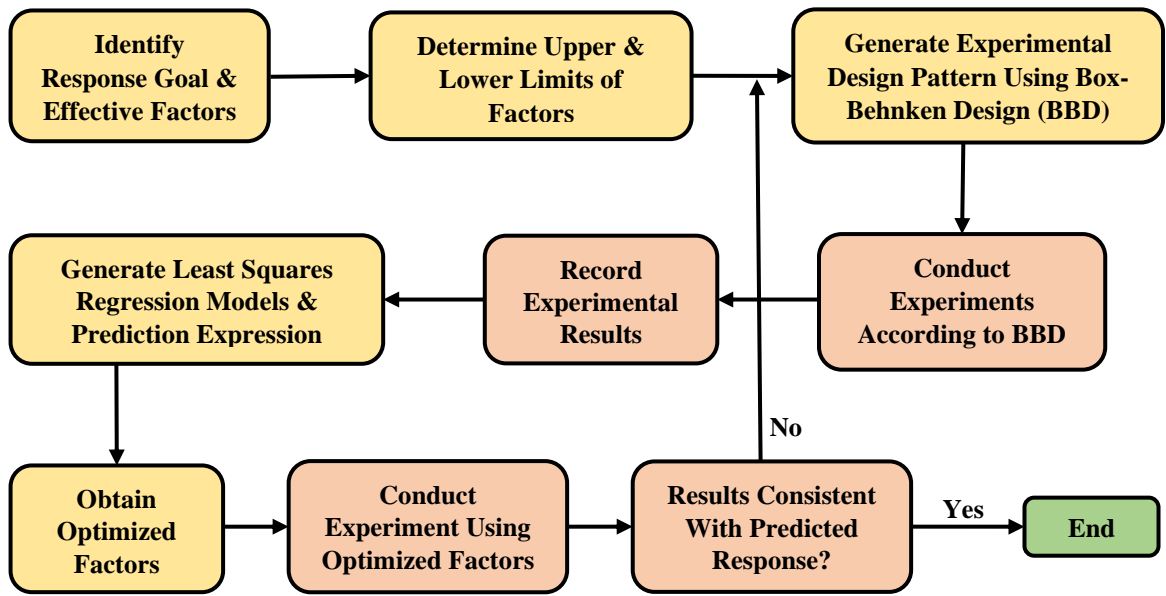


Figure III.2. Flowchart illustrates the overall optimization process.

Characterization of nanofibers

Field Emission Scanning Electron Microscopy (FE-SEM, FEI 235) was used to characterize the fibers diameter and core-shell morphology of the fibers. Samples were mounted on aluminum stubs by carbon tape and a carbon paint was used for grounding. Prior to microscopy, samples were sputter-coated with a thin layer of gold using Denton Sputter Coater for 45 s at 40 mA. To confirm formation of core-shell fiber morphology, cross-section of the fibers was imaged after cryogenic fracture of the fibers in liquid nitrogen. For fibers diameter measurement, five samples of the same batch were randomly selected, and their SEM images were analyzed using ImageJ software to measure fibers diameter (100 measurements for each sample set). Additionally, fiber size distribution was

determined using coefficient of variation (*C.V.*) of fibers size measurements which is expressed as

$$\text{Fiber size distribution (\%)} = C.V. \times 100 = \left(\frac{\text{Standard error of mean}}{\text{Mean fiber diameter}} \right) \times 100. \quad \text{III.3}$$

To confirm protein encapsulation after coaxial electrospinning, fluorescent imaging of the core-shell nanofibers incorporated with the model protein (FITC-BSA) was conducted using Zeiss AxioImager Z1 microscope. To make sure the fluorescence response is from the core of coaxial fibers, samples were immersed in water prior to imaging. Single fibers of PEO/NGF are quickly dissolved in water, so the fluorescence response corresponds to the core material which is protected by PLGA shell.

NGF enzyme-linked immunosorbent assay (ELISA)

The NGF release from optimized core-shell nanofibers was detected using solid-phase sandwich ELISA. Five samples of the same batch were randomly selected and each individually incubated in 1 ml PBS containing 1% BSA at 37 °C for two weeks. At predetermined time intervals, 250 μ l of solution was collected from each sample vial and replaced with an identical volume of fresh medium, and then the collected samples were analyzed for NGF concentration. A two-fold serial dilution of recombinant rat β -NGF standard was conducted to generate a seven-point standard curve for quantification of the NGF concentration. The ELISA assay was conducted according to the protocol provided by the supplier (R&D Systems, MN), and each sample was analyzed in duplicate. Briefly, flat-bottom 96-well microplates were initially coated overnight with goat anti-rat β -NGF capture antibody in PBS (100 μ l/well), and non-specific sites were blocked for an hour

using a solution of 1% BSA (w/v) in PBS (300 μ l/well). The samples (standard, control, and collected) and the biotinylated goat anti-rat β -NGF detection antibody, appropriately diluted in a 1% BSA (w/v) PBS solution, were sequentially added to the microplates and incubated for two hours each. The streptavidin-HRP was diluted in a 5% BSA (w/v) PBS solution and then added to the microplates (100 μ l/well) and incubated for 20 min. It should be noted that between every step of the above-mentioned procedure microplates were washed three times with a 0.05% Tween 20 in PBS solution of pH 7.4 (300 μ l/well). In the following, 100 μ l of substrate solution with 1:1 mixture of hydrogen peroxide and tetramethylbenzidine was added to each well and incubated for 20 min. The reaction was stopped by the addition of 50 μ l of 2 N H₂SO₄. Ultimately, the optical density of each well was determined using a microplate reader at the wavelength of 450 nm.

Results and Discussion

Nanofibers morphology and NGF encapsulation

Formation of core-shell nanofibers from a stabilized compound droplet, composed of PEO/NGF solution in the core covered by a thin shell of PLGA solution, at the coaxial needle tip is illustrated in Figure III.3(A-B). As shown in Figure III.3(A), at a critical voltage a coaxial Taylor cone and jet generated on the surface of the stabilized compound droplet. Further, at super critical voltages, multiple Taylor cones and jets ejected from the stabilized droplet (Figure III.3(B)) [192], so aligned core-shell nanofibers are collected in the form of separate bundles (Figure III.3(C-D)). Figure III.3(C-D) demonstrate SEM images of the NGF-loaded nanofiber electrospun using optimized processing parameters obtained in this study (Table III.2). As shown in Figure III.3(C), aligned nanofibers are

formed in bundles as a result of presence of multiple Taylor cones. Figure III.3(D) demonstrates aligned nanofibers in a single bundle. Fluorescent imaging of the coaxial nanofibers electrospun using the same processing parameters but replacing the NGF with a fluorescence-labeled model protein (FITC-BSA) confirmed the successful and continuous incorporation of proteins into the core material (Figure III.3(E)). In Figure III.3(E), the continuous green lines belong to the core material incorporated with FITC-BSA, and each line corresponds to a bundle of core-shell nanofibers as illustrated earlier in Figure III.3(C). A SEM image from the cross section of the fabricated core-shell fiber is shown in Figure III.3(F). As observed in this figure, the PEO/NGF core fiber is enveloped by a thin PLGA sheath. This image demonstrates that the core material possesses most of the fiber diameter.

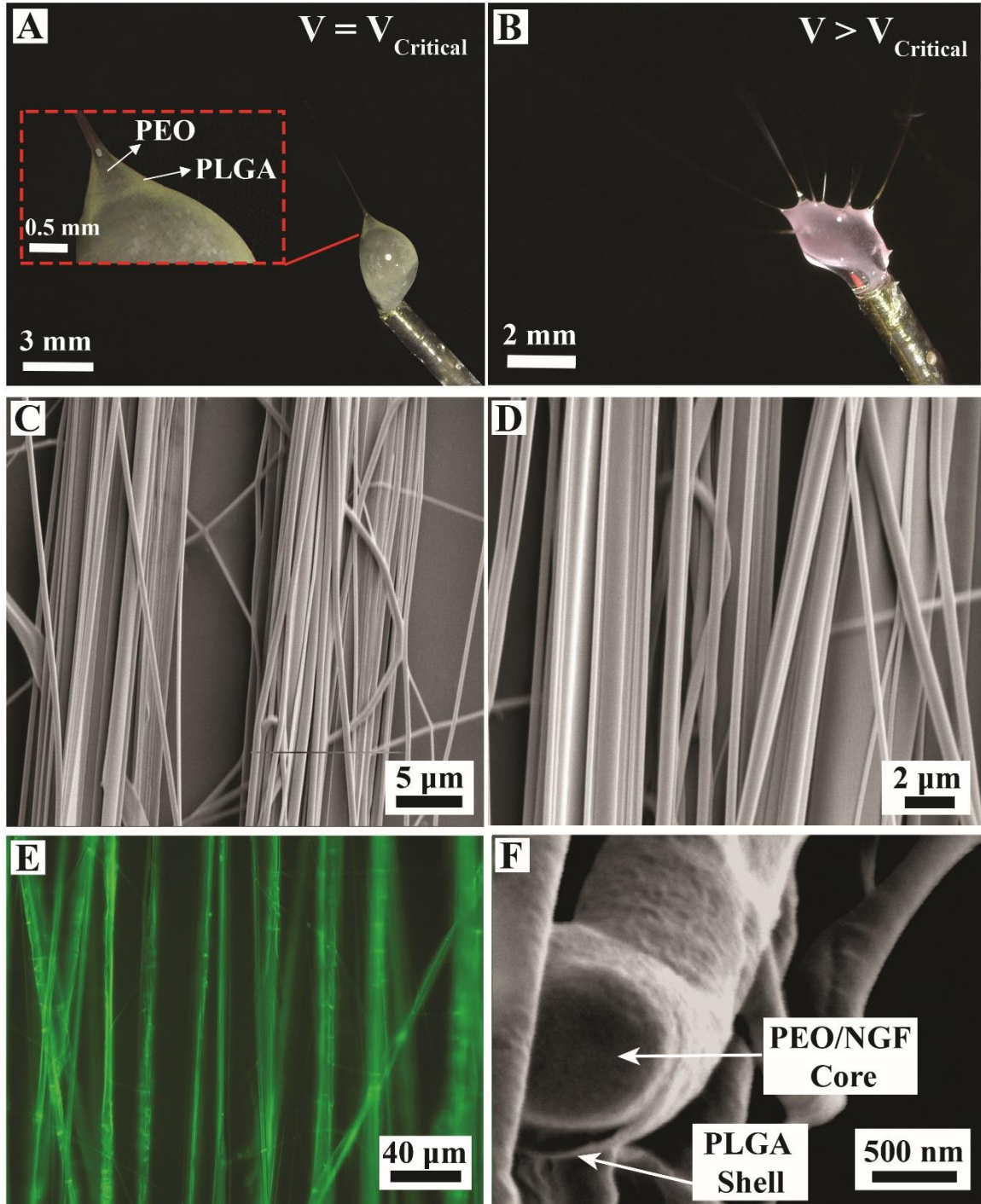


Figure III.3. A-B) Core-shell Taylor cones and jets form at the needle tip. C-D) SEMs of aligned core-shell nanofibers. E) Fluorescent image of the nanofibers loaded with FITC-BSA. F) SEM indicates cross-section of a core-shell nanofiber.

Multivariable optimization

Coaxial electrospinning parameters, including inner flow rate (Q_{in}), outer flow rate (Q_{out}), collector speed (ω), applied voltage (Φ), and the needle-collector distance (λ) were identified as the controllable processing parameters for fabrication of aligned core-shell nanofibers (Figure III.1). A Box–Behnken design (BBD) was utilized to optimize the diameter and size distribution (response variables) of the core-shell nanofibers based on these processing parameters. The experimental range of parameters for the design were obtained from a single-parameter study (data not shown). A summary of the independent variables and their variation levels is given in Table III.1. The BBD comprised of 45 experimental runs with various combinations of parameter levels as given in Table III.2. The experimental measurements of the fiber diameter and fiber size distribution were used to construct predicative quadratic models expressed as

$$\begin{aligned}
 Y = & \beta_0 + \beta_1 \left(\frac{(Q_{in}-0.665)}{0.335} \right) + \beta_2 (Q_{out} - 2) + \beta_3 \left(\frac{(\omega-750)}{250} \right) + \beta_4 \left(\frac{(\Phi-14)}{3} \right) + \beta_5 \left(\frac{(\lambda-10)}{3} \right) + \\
 & \beta_{12} \left(\frac{(Q_{in}-0.665)}{0.335} \right) (Q_{out} - 2) + \beta_{13} \left(\frac{(Q_{in}-0.665)}{0.335} \right) \left(\frac{(\omega-750)}{250} \right) + \beta_{14} \left(\frac{(Q_{in}-0.665)}{0.335} \right) \left(\frac{(\Phi-14)}{3} \right) + \\
 & \beta_{15} \left(\frac{(Q_{in}-0.665)}{0.335} \right) \left(\frac{(\lambda-10)}{3} \right) + \beta_{23} (Q_{out} - 2) \left(\frac{(\omega-750)}{250} \right) + \beta_{24} (Q_{out} - 2) \left(\frac{(\Phi-14)}{3} \right) + \\
 & \beta_{25} (Q_{out} - 2) \left(\frac{(\lambda-10)}{3} \right) + \beta_{34} \left(\frac{(\omega-750)}{250} \right) \left(\frac{(\Phi-14)}{3} \right) + \beta_{35} \left(\frac{(\omega-750)}{250} \right) \left(\frac{(\lambda-10)}{3} \right) + \\
 & \beta_{45} \left(\frac{(\Phi-14)}{3} \right) \left(\frac{(\lambda-10)}{3} \right) + \beta_{11} \left(\frac{(Q_{in}-0.665)}{0.335} \right)^2 + \beta_{22} (Q_{out} - 2)^2 + \beta_{33} \left(\frac{(\omega-750)}{250} \right)^2 + \\
 & \beta_{44} \left(\frac{(\Phi-14)}{3} \right)^2 + \beta_{55} \left(\frac{(\lambda-10)}{3} \right)^2,
 \end{aligned}
 \tag{III.4}$$

where Y is the response variable, β_0 is the model constant, and β_1 - β_{55} are the regression coefficients calculated using experimental data (Table III.3). β_1 - β_5 coefficients correspond

to the linear terms, β_{12} - β_{45} coefficients correspond to the interaction terms, and β_{11} - β_{55} coefficients are relating to the quadratic terms. As mentioned earlier, Q_{in} , Q_{out} , ω , Φ , and λ are the independent variables representing the processing parameters. The responses at any regime in the interval of experimental design could be predicted by Equation III.4. The experimental and predicted values of the response variables, i.e., fiber diameter and fiber size distribution, for all runs are presented in Table III.2. As given in this table, the minimum fiber diameter of 323 nm with minimum fiber size distribution of 2.37% were obtained using the optimized processing parameters ($Q_{in} = 0.33$ ml/hr, $Q_{out} = 2$ ml/hr, $\omega = 500$ rpm, $\Phi = 17$ kV, and $\lambda = 10$ cm).

Table III.3. The coefficients for quadratic models.

Terms	Coefficient	Fiber Diameter (nm)				Fiber Size Distribution (%)			
		Estimate	S.E.	Lower 95%	Upper 95%	Coefficient	S.E.	Lower 95%	Upper 95%
Constant	β_0	497.40	71.11	350.64	644.16	3.92	0.49	2.90	4.93
Q_{in}	β_1	88.92	39.75	6.88	170.96	0.31	0.28	-0.26	0.88
Q_{out}	β_2	29.01	39.75	-53.03	111.05	-0.38	0.28	-0.95	0.18
ω	β_3	66.53	39.75	-15.51	148.57	-0.03	0.28	-0.60	0.54
Φ	β_4	-276.05	39.75	-358.09	-194.01	-0.18	0.28	-0.74	0.39
λ	β_5	92.06	39.75	10.02	174.09	0.42	0.28	-0.15	0.99
$Q_{in} \times Q_{out}$	β_{12}	44.77	79.50	-119.31	208.85	0.23	0.55	-0.91	1.37
$Q_{in} \times \omega$	β_{13}	-40.38	79.50	-204.46	123.70	-0.27	0.55	-1.41	0.86
$Q_{in} \times \Phi$	β_{14}	-90.47	79.50	-254.55	73.61	0.49	0.55	-0.64	1.63
$Q_{in} \times \lambda$	β_{15}	-28.89	79.50	-192.97	135.19	-0.29	0.55	-1.43	0.85
$Q_{out} \times \omega$	β_{23}	-7.76	79.50	-171.84	156.31	-0.28	0.55	-1.42	0.86
$Q_{out} \times \Phi$	β_{24}	-63.60	79.50	-227.67	100.48	0.38	0.55	-0.76	1.52
$Q_{out} \times \lambda$	β_{25}	2.79	79.50	-161.29	166.86	-0.03	0.55	-1.17	1.11
$\omega \times \Phi$	β_{34}	62.75	79.50	-101.33	226.83	0.24	0.55	-0.90	1.37
$\omega \times \lambda$	β_{35}	53.54	79.50	-110.54	217.62	-0.23	0.55	-1.37	0.90
$\Phi \times \lambda$	β_{45}	-259.14	79.50	-423.21	-95.06	0.59	0.55	-0.55	1.72
Q_{in}^2	β_{11}	-25.90	55.74	-140.95	89.15	-0.44	0.39	-1.23	0.36
Q_{out}^2	β_{22}	81.76	55.74	-33.29	196.81	0.60	0.39	-0.20	1.40
ω^2	β_{33}	20.85	55.74	-94.20	135.90	0.90	0.39	0.10	1.69
Φ^2	β_{44}	197.41	55.74	82.36	312.46	-0.16	0.39	-0.95	0.64
λ^2	β_{55}	35.37	55.74	-79.68	150.42	0.08	0.39	-0.72	0.88

Effects of processing parameter

The linear, interaction, and quadratic effects of the processing factors on the response variables are determined by the coefficient values presented in Table III.3. The linear terms of Q_{in} , Q_{out} , ω , and λ were observed to have a positive correlation with fiber diameter, whereas the linear term Φ had a negative correlation on this response variable. The linear

effects of the investigated factors on the diameter of coaxial fibers are in agreement with prior reports in literature as follows: i) an increase in fibers diameter with increasing inner and outer flow rates, which is attributed to the extrudate swell effect of viscoelastic polymers that renders expansion of the core/shell layer to a certain extent [177, 179]; ii) a decrease in fiber diameter by elevating the applied voltage that leads to higher electrostatic charges in the coaxial jet and also further stretching of coaxial fibers [165, 193, 194]; iii) a longer collection distance induced thicker fibers as solvent volatilization increases with a distance the fluid jet has to travel [195]; and iv) an increase in fiber diameter observed for collector speeds over 500 rpm [151]. For fiber size distribution, the linear terms of Q_{in} and λ exhibited a positive correlation, whereas that of Q_{out} , ω , and Φ was negative for this response variable. The linear effects of the studied factors on the size distribution of coaxial fibers are in agreement with prior works: i) a reduction in fiber size distribution with decreasing inner flow but increasing outer flow rate [177, 179]; ii) a narrower fiber size distribution achieved at higher voltages [175]; iii) a broader fiber size distribution at longer collector distances [195]; and iv) a narrower fiber size distribution at higher collector speeds [151, 196].

The interaction terms $Q_{in} \times \omega$, $Q_{in} \times \Phi$, $Q_{in} \times \lambda$, $Q_{out} \times \omega$, $Q_{out} \times \Phi$, and $\Phi \times \lambda$ showed a negative effect on fibers diameter. In contrast, the interactions $Q_{in} \times Q_{out}$, $Q_{out} \times \lambda$, $\omega \times \Phi$, and $\omega \times \lambda$ were found to have a positive effect (Table III.3). Positive interaction coefficients signify a synergistic effect on the response value, while negative values indicate an antagonistic effect [197]. For fiber size distribution, the interactions $Q_{in} \times \omega$, $Q_{in} \times \lambda$, $Q_{out} \times \omega$, $Q_{out} \times \lambda$, and $\omega \times \lambda$ had a negative impact (antagonistic); conversely, the

interactions $Q_{in} \times Q_{out}$, $Q_{in} \times \Phi$, $Q_{out} \times \Phi$, $\omega \times \Phi$, and $\Phi \times \lambda$ had a positive effect (synergistic) on the fiber size distribution (Table III.3).

The quadratic effect of Q_{out} , ω , Φ , and λ were positive on fibers diameter, while that of Q_{in} was negative. For fiber size distribution, the quadratic effects of Q_{out} , ω , and λ were positive, while that of Q_{in} and Φ were negative. The ANOVA test results for the regression models and their corresponding coefficients are presented in Table III.4. According to the p -values, Q_{in} , Φ , λ , $\Phi \times \lambda$, and Φ^2 were significant terms for fiber diameter response, while ω^2 was the only significant model term for the fiber size distribution response. These results indicate that the inner flow rate, collector distance, and voltage are significant variables for fiber diameter, while the collector speed is the only significant factor for fiber size distribution. In addition, the interaction between voltage and collector distance showed significance effect on fiber diameter, while there was no significant interaction effect on fiber size distribution.

Table III.4. Analysis of variance for response surface quadratic models.

Terms	Fiber Diameter		Fiber Size Distribution	
	F ratio	P-value	F ratio	P-value
Quadratic model	4.6338	0.0003*	1.1018	0.4063
Q_{in}	5.0042	0.0348*	1.2509	0.2745
Q_{out}	0.5327	0.4725	1.9472	0.1757
ω	2.8017	0.1072	0.0132	0.9095
Φ	48.2282	<.0001*	0.4080	0.5290
λ	5.3633	0.0294*	2.3314	0.1399
$Q_{in} \times Q_{out}$	0.3171	0.5786	0.1764	0.6782
$Q_{in} \times \omega$	0.2580	0.6161	0.2490	0.6223
$Q_{out} \times \omega$	0.0095	0.9230	0.2617	0.6136
$Q_{in} \times \Phi$	1.2950	0.2664	0.8049	0.3785
$Q_{out} \times \Phi$	0.6399	0.4316	0.4805	0.4948
$\omega \times \Phi$	0.6230	0.4377	0.1823	0.6732
$Q_{in} \times \lambda$	0.1320	0.7195	0.2788	0.6023
$Q_{out} \times \lambda$	0.0012	0.9723	0.0029	0.9574
$\omega \times \lambda$	0.4536	0.5071	0.1786	0.6763
$\Phi \times \lambda$	10.6249	0.0033*	1.1284	0.2987
Q_{in}^2	0.2158	0.6464	1.2750	0.2700
Q_{out}^2	2.1514	0.1554	2.4027	0.1342
ω^2	0.1400	0.7116	5.3989	0.0289*
Φ^2	12.5416	0.0017*	0.1624	0.6906
λ^2	0.4026	0.5318	0.0441	0.8355
Lack of fit	3.3324	0.1256	1.2915	0.4452

*Significant p -values

Further, to visualize the interaction effects of the processing parameters, 3D surface response plots were generated based on the quadratic models for fiber diameter and fiber size distribution (Figure III.4 and Figure III.5). Each 3D plot displays the interaction effect between two different factors on a response variable, while keeping the other factors constant at their center-point values. The interaction of each pair of parameters can be explained by the contour profiles projected under the surface plots. The interaction response between Q_{in} and Q_{out} exhibited a roughly parabolic cylinder for the fiber diameter (Figure III.4(A)) and a hyperbolic paraboloid for the fiber size distribution (Figure III.5(A)). As illustrated by the contour profiles, the minimum fiber diameter and fiber size distribution are achieved at low Q_{in} and medium Q_{out} . The interaction response between Q_{in} and ω indicated a nearly planar surface for the fiber diameter (Figure III.4(B)) but a hyperbolic paraboloid for the fiber size distribution (Figure III.5(B)). The minimum fiber diameter is obtained at low Q_{in} and low ω , while the minimum fiber size distribution is observed at low Q_{in} and medium ω . The interaction response between Q_{in} and Φ showed a nearly planar surface for the fiber diameter (Figure III.4(C)) and a paraboloid for the fiber size distribution (Figure III.5(C)). As shown, the fiber diameter and fiber size distribution are minimized at low Q_{in} but high Φ values. The interaction response between Q_{in} and λ revealed a nearly planar surface for the fiber diameter (Figure III.4(D)) and a roughly parabolic cylinder for the fiber size distribution (Figure III.5(D)). Both fiber diameter and fiber size distribution are minimized at low Q_{in} and medium λ values. The interaction response between Q_{out} and ω indicates a parabolic cylinder for the fiber diameter (Figure III.4(E)) and an elliptic paraboloid for the fiber size distribution (Figure III.5(E)). As

illustrated, the minimum fiber diameter is observed at medium Q_{out} and low ω , while the minimum fiber size distribution is obtained at medium values of Q_{out} and ω . The interaction response between Q_{out} and Φ exhibited a roughly planar surface for the fiber diameter (Figure III.4(F)) and a hyperbolic paraboloid for the fiber size distribution (Figure III.5(F)). The minimum fiber diameter and fiber size distribution are acquired at medium Q_{out} and high Φ values. The interaction response between Q_{out} and λ represents a parabolic cylinder for both fiber diameter (Figure III.4(G)) and fiber size distribution (Figure III.5(G)). As depicted, both fiber diameter and fiber size distribution are minimized at medium Q_{out} and low λ values. The interaction response between ω and Φ demonstrated a nearly planar surface for the fiber diameter (Figure III.4(H)) and a parabolic cylinder for the fiber size distribution (Figure III.5(H)). The minimum fiber diameter is achieved at low ω and high Φ , while fiber size distribution is minimized at medium ω and high Φ . The interaction response between ω and λ illustrated a nearly planar surface for fiber diameter (Figure III.4(I)) and a parabolic cylinder for fiber size distribution (Figure III.5(I)). The fiber diameter is minimized at low ω and λ values, while the minimum fiber size distribution is attained at medium ω and low λ . Lastly, the 3D surface plot for both fiber diameter (Figure III.4(J)) and fiber size distribution (Figure III.5(J)) exhibited a non-planar shape with arbitrary contour profiles between Φ and λ . According to these 3D plots, the fiber diameter is minimized at high Φ and λ values, while the minimum fiber size distribution is obtained at high Φ and low λ values.

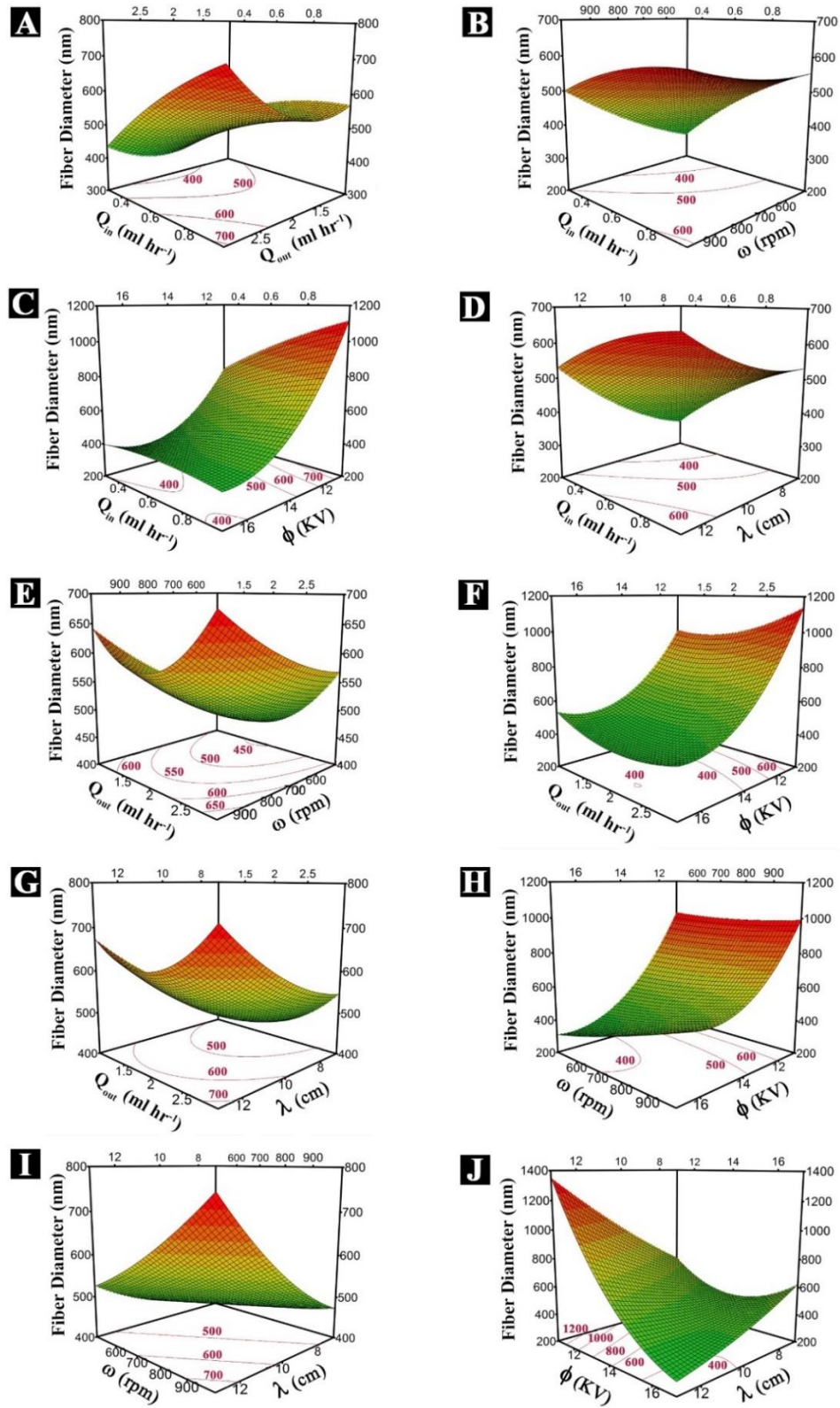


Figure III.4. 3D surface response plots for fiber diameter.

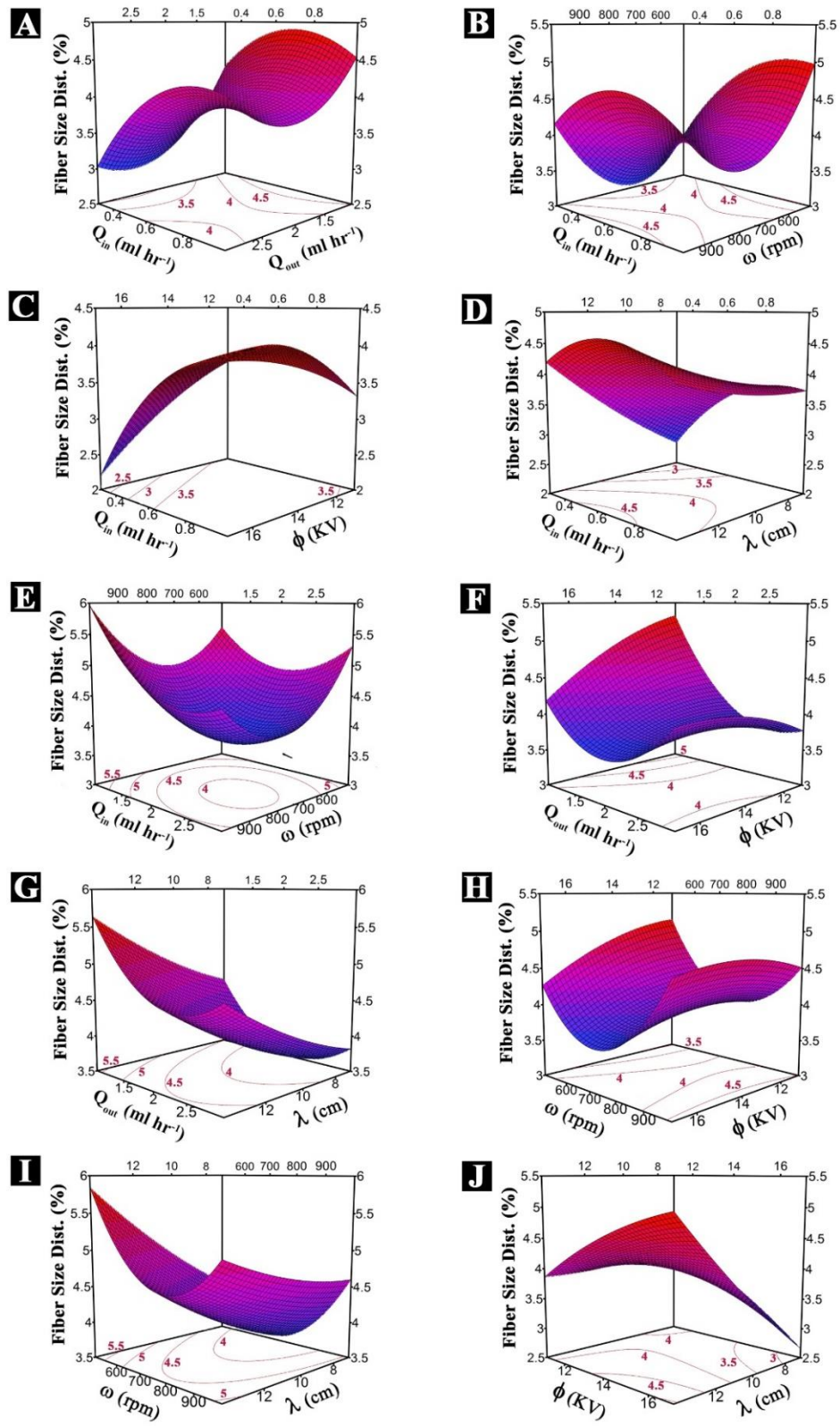


Figure III.5. 3D surface response plots for fiber size distribution.

Model validation

The validity of the regression models can be assessed through the diagnostic plots demonstrated in Figure III.6. The scatter plots of experimental versus predicted responses for fiber diameter and fiber size distribution alongside a “perfect fit line” ($y=x$) and a 0.05 significance curve are displayed in Figure III.6(A-B). As illustrated, the data points for the fiber diameter are mostly arranged close to the perfect-fit line, while the data points for the fiber size distribution are more scattered around the straight line. The coefficient of determination (R^2) of 0.8 and 0.5 were obtained for the fiber diameter and fiber size distribution responses, respectively. This indicates that the quadratic model was an appropriate fit for fiber diameter, whereas it was not an accurate fit for fiber size distribution.

The studentized residual plots for the fiber diameter and fiber size distribution are presented in Figure III.6(C-D). As demonstrated for both fiber diameter and fiber size distribution, the studentized residual plots as a function of run number represent a random scattering of data points. This implies that the prediction models give no violations of the independence or constant variance assumptions [198]. In general, studentized residuals must be between ± 3.5 , and the predicted value corresponds to the data points beyond these thresholds are not valid [191]. Here, the studentized residuals for both fiber diameter and fiber size distribution were less than ± 3.5 , which confirms the validity of the predicted values obtained by the proposed models.

As presented in Table III.4, the model F-value for fiber diameter and fiber size distribution were 4.6338 and 1.1018, respectively. The model p -value for fiber diameter

and fiber size distribution were 0.0003 and 0.4063, respectively. Accordingly, we can conclude that the model was significant for fiber diameter but not for fiber size distribution. In addition, the “lack of fit” F-value for fiber diameter and fiber size distribution were 3.3324 and 1.2915, respectively; and the corresponding p -values were 0.1256 and 0.4452, which suggests that the lack of fit was not significant.

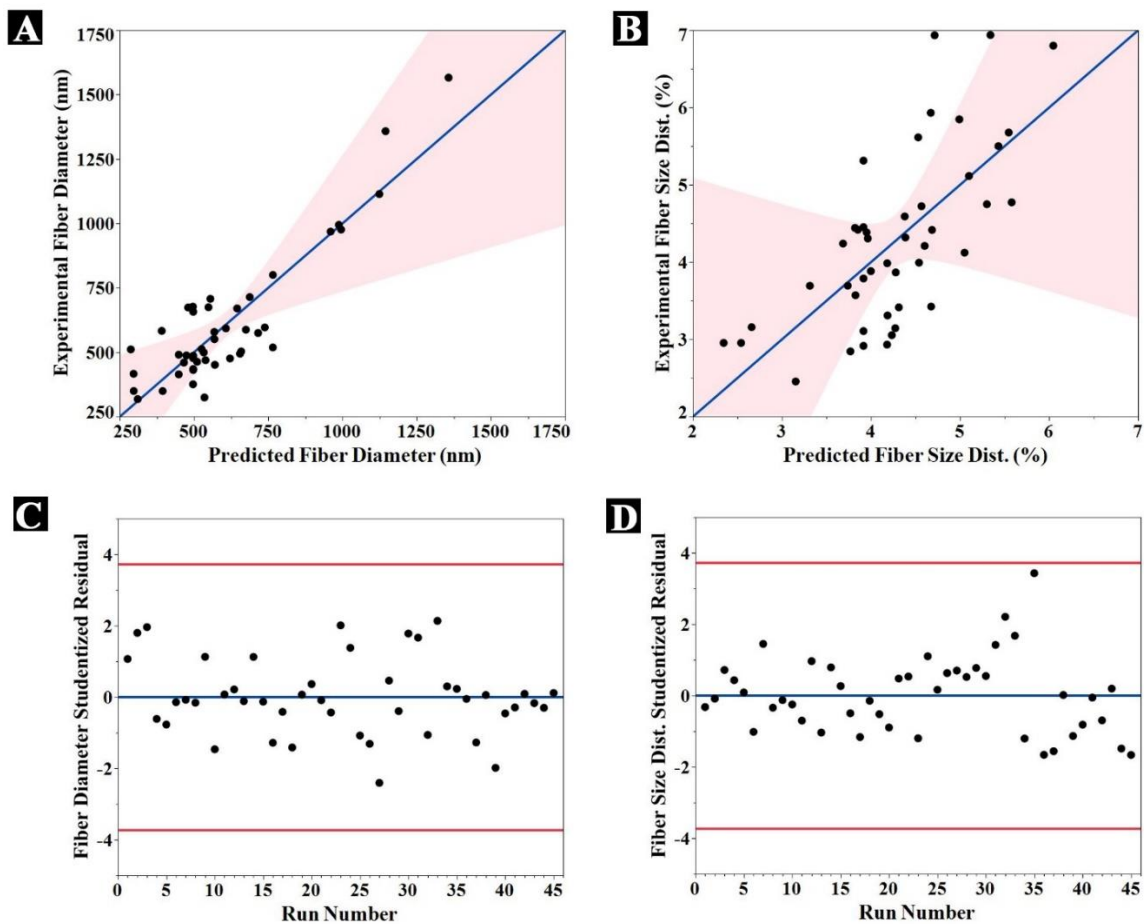


Figure III.6. A-B) Scatter plots of experimental vs predicted responses for fiber diameter and size distribution. C-D) Studentized residual plots of the fiber diameter and size distribution. Studentized residuals with 95% limits (Bonferroni).

NGF release assessment and release modeling

Figure III.7(A) shows the *in-vitro* cumulative release profile of NGF from the aligned core-shell nanofibers fabricated using optimized processing parameters and incubated in PBS at 37°C for two weeks. As seen in this figure, the release profile indicates a biphasic behavior: an initial burst release lasting for approximately 8 hrs, followed by a period of slow and sustained release over the course of incubation. Figure III.7(B) demonstrates the release fraction ($\frac{C_t}{C_{max}}$) profile, which is obtained by dividing the NGF concentration at time t (C_t) by the maximum NGF released (C_{max}) from the nanofibers. Here, we obtained the best curve-fit to the fractional release profile using Michaelis-Menten kinetics function which is previously described for drug release modeling of hydrolytically degradable devices exhibit bi-phasic release profiles consisting of an initial diffusive burst followed by a first order (or zero order) phase [190, 199]. Accordingly, the release fraction is expressed as

$$\text{Release Fraction (RF)} = \frac{(RF)_{max} \cdot t}{K_m + t}, \quad \text{III.5}$$

where K_m is Michaelis constant, $(RF)_{max}$ is the maximum release fraction ($\frac{C_t}{C_{max}}$), and t is incubation time. The K_m and RF_{max} values of 1.19 and 0.94 were respectively obtained for the fit curve based on this kinetic model, which provided an excellent fit to the experimental data ($R^2 = 0.993$). According to the Michaelis–Menten kinetics, the degradation of the matrix rather than diffusion of the mobile agent controls the long-term release process [189]. As illustrated in Figure III.7(B), this process include a short burst release that is followed by a nearly zero-order release caused by degradation of the matrix [189].

Accordingly, we can infer that the hydrolytic degradation of the shell layer (PLGA) controls the NGF release kinetics.

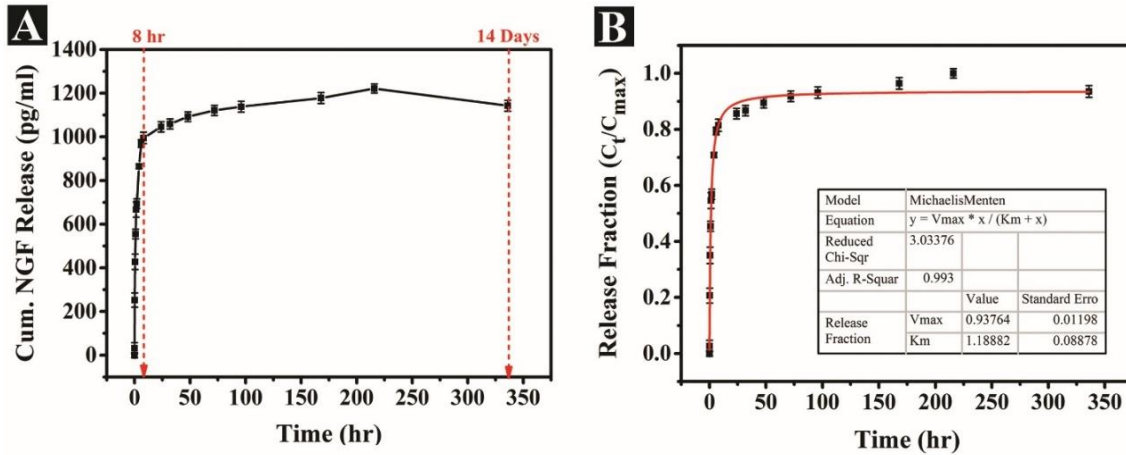


Figure III.7. A) NGF cumulative release profile during incubation in PBS at 37°C for two weeks. B) Release fraction profile associated with a curve fit (red line) based on Michaelis-Menten kinetics equation.

Further, we characterized the surface degradation of the aligned core-shell nanofibers over the course of incubation. Figure III.8 represents scanning electron micrographs of the aligned nanofibers after incubation in PBS for different periods of time. As seen in this figure, some tiny holes appears on of the shell layer of nanofibers when the polymer is exposed to the PBS (Figure III.8(A)), and they become more populated and enlarged as the incubation time proceeds (Figure III.8(B-F)). These observations suggest that the primary mechanism for the NGF burst release is the heterogeneous surface degradation of the shell PLGA layer. As observed in Figure III.8(A-B), the tiny holes which form during the first 8 hrs of incubation are responsible for the burst release regime (Figure III.7(A)). Presumably, these holes serve as channels which facilitate the fast dissolution and diffusion

of the core material into the PBS medium. Afterwards, over the bulk/homogenous degradation of the PLGA shell the holes extended (Figure III.8(C-F)), so the remaining NGF is released from the nanofibers in a sustained manner.

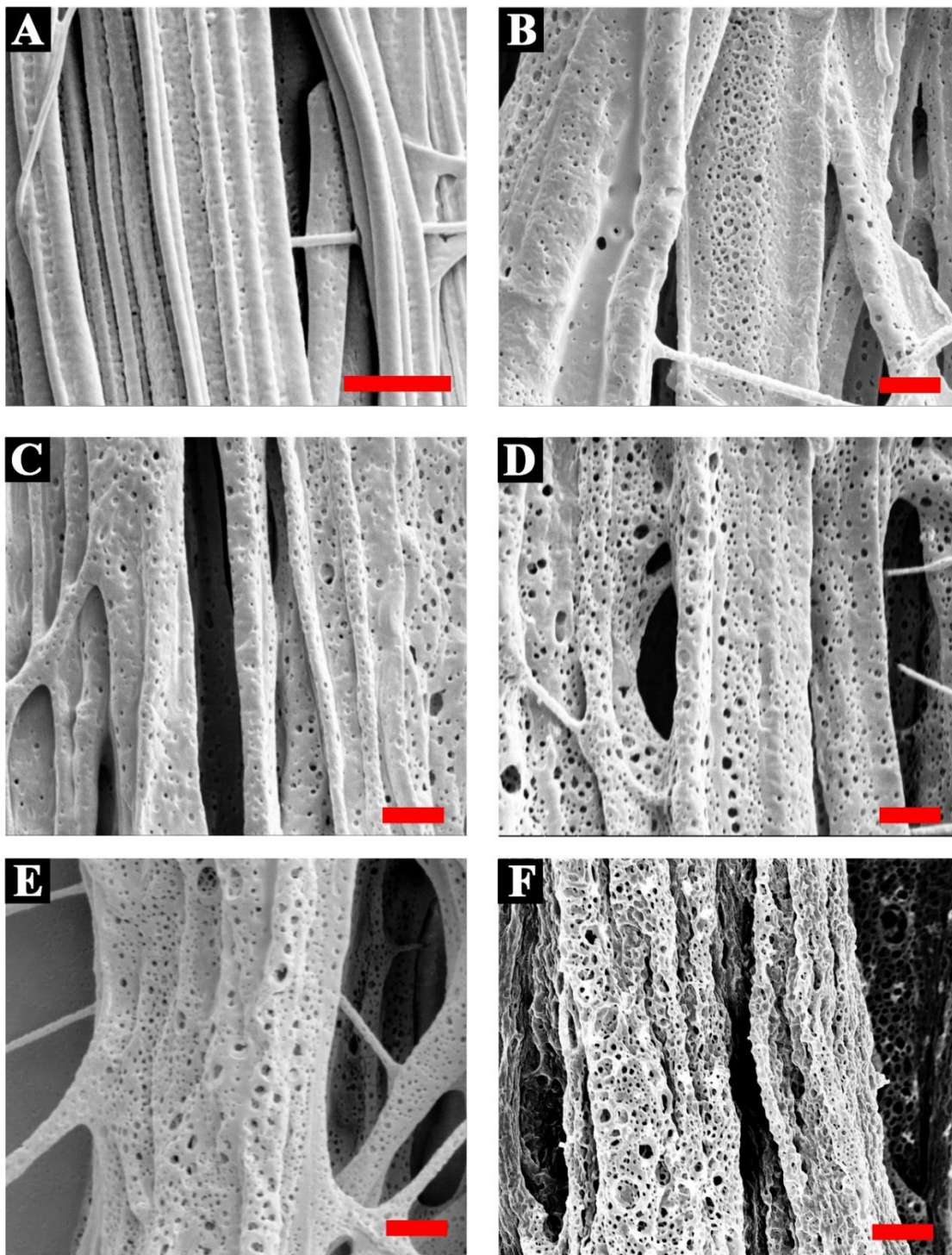


Figure III.8. SEM images of the aligned core-shell nanofibers after incubation in PBS at 37°C for different periods of time: A) 5 min, B) 8 hrs, C) 2 days, D) 3 days, E) 4 days, and F) 2 weeks. All scale bars represent 2 μm .

Conclusions

We successfully encapsulated NGF into biodegradable PEO/PLGA (core/shell) aligned nanofibers through coaxial electrospinning, while the NGF could preserve its bioactivity during fabrication and delivery. Utilizing response surface methodology (Box-Behnken Design), we revealed the linear, interaction, and quadratic effects of controllable processing parameters including inner and outer flow rates, applied voltage, needle-collector distance, and collector speed, on the diameter and size distribution of the core-shell nanofibers. According to ANOVA test results, inner flow rate, collector distance, and voltage showed significant effects on nanofibers diameter, while the collector speed was the only significant factor for the fibers size distribution. Optimizing each processing variable for minimizing the diameter and size distribution, we achieved nanofibers with a minimum diameter (down to 323 nm) and a very narrow size distribution (*C.V.* 2.37%). Diagnostic tests indicated that the predictive quadratic regression model was an appropriate fit for fiber diameter ($R^2 = 0.8$), whereas it was not an accurate fit for fiber size distribution ($R^2 = 0.5$). The NGF release profile from the core-shell nanofibers indicated a short burst release (81% in ~8 hr) followed by a sustained and nearly zero-order release (~13%) over 2 weeks of incubation in PBS. Mathematical modeling of the release fraction profile based on Michaelis–Menten kinetics function provided an excellent curve-fit to the experimental data ($R^2 = 0.993$). Accordingly, it was suggested that the hydrolytic degradation of the PLGA shell layer controls the NGF release kinetics. We believe that the theoretical and experimental outcomes of this study can be used as a comprehensive technical guide for

utilization of NGF-loaded aligned nanofibers in nerve regeneration application as potential physical and chemical guidance cues for neurite outgrowth.

IV A Transdermal Patch Based on Biodegradable Fibers for Skin Drug Delivery

Abstract

Transdermal drug delivery is an emerging pathway for continuous delivery of therapeutic agents through the skin. Development of flexible transdermal patches has been of great attention for sustained, noninvasive, and on-demand delivery of therapeutic compounds. Polymeric fibers are one of the most versatile materials utilized in drug delivery, wound healing, and tissue scaffold applications, however, their use as drug carriers for development of transdermal patches has not been well addressed yet. In this work, we present a transdermal patch design based on biodegradable fibers encapsulated with an anti-inflammatory drug (dexamethasone). We further assess the drug transport efficacy of the designed patch both in-vitro and in-vivo.

Introduction

In recent decades, scientists have made tremendous achievements in the field of drug delivery through transdermal pathway, as the skin provides a large surface area accessible for delivering drugs [200]. However, further studies are in progress to design efficient transdermal delivery systems that support sustained drug release at the targeted area in the desired therapeutic level without posing side effects [201]. Recent advancements in the field of nanotechnology have enabled the development of new approaches to design more efficient and controlled drug delivery systems [202].

Transdermal delivery is an emerging approach for continuous transport of therapeutic agents across the skin [203]. The stratum corneum layer of the epidermis is responsible for regulating the transport of different drugs or active compounds into the skin [204]. Transdermal delivery systems offer a variety of advantages over other delivery routes. Remarkably, the delivery of medication through transdermal route is less invasive compared to intravenous and oral routes. Hypodermic injections are painful, generate dangerous medical waste and pose the risk of disease transmission by needle reuse. The oral route may cause drug degradation, under extreme acidity of the stomach, and erratic delivery due to interaction with food. Accordingly, the transdermal delivery provides enhanced bioavailability and biocompatibility by evading the hepatic first-pass metabolism, improves patient compliance, and allows ceasing the drugs or compounds absorption, preventing undesired effects and overdose [200, 204]. On the other hand, the application of this method is more challenging, as only a limited number of drugs are amenable to administration by this route. The penetration rate can vary by the skin type, the application site, race, age, etc. [204]. A transdermal delivery system should be incorporated with an adequate drug formulation and allow considerable amount to overcome the skin barrier. Moreover, it is necessary to develop biocompatible drugs to avoid skin irritation and must ensure that the drug will not be inactivated on the skin surface and/or during the penetration process.

Flexible transdermal delivery patches have been developed for sustained, noninvasive or minimally invasive, and on-demand delivery of therapeutic compounds [205-208]. Compared to their rigid counterparts, flexible transdermal delivery systems can conform

to the skin for a long period with minimal pain or irritation on the skin [209-211]. To date, transdermal patches are able deliver over twenty drugs and drug combinations [212]. More recently, buprenorphine and capsaicin skin patches have respectively been approved for chronic and neuropathic pain control. Several other drug candidates, such as insulin, loxoprofen sodium, dextroamphetamine, abaloparatide, sumatriptan, donepezil, and dexamethasone, are also in clinical trials for transdermal delivery [213].

In recent years, polymeric fibers have been of great interest for development of drug carriers in wound healing, skin burn therapy and transdermal drug delivery systems [214, 215]. Electrospinning is a straightforward, cost-effective, and versatile technique for fabrication of polymeric micro/nanofibers with tunable structural properties [151]. Using this technique, it is possible to fabricate porous fibrous materials from natural or synthetic polymers with some specific characteristics such as high porosity and large surface area to volume ratio [216]. Pharmaceutical ingredients which are commonly delivered using electrospun fibers include antibiotics, antitumor drugs, anti-inflammatory drugs, proteins and nucleic acids [217]. Most studies have utilized fiber drug delivery systems in implantable scaffolds or wound dressing, whereas few works reported the application of fibrous transdermal patch on the healthy skin thus far [218, 219]. However, these few studies have been promising for practical applications in future [218, 220, 221].

In this work, we present a novel transdermal patch based on poly (lactic-co-glycolic acid) (PLGA) for skin delivery of dexamethasone (DEX, an anti-inflammatory drug). PLGA is approved by the European Medicine Agency and the US Food and Drugs Administration as a biodegradable polymer to design various drug delivery systems [222].

To the best of our knowledge, this is the first report on transdermal delivery of DEX using a fiber delivery system.

Methods

Materials

A commercially available blister adhesive bandage was supplied from KT Tape. Poly(lactic-co-glycolic) (PLGA 50:50, $M_w = 44.5$ KDa, Acid terminated) with inherent viscosity of 0.68 dL/gr and polydispersity index (PDI) of 1.78 was purchased from LACTEL Absorbable Polymers. Organic soluble dexamethasone (DEX) was purchased from Enzo Company. Agarose powder (Agarose ITM, Gel strength ≥ 1200 g/cm) was purchased from VWR Life Science. To prepare polydimethylsiloxane (PDMS) mold, SYLGARD 184 silicon elastomer base and curing agents were supplied from Dow Chemical Co. Transwell[®] 12-well plate (12 mm diameter) was purchased from Corning Inc.

Fabrication of the transdermal patch

Electrospinning of drug-loaded fibers

A typical electrospinning setup consisting of a syringe pump (Logato 100, kd Scientific) and a high voltage power supply (PS/ER40P07, Glassman High Voltage, Inc.) were used to produce PLGA fibers. A set of preliminary experiments was performed to determine the spinnable range of processing parameters, including applied voltage, flow rate, needle-collector distance, and syringe needle gauge. In addition, various solution compositions with different amount of polymer and drug loadings were tested to identify

the appropriate composition for generation of consistent and uniform fibers with maximum drug loading. Accordingly, to prepare the electrospinning solution, 372 mg PLGA (20 wt.%) with 20 mg DEX were dissolved in 1 ml chloroform and stirred over night at room temperature. The prepared solution was then electrospun at 25 °C and 30% humidity on a rectangular shaped (1.5 cm × 2 cm) gold-coated silicon wafers for 30 min using a syringe needle gauge 22, voltage 13 kV, flow rate 1 ml/hr, and collector distance of 10 cm.

Patch Assembly

The fabricated DEX/PLGA fibrous mat (dimensions 1.5 × 2 cm, weight ~ 40 mg) was removed from the silicon substrate and mounted on the adhesive bandage. A rectangle hole was previously created at the center of the adhesive bandage to provide an opening for adding water to keep the hydrogel wet while the patch is applied on the skin. An agarose solution (0.5 w/v%) was prepared by adding 10 mg agarose powder to 2 ml deionized water and then heating up the slurry using microwave to dissolve agarose in water. The fibrous mat was surrounded by a rectangular PDMS mold to make a hydrogel layer on top of the fibrous layer. About 200 µl of the agarose solution was poured into the mold and let it to be cooled down. After the hydrogel layer cured, the PDMS mold was removed from the patch. Figure IV.1 illustrates the patch assembly process, step-by-step.

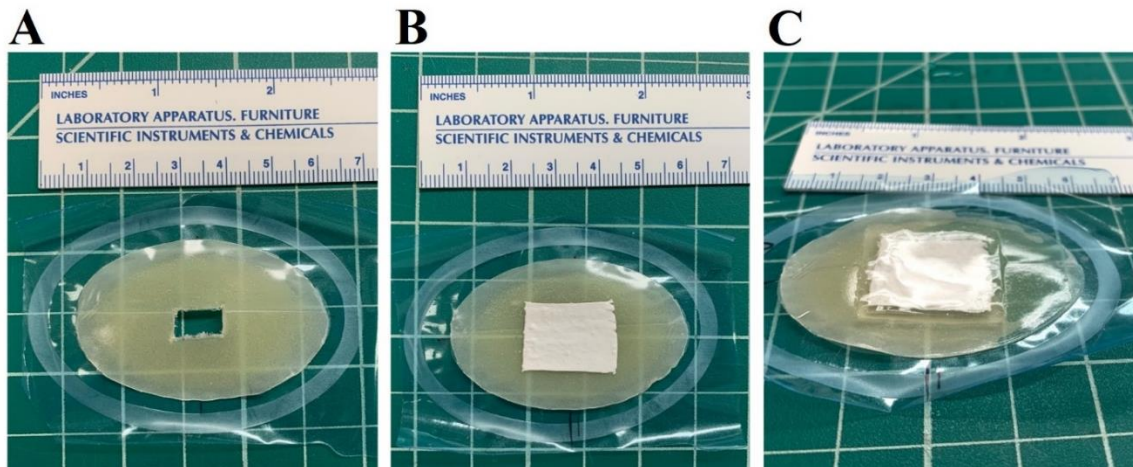


Figure IV.1 Patch assembly: A) An adhesive bandage with an opening at the center, B) Placing a fibrous mat on the bandage, and C) making a hydrogel layer on top of the fibrous mat.

Fibers morphology characterization

The morphology of the electrospun fibers was characterized using Field Emission Scanning Electron Microscopy (FESEM, FEI 235). Samples were mounted on aluminum stubs by carbon tape and a carbon paint was used for grounding. Prior to microscopy, probes were sputter-coated with a thin layer of gold using Denton Sputter Coater for 70 s at 40 mA.

In-vitro drug release assessment

The drug release behavior of the fabricated transdermal patch across a porous membrane was studied using a tissue culture treated Transwell plate as a simplified cell barrier model. For this purpose, three circular shape patches with the diameter of 1 cm were prepared and each separately placed into the apical chambers of the plate with a polyester membrane with the pore size of 400 nm (see Figure IV.2). Then, 1 ml PBS was added to

each basal chamber. For sampling, the apical chambers associate with the patches were removed from the plate, and then 2 ml methanol was added to the PBS medium within each basal chamber to ensure the dissolution of the transported DEX for further quantification analysis. To quantify the transported DEX, the resultant PBS/methanol solution (3 ml) in each basal chamber was transferred into a glass cuvette for UV detection at $\lambda = 240$ nm. After sampling at each time-point, the basal chambers were refilled with 1 ml fresh PBS solution.

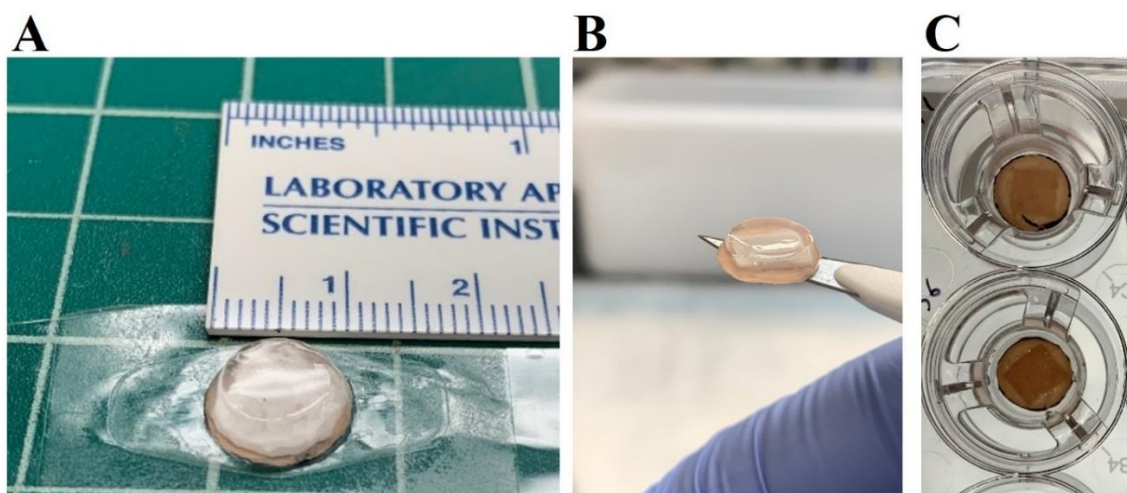


Figure IV.2. Circular shape patch (A and B) prepared for in-vitro drug transport assessment using Transwell plate system (C).

In-vivo skin drug delivery

Three 12-week-old C57/B6 mice were anaesthetized using isoflurane and the fur on the dorsal side of the mouse was removed after trimming and using a depilatory cream. The shaved region was then cleaned with 70% alcohol and the patch was applied to the region. The hydrogel was hydrated every 24 hours by adding a drop of water to the exposed

hydrogel. About 100 μ l of blood was collected on day 0, day 2 and day 4 by submandibular vein puncture. The blood was allowed to clot for 60 minutes and then centrifuged at 1500 RPM for 15 minutes to separate the serum. Serum samples were frozen in -80 °C until analysis. For DEX analysis, the serum samples were thawed and then the DEX within the samples was quantified via liquid chromatography mass spectrometry (LCMS).

Results and discussion

Morphology of DEX-loaded PLGA fibers

Scanning electron micrographs of the PLGA fibers encapsulated with DEX are shown in Figure IV.3. As observed, randomly oriented fibers with the average diameter of 5.5 μ m (C.V. 23%, n = 50) are created after electrospinning, while no bead has been formed along the fibers length. Formation of uniform fibers without beads is of great importance to achieve a consistent and controlled drug release. According to the solution composition formulated for electrospinning, the drug to polymer ratio of the fabricated fibers is 4%. This means that each patch (with ~40 mg fibrous mat) is loaded with 1.6 mg DEX. As the agarose hydrogel topping is added onto the fibrous mat (Figure IV.1(C)), the fiber interspaces are filled with the hydrogel. The hydrogel layer facilitates the hydrolytic degradation of the PLGA fibers, and it is assumed to provide a pathway for DEX transportation towards the membrane barrier (skin) as well.

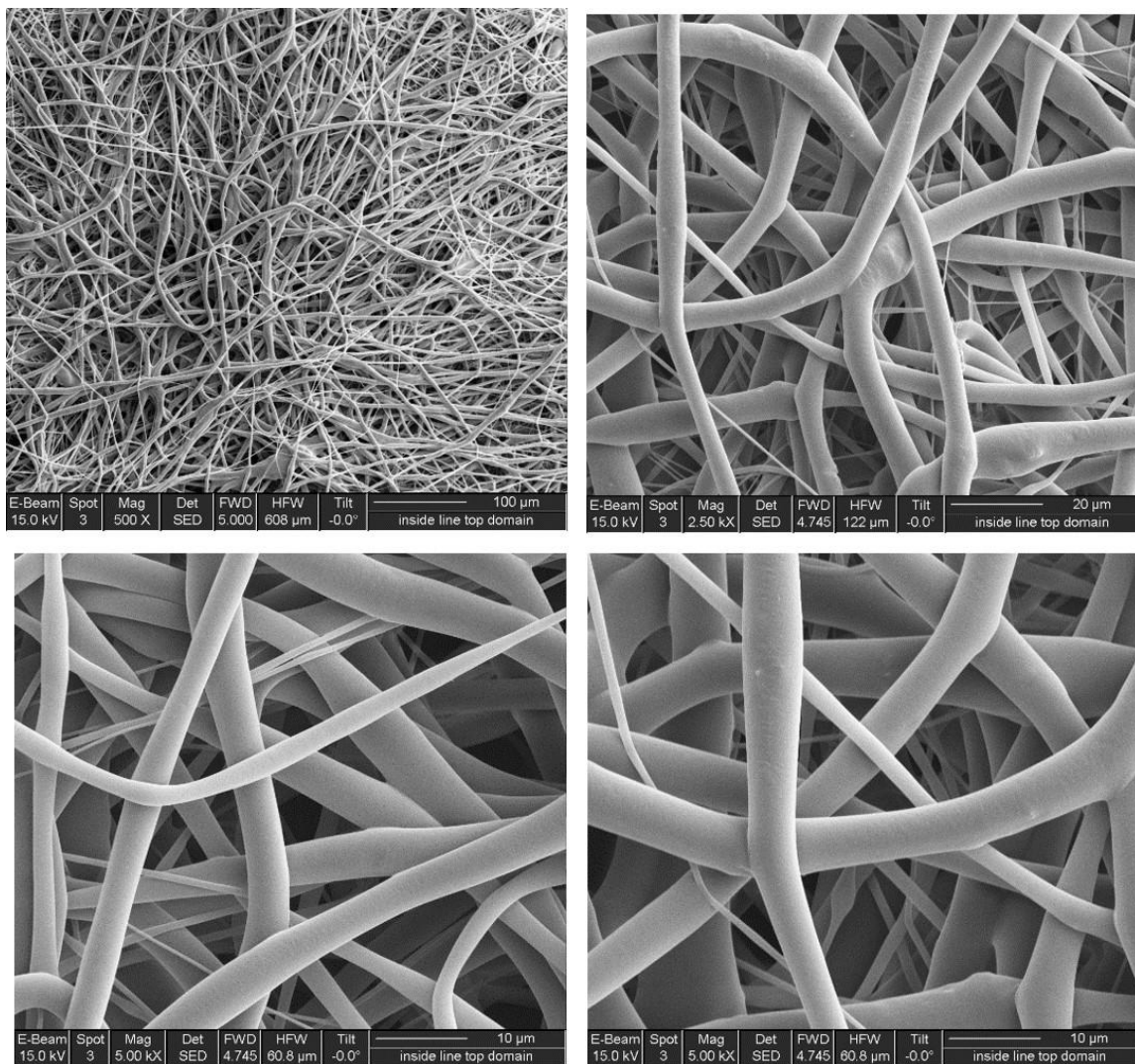


Figure IV.3. Scanning electron micrographs of the PLGA fibers encapsulated with DEX at various magnifications.

In-vitro drug release and transport

Here, we used a Transwell plate system to simulate the release/transport of DEX across a membrane barrier (a tissue culture treated membrane with the pore size of 400 nm). The fabricated patch was placed in the apical chamber, while the basal chamber contained PBS. Accordingly, the amount of DEX released from the fibers into the hydrogel and then

transported through the membrane was measured over 28 days at room temperature. The obtained release/transport profile is demonstrated in Figure IV.4(A). As seen, the cumulative DEX release/transport over 28 days is 56.2 $\mu\text{g/ml}$, which corresponds to the fractional release/transport of 14.6% as depicted in Figure IV.4(B). This low release/transport percentage is attributed to the limited solubility of organic DEX within the hydrogel. The release/transport profile indicated a nonlinear correlation with time. (Figure IV.4(B)). The third order polynomial curve fit to the experimental data obtained the R-squared value of 0.999.

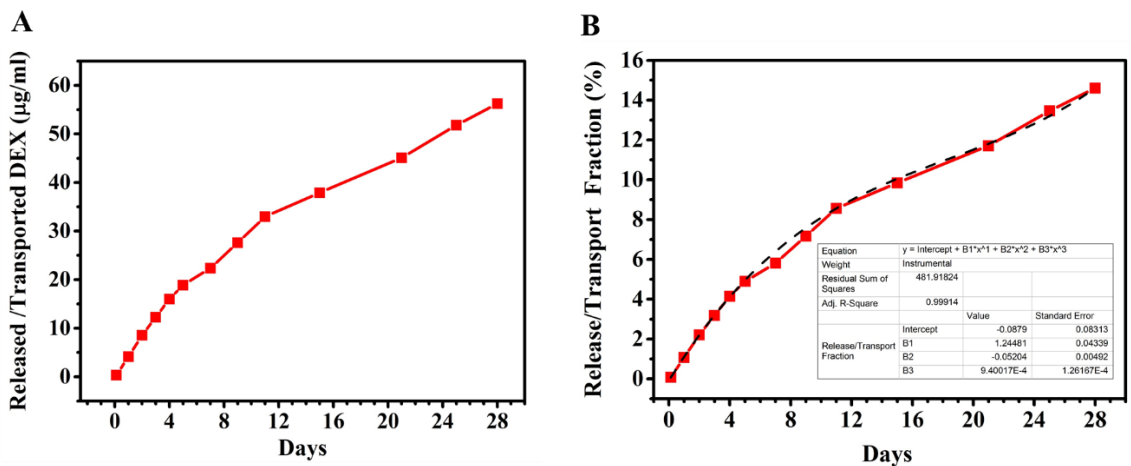


Figure IV.4. A) DEX release profile through Transwell plate membrane into PBS. B) DEX release percentage from PLGA fibers with a third order polynomial curve fit. Data is shown in mean \pm S.E. (n = 3, error bars are masked by data points).

In-vivo study of the transdermal patch

To assess the patch efficacy for transdermal delivery of DEX, the patch was applied to the dorsal side of the mouse as illustrated in Figure IV.5(A-B). The blood sampling was scheduled every other day until the patch peeled off from the mouse skin at day 4 (Figure

IV.5(C)). LCMS analysis of the blood serum revealed the average DEX concentrations of 114, 450, and 145 ng/ml for sampling at day 0 (control), day 2, and day 4, respectively. The day 0 measurement showed a high value background. However, there was a significant increase in the DEX concentration from Day 0 to Day 2, which confirms the DEX transport across the mouse skin. The peak value obtained at Day 2 was 650 ng/ml, which is quite less than the therapeutic target (12.5 μ g/ml) considered for IP injections (1-10 mg/kg). In addition, this peak value is <0.1% of the total amount of DEX encapsulated into the fibers (with the assumption of 2 ml blood in the mouse body), which indicates a very low release/transport fraction than that obtained for in-vitro study (~ 2% after 2 days in Transwell plate system). Based on our observations, the patch was getting dried and too rigid over time under mouse cage ventilation and adding water droplet could not keep it wet and flexible. Accordingly, the decrease in DEX concentration from Day 2 to Day 4 may presumably due to the lack of good contact between the patch and the mouse skin as the patch and the hydrogel get dry.

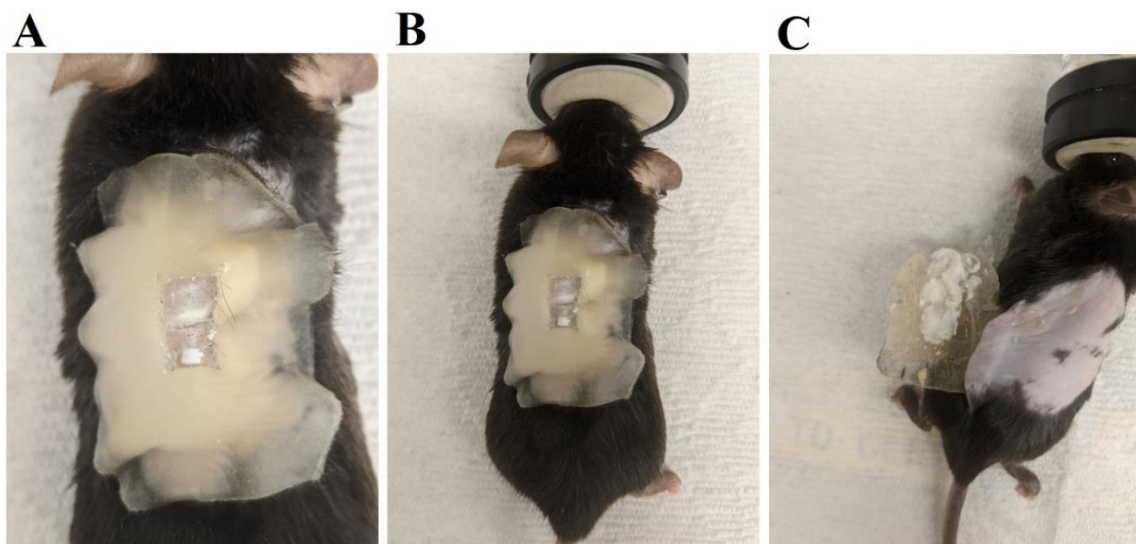


Figure IV.5. A-B) Photographs of the patch applied on the mice skin. C) The patch peeled off from the mice skin at day 4.

Conclusions

In summary, we presented a new design for development of transdermal patches based on biodegradable fibers for drug delivery through the healthy skin. We successfully electrospun uniform PLGA fibers encapsulated with DEX, and then utilized them as a drug release layer associated with a hydrogel topping as the drug pathway towards the skin. In-vitro assessments revealed a linear release/transport behavior over the course of study. The patch efficacy for in vitro drug transport was about 15% after 28 days, while the in-vivo efficacy after 2 days on mouse skin was less than 0.1%. The low efficiency of the patch is due to the insolubility of organic DEX in the hydrogel layer. The hydrogel was utilized to facilitate the hydrolytic degradation of the PLGA fibers for DEX release, but it showed a limited drug transport towards the skin layer. The patch at the current design does not possess the required therapeutic efficacy and it needs further modifications. For future

directions, it is suggested to replace the hydrogel with an organic polyol compound with polar groups (e.g., glycerol) to provide the conditions for both fibers degradation and also organic DEX diffusion towards the skin.

V Direct Measurement of Mass Transport in Actuation of Conducting Polymers Nanotubes

This chapter is published as is in 2018 40th Annual International Conference of the IEEE Engineering in Medicine and Biology Society (EMBC), pp. 4472-4475.

Abstract

Nanostructured Conducting polymer (CP) actuators are promising materials for biomedical applications such as drug release systems. However, understanding the actuation behavior at the nanoscale has not yet been explored. In this work, poly(3,4-ethylenedioxythiophene) (PEDOT) and poly(pyrrole) (PPy) nanotubes doped with a large counter ion (i.e., poly(styrene sodium sulfonate) (PSS)) were fabricated using electrochemical deposition of PEDOT and PPy around poly(L-lactide) (PLLA) nanofiber templates, followed by template removal in chloroform. The actuation and mass transport behavior of PPy and PEDOT nanotubes were investigated and compared. The nanotubes were subjected to a redox process using cyclic voltammetry in 0.1 M NaPSS electrolyte solution as the potential swept between -0.8 V and +0.4 V for 20 cycles at 10, 50, 100, and 200 mV/s scan rates. The mass transport behavior of these nanotubes was characterized via electrochemical quartz crystal microbalance (EQCM) technique. The EQCM results showed that PEDOT nanotubes had a higher mass exchange capability than their PPy counterparts, especially at higher scan rates. Also, it was revealed that PPy nanotubes were more sensitive to the scan rate than the PEDOT nanotubes, and the maximum mass

exchange capability of the PPy nanotubes was noticeably reduced by increasing the scan rate.

Introduction

Conducting polymer actuators are promising materials for biomedical applications ranging from artificial muscles to drug delivery devices [3, 13, 223, 224]. These devices rely on bulk volume changes of conducting polymers (CPs) which arise from electrochemical redox processes. It is believed that changes in polymer chain conformations combined with the transportation of ions and solvent in and out of the polymer matrix are responsible for the micro and macro-scale expansion/contraction of the polymer [225]. The presence of multiple ion species in a liquid electrolyte can significantly complicate the study of actuation behavior of conducting polymer. Small counter ions in particular result in simultaneous motions of cations and anions in/out of the polymer matrix. Further, this multiple ion motion results in poor actuation [226]. In order to simplify the ion transport analysis, it is preferable to use large dopant molecules such as dodecylbenzenesulfonate (DBS) or poly(styrene sodium sulfonate) (PSS), as they become immobilized in the CP matrix during electrochemical deposition, allowing only cation motion during actuation [227].

Biocompatible conducting polymers such as poly(pyrrole) (PPy) and poly(3,4-ethylenedioxythiophene) (PEDOT) have been widely employed for biomedical applications [110, 228-230]. PPy films have garnered the most attention owing to their well-defined actuation behavior [3]. PEDOT has not received much attention despite its superior conductivity, chemical stability, and biocompatibility. Therefore, it is of interest

to compare the actuation behavior of both PPy and PEDOT. Electrochemical quartz crystal microbalance (EQCM) is a highly accurate and effective tool (nanogram precision) to study mass transport phenomena and molecular interactions at electrode-electrolyte interfaces. EQCM can be utilized for the analysis of mass changes during ion/solvent migration at the polymer-electrolyte interface. The ion exchange behavior of CP films have been previously studied using EQCM as a function of various dopant/electrolyte systems [231]. Here we investigate for the first time, the ion transport behavior of PPy:PSS and PEDOT:PSS in the form of randomly-oriented nanotubes during cyclic voltammetry controlled actuation using EQCM as a function of applied voltage and scan rate.

Methods

Materials

Poly-L-Lactide (PLLA, Resomer 210) with the inherent viscosity of 3.3 - 4.3 dL/g was purchased from Evonik Industries. Benzyltriethylammonium chloride (BTEAC) and pyrrole ($M_w = 67.09$ g/mol) were purchased from Fisher Scientific. 3,4-ethylenedioxythiophene (EDOT, $M_w = 142.2$ g/mol) was purchased from Sigma Aldrich. Poly (sodium-p-styrenesulfonate) (PSS, $M_w = 70$ kD) was purchased from Acros-Organics. Chloroform was purchased from SupraSolv Company. EQCM crystals (6 MHz, Au/TiO₂, quartz) were purchased from Metrohm USA. N-type Silicon wafers coated with SiO₂ were purchased from University Wafer Company.

Electrospinning of template nanofibers

A homogeneous solution of 3% wt PLLA and 10% wt BTEAC (respect to PLLA) in 5 ml chloroform was prepared by stirring the mixture overnight at room temperature. Then, the solution was electrospun using a syringe pump with the spinneret gauge of 23, an applied voltage of 10 kV, a flow rate of 50 $\mu\text{l/hr}$, and a syringe-substrate distance of 11 cm for 2 min. Temperature and humidity were kept constant at 26°C and 32%, respectively. The fabricated nanofibers were deposited directly onto one side of each EQCM crystal.

Electrochemical deposition of CPs

Galvanostatic polymerization was performed at room temperature using an Autolab PGSTAT 128N (METROHM USA) equipped with an EQCM kit in a two-electrode configuration. An EQCM crystal was the working electrode (0.35 cm^2), and an Au wire served as counter electrode. Pyrrole: PSS and EDOT:PSS solutions (0.2 M Pyrrole and 0.2 M PSS for Py:PSS, 0.02 M EDOT and 0.2 M PSS for EDOT:PSS in deionized water) were prepared for electropolymerization of PPy and PEDOT on EQCM crystals covered with PLLA nanofibers. The current density was set at 0.5 mA/cm^2 , and the electrodeposition was conducted for 15 min. Before deposition, the sample was kept in the electrolyte for 15 min to ensure that the CP solutions have completely diffused into spaces between the nanofibers. After electrodeposition of CPs on the PLLA nanofibers, the nanofibers were dissolved in chloroform for two days to form hollow CP nanotubes.

Cyclic voltammetry and EQCM measurements

Ion/solvent mass exchange behavior of the CP nanotubes were characterized in a 0.1 M NaPSS electrolyte by performing simultaneous cyclic voltammetry (CV) and EQCM measurements (Autolab PGSTAT 128N equipped with EQCM kit), in a three-electrode configuration with a saturated Ag/AgCl reference electrode and a gold counter electrode. The CP nanotubes were cycled in the potential range of -0.8 to +0.4 V (versus the Ag/AgCl reference electrode) for 20 cycles, at different scan rates (10, 50, 100, and 200 mV/s) at room temperature ($n = 3$ per each scan rate). Prior to the measurements, a stable concentration of Na^+ ions within the CP structure was ensured by subjecting the samples to five cycles at the scan rate of 10 mV/s.

Results and discussion

Figure V.1(A) shows the electrospinning setup used in this study for the fabrication of randomly oriented PLLA nanofibers on the surface of quartz crystals. As shown in Figure V.1(B), the fibers were randomly oriented and had a diameter of 200 ± 30 nm ($n = 100$). Figure V.1(C-D) illustrate PEDOT and PPy nanotubes with the average outer diameter of 552 ± 88 nm and 624 ± 121 nm, respectively ($n = 40$). The mass of electrodeposited CP can be calculated using EQCM measurement and Sauerbrey's equation [232] which relates changes in quartz crystal oscillation frequency (Δf) to the change in mass (Δm),

$$\Delta m = -\Delta f / C_f. \quad \text{V.1}$$

C_f is a sensitivity factor depending on the resonance frequency and operating temperature of the quartz crystal. Here, $C_f = 0.0815 \text{ Hz/ng/cm}^2$ was considered for determining delta mass. Based on the calculations, the total deposited mass of PEDOT and PPy were $270 \pm 38 \mu\text{g}$ and $299 \pm 14 \mu\text{g}$, respectively ($n = 3$), showing that approximately the same amount of both CPs has been deposited on the PLLA nanofibers under the same deposition conditions.

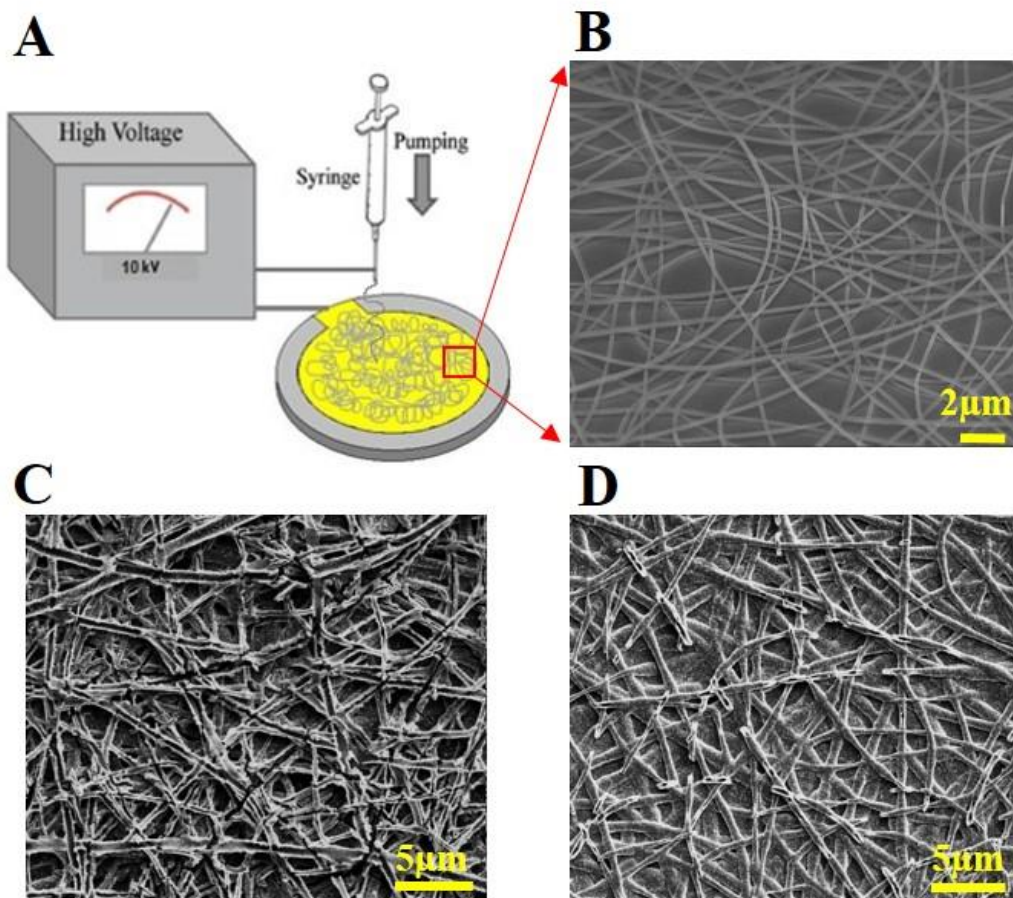


Figure V.1. A) Electrospinning setup for formation of PLLA nanofibers on the gold coated quartz crystal. B) SEM of the random PLLA nanofibers. C-D) SEM images of PEDOT (C) and PPy (D) nanotubes after dissolving the PLLA template.

Figure V.2 demonstrates the change of mass (Δm) as a function of time during CV of the PEDOT and PPy nanotubes at different scan rates. Since both PEDOT and PPy nanotubes were doped with immobile PSS anions, Δm is only attributed to the transportation of solvated Na^+ ions and water molecules in/out of the CPs. Each spike is related to the transportation of mass during individual cycles (20 cycles total). As shown in Figure V.2, as the scan rate increased from 10 to 50, 100, and 200 mV/s, the maximum of Δm (Δm_{max}) decreased from $8.7 \pm 0.53 \mu\text{g}$ to $7.47 \pm 0.22 \mu\text{g}$, $4.3 \pm 0.18 \mu\text{g}$, $2.43 \pm 0.04 \mu\text{g}$ for PPy nanotubes and from $9.17 \pm 0.54 \mu\text{g}$ to $8.25 \pm 0.21 \mu\text{g}$, $7.42 \pm 0.1 \mu\text{g}$, and $5.77 \pm 0.08 \mu\text{g}$ for PEDOT nanotubes. This behavior is most likely due to the limited time available for transportation of solvated ions at higher scan rates, which occurs in order to equilibrate the electrical charge in polymer. In addition, the waveform of mass fluctuation was similar as the number of scans/time increased.

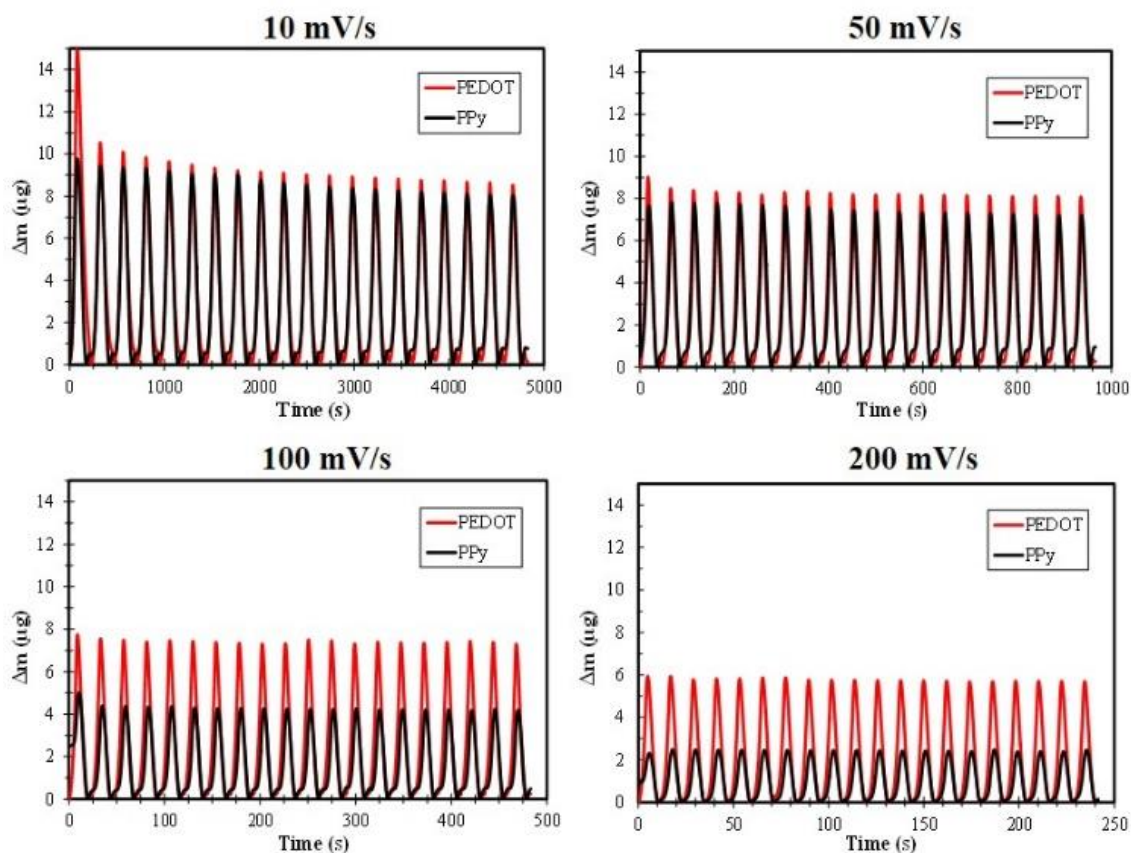


Figure V.2. Mass change (Δm) as a function of time during cycling of the PEDOT and PPy nanotubes at different scan rates (20 cycles).

Figure V.3 shows the maximum mass exchange (Δm_{max}) values attributed to the cycle of 20th for PPy and PEDOT nanotubes at different scan rates. Δm_{max} for PPy nanotubes was $8.03 \pm 0.78 \mu\text{g}$, $6.81 \pm 0.7 \mu\text{g}$, $4.2 \pm 0.57 \mu\text{g}$, and $2.47 \pm 0.43 \mu\text{g}$ and for PEDOT nanotubes was $8.53 \pm 0.69 \mu\text{g}$, $8.09 \pm 0.54 \mu\text{g}$, $7.28 \pm 0.4 \mu\text{g}$, and $5.7 \pm 0.33 \mu\text{g}$ at 10, 50, 100, and 200 mV/s respectively ($n = 3$). PEDOT nanotubes showed significantly higher Δm_{max} than their PPy nanotube counterparts, especially at 100 mV/s and 200 mV/s ($p < 0.05$). The trends in mass exchange capability for PEDOT and PPy nanotubes can be explained by comparing their surface morphologies during CV.

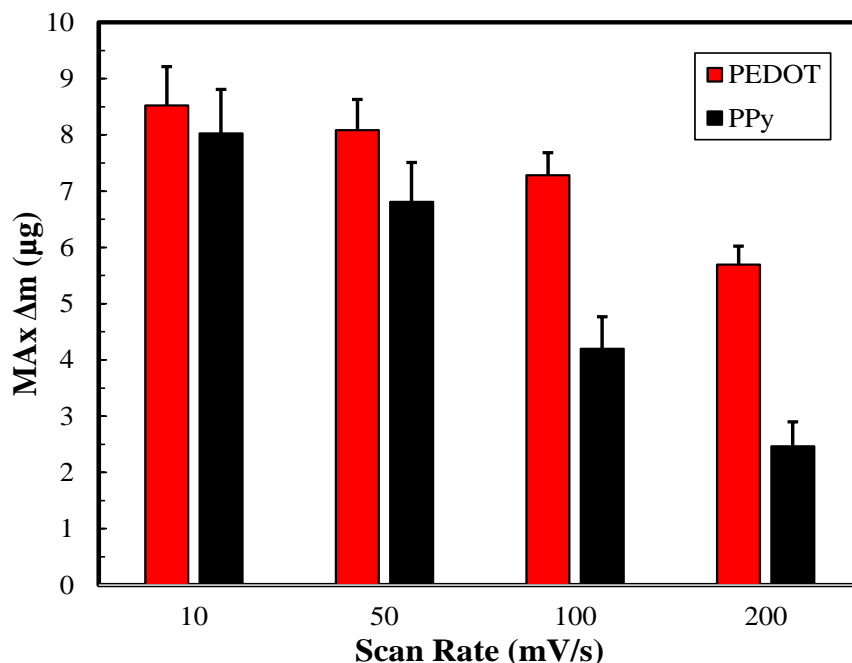


Figure V.3. The maximum Δm values related to the 20th cycle for PPy and PEDOT nanotubes at different scan rates ($n = 3$).

Figure V.4 demonstrate the surface morphology of PEDOT and PPy nanotubes before and after CV at the scan rate of 100 mV/s for 20 cycles. As shown in this figure, after 20 cycles the surface morphology of the PEDOT nanotubes noticeably changed (Figure V.4(A-B)). In contrast, the morphology of PPy nanotubes remained relatively unchanged (Figure V.4(C-D)). These observations in surface morphologies might be explained by the difference in the mechanical properties of PPy and PEDOT. PEDOT:PSS is less flexible and has a higher mechanical strength than PPy:PSS. The elastic modulus of doped PPy and PEDOT was reported in the range of 0.03-1 GPa, and 2.2-4.2 GPa, respectively [233, 234]. Thus, during CV (expansion and contraction), PEDOT nanotubes were deformed and fractured, resulting in the appearance of cracks on the surface of PEDOT nanotubes (yellow arrows in Figure V.4(B)). The crack formation increased the surface area available to the

electrolyte, facilitating the transportation of solvated Na^+ ions and water molecules in/out of the CP matrix, and resulting in a higher mass exchange capability (Figure V.2 and Figure V.3).

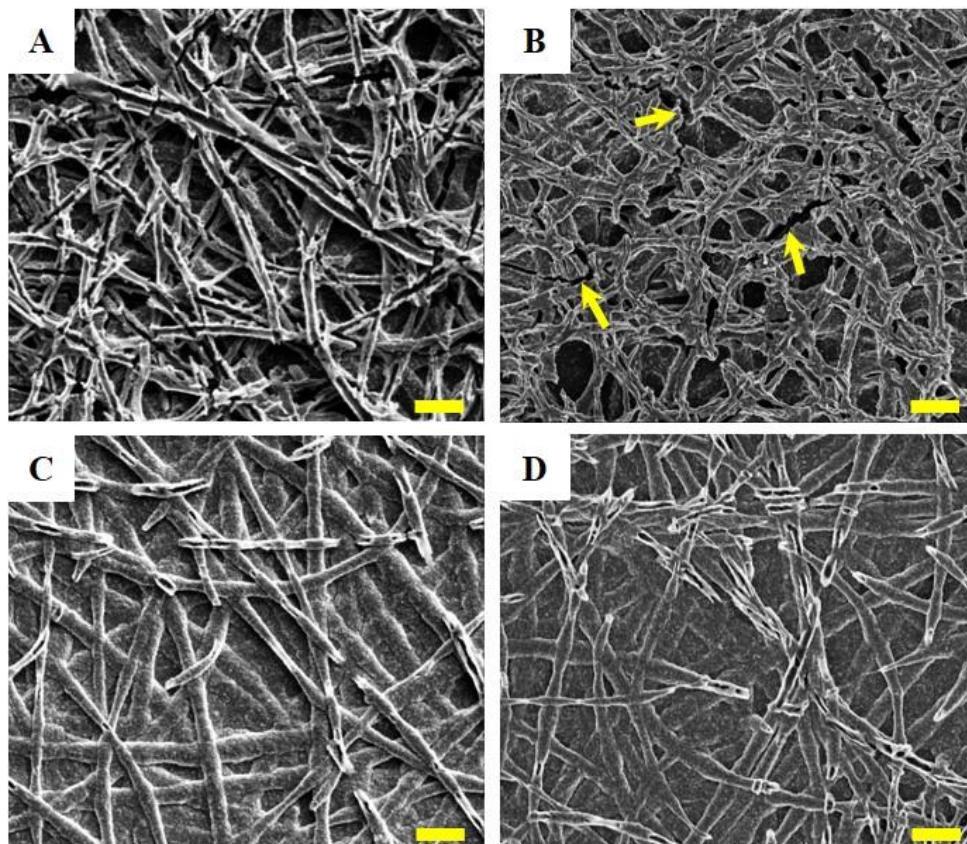


Figure V.4. SEM images of CP nanotubes before and after CV at 100 mV/s for 20 cycles: A) PEDOT (before), B) PEDOT (after), C) PPy (before), and D) PPy (after). Arrows point to the cracks appeared after cycling. Scale bars equal to 2 μm .

Figure V.5 and Figure V.6 show the measured current (i) and mass change (Δm) as a function of applied voltage at 10, 50, 100, and 200 mV/s for PEDOT and PPy nanotubes, obtained from the 20th cycle. As depicted in these figures, reduction of the samples from 0 to -0.8 V resulted in mass increase for both CPs, presumably due to the (1) transportation

of solvated Na^+ ions into the polymer in order to maintain the charge neutrality, and (2) migration of water molecules into the polymer induced by osmotic pressure [235]. By reversing the potential (i.e., oxidation), the mass continued to increase until the oxidation peak appeared. In this stage, further ion migration is less likely, indicating that the mass increase is due to only water molecule migration inside the polymer as an effort to balance the osmotic pressure in the system [235]. Thereafter, further oxidation resulted in mass decrease until the oxidation peak on the CV plot vanished. This phenomenon is shown by green dash lines in Figure V.5 and Figure V.6 for the scan rates of 10 mV/s and 50 mV/s. As demonstrated, the oxidation peak, which is characterized by a very broad peak in both CPs, is well-matched with the mass depreciation region in the Δm -potential graphs. This implies that the mass reduction was mainly due to the departure of solvated Na^+ ions from CP matrix. It is noteworthy that for both CPs, by increasing the scan rate from 10 mV/s to 50 mV/s, the region between the two green dash lines shifts from -0.77 V/+0.25 V to -0.74 V/0.3 V for PEDOT nanotubes and -0.76 V/+0.16 V to -0.61 V/+0.26 V for PPy nanotubes. In fact, by increasing the scan rate, the oxidation range shifts to a more positive potential, thus the mass reduction is postponed.

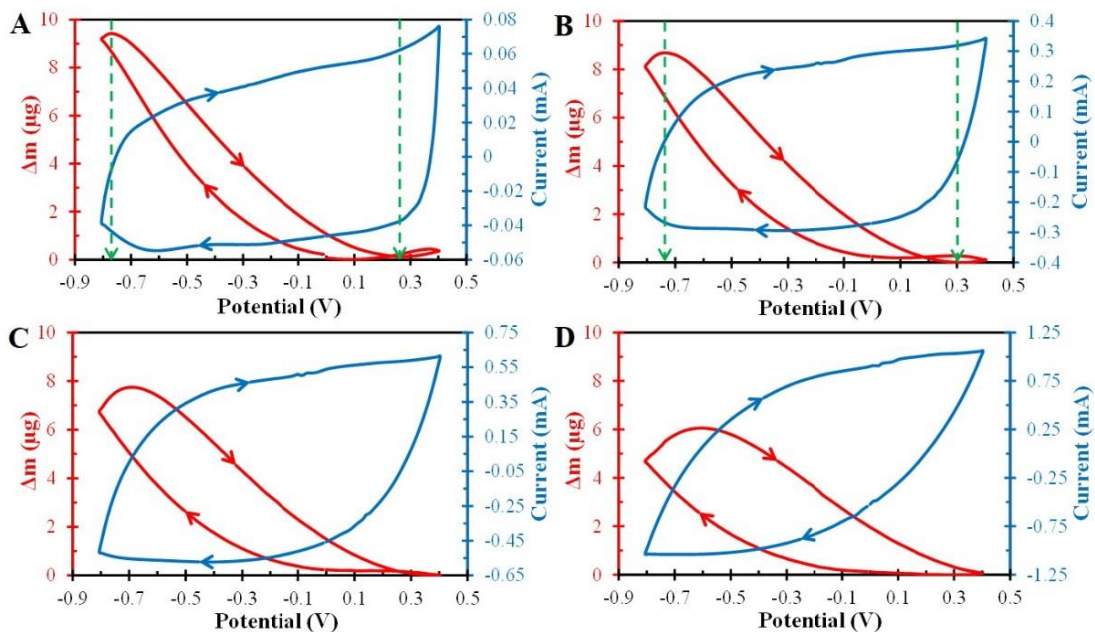


Figure V.5. Plots of measured current (blue) and Δm (red) as a function of potential for PEDOT nanotubes at different CV scan rates: A) 10 mV/s, B) 50 mV/s, C) 100 mV/s, and D) 200 mV/s. The arrows indicate the cycling direction.

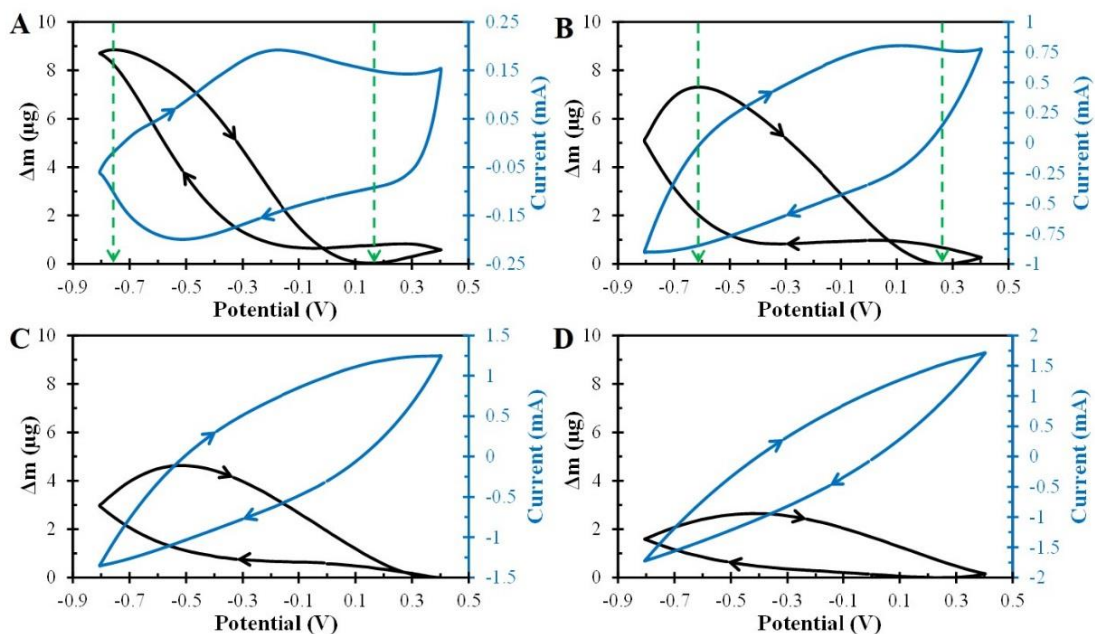


Figure V.6. Plots of measured current (blue) and Δm (black) as a function of potential for PPy nanotubes at different CV scan rates: A) 10 mV/s, B) 50 mV/s, C) 100 mV/s, and D) 200 mV/s. The arrows show the cycling direction.

Table V.1 shows the potential at which the maximum Δm (Δm_{max}) was measured during the 20th cycle of both CPs at all scan rates. According to this table, by increasing the scan rate from 10 mV/s to 200 mV/s, the voltage at the maximum Δm decreased to less negative values for both CPs (-0.77 V to -0.6 V for PEDOT nanotubes and -0.76 V to -0.42 V for PPy nanotubes). However, this shift is greater for PPy nanotubes than PEDOT nanotubes, again indicating that the PPy nanotubes are more sensitive to the increase of scan rate than their PEDOT counterparts. This also confirms that by increasing the scan rate, the mass depreciation is postponed, i.e., the mass depreciation starts at a less negative potential, because of the delay in the oxidation. Past the oxidation peak, the mass builds up to voltage +0.4 V, after which it finally reaches its initial value at voltage 0 V. Again, water migration into the CP matrix in an effort to maintain the osmotic pressure balance in the system is most likely responsible for the mass increase in the final stage.

Table V.1. The potential (V) at the maximum Δm (Δm_{max}) for PEDOT and PPy samples at various scan rates obtained from the 20th cycle.

Sample	Potential (V) @ Δm_{max}			
	10 mV/s	50 mV/s	100 mV/s	200 mV/s
PEDOT	-0.77	-0.74	-0.69	-0.6
PPy	-0.76	-0.61	-0.51	-0.42

Conclusions

We fabricated PEDOT and PPy nanotube on the surface of Au coated quartz crystals. we found that the morphology of PEDOT nanotubes considerably changes during CV while PPy nanotubes does not exhibit any noticeable changes. The resultant higher surface

area of the PEDOT nanotubes leads to the higher mass exchange capabilities than their PPy counterparts. Increasing the CV scan rate restricts the transportation of solvated Na⁺ ions and water molecules into/out of the CP nanotubes. This effect was especially pronounced for PPy nanotubes. The findings in this study may greatly impact the ongoing efforts to apply CP actuators for biomedical applications.

VI High-Performance Conducting Polymer Nanofiber-Based Actuators for Soft Robotics and Bioinspired Applications

Abstract

Actuators that transform electrical energy to mechanical energy through an electrochemical process have numerous applications ranging from soft robotics and micropumps to autofocus microlenses and bioelectronics. To date, achievement of large deformation strains with fast response times remains a challenge for electrochemical actuators operating in liquid wherein drag forces restrict the actuator motion and electrode materials and structures limit the ion transportation. Herein, a novel organic electronic actuator based on poly(pyrrole) nanofibers (PPy NFs) is presented that exhibits high electrochemical performance in liquid and gel electrolytes. This actuator demonstrates an impressive performance, including low power consumption/strain ($0.5 \text{ mW}/(\text{cm}^2\cdot\%)$), a large deformation (displacement 7.88 mm; strain 3.35%), fast response (speed $1280 \text{ }\mu\text{m/s}$; response times $<1\text{s}$), and excellent actuation stability ($>96.5\%$ in liquid electrolyte over 15000 actuations; 25 hours of continuous operation). This outstanding performance stems from excellent chemo-electro-mechanical properties of nanofibrous structure of PPy, including large ion transport and accumulation ($\sim 167 \text{ g/m}$), high charge storage density ($\sim 448 \text{ mC}/\text{cm}^2$), large capacitance ($\sim 170 \text{ F/g}$), and soft mechanical properties (average modulus $\sim 6.79 \text{ MPa}$). We utilize experimental studies of motion and mass transport along with the theoretical analysis for a variable-mass system to establish the dynamics of the actuator and to introduce a modified form of Euler-Bernoulli's deflection equation for this

PPy NFs actuator. This work provides new opportunities for next generation electrochemical actuators that can be utilized in soft robotics, artificial muscles, and biomedical devices.

Introduction

Ions play a key role in the life of living organisms, particularly for nerve signal transduction that is essential for contractile cells to produce muscle deformation and/or motion [236]. Inspired by function of biological muscle, artificial muscles concerning ion migration into/out of electrodes (e.g., ionic polymer-metal composites) have gained much attention in biomimetic technologies [237, 238]. Soft ionic actuators, also called electrochemical actuators, generate actuation deformation in response to applied voltage (below 1 V and up to several volts) by reversible intercalation and deintercalation of ions into/out of an electroactive layer. Such actuators have been intensively investigated for the use in soft robotic, artificial muscles, and biomedical devices [239-242]. One group of these actuators is air-working electrochemical actuators that are composed of one semipermeable ion-conductive electrolyte polymer membrane sandwiched between two electroactive layers [243, 244]. This type of actuators often utilizes conductive carbon nanomaterials such as carbon nanotubes [245], graphene [246], and graphdiyne [247]. Recent advances in materials science and fabrication techniques have enabled development of durable and lightweight air working electrochemical actuators capable of generating large strains and fast responses [248]. Most of these actuators are however, composed of multiple electroactive materials and thus, require rather complex fabrication processes.

Another group of electrochemical actuators are those that operate in an ion-conductive electrolyte. These actuators are commonly composed of an electroactive film layer deposited on an electrode to construct a bilayer actuator device. The volume change of the electroactive layer in a bilayer configuration can be used to generate out-of-plane movement and produce bending deformation [249]. Among materials that have been utilized as the electroactive layer in these actuators, conducting polymers (CPs) such as polyaniline [250], polypyrrole [251], and polythiophene [80] have unique properties for actuators as they can provide large strains, operate under low voltages, and hold strain under voltage or open circuit. Polypyrrole (PPy) is considered as one of the most promising CPs for electrochemical actuators owing to its high conductivity and excellent cycling-stability. CP films with controlled thickness can be electrochemically synthesized and miniaturized, making them versatile for various applications such as medical devices [59, 252, 253]. The volume changes in CP actuators is generated by transportation of ions and solvent molecules [254, 255]. Because of their good biocompatibility, CPs have been extensively used in biomedical devices and actuators operating in biofluids [3, 242, 256-260]. However, achievement of large deformation strains with fast response times remains a challenge for CP film-based bilayer actuators wherein drag forces and rigidity of film structures restrict the actuator motion and limit the ion transportation.

Herein, we present a novel and high-performance bilayer electrochemical actuator based on polypyrrole nanofibers (PPy NFs) formed on a gold-coated polypropylene (Au-PP) film. We assess the performance of this actuator within two distinct electrolytes, liquid and hydrogel, under the cyclic voltammetry stimulation (potential sweep was carried out

within a range of -0.8 to $+0.4$ V at various scan rates of 10, 50, 100, and 200 mV/s). We demonstrate the ability of this actuator to efficiently operate in both liquid and gel electrolytes with low power consumption/strain (~ 0.5 mW/(cm² %)), large deformation (displacement ~ 7.88 mm; strain $\sim 3.35\%$), fast response (speed ~ 1280 μ m/s; times < 1 s), and excellent actuation stability ($> 96.5\%$ after 25 hrs of continuous operation). These high-performance characteristics are ascribed to the PPy NFs associated with large ion exchange (mass flux ~ 167 g/cm³), soft mechanical properties of PPy NFs (average elastic modulus ~ 6.79 MPa), high charge storage density (charge density ~ 448 mC/cm²), and large specific capacitance (~ 170 F/g) of PPy NFs.

Methods

Materials

Poly (L-lactide) (PLLA, Resomer 210) with the inherent viscosity of 3.3-4.3 dL/g was purchased from Evonik Industries. Benzyl triethylammonium chloride and pyrrole ($M_w = 67.09$ g/mol) were purchased from Fisher Scientific. Poly (sodium-p-styrene sulfonate) (NaPSS, $M_w = 70$ kD) and chloroform were purchased from Acros-Organics. Agarose powder (Agarose ITM, Gel strength ≥ 1200 g/cm) was purchased from VWR Life Science. 6 MHz Au/TiO₂ quartz crystal wrap-around electrodes were purchased from Metrohm, USA. Biaxially-oriented poly(propylene) (PP) films were obtained from backing layer of Scotch removable double-sided tape (3MTM).

Fabrication of Nanoscale Fiber Templates

A homogeneous solution of PLLA (3 wt.%) in chloroform was prepared by adding 230 mg PLLA in 5 ml chloroform and stirring the mixture overnight at room temperature. To enhance the solution charge strength, 23 mg Benzyl triethylammonium chloride (an organic salt) was added to the solution prior to stirring. PLLA NFs were directly electrospun onto Au-coated substrates using a syringe pump with the spinneret gauge of 23. The electrospinning process was carried out in an electric field of 0.91 kV/cm with a flow rate of 50 $\mu\text{L/hr}$, and a syringe-substrate distance of 11 cm for 6 min. Temperature and humidity were kept constant at 26°C and 30%, respectively. For the bilayer beam actuator, the passive layer was a PP film (30 μm thick, 1 mm wide, and 20 mm long) coated with a thin gold layer ($\sim 0.3 \mu\text{m}$, Figure VI.8 in Supporting Information) using a desktop sputtering system (Denton Desk II) at 40 mA for 8 min. For electrochemical quartz crystal microbalance (EQCM) measurements, PLLA NFs were electrospun on Au-coated quartz crystals (diameter $\sim 6.7 \text{ mm}$) for 1 min using the same process parameters.

Electrochemical Deposition of Conducting Polymer

0.2 M pyrrole:PSS electrolyte solution was prepared by dissolving 277 μL pyrrole monomer and 824 mg NaPSS in 20 ml deionized water. Prior to electrodeposition, samples were kept in the electrolyte solution for 30 min to ensure that the solution has completely diffused into the fiber interspaces. Then, the electrodeposition was carried out at the current density of 0.5 mA/cm for 2 hrs. To fabricate conducting polymer NFs, PPy was electropolymerized around template PLLA NFs. The Electrochemical deposition of PPy was performed using an Autolab PGSTAT 128N (Metrohm, USA) in galvanostatic mode

with a two-electrode configuration at room temperature. For EQCM samples, electrodeposition was performed for 15 min using an Autolab EQCM kit in which a gold wire served as the counter electrode. For bilayer beam actuator, samples were connected to the working electrode and a platinum (Pt) foil served as the counter electrode.

Beam Actuation using Cyclic Voltammetry (CV)

Actuation of the bilayer beam actuator was performed using Autolab PGSTAT 128 in a three-electrode configuration with a saturated Ag/AgCl reference electrode and a 1×2 cm Pt foil as counter electrode (Figure VI.6, Supporting Information). The CV was performed within the potential range of -0.8 to $+0.4$ V at various scan rates of 10, 50, 100, and 200 mV/s. The actuation behavior of the constructed bilayer beam was assessed in aqueous and agarose hydrogel (0.2 wt.%) electrolytes containing 0.1 M NaPSS. To prepare the aqueous electrolyte, 824 mg NaPSS was dissolved in 40 ml deionized water at room temperature. For gel preparation, 80 mg agarose powder was added into 40 ml NaPSS solution (0.1 M), and the slurry was heated in a microwave oven for a minute to dissolve agarose in the NaPSS solution. The agarose solution was then cooled down in refrigerator at 4°C for 15 min. Prior to actuation, all samples were primed in the NaPSS solution at the scan rate of 100 mV/s for ten cycles.

Electrochemical Quartz Crystal Microbalance (EQCM) Measurements

The EQCM measurement was carried out using Autolab PGSTAT 128N equipped with EQCM kit in a three-electrode configuration with a saturated Ag/AgCl reference electrode and a gold counter electrode. The mass measurements of PPy NFs under CV was

characterized in the liquid and gel electrolytes containing 0.1 M NaPSS. The PPy NFs were cycled in the potential range of -0.8 to $+0.4$ V (versus the Ag/AgCl reference electrode) for 20 cycles, at different scan rates of 10, 50, 100, and 200 mV/s at room temperature. Prior to the measurements, a stable ion concentration within the PPy structure was ensured by subjecting the samples to five CV cycles at the scan rate of 10 mV/s. The mass change was calculated using Sauerbrey's equation which correlates the frequency variation (Δf) in quartz crystal oscillation to the change in mass (Δm),

$$\Delta F = -C_f \Delta m. \quad \text{VI.1}$$

Here, C_f is a sensitivity factor that depends on the resonant frequency and operating temperature of the quartz crystal. The value of C_f was 0.0815 Hz/(ng.cm) for this 6 MHz quartz crystal at 20°C. Compared to the actuator, a thinner layer of PPy NFs (1.44 μm) was used for EQCM measurements to avoid viscoelastic effects [227]. The mass change of the actuator was estimated by multiplying the EQCM values by the volume ratio of PPy layer on the actuator and the EQCM sample (Volume ratio $\cong 5$).

Actuator Tip Kinematic Measurements

The bending deflection of the actuator was recorded using a digital camera (Dino-Lite) with 30 frames per second. The recorded videos were then processed using an open-source software (Tracker 5.0.6, <https://physlets.org/tracker>) to track the actuator tip deflection upon actuation. The response time (t_R) at the maximum tip deflections was calculated by subtraction of the time that actuator positioned at the maximum deflection from the time that stimulus cathodic current reached zero.

Mechanical characterization of the actuator

Elastic modulus of the actuator components (i.e., PP film, Au layer, PLLA NFs, and PPy in both reduced and oxidized states) were obtained by atomic force microscopy (AFM) in fluid in either contact mode and/or peak force mode as appropriate and indicated below. Force-indentation curves were obtained on a Bruker BioScope Resolve (Bruker nanoSurfaces, CA) AFM employing a ScanAssyst-Fluid+ cantilever (Bruker NanoSurfaces, CA) with a pyramidal tip (qualified tip radius ~ 3.26 nm), nominal spring constant of 0.7 N/m assuming sample Poisson's ratio as 0.5. Prior to experimental samples, cantilever was calibrated on a silicon wafer in fluid. To determine the elastic modulus of individual PLLA NFs, samples were imaged in PeakForce quantitative nanoscale mechanical characterization (QNM) mode (Bruker NanoSaurfaces, CA) at peak-force frequency of 0.25 kHz, amplitude of 150 nm, scan rate of 0.3 Hz, and at 512 \times 512 lines with 512 samples/line, with capture enabled for individual force vs displacement curves. Force curves along individual fibers ($n = 10$ fibers, four locations per fiber) were extracted and analyzed using the Sneddon model [261]. For all other samples, force curves were obtained in contact mode ($n = 7$ to 10 locations, four force curves per location) and analyzed using the Sneddon model. Elastic moduli were estimated using a custom MATLAB code.

Rheological Characterization of Liquid and gel electrolytes

The viscosity of 0.1 M NaPSS solution and 0.2 wt.% agarose gel containing 0.1 M NaPSS was characterized using an AR2000ex rheometer (TA instruments) at room

temperature. Viscosity measurement was carried out within the shear rate of $10^{-3} - 10^{-1}$ using a 40 mm parallel plate with a gap of 0.5 mm.

Structural Characterization of the Actuator

The surface morphology of PLLA and PPy NFs were characterized using Field Emission Scanning Electron Microscopy (FESEM, FEI 235). Samples were mounted on aluminum stubs by carbon tape and a carbon paint was used for grounding. Prior to microscopy, non-conductive PLLA sample was sputter-coated with a thin gold layer using Denton Sputter Coater for 45 s at 40 mA. Thickness of actuator layers including gold and PPy NFs were measured using materials confocal microscopy (LSM800 Zeiss, Germany). For higher precision, the gold and PPy nanofiber layers were constructed on a polished Si wafer using the same processing parameters. Thickness profiles and 3D surface topography of PPy NFs layer (Figure VI.8, Supporting Information) were generated through a z-stack experiment followed by step height analysis using Confomap software (Zeiss, Germany).

Statistical Analysis

The statistical significance of difference of data was performed by one-way ANOVA and post hoc test (Tukey's test) to analyze significances between sample groups (Origin Pro, Northampton, MA). In this paper, all data are presented as mean \pm standard error, unless otherwise noted.

Results and discussion

To fabricate the PPy NFs actuator, we electrodeposited an electroactive layer of PPy doped with polystyrene sulfonate (PSS) around template poly-L-lactide (PLLA) NFs that

were previously electrospun onto a thin layer of gold (Au) coated on a structural layer of PP (Figure VI.1(A-C)). The average diameter of PLLA NFs and the resultant PPy NFs (Figure VI.1(D-E)) were 140 ± 4 nm and 626 ± 16 nm, respectively (size distribution histograms are given in Figure VI.5, Supporting Information). As previously reported, PLLA is a biodegradable material with extremely slow degradation rate that can be processed into electrospun fibers, which remain stable during electrochemical deposition [108]. Cross-sectional scanning electron micrographs of the PPy NFs confirmed the presence of intact PLLA NFs (Figure VI.1(F-G), red arrows in image G point to the PLLA NFs). The PPy NFs were subjected to cyclic voltammetry (CV) in aqueous solution and 0.2 wt.% agarose hydrogel both containing 0.1 M poly(sodium 4-styrenesulfonate) (NaPSS) (Figure VI.6, Supporting Information). Low concentration gel polymer electrolytes with high ionic conductivity have been previously utilized for energy storage [262, 263], air working electrochemical actuators [264], and biomedical applications [265-267]. Agarose hydrogel is optically transparent and allows for transportation of cations and/or solvated cations between the electrolyte and the actuator during CV cycling. The CV potential sweep was carried out within a range of -0.8 to $+0.4$ V at various scan rates of 10, 50, 100, and 200 mV/s.

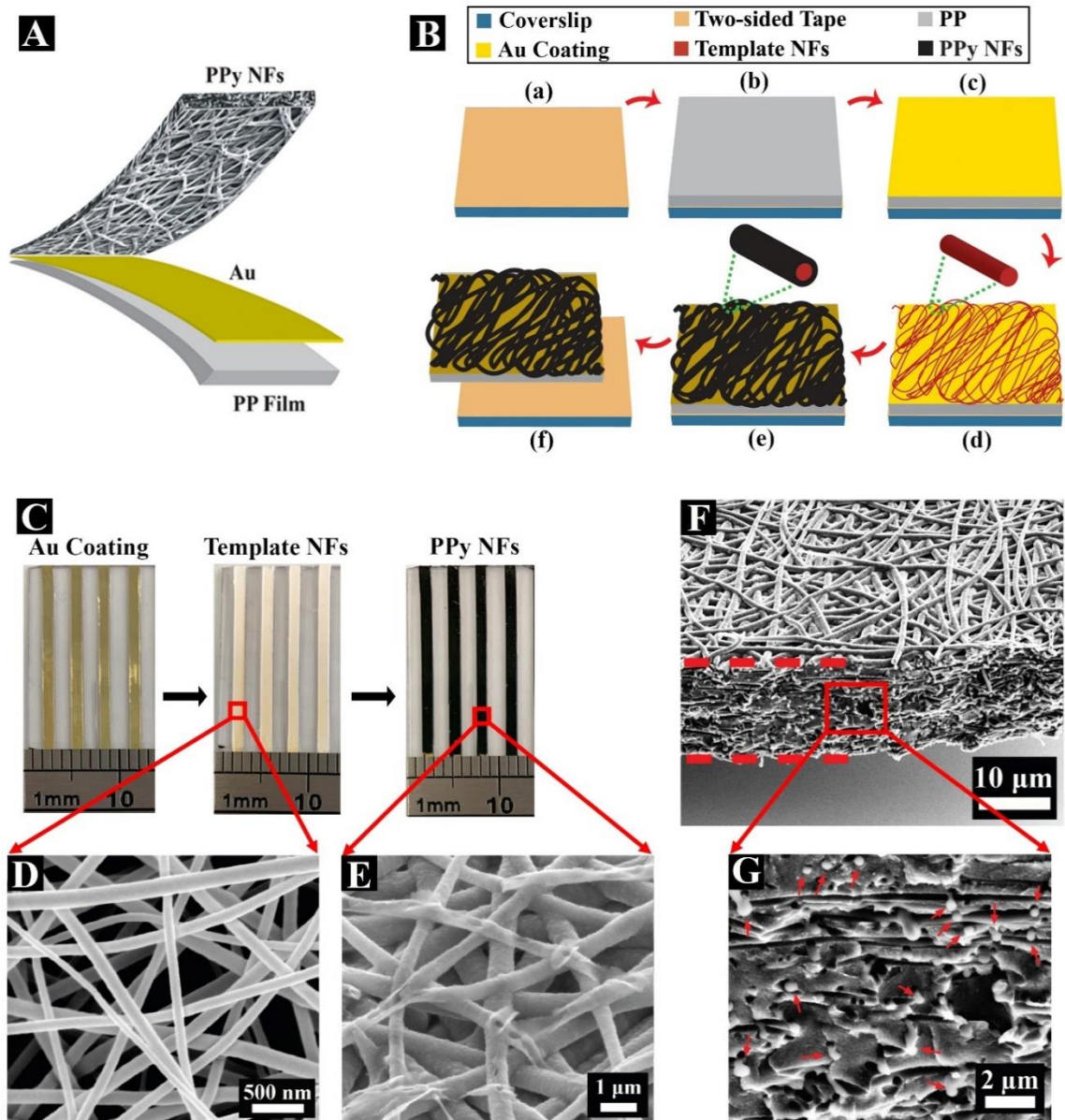
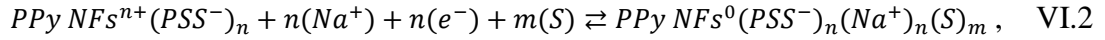


Figure VI.1. A-B) Design of PPy NFs actuator and step-by-step fabrication process. C) Photographs of the actuator beams during fabrication process. D-G) SEMs of template PLLA NFs (D), PPy NFs (E), and cross-section of PPy NFs (F, G).

We investigated the bending displacement of the actuator under CV cycling in both liquid and gel electrolytes (Figure VI.2(A-C)). The actuator showed fully reversible bending deformation under consecutive reduction-oxidation (redox) reactions in each

cycle. The primary mechanism for bending deformation is the volume change of PPy NFs due to the insertion and ejection of ions and solvent molecules into/out of the polymer matrix (Figure VI.2(A)). When ions and solvent enter the PPy NFs, the polymer expands, and when they exit the PPy NFs, the polymer contracts according to the following reaction.



where n represents the number of electrons (e^-), m represents the number of solvent molecules (S), $PPy NFs^{n+}$ is the oxidized state of the polymer and $PPy NFs^0$ represents the neutral state of the polymer. $PPy NFs^{n+}(PSS^-)_n$ indicates that anion PSS is entrapped into PPy NFs as a dopant during electro-polymerization, and $PPy NFs^0(PSS^-)_n(Na^+)_n(S)_m$ indicates that Na^+ cations and solvent molecules are inserted as the polymer is reduced [268]. According to Equation VI.2, when the PPy NFs are reduced, cations (here Na^+) and solvent molecules (here water) migrate from the electrolyte to the polymer to compensate the net charge and, resulting in swelling of the NFs. In contrast, when the PPy NFs are oxidized, Na^+ cations and water molecules migrate from the polymer to the electrolyte, leading to shrinkage of the NFs [255]. The in-plane actuation strain generated upon reduction and oxidation of the PPy NFs is converted into a bending deformation due to the strain mismatch between the active PPy NFs and the passive underneath layers at the interface. Figure VI.2(D-I) depict the induced current, mass flux (influx/efflux), and tip displacement of the PPy NFs actuator measured under a CV cycle at various scan rates of 10, 50, 100, and 200 mV/s in both liquid electrolyte (Figure VI.2(D,F,H)) and gel electrolyte (Figure VI.2(E,G,I)). During the initial forward scan (i.e., potential swept from 0 to -0.8 V), reduction of the PPy NFs resulted in a steep

increase in mass influx of cations into the PPy NFs and in actuator displacement (counter-clockwise) as the potential swept to the cathodic peak potential, followed by a gradual increment in both mass flux and displacement curves. Interestingly, during the reverse scan (i.e., potential swept from -0.8 to $+0.4$ V), the mass flux and displacement further increased to their maximum values where the cathodic current reached zero at potentials -0.64 , -0.61 , -0.54 , and -0.46 V in liquid electrolyte and -0.64 , -0.59 , -0.54 , and -0.43 V in gel electrolyte at the scan rates of 10, 50, 100, and 200 mV/s, respectively. As the anodic current increased (i.e., PPy NFs were oxidized), both mass flux and displacement values gradually decreased due to the efflux of Na^+ cations with clockwise deflection of the actuator. Subsequently, steep decreases were observed in the mass flux and displacement curves as the potential swept to the anodic peak potential. These decreases continued till all cations were expelled from PPy NFs and actuator returned to its original position as depicted in inset Figure VI.2(F-I). Furthermore, by increasing the potential, the mass flux slightly increased and the actuator deflected counter-clockwise (i.e., displacement increased) likely due to solvent transport into the PPy NFs as an attempt to balance the osmotic pressure in the system [269, 270]. As the scan rate decreased, the time-dependent diffusion of water molecules led to a more significant increase in the mass flux and the resulting displacement (insets in Figure VI.2(F-I)). Finally, during the second step of forward scan (i.e., potential swept from $+0.4$ to 0 V), as PPy NFs were still oxidized, the actuator mass flux and displacement remained unchanged or slightly decreased. These results demonstrate that the actuator displacement can be controlled precisely by adjusting

the applied voltage and scan rate. Such precision control of actuator displacement is of critical advantage in soft robotics and artificial muscles.

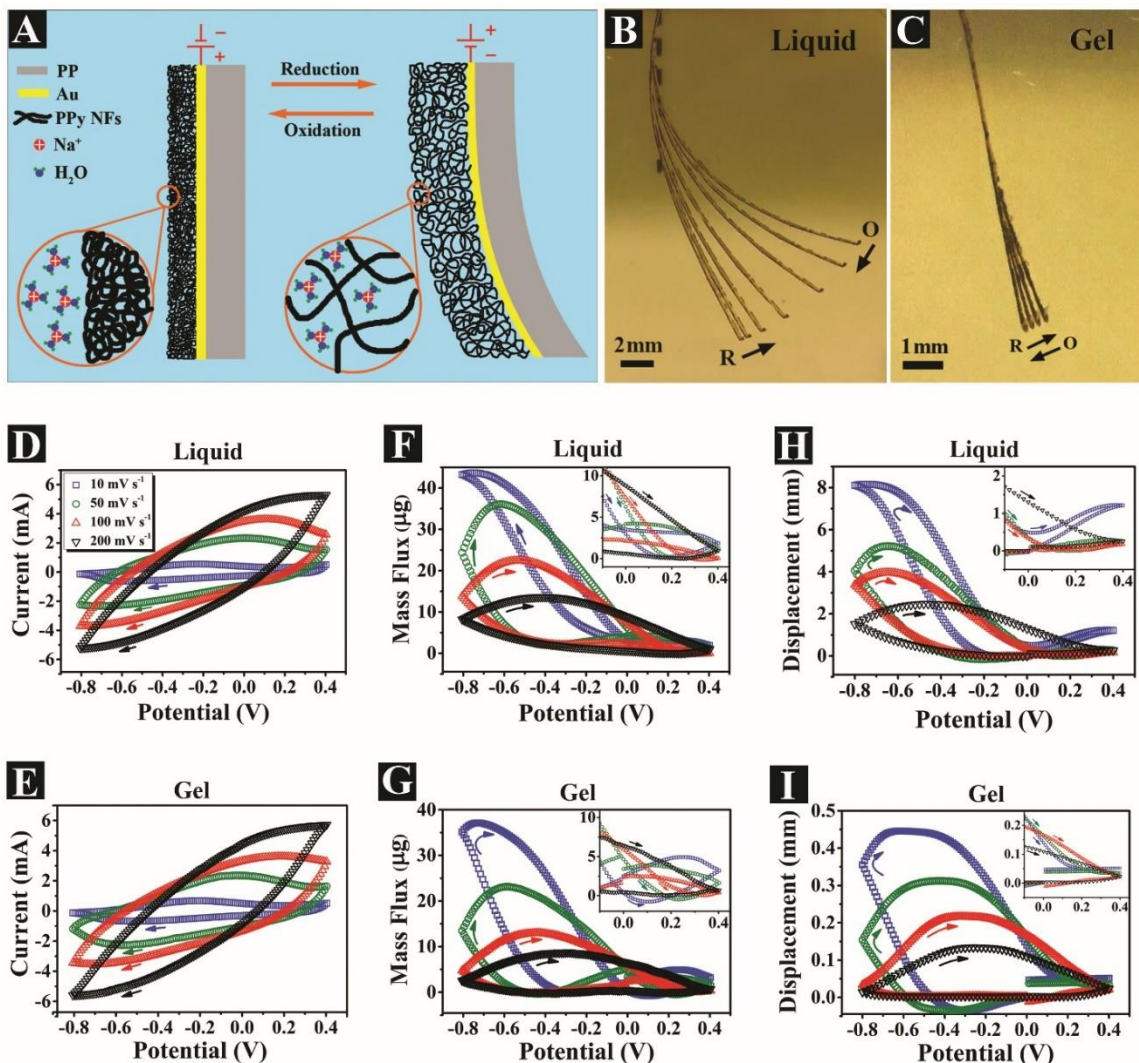


Figure VI.2. A-C) Schematic and composite photographs represent ions transportation and bending motion of the actuator under redox processes. D-I) Cyclic voltammograms, mass flux, and displacement at various CV scan rates.

Next, we characterized the electro-chemo-mechanical response of the PPy NFs actuator at various CV scan rates 10, 50, 100, and 200 mV/s in liquid and gel electrolytes (Figure

VI.3). Remarkably, the actuator exhibited the largest mass flux ($\sim 167 \text{ g/cm}^3$), charge storage density ($\sim 448 \text{ mC/cm}^2$; Equation VI.5 in Supporting Information), specific capacitance ($\sim 170 \text{ F/g}$; Equation VI.6 in Supporting Information), maximum displacement ($\sim 7.88 \text{ mm}$), and maximum strain ($\sim 3.35\%$; Equation VI.15 in Supporting Information) at a scan rate of 10 mV/s in liquid electrolyte. In fact, the high surface area to volume ratio along with high electrical conductivity and electrochemical activity of PPy NFs provide smooth pathways for adequate ion transport and accumulation. To the best of our knowledge, the energy storage performance (i.e., charge storage density and specific capacitance) of our actuator exceeds those of reported CP based electrochemical actuators and devices [271-274]. An increase in scan rate requires faster ion transport in the solvent and quicker intercalation and deintercalation of ions into/out of PPy NFs respectively. However, due to restricted mobility of ions in an electrolyte under the influence of an electric field [275], at higher scan rates fewer ions migrate into/out of polymer. Thus, the mass flux significantly declined ($p < 0.01$) from 166.81 ± 8.12 to $47.08 \pm 4.15 \text{ g/cm}^3$ in the liquid electrolyte and from 142.38 ± 20.54 to $34.38 \pm 9.27 \text{ g/cm}^3$ in the gel electrolyte when scan rate was increased from 10 to 200 mV/s (Figure VI.3(C)). It is noteworthy that the charge storage density (Figure VI.3(D)) and specific capacitance (Figure VI.9, Supporting Information) significantly decreased from 447.9 ± 17 to $193.15 \pm 9.05 \text{ mC/cm}^2$ and from 169.7 ± 6.7 to $73.2 \pm 3.4 \text{ F/g}$, respectively in the liquid electrolyte and from 410.15 ± 33.95 to $195.45 \pm 6.25 \text{ mC/cm}^2$ and from 155.4 ± 12.9 to $74.0 \pm 2.4 \text{ F/g}$, respectively in the gel electrolyte ($p < 0.01$). In addition, there was no statistically significant difference between the charge storage density and specific capacitance of the actuator in liquid and gel

electrolytes at same scan rates, suggesting that PPy NF actuators maintain the same electroactivity in both gel and liquid electrolytes. Remarkably, the actuator generates a large maximum strain of 3.35% and a maximum displacement of 7.88 mm in liquid electrolyte at scan rate 10 mV/s (Figure VI.3(E-F)). More importantly, at scan rate 200 mV/s the actuator can generate a strain (1.24%) that is greater compared with those reported previously [247, 271, 272, 276]. Notably, maximum displacement (Figure VI.3(E)) and actuation strain (Figure VI.3(F)) decreased with increasing scan rate, presumably due to insufficient time for ion transport into/out of polymer at higher scan rates, as discussed earlier. The smaller displacement observed in the gel electrolyte compared to liquid can be attributed to the greater resistive forces exerted on the actuator by the surrounding viscoelastic gel, compared to aqueous solution.

To investigate the dynamics of the actuator, we assessed its speed, response time, and generated actuation force. The instantaneous velocity of the actuator tip was calculated from the rate of changes of the tip displacement (Figure VI.15, Supporting Information). As shown in Figure VI.3(G), the maximum speed of actuator increased with increasing the scan rate. In liquid electrolyte, the actuator exhibited a high maximum speed of 190 ± 10 $\mu\text{m/s}$ at scan rate 10 mV/s and impressively a higher maximum speed of 1280 ± 210 $\mu\text{m/s}$ at scan rate 200 mV/s. Notably, the actuator demonstrated faster response ($<1\text{s}$) at higher scan rates of 100 and 200 mV/s (Figure VI.3(H)), that are substantially improved compared with those observed in other CP based electrochemical actuators (e.g., PPy film with response time of 5s and maximum speed of ~ 1000 $\mu\text{m/s}$) [277]. In addition to offering a high maximum speed and a fast response time, this actuator was able to produce a large

maximum force. The generated actuation force (F_{act}) was calculated by the moment equation of motion for a rigid body with variable mass that is submerged in a liquid. In fact, this equation relates the moment of forces acting on the actuator to angular momentum (Figure VI.14, Equations VI.16–VI.19, Supporting Information), expressed as

$$F_{act} = \frac{1}{6} [(m_0 + \Delta m) a + \dot{m} v] \left[4 + \frac{h^2}{l^2} \right] + \frac{1}{2} C_d l b \rho v(t)^2 + [(m_0 + \Delta m)g - \rho h l b g] \sin \left[\frac{\delta}{l} \right], \quad \text{VI.3}$$

where m_0 is initial mass of actuator ($\sim 1360 \mu\text{g}$), Δm is mass change, $\dot{m} = \frac{dm}{dt}$ is rate of mass change (Figure VI.15), δ is deflection, v is velocity (Figure VI.15), a is acceleration (Figure VI.15), h is actuator thickness ($\sim 43.3 \mu\text{m}$), b is actuator width (1 mm), l is actuator length (20 mm), C_d is drag coefficient (Equation VI.24, Supporting Information), ρ is electrolyte density ($\sim 1 \text{ g/cm}^3$), and g is gravitational acceleration constant (9.81 m/s^2). Prior modeling studies on bilayer [254, 278, 279] CP actuators operating in an electrolyte solution were based on the classical beam theory [280] for metal bimorphs that bend upon heating due to difference in thermal expansion coefficients (Timoshenko's model) [281], whereas the normal force and bending moment at any cross section of the beam are zero. However, these models did not dynamically evaluate the actuator movement and did not consider the effect of fluid forces exerted on the actuator to determine the generated actuation force (blocking force). In contrast, our dynamic model, the moment equation of motion for a rigid body with variable mass that is submerged in a liquid, is more realistic and accurate as it considers the motion of the actuator under action of forces in a fluid. The actuator generated a force of $0.65 \pm 0.10 \mu\text{N}$ in liquid electrolyte at the scan rate 200 mV/s . Impressively, the actuation force increased to $2.00 \pm 0.12 \mu\text{N}$ as the scan rate decreased to

10 mV/s. Similarly, the generated actuation force had a substantial increase in gel electrolyte with decreasing the scan rate (Figure VI.3(I)).

The correlation between the generated actuation force and the resultant deflection at various scan rates in liquid and gel electrolytes are plotted in Figure VI.3(J-K). As shown, the actuator exhibited a reversible linear relation between actuation force (F_{act}) and deflection (δ) (Equations VI.25 and VI.26, Supporting Information). Interestingly, there was no significant difference between the slope of the plots in liquid and gel electrolytes at all scan rates ($p > 0.05$) (for detailed calculations see Table VI.2 in Supporting Information). Furthermore, the deflection of PPy NFs actuator was investigated according to Euler-Bernoulli's composite beam theory. Such a linear relationship for a cantilever beam can be described by a modified form of deflection expressed as

$$\delta = \frac{\gamma l^3}{(EI)_{eff}} F_{act} , \quad \text{VI.4}$$

where γ is a constant, l is actuator length, and $(EI)_{eff}$ is the effective flexural rigidity of the composite beam that can be obtained using transformed sections method (see Supporting Information for details, Figure VI.10, Figure VI.11, Figure VI.12, Equations VI.7–VI.15, and Table VI.1). Using this approach, we obtained a value of $\gamma \approx 7.35$ for the deflection equation, interestingly, in both liquid and gel electrolytes and statistical analysis revealed no significant difference ($p > 0.05$) between γ values obtained from deflection at various CV scan rates in liquid and gel electrolytes (Table VI.2, Supporting Information).

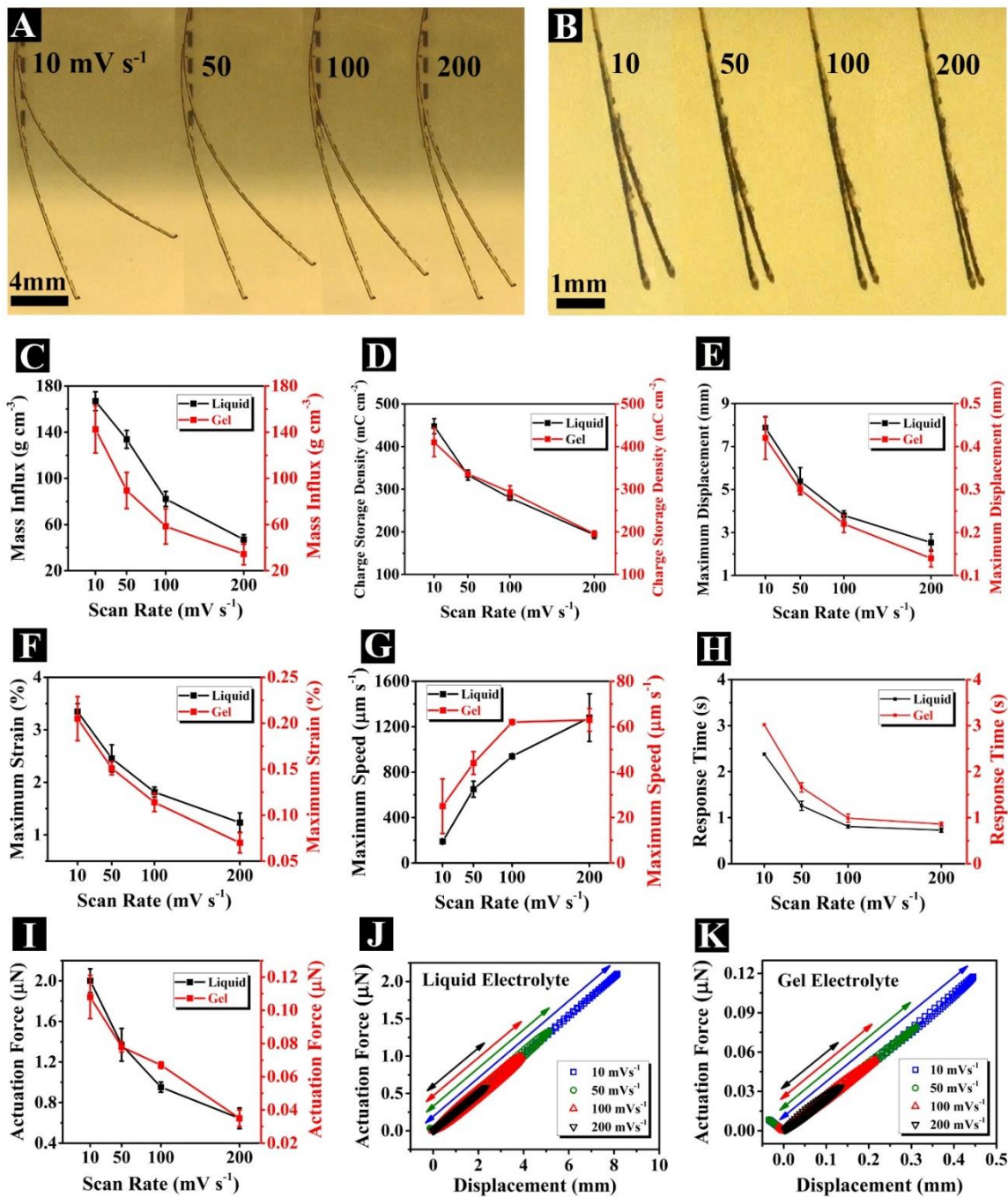


Figure VI.3. A-B) Maximum deflection of actuator at various CV scan rates in liquid (A) and gel (B) electrolytes. C-I) The electro-chemo-mechanical responses of actuator as a function of scan rate. J-K) Actuation force-displacement plots.

Considering that the actuation strain in the electrochemical actuator depends on the electro-mechanical efficiency, the power consumption per generated strain is a particularly relevant metric to evaluate the actuation's performance. Figure VI.4(A) illustrates the power consumption/strain of the PPy NFs actuator at various CV scan rates in liquid and gel electrolytes. As shown, the power consumption/strain of the PPy NFs actuator is within the ranges of 0.5 – 9.1 mW/(cm² %) in liquid electrolyte, and 9 – 159 mW/(cm² %) in gel electrolyte. The low power consumption/strain values for the PPy NFs actuator operating in liquid electrolyte mark a profound improvement compared with previously reported electrochemical actuators operating in liquid [250, 282-284] and air [159, 165, 244, 276, 285-291] (Figure VI.4A). To the best of our knowledge, there is no previous report on operation of electrochemical actuators in gel-polymer electrolytes. Notably, the PPy NFs actuator yielded relatively low power consumption to strain in the gel electrolyte, which is comparable with air operating actuators and much less than those operating in liquid electrolyte. Such low power consumption/strain vastly raises their utility in various applications where power consumption/strain is desired to be minimal with maximal yield and actuation power.

Lastly, we evaluated the long-term stability (i.e., mechanical durability) of the PPy NFs actuator over a great number of actuations (Figure VI.4(B)). Remarkably, the PPy NFs actuator showed a bending stability >96.5% in liquid electrolyte over 15,000 actuations (25 hours of continuous operation) at scan rate 200 mV/s (cycling frequency 0.08 Hz). Here, the bending stability was defined as δ/δ_0 , where δ_0 corresponds to the actuator deflection in the first cycle and δ corresponds to the deflection in the nth cycle. The inset graph in Figure

VI.4(B) represents the sample variation in the maximum tip deflection (δ_{\max}) within the first 1000 actuations in liquid and gel electrolytes (\pm SEM, $n = 3$). There was no significant difference in the δ_{\max} over the course of actuation in both liquid and gel electrolytes ($p > 0.05$). While electron micrographs (Figure VI.4(C-D)) and optical micrographs (Figure VI.4(E-F)) did not indicate any obvious mechanical damage or delamination of PPy NFs over the course of actuation (1000 actuations), the slight degradation in actuator displacement ($\sim 3.5\%$) may be attributed to the nanoscale deformation and stress relaxation in PPy NFs. These results suggest that the PPy NFs actuator can effectively operate in liquid and gel electrolytes and can mechanically endure a great number of actuations. In fact, this PPy NFs actuator exhibited superior long-term stability compared with previously reported PPy based actuators operating in liquid electrolytes [292-294] (e.g., PPy film [293] with substantial bending degradation after 11 hr).

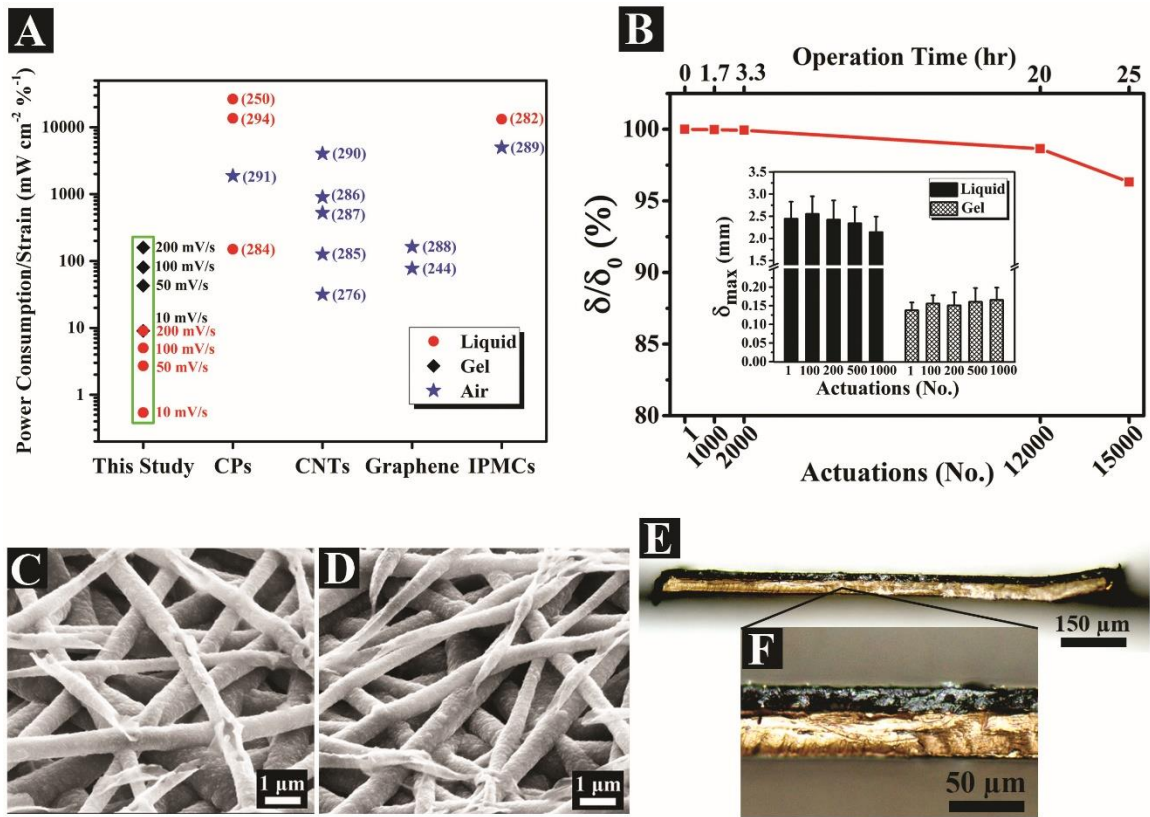


Figure VI.4. A) Power consumption/strain of the PPy NFs actuator compared to other actuators. B) Bending stability of the actuator. C-D) SEM of PPy NFs before (C) and after actuation (D). E-F) Cross-section of the actuator after actuation.

Conclusions

In summary, this study presents a novel and versatile method for the development and validation of flexible electrochemical actuators, with conducting polymer nanofibers as the main constituent, capable of operating in both liquid and gel electrolytes. This actuator may provide soft robots and artificial muscles with controlled dynamics and high actuation performance, including low power consumption/strain, a large deformation, fast response, and excellent actuation stability. Various types of chemically derived and functionalized conducting polymers can be formulated to further enhance electro-chemical-mechanical

properties of this actuator, exceeding the actuation performance. The experimental studies of motion and mass transport along with theoretical analysis of a body system with variable mass are utilized to establish the dynamics of the actuator and to introduce a modified form of Euler-Bernoulli's deflection equation for the PPy NFs actuator. Considering these achievements along with versatile application of conducting polymer nanofibers [101, 108, 258, 259], we anticipate that the conducting polymer nanofibers-based actuators will be utilized for advancement of next generation actuators in the fields of soft robotics, artificial muscles, and biomedical devices.

Supporting Information

Characterization of fiber dimensions

Scanning electron micrographs of the PLLA and PPy nanofibers (PLLA NFs and PPy NFs) were used for fiber size measurements. The diameter of PLLA NFs and PPy NFs were measured using ImageJ software. Histograms of the diameter of fibers were generated after 100 measurements ($n = 100$) (Figure VI.5). The calculated diameter of PLLA and PPy NFs were 140 ± 4 nm and 626 ± 16 nm, respectively.

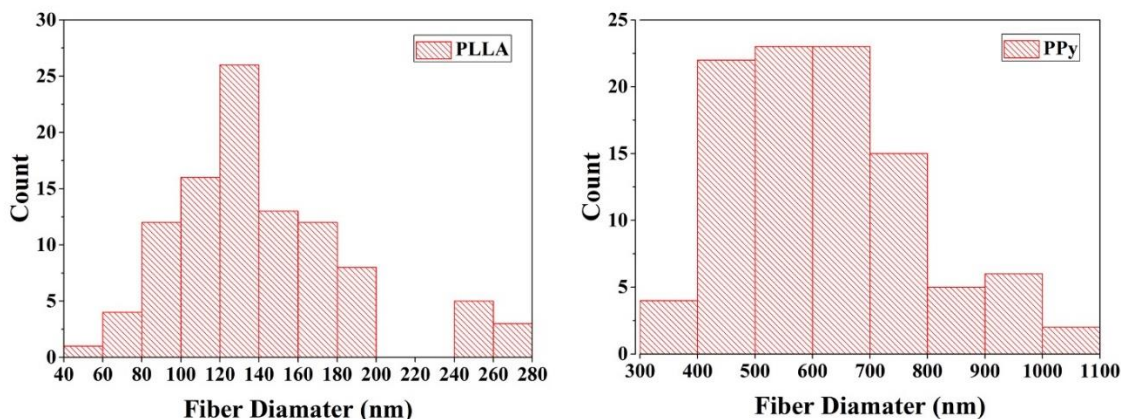


Figure VI.5. Histograms demonstrate the diameter of PLLA and PPy NFs obtained from 100 measurements. The diameter of PLLA and PPy NFs are 140 ± 4 nm and 626 ± 16 nm, respectively ($n = 100$).

Electrode configurations for actuation experiment

As shown in Figure VI.6, the actuation experiment was performed using a three-electrode configuration in a transparent rectangular cell. A platinum foil served as the counter electrode, an Ag/AgCl electrode as reference electrode, and the actuator as working electrode. The actuator deflection was monitored and recorded using a digital camera during cyclic voltammetry (CV). The actuator movement upon reduction and oxidation processes is depicted as a schematic in Figure VI.7.

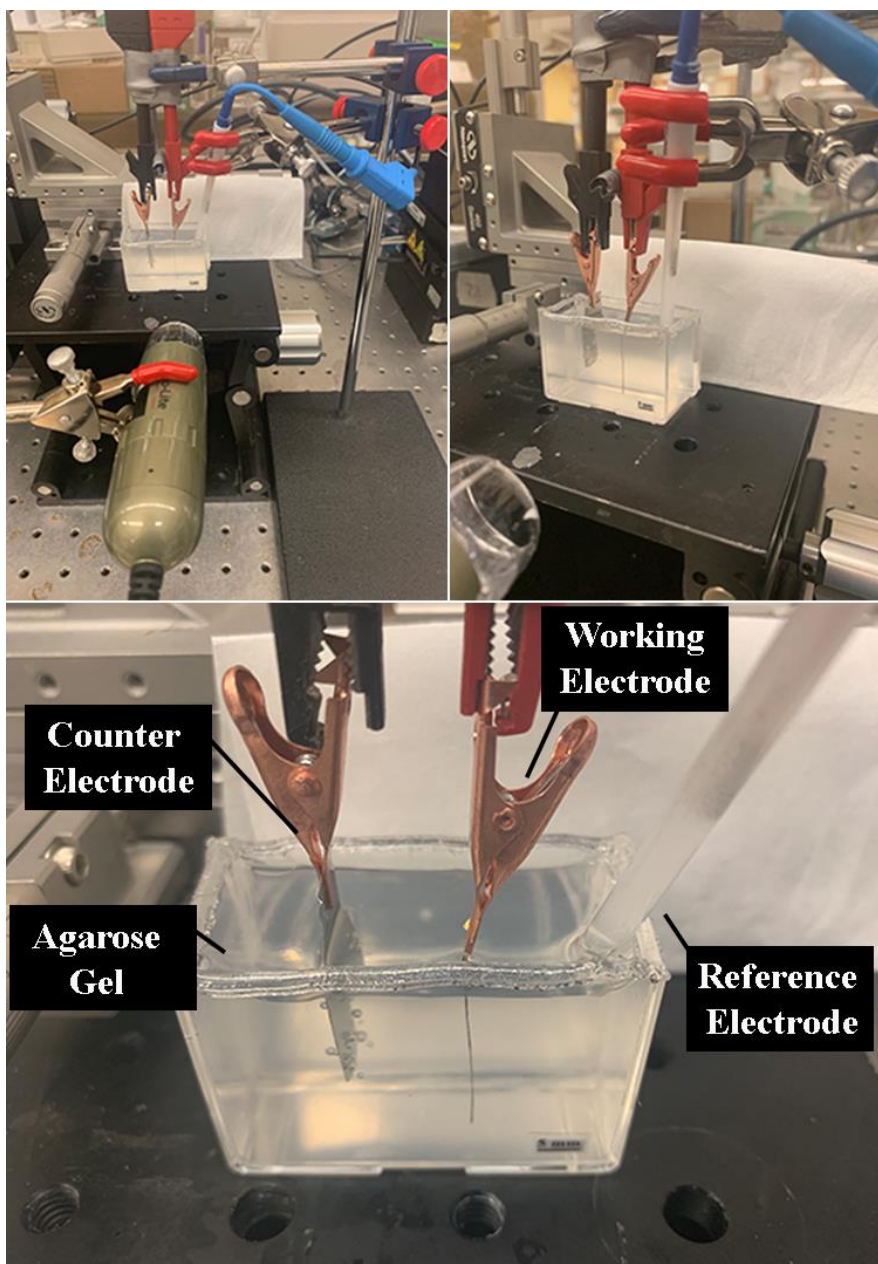


Figure VI.6. Photographs of the actuation setup at different view angles. Images show the three-electrode configuration was used for CV. In these photos, the electrolyte is in hydrogel.

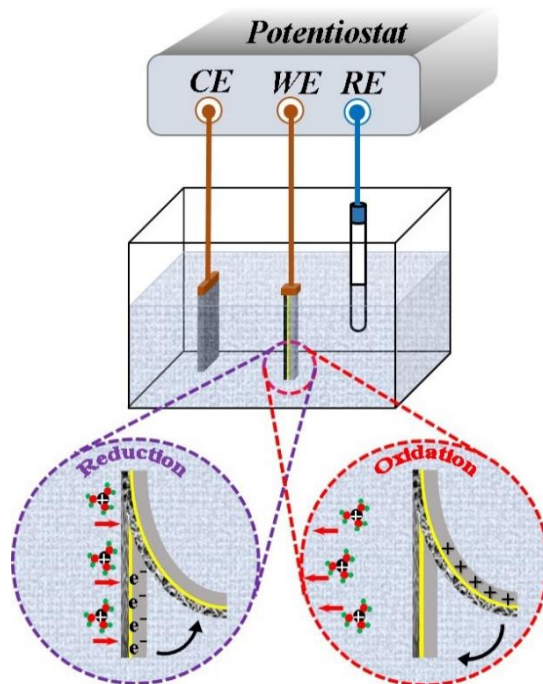


Figure VI.7. Schematic of the actuator deflection upon transportation of solvated cations into/out of the PPy NFs during CV. The actuator deflects counterclockwise upon reduction, and it deflects clockwise upon subsequent oxidation.

Thickness measurement of the actuator layers

The thickness of the sputtered gold (Au) and the constructed PPy NFs layer were measured using Zeiss Materials Confocal Microscope (Figure VI.8). The height profiles were generated using Ziess Confomap software. In Figure VI.8, measurements represent the mean profiles obtained from a series of profiles (graph A: 150 profiles, graphs B and C: 250 profiles). As indicated by orange boxes on the graphs, the step-heights were determined according to standard ISO 5436-1 and given as the mean depth in the corresponding tables. As mentioned in Experimental Section, the Au and PPy NFs layers were constructed on a polished silicon (Si) wafer using the same processing parameters as the beam actuator. In fact, the use of a flat surface of Si wafer rather than the rough

polypropylene (PP) substrate provided more precise thickness profiles, especially for the Au thin film. As shown in Figure VI.8, the mean thickness of the Au and PPy NFs layers constructed on the beam actuator were 309 nm and 12.8 μm , respectively. Also, the mean thickness of 1.44 μm was obtained for the PPy NFs constructed on the QCM crystals for mass measurements.

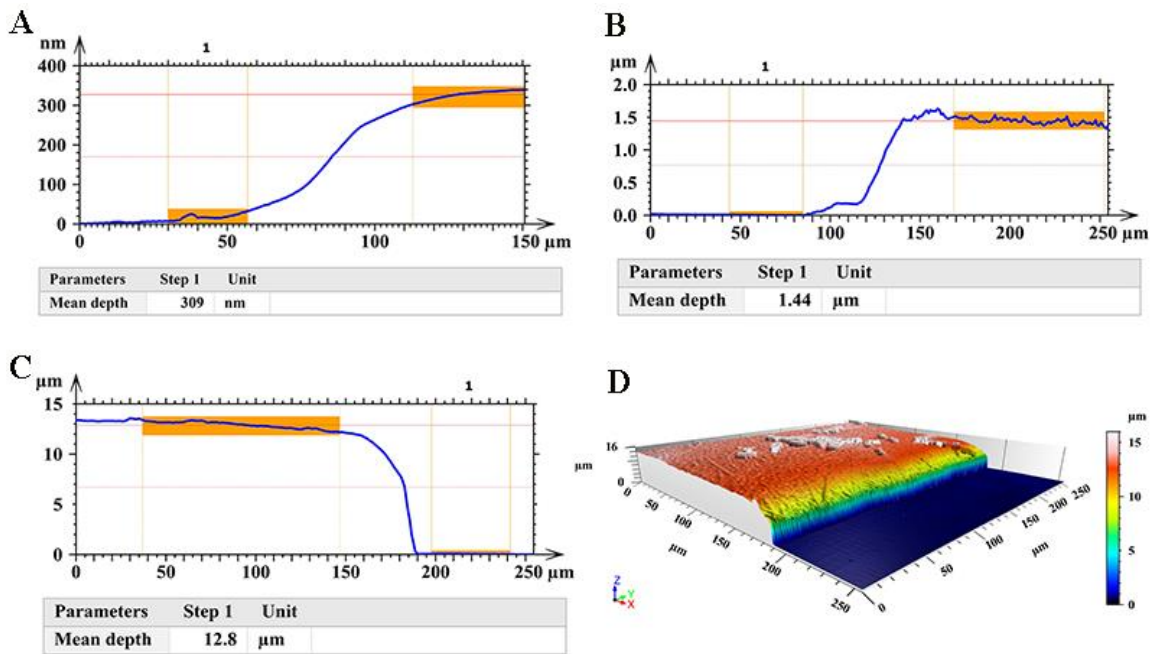


Figure VI.8. A-C) Step-height for the Au layer (A), PPy NFs constructed on EQCM crystal (B), and PPy NFs constructed on the actuator beam (C). D) 3D reconstructed confocal image represents the surface topography of the PPy NFs layer.

Calculation of charge storage density and specific capacitance

The charge storage density (Q) and specific capacitance (C_{SP}) of the PPy NFs were calculated by

$$Q = \frac{1}{vA} \int_{V_1}^{V_2} i dV \quad \text{VI.5}$$

and

$$C_{sp} = \frac{1}{\Delta V v m} \int_{V_1}^{V_2} i dV, \quad \text{VI.6}$$

where v is CV scan rate, A is surface area (20 mm × 1 mm), m is the mass of the PPy NFs layer (~440 μg), and ΔV is the potential window ($\Delta V = 1.2 V$).

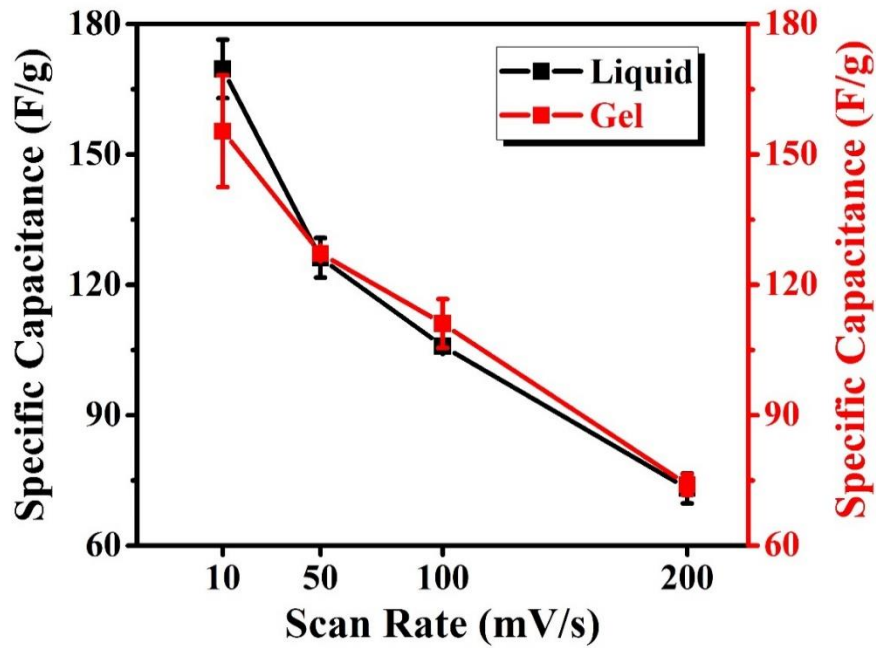


Figure VI.9. Specific capacitance of the PPy NFs actuator as a function of CV scan rate during cycling in liquid (black color) and gel (red color) electrolytes.

Elastic modulus of the actuator components

Elastic modulus of the actuator components, including polypropylene (PP), Au, PLLA NFs, and PPy NFs, were obtained by atomic force microscopy (AFM) in fluid in either contact mode and/or peak force mode (Figure VI.10). For all force-indentation curves

obtained, contact point was determined as described previously [295]. Contact point was also verified randomly using the conventional manual method. Elastic moduli were only considered if curve fitting was greater than 98%, i.e., $r^2 \geq 0.98$. As expected, the Au had the greatest elastic moduli at 20.55 ± 6.14 GPa followed by PP film with 5.95 ± 2.09 GPa. Elastic modulus of individual PLLA NFs was obtained by fitting Sneddon's model over 25-35 nm nanoindentation depth over the maximum height of the fiber to minimize effect of substratum; mean moduli of fibers was 75.68 ± 18.39 MPa. The ratio of moduli between oxidized PPy (11.86 ± 6.85 MPa) and reduced PPy (1.73 ± 0.49 MPa) was approximately 6.85:1. The obtained elastic moduli are summarized in Table VI.1. The order of magnitude of obtained elastic moduli are in the range of those reported in the literature measured by alternative methods [296-298].

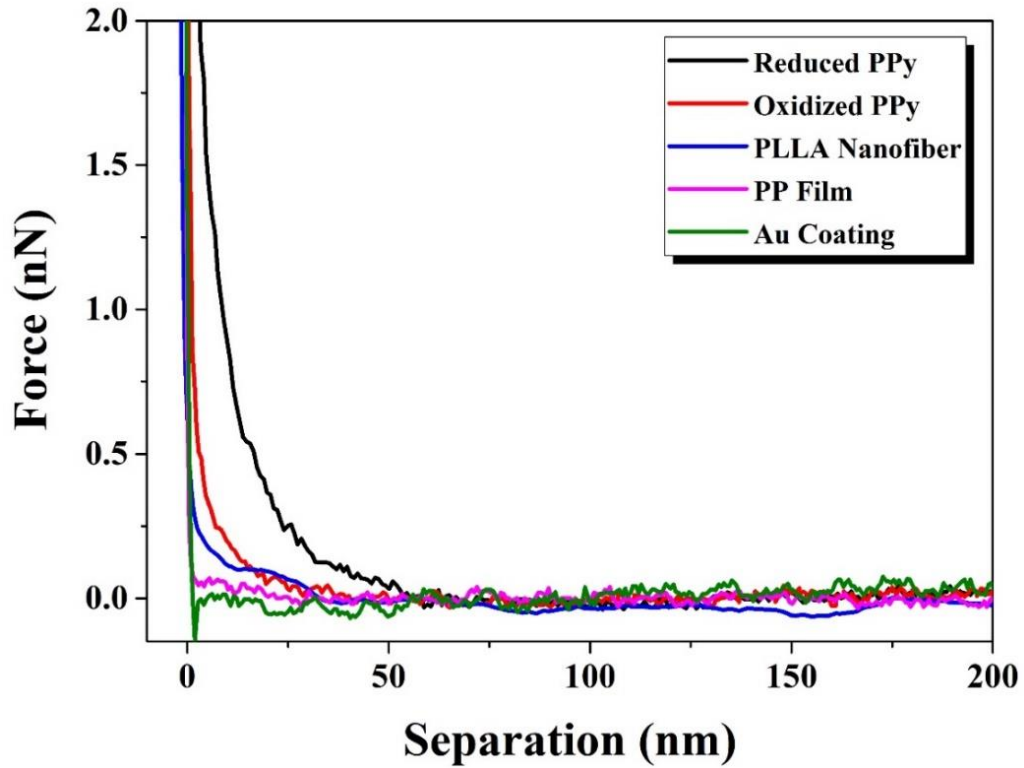


Figure VI.10. Force-separation curves for the actuator components, including PP film, Au, PLLA NFs, and PPy (reduced and oxidized states). The presented data were obtained using AFM in fluid in either contact mode and/or peak force mode.

Table VI.1. Elastic modulus of the actuator components measured by AFM.

Component	Elastic Modulus
Au	20.55 ± 6.14 GPa
Polypropylene (PP) film	5.95 ± 2.09 GPa
PLLA NFs	75.68 ± 18.39 MPa
PPy in reduced state	1.73 ± 0.49 MPa
PPy in oxidized state	11.86 ± 6.85 MPa

The relationship between the elastic modulus of a core-shell fiber and the elastic modulus of fiber components can be explained by the rule of mixtures [299],

$$E_{Fiber} = f E_{Core} + (1 - f)E_{Shell}, f = \frac{\pi r_c^2 l}{\pi r_s^2 l} = \left(\frac{r_c}{r_s}\right)^2. \quad \text{VI.7}$$

Here, E_{Core} and E_{Shell} are the elastic modulus of the core and shell components, respectively. f is the volume fraction of core component which can be calculated knowing the radius of core (r_c) and the radius of shell (r_s) (Figure VI.11). From Figure VI.5, the r_c and r_s for the PPy NFs shell with PLLA NFs core were 70 ± 2 nm and 313 ± 8 nm. Therefore, the elastic modulus of PPy NFs with core PLLA can be calculated using Equation VI.5. The modulus values of 5.43 MPa and 15.05 MPa were obtained for the PPy/PLLA (shell/core) NFs in the reduced and oxidized states, respectively.

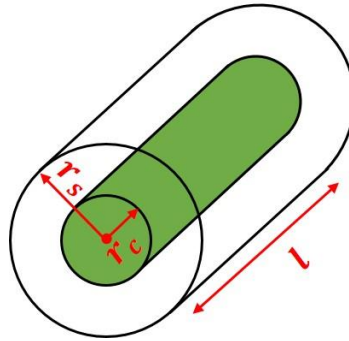


Figure VI.11. Schematic illustrates the dimensions of a core-shell fiber. As indicated, r_c and r_s correspond to the core radius and shell radius, and l represents the fiber length.

Calculation of effective modulus of the composite material

The effective elastic modulus of the multilayer beam was determined by method of transformed sections, which converts a multilayer beam into a transformed beam composed of only one material (Figure VI.12). According to this method, the transformation factor

(n_{ij}) equals to the ratio of the elastic modulus of transferred layer (i) respect to the reference layer (j) expressed as

$$n_{ij} = \frac{E_i}{E_j}. \quad \text{VI.8}$$

Here, Au layer is considered as the reference layer. Therefore, the transformation factors are defined as

$$n_{12} = \frac{E_1}{E_2} = \frac{E_{PP}}{E_{Au}} \quad \text{VI.9}$$

and

$$n_{32} = \frac{E_3}{E_2} = \frac{E_{NFs}}{E_{Au}}, \quad \text{VI.10}$$

where n_{12} is the transformation factor of PP layer, n_{32} is the transformation factor of PPy NFs layer, E_{PP} is the elastic modulus of PP, E_{NFs} is the elastic modulus of PPy NFs, and E_{Au} is the elastic modulus of Au.

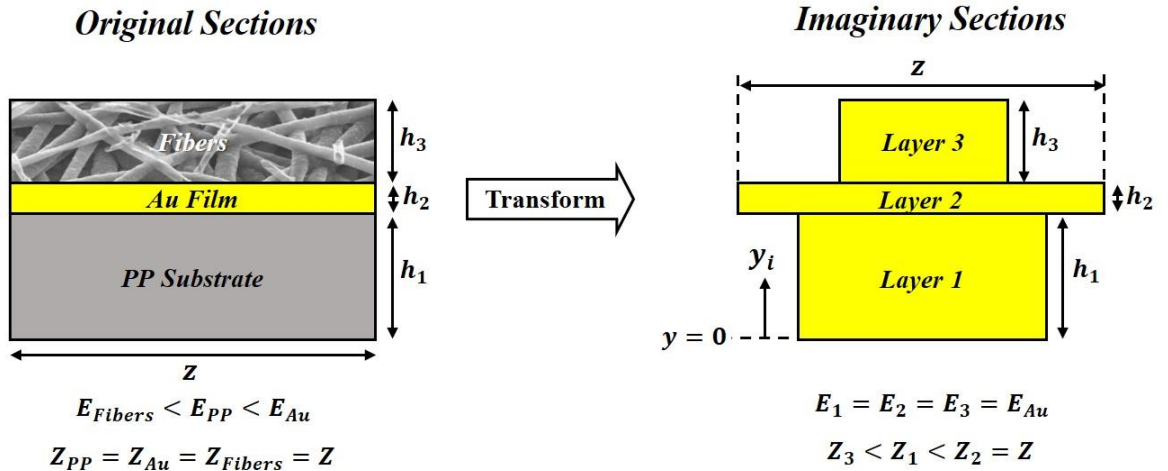


Figure VI.12. Schematics illustrate the cross-section of the beam actuator before and after transformation.

The location of centroid \bar{y}'_{Au} of transformed composite beam to Au can be calculated by

$$\bar{y}'_{Au} = \frac{\sum_{i=1}^3 y_i A_i}{\sum_{i=1}^3 A_i} = \frac{n_{12} h_{PP} \left(\frac{h_{PP}}{2}\right) + h_{Au} \left(h_{PP} + \frac{h_{Au}}{2}\right) + n_{32} h_{NFS} \left(h_{PP} + h_{Au} + \frac{h_{NFS}}{2}\right)}{n_{12} h_{PP} + h_{Au} + n_{32} h_{NFS}} = \frac{h_{PP} \left(\frac{E_{PP}}{E_{Au}}\right) \left(\frac{h_{PP}}{2}\right) + h_{Au} \left(h_{PP} + \frac{h_{Au}}{2}\right) + h_{NFS} \left(\frac{E_{NFS}}{E_{Au}}\right) \left(h_{PP} + h_{Au} + \frac{h_{NFS}}{2}\right)}{h_{PP} \left(\frac{E_{PP}}{E_{Au}}\right) + h_{Au} + h_{NFS} \left(\frac{E_{NFS}}{E_{Au}}\right)}, \quad \text{VI.11}$$

where y_i is the centroid of surface area A_i , h_{PP} is the thickness of PP, h_{NFS} is the thickness of PPy NFs, and h_{Au} is the thickness of Au, E_{PP} is the elastic modulus of PP, E_{NFS} is the elastic modulus of PPy NFs ($E_{NFS(reduction)}$, $E_{NFS(oxidation)}$), and E_{Au} is the elastic modulus of Au. The area moment of inertia of composite beam relative to neutral axis can be calculated using parallel-axis theorem. The area moment of inertia of a composite beam ($I'_{\bar{y}}$) relative to centroid is sum of the area moments of inertia of all layers with respect to a specified reference plane expresses as

$$I'_{\bar{y}} = \sum_{i=1}^3 (I_{y_i} + A_i r_i^2); \quad r_i = y_i - \bar{y}, \quad \text{VI.12}$$

where I_{y_i} is the area moment of inertia of layer i relative to its centroid plane (y_i), A_i is the transformed cross-section area of layer i , and \bar{y} is the centroid of composite beam (neutral axis). Therefore, the area of moment of inertia of transformed beam to Au (I'_{Au}) can be obtained as

$$I'_{Au} = b \left(\frac{1}{12} \left(\frac{E_{PP}}{E_{Au}} \right) h_{PP}^3 + \left(\frac{E_{PP}}{E_{Au}} \right) h_{PP} \left(\frac{h_{PP}}{2} - \bar{y}'_{Au} \right)^2 + \frac{1}{12} h_{Au}^3 + h_{Au} \left(h_{PP} + \frac{h_{Au}}{2} - \bar{y}'_{Au} \right)^2 + \right. \\ \left. \frac{1}{12} \left(\frac{E_{NFs}}{E_{Au}} \right) h_{NFs}^3 + \left(\frac{E_{NFs}}{E_{Au}} \right) h_{NFs} \left(h_{PP} + h_{Au} + \frac{h_{NFs}}{2} - \bar{y}'_{Au} \right)^2 \right), \quad \text{VI.13}$$

where b is the width of actuator, h_{PP} is the thickness of PP, h_{NFs} is the thickness of PPy NFs, h_{Au} is the thickness of Au, E_{PP} is the elastic modulus of PP, E_{NFs} is the elastic modulus of PPy NFs ($E_{NFs(reduction)}$, $E_{NFs(oxidation)}$), E_{Au} is the elastic modulus of Au, and \bar{y}'_{Au} is the location of centroid (neutral axis) of transformed composite beam to Au (Equation VI.11).

Ultimately, the effective flexural rigidity of the composite beam $(EI)_{eff}$ can be obtained by

$$(EI)_{eff} = E_{Au} I'_{Au}. \quad \text{VI.14}$$

By substitution of the known values ($h_{PP} = 30 \mu\text{m}$, $h_{Au} = 309 \text{ nm}$, $h_{NFs} = 12.8 \mu\text{m}$, $b = 1 \text{ mm}$, $E_{PP} = 5.95 \text{ GPa}$, $E_{Au} = 20.55 \text{ GPa}$, $E_{Fiber}^{Red} = 5.43 \text{ MPa}$, $E_{Fiber}^{Ox} = 15.05 \text{ MPa}$) in Equations VI.9-VI.14, we obtained the $(EI)_{eff}$ of $14828 \mu\text{N}\cdot\text{mm}^2$ and $14884 \mu\text{N}\cdot\text{mm}^2$ for the composite actuator in the reduced and oxidized states, respectively.

Viscosity measurement of the liquid and gel electrolytes

The apparent viscosity of the aqueous electrolyte and agarose hydrogel electrolyte containing 0.1 M NaPSS as a function of shear rate is presented in Figure VI.13. The measured viscosity values were used for calculation of the drag coefficient. The equivalent

velocity is obtained by multiplying the shear rate by the gap between the two plates (0.5 mm). Here, the shear rate range for viscosity measurement was chosen according to the equivalent share rate of actuator velocity in liquid and gel electrolytes at various scan rates. As shown in Figure VI.13, both liquid and gel electrolytes display a decreasing viscosity by increasing shear rate (shear-thinning), which is a typical behavior of non-Newtonian fluids.

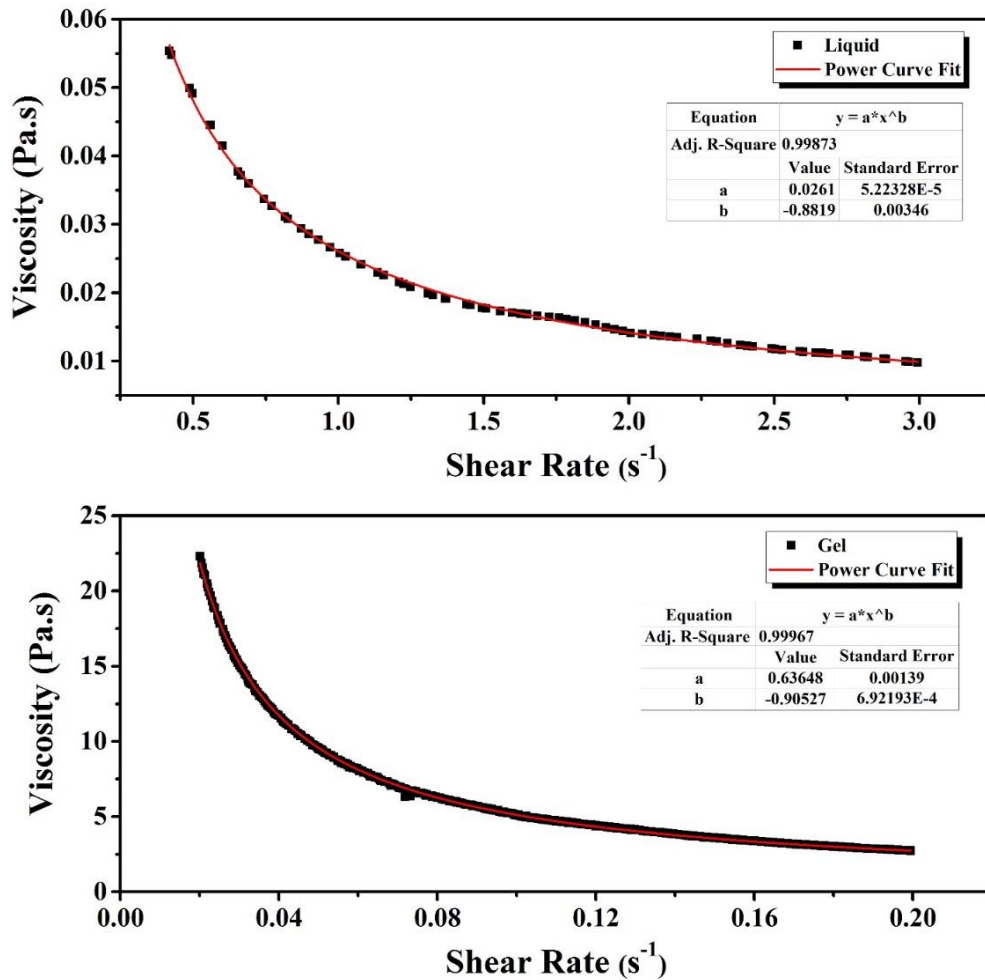


Figure VI.13. Apparent viscosity of liquid and gel electrolytes containing 0.1 M NaPSS as a function of shear rate measured by 40 mm parallel plates with a gap of 0.5 mm at room temperature.

Calculation of actuation strain

The actuation strain was calculated from the beam curvature using an equation previously developed for PPy bilayer microactuators [278] expressed as

$$k = \frac{\varepsilon}{h_{sub}} \frac{6mn(1+m)}{1+4mn+6m^2n+4m^3n+m^4n^2} ; k = \frac{2\delta}{\delta^2+L^2}, \quad \text{VI.15}$$

where ε is actuation strain, k is beam curvature, δ is beam deflection, L is the actuator length (20 mm), h_{sub} is the substrate thickness (30.3 μm), m is the thickness ratio (h_{PPy}/h_{sub} ; where $h_{PPy} = 12.8 \mu\text{m}$), and n is the elastic modulus ratio (E_{PPy}/E_{sub}). An effective E_{sub} of 6.38 GPa was determined using the method of transformed sections as described earlier in Part S6.

Calculation of actuation force

The actuation force (F_{act}) generates during reduction and oxidation of PPy NFs can be calculated by the moment equation about the contact end (point O in Figure VI.14) of the actuator as generally expressed as

$$\sum M_O = \dot{H}_O \quad \text{VI.16}$$

and

$$\dot{H} = \frac{d}{dt}(I\omega) = \dot{I}\omega + I\dot{\omega}, \quad \text{VI.17}$$

where $\sum M_O$ is sum of the moments exert on the actuator about its contact point O (about the axis perpendicular to the plane of motion), \dot{H}_O is the rate of change of angular momentum about the contact point O , I is the mass moment of inertia, \dot{I} is the rate of change of the mass moment of inertia, ω is the angular velocity, and $\dot{\omega}$ is the angular acceleration

of actuator. The forces exert on the center of mass of actuator are indicated in the free body diagram depicted in Figure VI.14. In this figure, F_{act} is the actuation force; F_d is the drag force, which is opposed to the v vector; W and F_B respectively are the weight and buoyancy forces. Accordingly, Equations VI.16 and VI.17 can be combined and extended as

$$\left[F_{act}(t) - F_d(t) + [F_B - W] \sin \left[\frac{\delta(t)}{l} \right] \right] \times \frac{l}{2} = \omega \frac{d}{dt} [I_G(t) + m(t) d^2] + [I_G(t) + m(t) d^2] \alpha(t), \quad \text{VI.18}$$

where $F_{act}(t)$ and $F_d(t)$ respectively are the actuation and drag forces; $\delta(t)$ is the actuator tip deflection; l is the actuator length, $m(t)$ is the actuator mass; $I_G(t)$ is the mass moment of inertia of the actuator about its center of mass ($I_G(t) = \frac{m(t)}{12} [l^2 + h^2]$), h is the total actuator thickness; d is the distance between the center of mass and the contact point ($d = \frac{l}{2}$); $\omega(t)$ is the angular velocity ($\omega(t) = \frac{v(t)}{l}$, where $v(t)$ is the linear velocity); and $\alpha(t)$ is the angular acceleration ($\alpha(t) = \frac{a(t)}{l}$, where $a(t)$ is the tangential acceleration). Now, we can solve equation VI.18 for $F_{act}(t)$ as

$$F_{act}(t) = \frac{1}{6} [m(t)a(t) + \dot{m}(t)v(t)] \left[4 + \frac{h^2}{l^2} \right] + F_d(t) + [W - F_B] \sin \left[\frac{\delta(t)}{l} \right], \quad \text{VI.19}$$

where $\dot{m}(t)$ is the rate of mass change, and other variables are the same as defined earlier in Equation VI.18. It should be noted that $m(t) = m_0 + \Delta m(t)$; where m_0 is the dry mass of actuator before immersion in the electrolyte ($m_0 = 1359.33 \pm 71.39 \mu\text{g}$), and $\Delta m(t)$ attributes to the mass change during actuation.

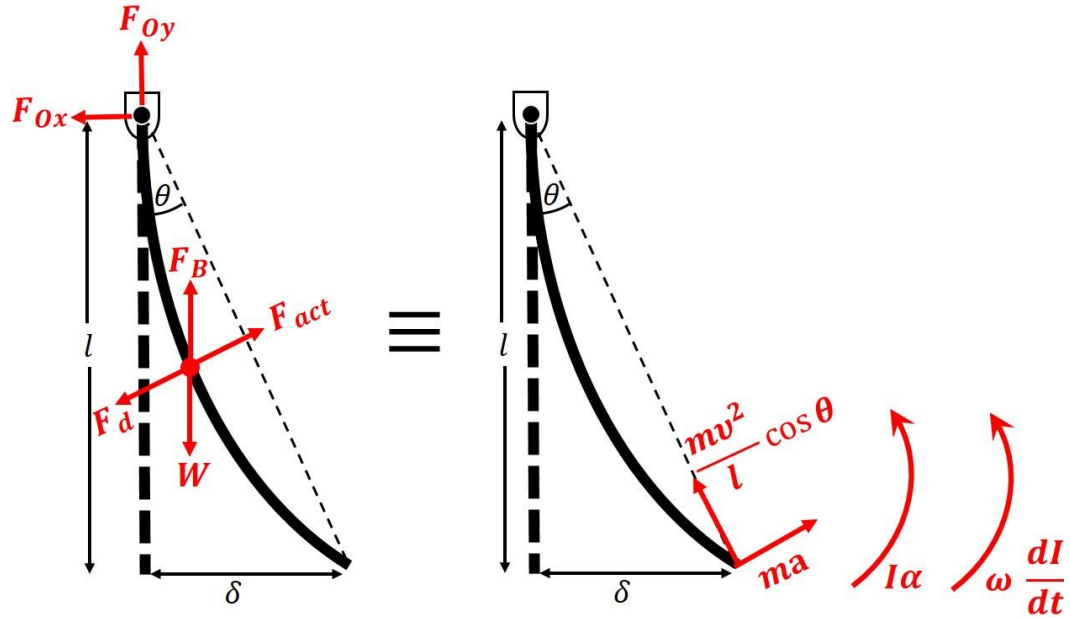


Figure VI.14. Free body-diagram and kinetic diagram of the actuator.

The weight (W) and buoyancy (F_B) forces are obtained by

$$W = mg \quad \text{VI.20}$$

and

$$F_B = \rho V g , \quad \text{VI.21}$$

where, m is the actuator mass, g is gravity constant, ρ is fluid density (for both liquid and gel electrolytes $\rho = 1 \text{ g/cm}^3$), and V is the volume of actuator submerged in the fluid ($V = hlb$; l actuator length, b actuator width, and h actuator thickness). The fluid drag force imposed on the actuator, i.e., $F_d(t)$, is calculated using Bernoulli's equation expressed as

$$F_d(t) = \frac{1}{2} C_d A \rho v(t)^2, \quad \text{VI.22}$$

where C_d is the drag coefficient, A is the frontal area of actuator ($A = 20 \text{ mm} \times 1 \text{ mm}$), ρ is the fluid density, and v is the velocity of actuator relative to fluid. Generally, the drag coefficient is a function the object shape and Reynold's number (Re) of the flow around the moving object. The Re number for a perpendicular flow past a flat plate is defined as

$$Re = \frac{\rho v D_e}{\mu}, \quad \text{VI.23}$$

where ρ is fluid density, v is the actuator velocity relative to fluid, D_e is the characteristic length of actuator ($D_e = 20 \text{ mm}$), and μ is fluid viscosity. Here, the obtained Re number for the flow in both liquid and gel electrolytes was $Re < 1$, which implies that the flow around the actuator is a laminar flow. Tomatika and Aoi theoretically reported the C_d for flat plates moving perpendicular to flow at low Re numbers in a viscous fluid (laminar flow) [300]. They reported this C_d as a logarithmic function of Re number given as

$$C_d = -10.16 \ln(Re) + 10.441. \quad \text{VI.24}$$

Knowing the velocity ($v(t)$) of actuator in the liquid and gel electrolytes, we can obtain the Re number and its corresponding C_d value at each time point using Equations VI.23 and VI.24. Then, by substitution of the obtained C_d value into Equation VI.22, the $F_d(t)$ imposed on the actuator in liquid and gel electrolytes is obtained. Finally, using the measured values of $\Delta m(t)$, $\dot{m}(t)$, $\delta(t)$, $v(t)$, $a(t)$ and also the calculated value of $F_d(t)$, we can determine the $F_{act}(t)$ at each time point.

Dynamic and kinematic measurements

We studied the dynamics, kinematics, and kinetics of the PPy NFs actuator with variable mass to relate the action of forces on the actuator to their resulting motion under linear potential waveform (CV) between -0.8 V and +0.4 V at various scan rates (10 mV/s to 200 mV/s) (Figure VI.15). The mass change ($\Delta m(t)$) and the rate of mass change ($\dot{m}(t) = dm/dt$) of the PPy NFs during CV in liquid and gel electrolytes are depicted in Figure VI.15(C-F). It is noteworthy that the sign of rate of mass change indicates the direction of ion migration at the electrolyte-CP interface (Figure VI.15(E-F)); when the CP is reduced (negative voltage) cations migrate from the electrolyte into the polymer and thus, the rate of mass change is positive; when the CP is oxidized (positive voltage) cations migrate from the polymer to the electrolyte and the rate of mass change is negative.

The actuator kinematics including tip deflection $\delta(t)$, tip velocity $v(t)$, and tip acceleration ($a(t)$) as a function of time during CV at various scan rates in both liquid and gel electrolytes are demonstrated in Figure VI.15(G-L). Figure VI.15(G-H) show a reversible nonlinear deflection and a variable response time during linear potential sweep (CV) upon influx and efflux of cations/hydrated cations. As cations/hydrated cations entered the PPy NFs (reduction process), the $\delta(t)$ had a steep increase to the inflection point, followed by a gradual increase to the δ_{max} . Inversely, as the PPy NFs were oxidized and cations/hydrated cations left the polymer, the $\delta(t)$ gradually decreased to the inflection point and then steeply dropped to the initial position. While the δ_{max} substantially decreased with increasing scan rate (from 7.88 ± 0.49 mm to 2.53 ± 0.4 mm in the liquid electrolyte, and from 0.42 ± 0.05 mm to 0.14 ± 0.02 mm in the gel electrolyte, as the scan rate

respectively increased from 10 to 200 mV/s, $p < 0.01$); the speed of actuator significantly escalated ($p < 0.01$) with the scan rate increments (Figure VI.15(I-J)). In particular, in the liquid electrolyte, the absolute value of the maximum and minimum velocities ($|v_{max}|$ and $|v_{min}|$) at the inflection points significantly increased from 0.19 ± 0.01 mm/s and 0.15 ± 0.01 mm/s for 10 mV/s scan rate to 1.28 ± 0.21 mm/s and 0.96 ± 0.16 mm/s for 200 mV/s scan rate ($p < 0.01$). In the gel electrolyte, the absolute value of the velocities $|v_{max}|$ and $|v_{min}|$ at the inflection points remarkably increased from 0.025 ± 0.012 mm/s and 0.016 ± 0.008 mm/s for 10 mV/s scan rate to 0.063 ± 0.005 mm/s and 0.052 ± 0.004 mm/s for 200 mV/s scan rate, respectively ($p < 0.01$). The actuator dynamics including the calculated drag force ($F_d(t)$) and actuation force ($F_{act}(t)$) under CV cycling at various scan rates in liquid and gel electrolytes are presented as a function of time in Figure VI.16.

The correlation between the generated actuation force and the resultant deflection in a CV cycle at various scan rates in liquid and gel electrolytes are plotted in Figure VI.3(J-K). As observed, the actuator exhibited a reversible linear relation between actuation force $F_{act}(t)$ and deflection $\delta(t)$ as

$$\delta(t) = \beta F_{act}(t). \quad \text{VI.25}$$

Interestingly, there was no significant difference between the slope of the plots (β^{-1}) in liquid and gel electrolytes at all scan rates ($\beta = 3.95 \pm 0.09$, Table VI.2). We further investigated the deflection of PPy NFs actuator according to Euler-Bernoulli's composite beam theory. Such a linear relationship for a cantilever beam can be described by

$$\delta(t) = \frac{\gamma l^3}{(EI)_{eff}} F_{act}(t), \quad \text{VI.26}$$

where γ is a constant, l is the actuator length, and $(EI)_{eff}$ is the effective flexural rigidity of the composite beam that obtained from Equation VI.14. The calculated γ values for various scan rates in liquid and gel electrolytes are given in Table VI.2. Statistical analysis demonstrated that there was no significant difference ($p < 0.001$) in values of γ among different scan rates in liquid and gel electrolytes.

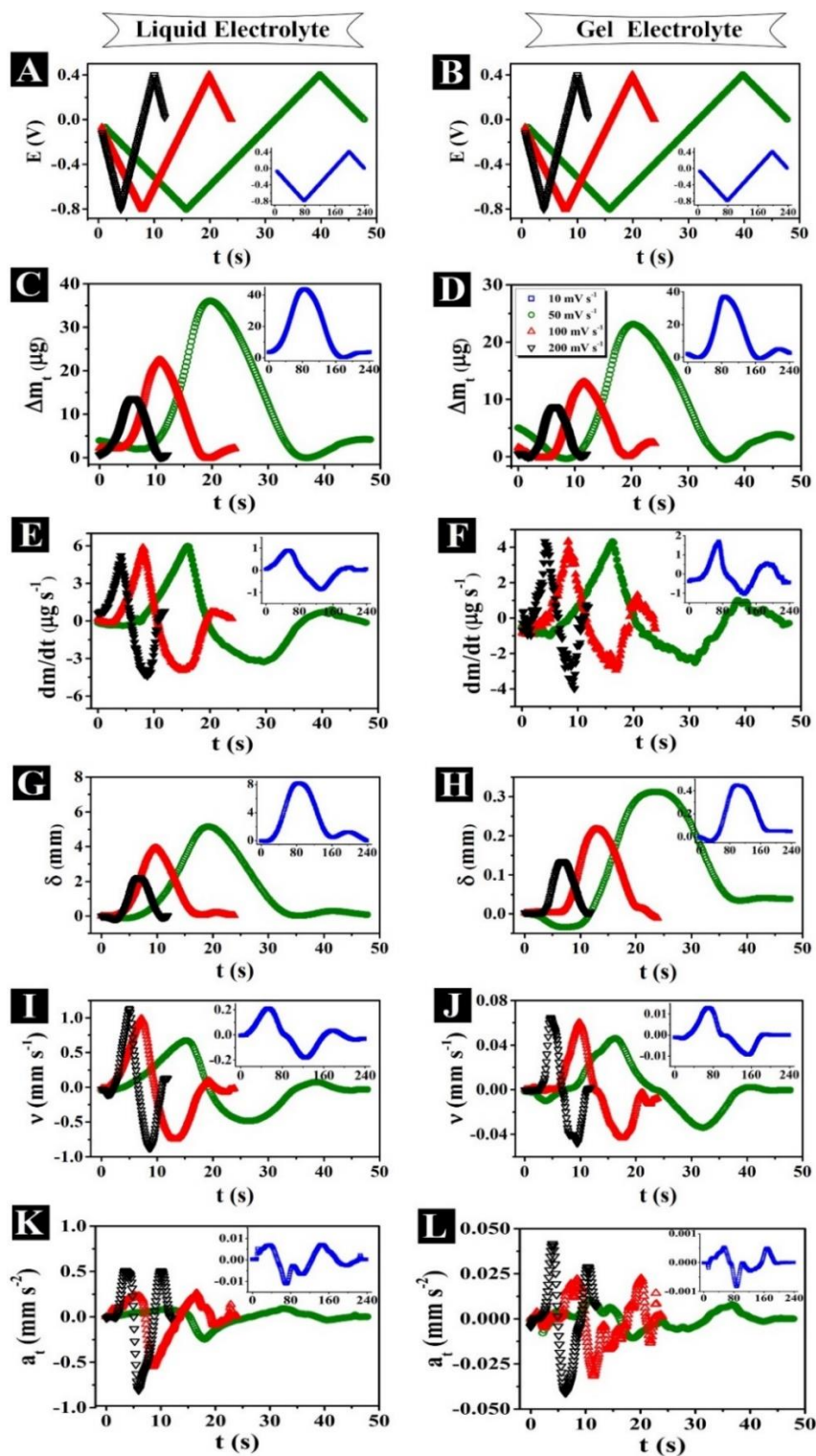


Figure VI.15. Applied linear potential waveforms (A,B), mass change $\Delta m(t)$ (C,D), the rate of mass change (dm/dt) (E,F), deflection (δ) (G, H), velocity (v) (I,J), and tangential acceleration $a(t)$ (K,L) of the actuator as a function of time.

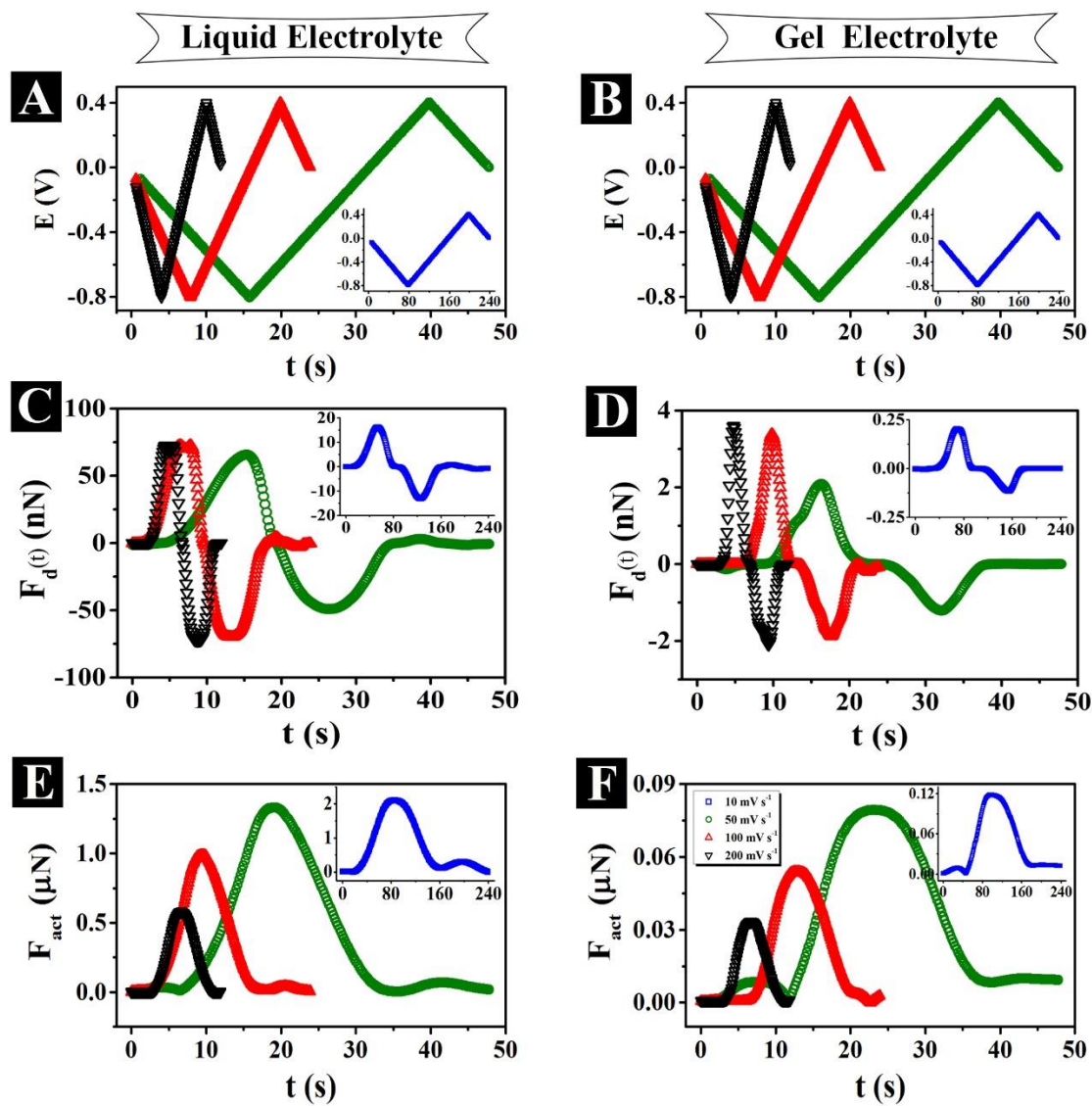


Figure VI.16. Applied linear potential waveforms (A,B), drag force $F_d(t)$ (C,D), and actuation force (F_{act}) (E,F) of as a function of time at various CV scan rates in liquid (A,C,E) and gel (B,D,F) electrolytes.

Table VI.2. Calculated β and γ values at various scan rates in liquid and gel electrolytes.

Electrolyte	Scan rate (mV/s)	β (reduction)	β (Oxidation)	γ (reduction)	γ (Oxidation)
Liquid	10	3.88 ± 0.01	3.92 ± 0.02	7.2 ± 0.02	7.29 ± 0.02
	50	3.82 ± 0.02	4.00 ± 0.02	7.08 ± 0.04	7.44 ± 0.03
	100	3.98 ± 0.06	4.13 ± 0.02	7.38 ± 0.15	7.69 ± 0.03
	200	4.01 ± 0.2	4.21 ± 0.06	7.43 ± 0.37	7.84 ± 0.11
Gel	10	3.88 ± 0.01	3.92 ± 0.02	7.2 ± 0.02	7.29 ± 0.02
	50	3.82 ± 0.02	4.00 ± 0.02	7.08 ± 0.04	7.44 ± 0.03
	100	3.98 ± 0.06	4.13 ± 0.02	7.38 ± 0.15	7.69 ± 0.03
	200	4.01 ± 0.2	4.21 ± 0.6	7.43 ± 0.37	7.84 ± 0.11

Short-term response over CV cycling

The short-term performance of the PPy NFs actuator over 20 cycles of actuation in liquid and gel electrolytes are shown Figure VI.17. The charge storage capacity (Q) of the actuator did not show any significant change in both liquid and gel electrolytes over 20 CV cycles at each scan rate (Figure VI.17(A-B)). In addition, there was no statistically significant difference between Q values in liquid and gel electrolytes at same scan rates. These results revealed that the PPy NFs maintained their electroactivity during 20 cycles of actuation. The maximum mass influx (Δm_{max}) and maximum tip deflection (δ_{max}) were stable in both liquid and gel electrolytes and did not vary significantly between each cycle for scan rates of 50, 100, and 200 mV/s (Figure VI.17(C-F)). At low scan rate (10 mV/s), however, there was a gradual decrease in the Δm_{max} during about ten cycles followed by a plateau (Figure VI.17(C-D)). This reduction may be due to excess influx of cations/hydrated cations in the initial cycles until it reaches equilibrium.

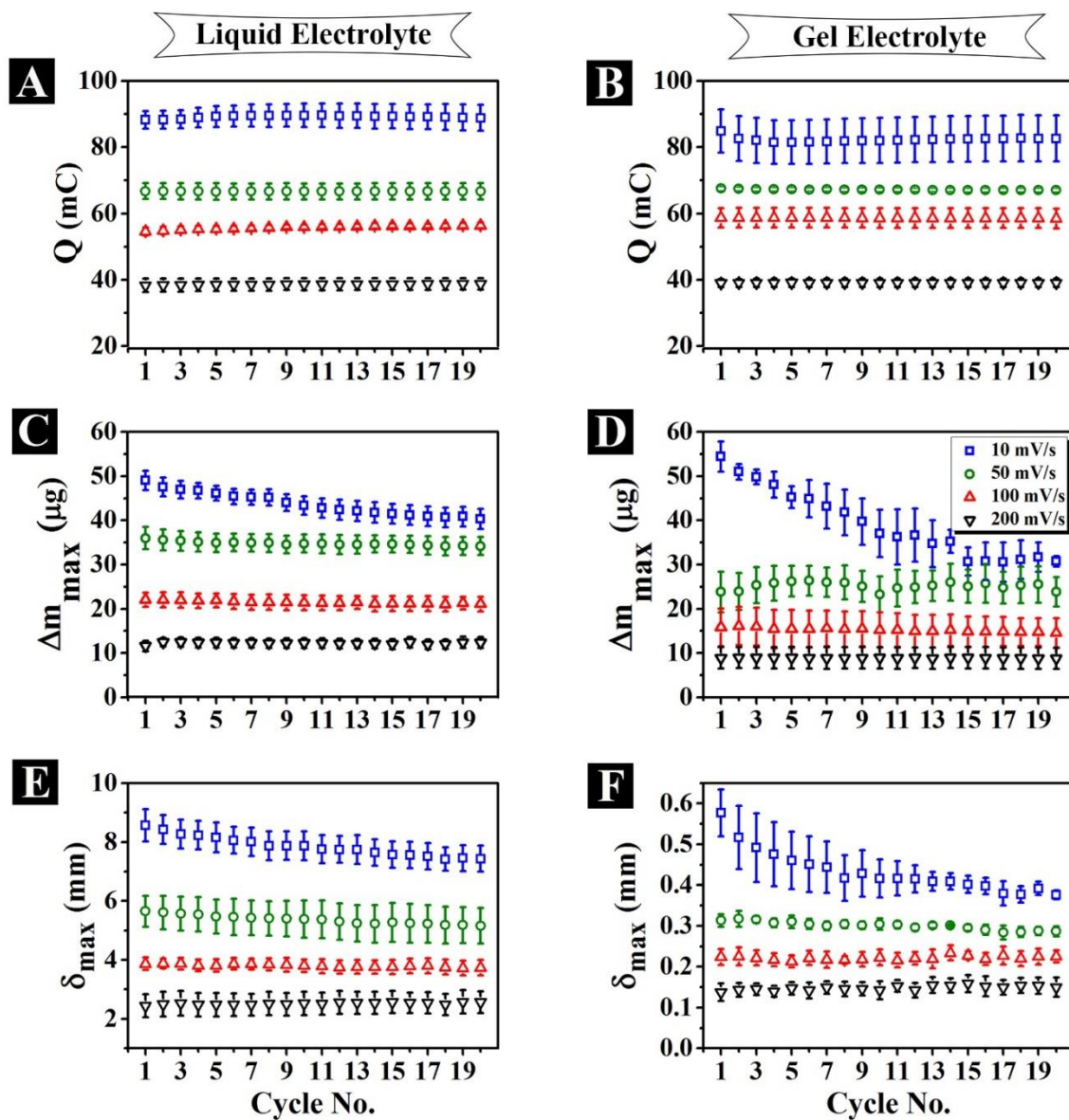


Figure VI.17. Charge storage capacity (Q) (A,B), maximum mass exchange (Δm_{max}) (C,D), and maximum tip deflection (δ_{max}) (E,F) of the PPy NFs actuator as a function of cycle number in liquid (A,C,E) and gel (B,D,F) electrolytes.

VII Conjugated Polymer Nanofiber Actuators for Articulating Flexible Neural Microelectrodes

Abstract

Conjugated polymer actuators have potential use in implantable neural interface devices for modulating the position of electrode sites within brain tissue or guiding insertion of neural probes along curved trajectories. The actuation of polypyrrole nanofibers (PPy NFs) doped with polystyrene sulfonate (PSS) is utilized for articulating flexible neural probes with multiple movable projections employed in the cerebral environment. Bilayer beam projections composed of structural SU-8 layer, Cr/Au contact traces, and electroactive layer of PPy NFs are electrochemically actuated through cyclic voltammetry in artificial cerebrospinal fluid (aCSF). The electrochemical properties and actuation performance of the projections of varying length coated with PPy NFs were investigated at various CV scan rates in aCSF electrolyte. This work demonstrates a proof of concept for actuated implantable neural interfaces.

Introduction

Recent advances in neuroscience have enabled the exploration of brain activity and neural disorders and allowed understanding of its mechanisms down to the microscopic level. Neural recording technologies have remarkably contributed to this understanding by revealing neuron activities and functional connectivity [301, 302]. Neural interfacing devices have been utilized in various clinical applications including cochlear [303] and retinal implants [304], spinal and peripheral nerve interfaces [305, 306], epilepsy

monitoring devices [307], and deep brain stimulators [308]. Initiating from tungsten and silicon neural probes [309, 310], next generation neural probes such as Michigan electrodes [311], Utah arrays [312], and Neuropixels electrodes [313] have enabled advanced spatiotemporal and multifunctional interrogation of neurons. The rigid nature of these probes facilitates direct implantation and accurate localization in the brain; however, the physical and mechanical properties mismatch between the neural probe and brain tissue restricts establishment of high-resolution chronic recordings and stimulations of surrounding neurons [314]. In fact, conventional electrodes for brain interfacing are made of metals or doped silicon, which are much stiffer than biological tissues. Consequently, the mechanical mismatch between probes and brain tissue induces neuroinflammatory responses and scar formation that resulted in gradual signal loss over time [50]. The strategy to improve the mechanical and physical compatibility of neural probes with brain tissue includes electrode design and materials engineering [315]. Basically, structural design (electrode thickness) and mechanical properties (elastic modulus and Poisson's ratio) of the probes determine their bending stiffness [316] expressed as

$$\text{Bending Stiffness} = \frac{Eh^3}{12(1-\nu^2)}. \quad \text{VII.1}$$

Here, E is the elastic modulus, h is thickness, and ν is Poisson's ratio. As the bending stiffness scales cubically with the thickness and linearly with the modulus, either reducing the thickness of the device or using low modulus materials can drastically decrease the device stiffness. Accordingly, soft materials are increasingly employed for neural electrodes to provide more mechanically-compatible interfaces while minimizing side

effects [314]. Many polymers have been explored for development of flexible neural probes, including SU-8, polyimide, parylene, polydimethylsiloxane (PDMS), liquid crystal polymers, cyclic olefin polymers, polymethyl methacrylate, polycarbonate, and polystyrene [317]. Combination of material properties, processing conditions, and performance demands determine selection of a particular polymer for a device. Among all above-mentioned polymers, SU-8, polyimide, and parylene are currently on the rise within microelectromechanical systems (MEMS) as free standing films and structural elements on flexible neural probe devices [318]. Compared to the other polymers, these three are compatible with standard microfabrication techniques (i.e., photolithography and wet/dry etch), so many researchers have been motivated to develop novel strategies for processing and device construction of neural probes based on these polymers [317]. However, implantation and localization of the soft material in soft tissues is challenging, owing to additional tissue damage caused by rigid auxiliary tools used for implantation, lengthy interface recovery and micromotion of the soft electrode [319-321]. The dilemma of choosing between facile implantation of rigid probes and compatible interface of soft electrodes has called for the evolution of materials and fabrication techniques for neuronal recording technology.

Neuronal recordings using current implantable microelectrode technologies have been found to be inconsistent and/or unreliable in long-term assessments [50, 322, 323]. This limitation is the most significant impediment toward the success of emerging cortical prostheses that rely on their recording stability over the lifetime of patients who use such prosthetic devices. As an alternative to fixed microelectrodes, movable microelectrodes

have been suggested as a potential approach to mitigate some of these limitations. Technologies that enable control of microelectrodes after implantation remarkably enhance the ability to (a) isolate activity from single neurons (b) maintain stable neuronal recordings over longer durations (c) maintain the signal-to-noise ratio in the neuronal recordings (d) seek neurons of interest after implantation [324]. There have been several attempts to create movable probes, but to the best of our knowledge, none of them have successfully met all the requirements for safe, reliable, and long-term chronic use. The use of electrothermal and capacitive actuators has been demonstrated for silicon probes embedded in the brain cap to vertically move neural probes which provided good signal recording for 12 weeks in vivo [325]. Cham and coworkers also developed microwire probes which move vertically in the brain by manually adjusting a screw on the head cap of the animal [326]. Pang et al. developed an electrolysis-based parylene balloon actuator in order to move neural probes [327].

In general, actuation methods can either be included in the microfabrication of neural probes or can be integrated in post-fabrication process. Capacitive, electrostatic, electrothermal, shape memory alloys, and piezoelectric actuation methods are usually incorporated at the microfabrication level. However, an actuation method that could be incorporated post-processing may allow for fabrication flexibility. In addition, actuation methods require to be evolved for biocompatible and safe use in the brain tissue, their power consumption, heat dissipation, voltage requirements, and overall size. Mechanisms of producing actuation at the micro-scale are limited and usually require incorporation during the fabrication processes [324]. Therefore, an actuation technology that can be

incorporated post standard microfabrication would have advantage over others that require process integration. Conjugated polymer actuators are one such technology within a class of smart materials that can be electrically polymerized on projections of interest and its low power requirement is promising for applications in medical microdevices. Conjugated polymers have already been utilized for neural electrode site coatings to improve signal recording, increase the charge capacity for stimulation, and actuation-controlled drug delivery [13, 328-330].

This work demonstrates the utilization of conjugated polymer nanofiber-based actuators for development of movable and flexible neural microelectrodes. Here, we provide a novel strategy to steer the neural electrode projections as a way to deploy electrode sites away from the probe. First, we microfabricated SU-8 based probes with Cr/Au projections/recording sites using standard photolithography, and then articulated the projection sites with conjugate polymer coatings to enable the probes for controlled actuation/movement. The electroactive coatings were created through electrochemical deposition of polypyrrole on the projection sites in the form of thin films and/or randomly oriented nanofibers. The actuation and electrochemical performance of the fabricated probes was investigated under cerebral physiological conditions. Remarkably, the electrode projections of 50 μm wide with varying length of 0.5 mm and 1 mm were able to deflect $\sim 87 \mu\text{m}$ and $\sim 262 \mu\text{m}$ away in artificial cerebrospinal fluid (aCSF), respectively. Given that immune response encapsulation of typical neural probes of 100 – 200 μm width occurs within 50 – 100 μm of the probe [50, 331], this approach may be feasible to place electrode sites in more favorable recording environments.

Methods

Materials

SU-8 3005 (negative photoresist) was purchased from MicroChem (Westborough, MA). Positive photoresist (KL6003), 0.26N TMAH Developer, and SU-8 Developer were supplied from Kemlab Inc (Woburn, MA). Plastic photomasks with probe patterns were provided from CAD/Art Service Inc. Cr/glass masks pre-coated with a 500 nm positive photoresist were purchased from Nanofilm (Westlake Village, CA) and patterned with Cr Etchant from MicroChem. Thermal oxide silicon wafers (SiO_2 on Si, oxide thickness = 2 μm) were supplied from UniversityWafer Inc. Poly(L-lactide) (PLLA, Resomer 210) with the inherent viscosity of 3.3 - 4.3 dL/g was purchased from Evonik Industries. Benzyl triethylammonium chloride and pyrrole ($M_w = 67.09$ g/mol) were supplied from Fisher Scientific. Poly(sodium-p-styrene sulfonate) (NaPSS, $M_w = 70$ kD) and chloroform were purchased from Acros-Organics. All ingredients for preparation of aCSF, including NaCl, KCl, $\text{CaCl}_2 \cdot 2\text{H}_2\text{O}$, $\text{MgCl}_2 \cdot 6\text{H}_2\text{O}$, $\text{Na}_2\text{HPO}_4 \cdot 7\text{H}_2\text{O}$, $\text{NaH}_2\text{PO}_4 \cdot \text{H}_2\text{O}$, were supplied from Sigma Aldrich.

Device design and fabrication

In this work, two series of probes with two and three electrode projections of the same width (50 μm) and thickness (~13 μm), but different lengths (1 mm for probes with two projections and 0.5 mm for probes with three projections) were designed as schemed in Figure VII.1. For in-vitro assessments, the electrical traces to the actuating segments (projections) were coupled together. Devices were fabricated using standard photolithography technique at the Nanofabrication Facility at the University of Houston.

The device was fabricated through layer-by-layer photolithography and etching processes. We patterned each layer using a designed photomask (total of six different photomasks, one for alignment marks and five masks for device patterns) for a 4 inch wafer. In this work, we first used inexpensive plastic photomasks for photolithography, but then switched to Cr/glass masks for their higher quality and ease of processing. The patterns on plastic photoamasks were transferred onto Cr/glass masks already coated with a thin layer of positive photoresist. To transfer the patterns, the plastic photomask was placed on the photoresist coated Cr/glass mask and UV exposed at 12.5 mJ/cm^2 for 7.2 s. Afterwards, the exposed photoresist layer was developed in 0.26N TMAH Developer for 60 s. The patterned Cr/glass mask was wet etched using Cr etchant to create patterns on the mask (etching time = 5 min). After etching, the remaining photoresist coating was dissolved in Acetone.

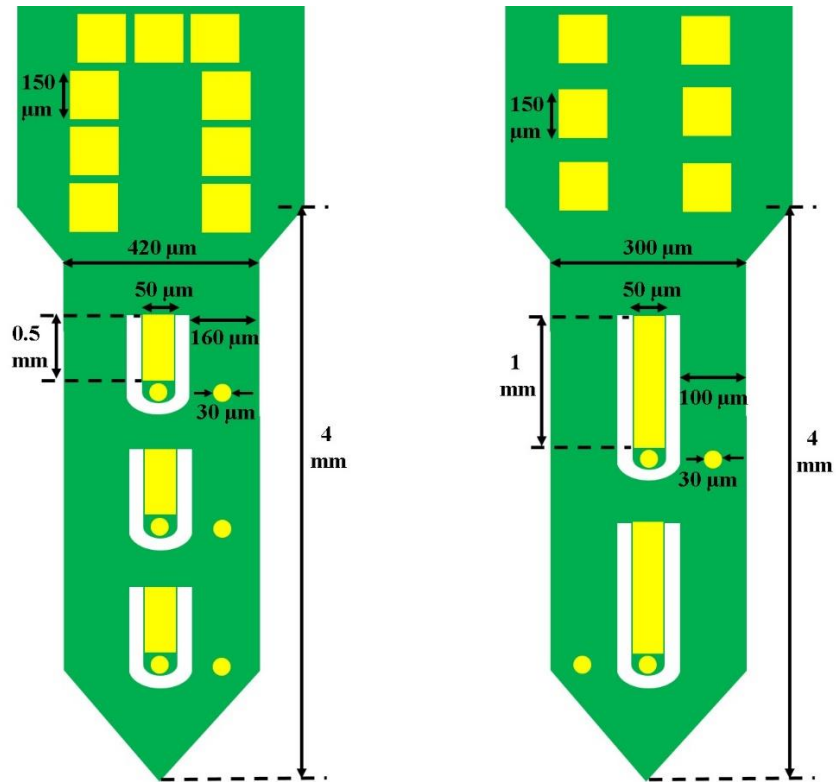


Figure VII.1. Schematics represent probe designs with two and three movable projection sites.

The probe fabrication process is overviewed in Figure VII.2 and described hereunder:

- i) A silicon wafer (Figure VII.2(a)) with a thermal oxide layer (SiO_2 , 2 μm thick) was used as the substrate. The oxide layer served as the final release layer (Figure VII.2(b)).
- ii) Patterning and development of first SU-8 layer: a SU-8 layer ($\sim 8 \mu\text{m}$ thick) was spun coated (at 1000 rpm for 30 s) onto the substrate and soft baked at 105°C for 15 min (very slow heating/cooling). To create the projection gap (Figure VII.2(c)), the SU-8 layer was patterned using Mask 1 under UV exposure at 12.5 mJ/cm^2 for 16 s. For post exposure baking, the exposed layer was slowly heated to 95°C and kept for 3 min and

- then slowly cooled down to room temperature. The exposed SU-8 layer was developed through immersion in SU-8 developer for 3 min, while shaking.
- iii) Deposition of first Cr/Au traces: A thin layer ($\sim 2 \mu\text{m}$) of positive liftoff resist (KL6003) was spun coated on the wafer at 2500 rpm for 45 s and soft baked at 105°C for 3 min. Then, the baked layer was UV exposed and patterned using Mask 2 at $12.5 \text{ mJ}/\text{cm}^2$ for 8 s (Figure VII.2(d)). The exposed layer was developed by immersion in 0.26N TMAH developer for 60 s. The patterned wafer was first descummed in oxygen plasma at 100 W for min, and then coated with a thin layer of Cr/Au (Cr thickness = 10 nm, Au thickness = 100 nm) using e-beam evaporation system (Thermionics evaporator). After Cr/Au deposition, the liftoff resist was removed through bath sonication in acetone (Figure VII.2(e)).
- iv) Patterning and development of second SU-8 layer (insulating layer, Figure VII.2(f)): a layer ($\sim 5 \mu\text{m}$) of SU-8 was spun coated on the wafer (at 3000 rpm for 30 s) and soft baked at 105°C for 20 min (very slow heating/cooling). Then, the SU-8 layer was UV exposed and patterned using Mask 3 at $12.5 \text{ mJ}/\text{cm}^2$ for 16 s. For post exposure baking, the exposed layer was slowly heated to 95°C and kept for 5 min and then slowly cooled down to room temperature. The exposed SU-8 layer was developed by immersion in SU-8 developer for 2.5 min (Figure VII.2(f)). The developed SU-8 layers were hard baked at 150°C for 10 min.
- v) Deposition of second Cr/Au traces: A thin layer ($\sim 2 \mu\text{m}$) of positive liftoff resist was spun coated on the wafer at 2500 rpm for 45 s and soft baked at 105°C for 3 min (Figure VII.2(g)). Then, the baked layer was UV exposed and patterned using Mask 4 at 12.5

- mj/cm² for 8 s. The exposed layer was developed by immersion in 0.26N TMAH developer for 60 s. The patterned layer was first descummed in oxygen plasma at 100 W for 5 min and then coated with a thin layer of Cr/Au (Cr thickness = 10 nm, Au thickness = 100 nm) through e-beam evaporation. After Cr/Au deposition, the liftoff resist was removed using bath sonication in acetone (Figure VII.2(h)).
- vi) Patterning and development of third SU-8 layer (Figure VII.2(i)): a SU-8 layer (~5 μm) was spun coated on the wafer (at 3000 rpm for 30 s) and soft baked at 105°C for 20 min (very slow heating/cooling). The baked SU-8 layer was UV exposed and patterned using Mask 5 at 12.5 mj/cm² for 12 s. For post exposure baking, the exposed layer was slowly heated to 95°C and kept for 5 min and then slowly cooled down to room temperature. The exposed SU-8 layer was developed by immersion in SU-8 developer for 2.5 min (Figure VII.2(i)). The developed SU-8 layers were hard baked at 150°C for 15 min.
- vii) To release the probe devices from the substrate, the wafer was immersed in HF solution (30%) to remove the sacrificial SiO₂ layer (Figure VII.2(j)). The released probes were collected from the HF solution and transferred to water containers for serial wash. Ultimately, the fabricated probes were annealed at 200 °C to release the residual stresses in the SU-8 layers.

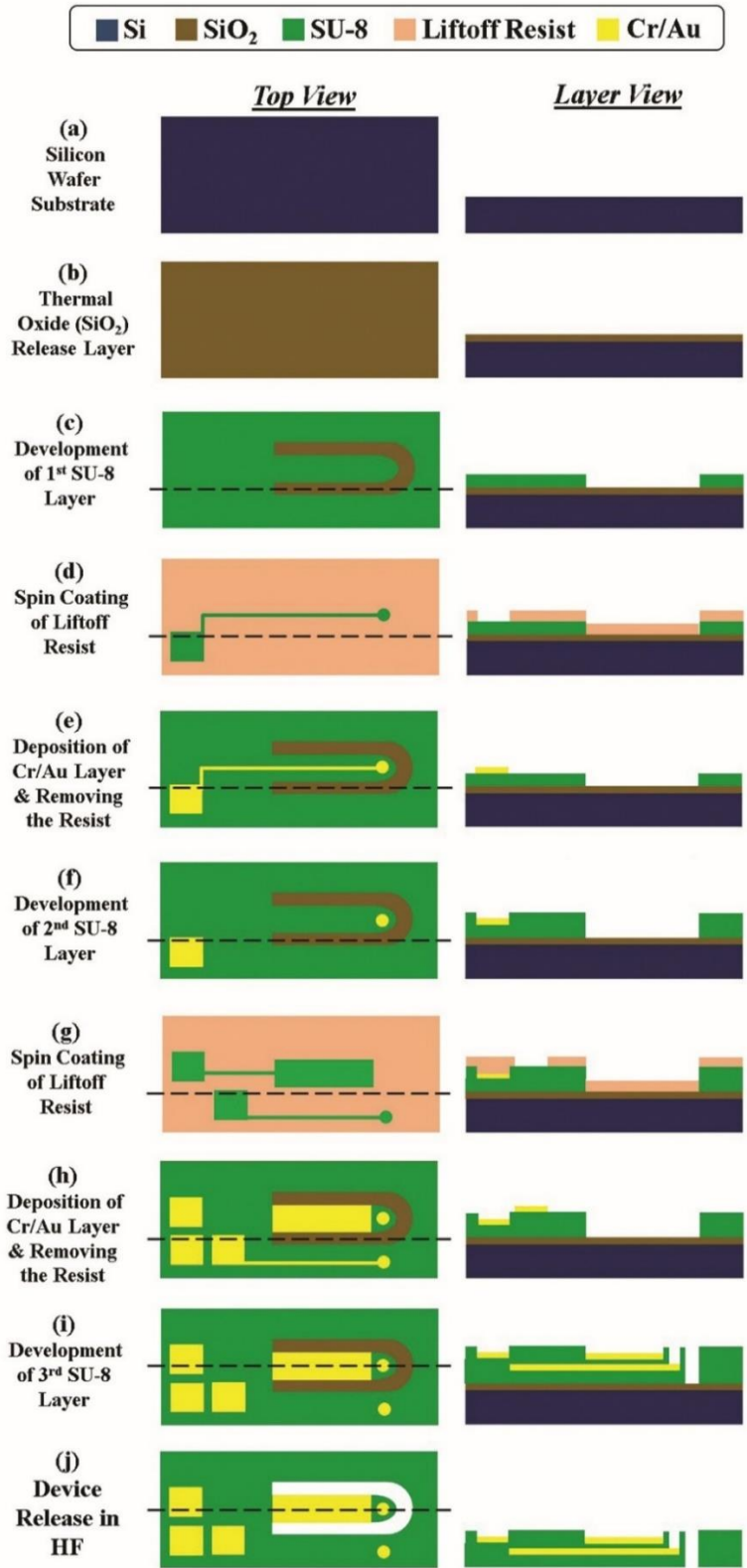


Figure VII.2. Overview of the fabrication process of the probe devices.

Coating of device projections with conjugated polymer film

The projections sites of the fabricated devices were electrochemically coated with an electroactive layer of polypyrrole (PPy) film. PPy was electrodeposited on the projection sites using 0.2 M pyrrole:PSS aqueous electrolyte at the current density of 0.5 mA/cm² for 2 hrs using Autolab PGSTAT 128N (Metrohm, USA) in galvanostatic mode with a two-electrode configuration at room temperature.

Coating of device projections with conjugated polymer nanofibers

To construct PPy nanofibers (PPy NFs) on the projection sites, first template poly(L-lactide) (PLLA) nanofibers were electrospun onto the gold projection sites and then PPy electrodeposited around the template nanofibers. For electrospinning, a homogeneous solution of PLLA (3 wt.%) in chloroform was prepared by adding 230 mg PLLA in 5 ml chloroform and stirring the mixture overnight at room temperature. To enhance the solution charge strength, 23 mg Benzyl triethylammonium chloride (an organic salt) was added to the solution prior to stirring. PLLA template nanofibers were electrospun using a syringe pump with the spinneret gauge of 23, an electric field of 0.91 kV/cm, a flow rate of 50 μ L/hr, and a syringe-substrate distance of 11 cm for 30 s. Temperature and humidity were kept constant at 26°C and 30%, respectively. For PPy deposition, 0.2 M pyrrole:PSS aqueous electrolyte was prepared by dissolving 277 μ L pyrrole monomer and 824 mg NaPSS in 20 ml deionized water. Prior to electrodeposition, the probe device was kept in the electrolyte for 30 min to ensure that the solution has completely diffused into the fiber interspaces. Then, the electrodeposition was carried out at the current density of 0.5 mA/cm² for 2 hrs. Ultimately, to remove the uncoated template nanofibers from the

surrounding areas of projection sites, the probe device was immersed in chloroform for 30s.

Preparation of artificial cerebrospinal fluid (aCSF)

To prepare the aCSF, first two different solutions containing the aCSF compounds were prepared. Solution A was composed of 8.66 g NaCl, 0.224 g KCl, 0.206 g CaCl₂·2H₂O, and 0.163 g MgCl₂·6H₂O in 500 ml deionized water. Solution B was composed of 0.214 g Na₂HPO₄·7H₂O and 0.027 g NaH₂PO₄·H₂O in 500 ml deionized water. Then, an equal volume of solutions (1:1 ratio) were mixed to end up with a multivalent physiological ion solution of aCSF.

Projections actuation using cyclic voltammetry

Actuation of the probe projections was performed through cyclic voltammetry (CV) using Autolab PGSTAT 128 in a three-electrode configuration with a saturated Ag/AgCl reference electrode and a 1 × 2 cm Pt foil as counter electrode. The CV was performed within the potential range of -0.8 to +0.4 V at various scan rates of 50, 100, 200, and 1200 mV/s. The actuation behavior of the probe devices was assessed in aCSF electrolyte. Prior to actuation, the probe projections were primed in the electrolyte at 100 mV/s for ten cycles.

Electrochemical impedance spectroscopy (EIS)

An Autolab PGSTAT12 and Frequency Response Analyzer software (EcoChemie B.V., Netherlands) were used to record impedance spectra of electrodesites for the neural probes. The impedance measurement was conducted in the aCSF electrolyte using a three-electrode cell configuration. The working electrode was connected to electrode site through

a connector. The counter electrode was connected to a platinum foil that was placed in the cell container, and an Ag/AgCl electrode was used as reference electrode. An AC sinusoidal signal of 5 mV in amplitude was used to record the impedance over a frequency range of 1-10⁵ Hz.

Projection deflection measurement

The bending deflection of the probe projection was recorded using a digital camera (Dino-Lite) with 30 frames per second. The recorded videos were then processed using an open-source software (Tracker 5.0.6, <https://physlets.org/tracker>) to measure the projection deflection upon actuation.

Structural characterization of the probe devices

The structure evaluation of the fabricated probes was performed using optical upright and stereo microscopes (Carl Zeiss Imager Z1, Germany). The surface morphology of the probe projections after coating with conjugated polymer layer was characterized using Field Emission Scanning Electron Microscopy (FESEM, FEI 235). Samples were mounted on aluminum stubs by carbon tape and a carbon paint was used for grounding. Prior to microscopy, probes were sputter-coated with a thin layer of gold using Denton Sputter Coater for 60 s at 40 mA.

Results and discussion

Structural design of probe devices

The optical images of the fabricated probes with two and three actuating projections are shown in Figure VII.3. As indicated, each projection includes a rectangular segment

for actuation along with a round site at the projection tip for signal recording. In addition, a fixed recording site has been placed on the device body next to the projection at the same vertical position as the movable recording site.

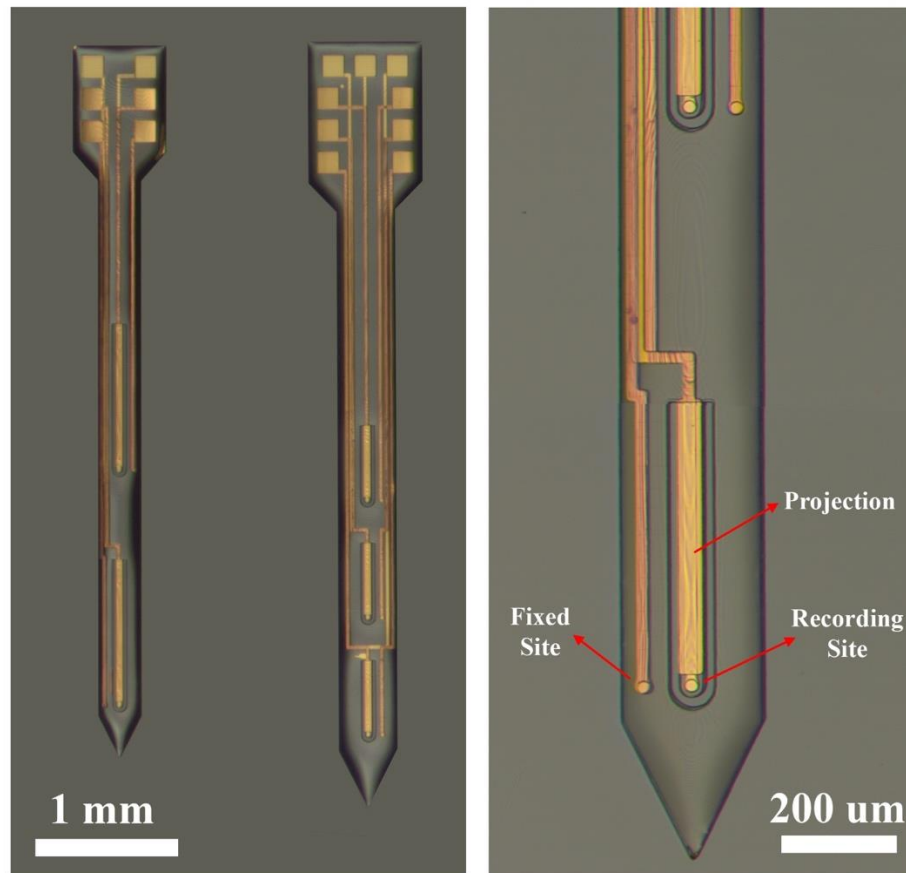


Figure VII.3. Optical micrographs of the fabricated neural probes with two and three projection sites.

Morphology of conjugated polymer coatings

To create movable projections, the projection segments of the microfabricated probes were coated with an electroactive layer of PPy in the form of film (Figure VII.4(A-C)) and randomly oriented PPy nanofibers (PPy NFs) (Figure VII.4(D-F)). To make PPy NFs layer,

PLLA template nanofibers were first electrospun onto gold projections and then they were coated with PPy through electropolymerization process (Figure VII.5). The thickness of the resultant PPy layer is controlled by the electrodeposition time and the applied current density, as well. For a comparable study between PPy film and PPy NFs, PPy electrodeposition was conducted at the same current density (0.5 mA/cm^2) and for the same deposition time (2 hrs) in both PPy forms. Construction of the PPy active layer on the gold-coated SU-8 passive layer forms a bilayer bending beam actuator, which is responsible for electrochemical actuation of the probe projections. Comparing the SEM images in Figure VII.4(C and F), the PPy film formed a continuous coating on the projection surface, while the PPy NFs formed a much porous layer with extremely high surface to volume ratio.

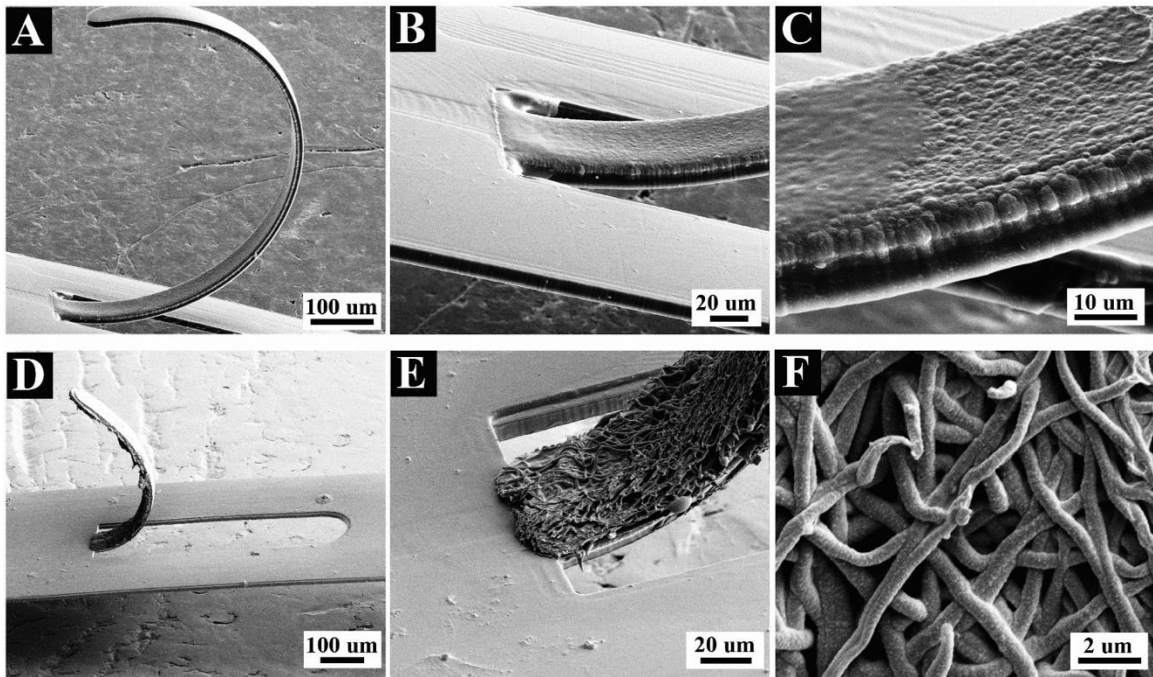


Figure VII.4. Scanning electron micrographs of probe projections coated with an electroactive layer of PPy film (A-C) and PPy NFs (D-F).

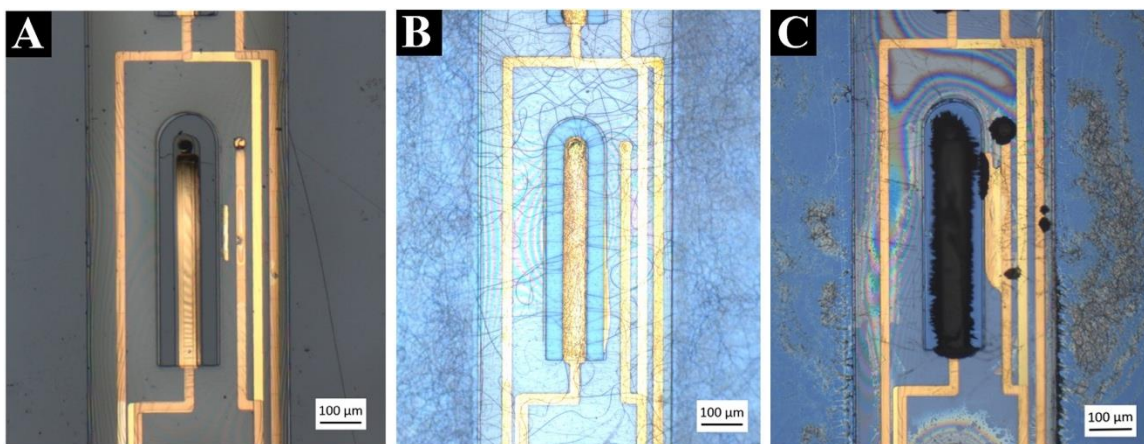


Figure VII.5. Coating of probe projections with PPy NFs: A) gold projection, B) electrospinning of template PLLA NFs, and C) electrodeposition of PPy around template NFs and removing of the uncoated template nanofibers.

Electrochemical impedance measurements

Electrochemical impedance spectroscopy was used to investigate and compare the electrical conductivity of the projection sites after coating with PPy film and PPy NFs. As demonstrated in Figure VII.6(A-B), the impedance of the gold projections was dramatically decreased after coating with PPy film or PPy NFs. For two projections probes, PPy NFs coating exhibited lower impedance across the whole frequency range (1-10⁵ Hz) than PPy film (Figure VII.6(A)). This is attributed to the higher effective surface area of the PPy nanofibers compared with the film counterpart. However, for three projections probes, PPy NFs coating resulted in a lower impedance at frequencies <100 Hz (Figure VII.6(A)). The phase angle and Nyquist plots in Figure VII.6(C-F) demonstrate the resistance and capacitance properties of projection sites. As observed in Figure VII.6(C-D), the gold projection is predominantly capacitive over the whole frequency range, while both PPy film and PPy NFs coatings decreased the capacitive component of the probes within the

frequency range, especially at high frequencies. Noticeably, in probes with three projections, PPy NFs coating exhibited very low capacitive response than film counterpart (Figure VII.6(D)). According to Nyquist plots demonstrated in Figure VII.6(E-F), both PPy coatings dramatically decreased the real (Z') and imaginary (Z'') impedances. In addition, the PPy NFs coating resulted in lower Z' and Z'' values than PPy film that is due to higher effective surface area of PPy NFs. In general, these results confirm that PPy NFs offers improved electrical conductivity over the film counterpart. Accordingly, the PPy NFs were utilized for the following actuation studies.

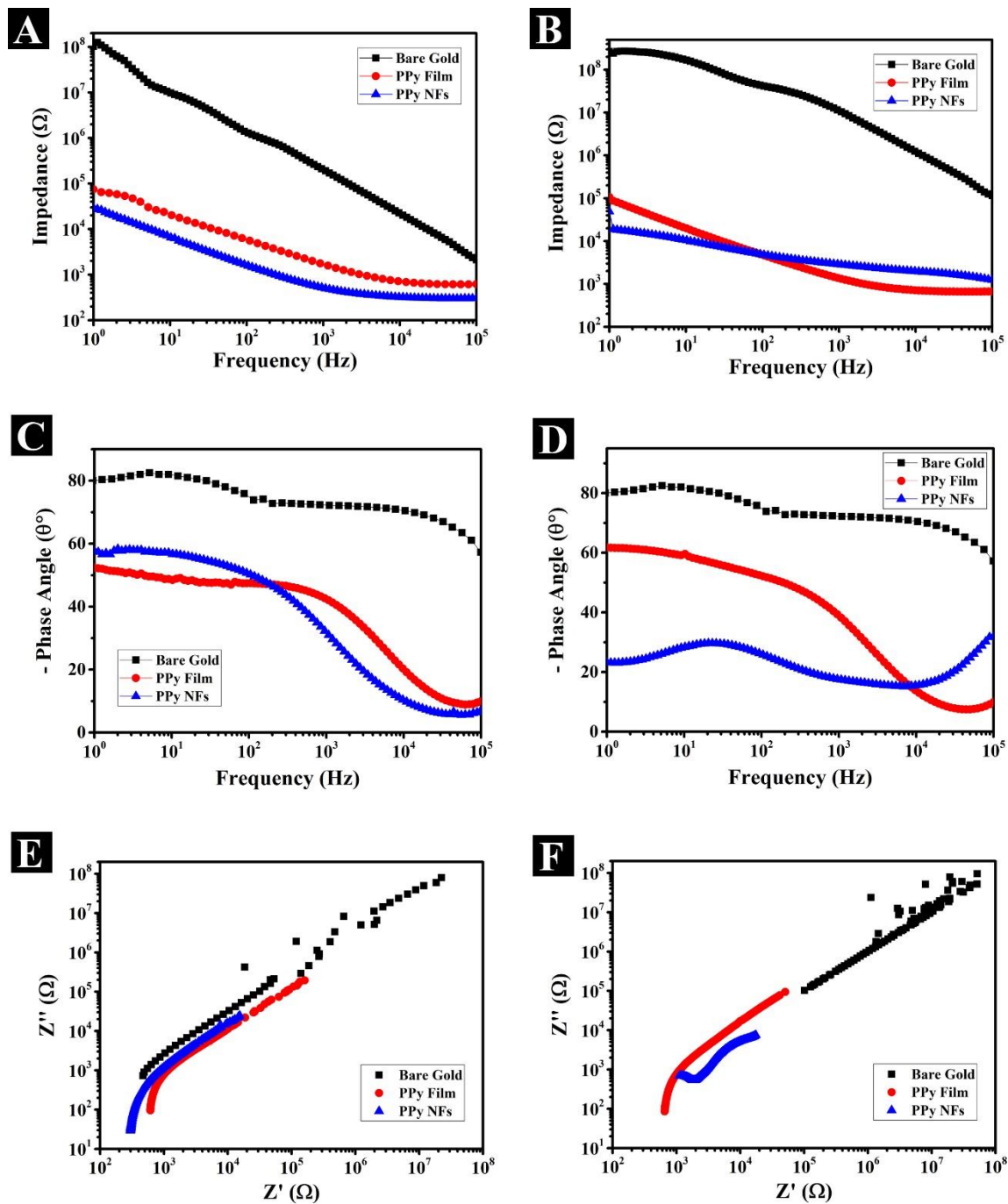


Figure VII.6. Electrochemical impedance, phase angle, and Nyquist (Z' - Z'') plots of the probes with two (A,C,E) and three (B,D,F) projections before (black squares) and after coating with PPy film (red circle) and PPy NFs (blue triangle).

Actuation performance of the probe devices

The actuation performance of the probe projections coated with PPy NFS were investigated in aCSF electrolyte under cyclic voltammetry (CV). The CV response of the probes with two and three projections at various scan rates of 50, 100, 200, and 1200 mV/s and within the potential range of -0.8 to +0.4 V are presented in Figure VII.7. According to the CV curves, the PPy NFs are reduced by applying negative potentials (from 0 V to -0.8 V), then by reversing the potential direction towards positive values they are oxidized. As observed in Figure VII.7, the probes with 1 mm projection sites induced higher currents than the probes with 0.5 mm projections. This is presumably due to larger total area of the probes with two projections than that of probes with three projections.

The reduction/oxidation reactions occurring during CV induce volume changes (swelling/shrinking) in the PPy NFs layer, which is responsible for bending movement of the probe projections (Figure VII.8). As the PPy NFs are reduced, the solvated cations are inserted into the PPy matrix doped with large PSS counterions, so the PPy NFs expand. Subsequently, as the PPy NFs are oxidized, the solvated cations leave the PPy matrix, therefore, the PPy NFs shrink. This microactuation of the PPy NFs is manifested in macroscale motion of the projection sites. As illustrated in Figure VII.8, the PPy coated projections bend outward under the reduction process (PPy NFs expansion), and then they become straight and return to their initial position (in the probe plane) upon subsequent oxidation process.

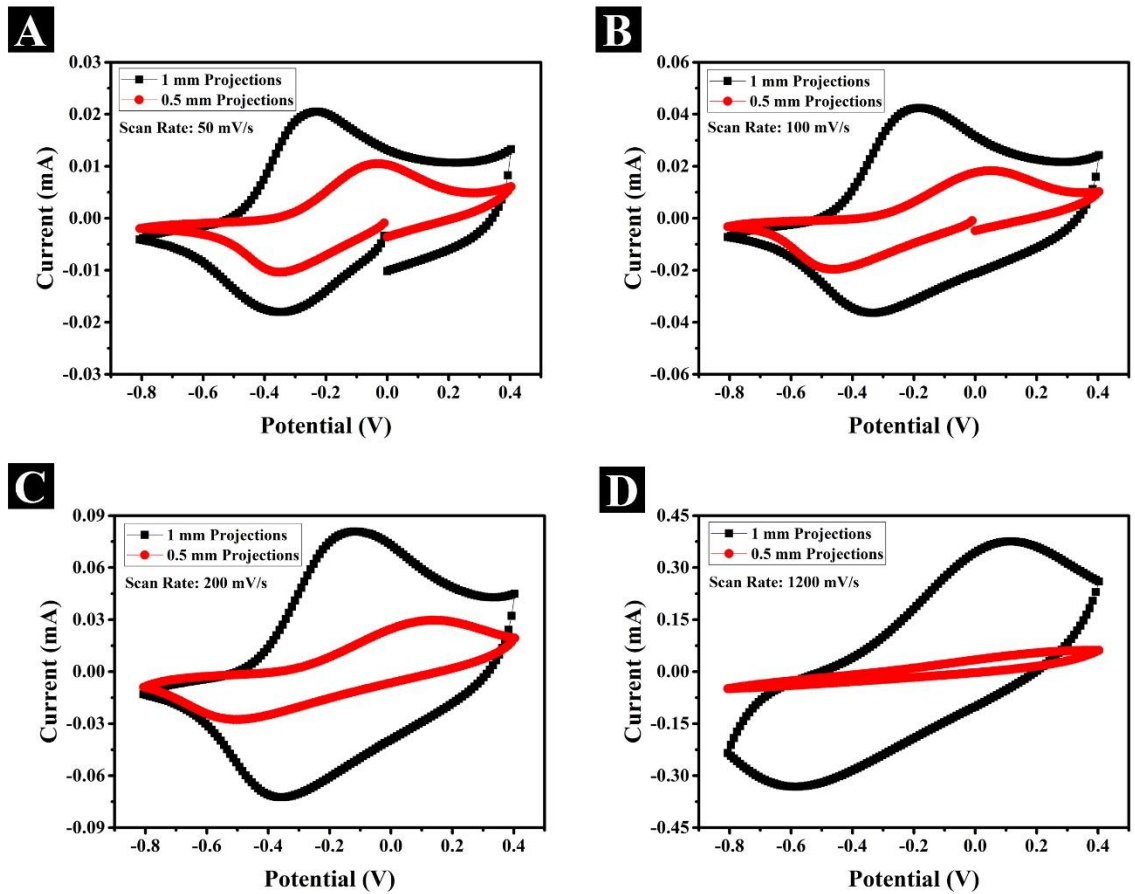


Figure VII.7. CV of the probe projections coated with PPy NFs at various scan rates. The black curves corresponding to the probes with two 1 mm projections and the red curves are attributed to the probes with three 0.5 mm projections.



Figure VII.8. Bending movement of the probe projections under cyclic voltammetry in aCSF electrolyte.

The charge storage density of the PPy-coated projections sites under electrical stimulation in aCSF electrolyte at various CV scan rates are presented in Figure VII.9(A). As seen in this figure, the charge storage density of the projection sites was slightly decreased with increasing the scan rate from 50 mV/s to 200 mV/s. However, the charge storage density significantly decreased as the scan rate increased to 1200 mV/s. The mixed ionic and electronic conductivity of conjugated polymers is responsible for their scan rate-dependent actuation response. In fact, the ionic conductivity requires diffusion/transportation of ions, which is a time-dependent phenomenon. By elevating the CV scan rate, the transportation of ions is restricted, therefore, the ionic conductivity and the resultant charge storage density decrease. For probe projections with 1 mm length, the charge storage density of 448.9, 434, 432.8, and 313.4 mC/cm² were respectively obtained at 50, 100, 200, and 1200 mV/s. For probe projections with 0.5 mm length, the charge

storage density of 222, 208.1, 172.4, and 31.2 mC/cm² were obtained at the scan rates of 50, 100, 200, and 1200 mV/s, respectively.

The projections displacement in aCSF electrolyte under CV at various scan rates were measured and presented in Figure VII.9(B). As shown, the projection displacement slightly reduced by increasing the CV scan rate from 50 mV/s to 200 mV/s. However, the projections displacement considerably decreased by increasing the scan rate to 1200 mV/s. For 1 mm long projections, the maximum displacement of 267 μm, 252 μm, 248 μm, and 129 μm were respectively obtained at scan rates of 50 mV/s, 100 mV/s, 200 mV/s, and 1200 mV/s. For projections with 0.5 mm length, the maximum displacement of 87.5 μm, 80 μm, 79 μm, and 30 μm were obtained at the scan rates of 50 mV/s, 100 mV/s, 200 mV/s, and 1200 mV/s, and respectively. The reduction in the projections displacement is attributed to the limited ions transportation into/out of the PPy NFs at higher scan rates. These results are in accordance with the limited charge storage density of the PPy NFs as the scan rate elevates (Figure VII.9(A)).

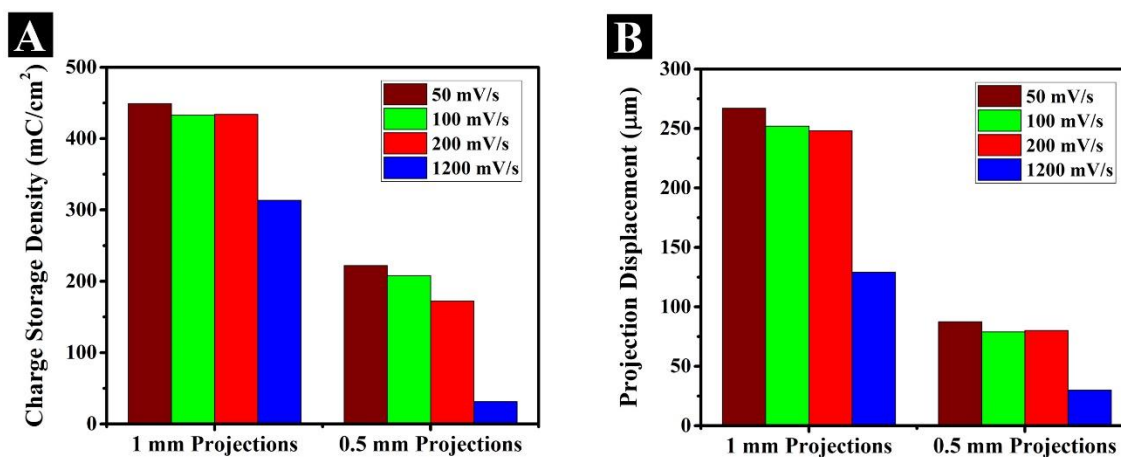


Figure VII.9. Charge storage density (A) and displacements (B) of actuating projection sites (1 mm and 0.5 mm projections) under various CV scan rates in aCSF. The data is obtained from a single probe actuated at various scan rates.

Long-term actuation of probe projections in aCSF electrolyte is restricted due to electrochemical induced precipitation of calcium phosphate (CaP) on the projections surface. As illustrated in Figure VII.10(A-B), the local precipitation of CaP on the projections blocks up the projection motion. The in-situ raised pH at the projection site (cathode) provides a local environment where calcium phosphate (CaP) becomes highly supersaturated [332]. Therefore, heterogeneous nucleation of CaP occurs at the projection surface (Figure VII.10(C)).

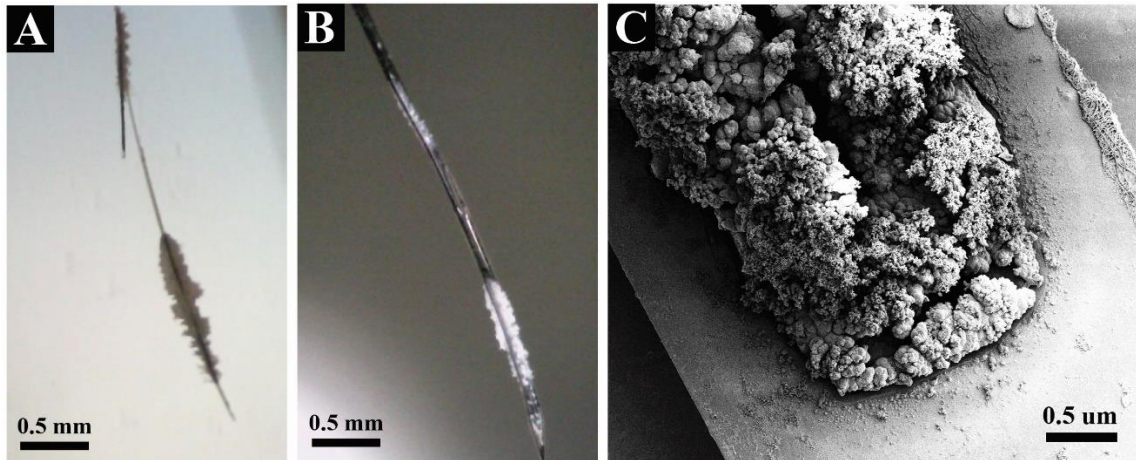


Figure VII.10. Electrochemical induced calcium phosphate (CaP) precipitation on the projection sites during CV actuation.

Conclusions

This study demonstrated utilization of conducting polymer nanofibers for articulating movable neural probes. Flexible SU-8 based microelectrodes with two and three projection sites were successfully fabricated using standard photolithography. To make movable probe devices, the projection sites were coated with PPy NFs with enhanced electrical properties than film counterparts. The electrode projections of 50 μm wide with varying length of 0.5 mm and 1 mm were able to deflect $\sim 87 \mu\text{m}$ and $\sim 267 \mu\text{m}$ away, respectively, in artificial cerebrospinal fluid (aCSF) under CV actuation. The long-term performance of the actuating projections in aCSF was restricted due to electrochemical induced precipitation of calcium phosphate on the on the projections surface. The results of this study may open a new window for development of flexible and movable neural probes.

VIII Conclusions and future directions

Conclusions

In summary, this research work utilized microactuation of CP nanofibers for development of high performance organic electronic bioactuators for articulating movable neural microelectrodes, soft robotics and bioinspired applications. The mass transport mechanism of the CP nanofibers was determined under cyclic voltammetry actuation. Construction of a bilayer beam actuator based on PPy NFs exhibited a high actuation performance, including low power consumption per strain percentage, a large deformation, fast response, and excellent actuation stability, with controllable dynamics. However, various types of chemically derived and functionalized CPs may be formulated to further enhance electro-chemical-mechanical properties of this actuator, exceeding the actuation performance. The experimental studies of motion and mass transport along with theoretical analysis of a body system with variable mass were utilized to establish the dynamics of the actuator and to introduce a modified form of Euler-Bernoulli's deflection equation for the PPy NFs actuator operate in liquid and gel-polymer electrolytes. It is anticipated that the CP nanofibers-based actuators will be utilized for advancement of next generation actuators in the fields of soft robotics, artificial muscles, and biomedical devices. Particularly, this work demonstrated that CP actuators may enable controlled movement of neural probes and electrode interfaces out-of-plane not possible before.

Future directions

Insertion and actuation of neural probes in brain phantom gel

In the present work, the actuation performance of the movable neural probes was assessed in artificial cerebrospinal fluid (aCSF) which is used in lab settings to match the electrolyte concentrations of CSF. For more realistic study of the probe's functionality, it is suggested to use a brain phantom gel which mimics the mechanical property of brain tissue. As described in [333, 334], 0.6 % agarose gel brain phantom is an appropriate choice for this purpose. Agarose gel allows ion transport, necessary for actuation of the PPy NFs, and its transparency permits visualization of the motion of the devices.

Neural probe insertion methods have a direct impact on the longevity of the device in the brain. Initial tissue and vascular damage caused by the probe insertion into the brain triggers a chronic tissue response that attenuates neural recordings and ultimately encapsulate the probes. One strategy to record from undamaged neural networks might be repositioning of the projection sites away from the probe after insertion, as demonstrated in Chapter VII. However, insertion forces required to penetrate the probes into brain tissue are affected by the elastic moduli of the tissue and the device and their interfacing geometry. Multiple studies have measured the force of neural probe penetration into brain tissue [335-337], and it has been shown that the force required for insertion increases linearly with insertion depth for a given tissue type and insertion method. The stiffness of the probe device must overcome these insertion forces to allow the device to reach the intended depth and avoid excessive buckling. Applications for neural electrodes are not standardized; therefore, the insertion method, the device stiffness and geometry should be

adjusted as needed. For the neural probe designs exhibited in this research work (Chapter VII), the ability to straighten the projections is essential to reach deep insertion targets. Accordingly, for insertion of the neural probes into the brain phantom it is suggested to utilize an electronic microdrive while simultaneously activating the projection actuators to remain flat during insertion. Other factors such as insertion speed and insertion method (manual vs. automated) can be investigated for their effects on tissue damage.

Neural probe projections with variable thickness ratio

The bending of probe projections can be varied by the thickness ratio of the active PPy layer and the substrate layer. Projections with a larger polymer to substrate thickness ratio resulted in smaller radii of curvature or larger bending deflections. The thickness of the active PPy layer can be controlled by the electrodeposition parameters such as current density and deposition time. Therefore, we can obtain a range of thickness ratio by changing these parameters. In this thesis, the thickness ratio for the probe projections (Chapter VII) was kept the same as the thickness ratio utilized for the PPy bioactuator presented in Chapter VI. However, to achieve a desired range of projections displacement, it is required to optimize this thickness ratio. Accordingly, it is suggested to investigate the effect of PPy electrodeposition parameters (current density and deposition time) on the bending actuation/displacement of the neural projections.

Alternate probe projection geometries

Multiple variations of neural probe projections can be designed. Two variations that would be useful to explore are the effect of the probe tip shape and the projection shape on

cutting forces during insertion into tissue. In addition, various projections shapes result in different 3D spatial distributions upon the projections bending out-of-plane.

Development of multifunctional neural probes devices

In this thesis, the utilization of CP nanofibers has been demonstrated for development of high performance bioactuators for movable neural probe application. However, the advantages of CP nanofibers have been previously shown for controlled drug delivery systems and biosensor applications [13, 101]. Accordingly, the presented movable neural probes in Chapter VII can be potentially upgraded into multifunctional neural probe devices. For instance, by incorporation of an anti-inflammatory drug into the CP nanofibers, we can create dual actuating-delivery neural probes that enable to release the anti-inflammatory drug into the surrounding tissue while actuating. Therefore, the reactive tissue response and encapsulation processes can be further avoided through drug incorporation. Similarly, dual actuating-sensing neural probes can be developed for detection of biomolecules while actuating the probe projections in brain tissue.

REFERENCES

1. A.S. Sarac, "*Nanofibers of conjugated polymers.*" 2017: CRC Press.
2. Z. Zhang, M. Liao, H. Lou, Y. Hu, X. Sun, and H. Peng, "*Conjugated polymers for flexible energy harvesting and storage.*" *Advanced Materials*, 2018. **30**(13): p. 1704261.
3. E. Smela, "*Conjugated polymer actuators for biomedical applications.*" *Advanced materials*, 2003. **15**(6): p. 481-494.
4. S. Inal, J. Rivnay, A.-O. Suii, G.G. Malliaras, and I. McCulloch, "*Conjugated polymers in bioelectronics.*" *Accounts of chemical research*, 2018. **51**(6): p. 1368-1376.
5. B. Guo and P.X. Ma, "*Conducting polymers for tissue engineering.*" *Biomacromolecules*, 2018. **19**(6): p. 1764-1782.
6. S.M. Won, E. Song, J. Zhao, J. Li, J. Rivnay, and J.A. Rogers, "*Recent advances in materials, devices, and systems for neural interfaces.*" *Advanced Materials*, 2018. **30**(30): p. 1800534.
7. S.M. Mirvakili and I.W. Hunter, "*Artificial muscles: Mechanisms, applications, and challenges.*" *Advanced Materials*, 2018. **30**(6): p. 1704407.
8. D. Svirskis, J. Travas-Sejdic, A. Rodgers, and S. Garg, "*Electrochemically controlled drug delivery based on intrinsically conducting polymers.*" *Journal of Controlled Release*, 2010. **146**(1): p. 6-15.

9. A. Sanati, M. Jalali, K. Raeissi, F. Karimzadeh, M. Kharaziha, S.S. Mahshid, and S. Mahshid, "A review on recent advancements in electrochemical biosensing using carbonaceous nanomaterials." *Microchimica Acta*, 2019. **186**(12): p. 1-22.
10. F.G. Zamani, H. Moulahoum, M. Ak, D.O. Demirkol, and S. Timur, "Current trends in the development of conducting polymers-based biosensors." *TrAC Trends in Analytical Chemistry*, 2019. **118**: p. 264-276.
11. N. Yi and M. Abidian, *Conducting polymers and their biomedical applications*, in *Biosynthetic polymers for medical applications*. 2016, Elsevier. p. 243-276.
12. D. Melling, J.G. Martinez, and E.W. Jager, "Conjugated polymer actuators and devices: progress and opportunities." *Advanced Materials*, 2019. **31**(22): p. 1808210.
13. M.R. Abidian, D.H. Kim, and D.C. Martin, "Conducting-polymer nanotubes for controlled drug release." *Advanced materials*, 2006. **18**(4): p. 405-409.
14. Y.-Z. Long, M.-M. Li, C. Gu, M. Wan, J.-L. Duvail, Z. Liu, and Z. Fan, "Recent advances in synthesis, physical properties and applications of conducting polymer nanotubes and nanofibers." *Progress in Polymer Science*, 2011. **36**(10): p. 1415-1442.
15. K.H. Hong and T.J. Kang, "Polyaniline–nylon 6 composite nanowires prepared by emulsion polymerization and electrospinning process." *Journal of applied polymer science*, 2006. **99**(3): p. 1277-1286.

16. S. Virji, J. Huang, R.B. Kaner, and B.H. Weiller, "*Polyaniline nanofiber gas sensors: examination of response mechanisms.*" *Nano letters*, 2004. **4**(3): p. 491-496.
17. A.N. Aleshin, "*Polymer nanofibers and nanotubes: Charge transport and device applications.*" *Advanced materials*, 2006. **18**(1): p. 17-27.
18. C.O. Baker, B. Shedd, P.C. Innis, P.G. Whitten, G.M. Spinks, G.G. Wallace, and R.B. Kaner, "*Monolithic actuators from flash-welded polyaniline nanofibers.*" *Advanced Materials*, 2008. **20**(1): p. 155-158.
19. K. Jackowska, A.T. Bieguński, and M. Tagowska, "*Hard template synthesis of conducting polymers: a route to achieve nanostructures.*" *Journal of Solid State Electrochemistry*, 2008. **12**(4): p. 437-443.
20. C. Martin, R. Parthasarathy, and V. Menon, "*Template synthesis of electronically conductive polymers—preparation of thin films.*" *Electrochimica acta*, 1994. **39**(8-9): p. 1309-1313.
21. V.P. Menon, J. Lei, and C.R. Martin, "*Investigation of molecular and supermolecular structure in template-synthesized polypyrrole tubules and fibrils.*" *Chemistry of materials*, 1996. **8**(9): p. 2382-2390.
22. M. Tagowska, B. Pałys, and K. Jackowska, "*Polyaniline nanotubules—anion effect on conformation and oxidation state of polyaniline studied by Raman spectroscopy.*" *Synthetic metals*, 2004. **142**(1-3): p. 223-229.

23. S. Yang, K. Chen, and Y. Yang, "*Synthesis of polyaniline nanotubes in the channels of anodic alumina membrane.*" *Nano-Architected and Nanostructured Materials*, 2004: p. 8.
24. Z. Cai and C.R. Martin, "*Electronically conductive polymer fibers with mesoscopic diameters show enhanced electronic conductivities.*" *Journal of the American Chemical Society*, 1989. **111**(11): p. 4138-4139.
25. M. Delvaux, J. Duchet, P.-Y. Stavaux, R. Legras, and S. Demoustier-Champagne, "*Chemical and electrochemical synthesis of polyaniline micro-and nano-tubules.*" *Synthetic Metals*, 2000. **113**(3): p. 275-280.
26. C.R. Martin, "*Template synthesis of electronically conductive polymer nanostructures.*" *Accounts of chemical research*, 1995. **28**(2): p. 61-68.
27. J. HakáOh, "*A facile synthesis of polypyrrole nanotubes using a template-mediated vapor deposition polymerization and the conversion to carbon nanotubes.*" *Chemical communications*, 2004(7): p. 882-883.
28. C.-G. Wu and T. Bein, "*Conducting polyaniline filaments in a mesoporous channel host.*" *Science*, 1994. **264**(5166): p. 1757-1759.
29. C.R. Martin, "*Nanomaterials: a membrane-based synthetic approach.*" *Science*, 1994. **266**(5193): p. 1961-1966.
30. J. Hulteen, "*A general template-based method for the preparation of nanomaterials.*" *Journal of Materials Chemistry*, 1997. **7**(7): p. 1075-1087.

31. Z. Zhang, J. Sui, L. Zhang, M. Wan, Y. Wei, and L. Yu, "*Synthesis of polyaniline with a hollow, octahedral morphology by using a cuprous oxide template.*" *Advanced Materials*, 2005. **17**(23): p. 2854-2857.
32. J. Jang, "*Conducting polymer nanomaterials and their applications.*" *Emissive materials nanomaterials*, 2006: p. 189-260.
33. F. Yin, D. Wang, Z. Zhang, C. Zhang, and Y. Zhang, "*Synthesis of mesoporous hollow polypyrrole spheres and the utilization as supports of high loading of Pt nanoparticles.*" *Materials Letters*, 2017. **207**: p. 225-229.
34. M. Wan, "*A template-free method towards conducting polymer nanostructures.*" *Advanced Materials*, 2008. **20**(15): p. 2926-2932.
35. S.J. Choi and S.M. Park, "*Electrochemical growth of nanosized conducting polymer wires on gold using molecular templates.*" *Advanced Materials*, 2000. **12**(20): p. 1547-1549.
36. P. Leclère, A. Calderone, D. Marsitzky, V. Francke, Y. Geerts, K. Müllen, J.-L. Brédas, and R. Lazzaroni, "*Highly Regular Organization of Conjugated Polymer Chains via Block Copolymer Self-Assembly.*" *Advanced materials*, 2000. **12**(14): p. 1042-1046.
37. P. Anilkumar and M. Jayakannan, "*Divergent nanostructures from identical ingredients: unique amphiphilic micelle template for polyaniline nanofibers, tubes, rods, and spheres.*" *Macromolecules*, 2008. **41**(20): p. 7706-7715.
38. R. Aeinehvand, P. Zahedi, S. Kashani-Rahimi, M. Fallah-Darrehchi, and M. Shamsi, "*Synthesis of poly (2-hydroxyethyl methacrylate)-based molecularly*

- imprinted polymer nanoparticles containing timolol maleate: morphological, thermal, and drug release along with cell biocompatibility studies.*" *Polymers for Advanced Technologies*, 2017. **28**(7): p. 828-841.
39. Y. Zhai, J.J. Whitten, P.B. Zetterlund, and A.M. Granville, "*Synthesis of hollow polydopamine nanoparticles using miniemulsion templating.*" *Polymer*, 2016. **105**: p. 276-283.
40. J.J. Langer, "*Polyaniline micro- and nanostructure.*" *Advanced Materials for Optics and Electronics*, 1999. **9**(1): p. 1-7.
41. J. Huang, S. Virji, B.H. Weiller, and R.B. Kaner, "*Polyaniline Nanofibers: Facile Synthesis and Chemical Sensors.*" *Journal of the American Chemical Society*, 2003. **125**(2): p. 314-315.
42. D.H. Reneker and I. Chun, "*Nanometre diameter fibres of polymer, produced by electrospinning.*" *Nanotechnology*, 1996. **7**(3): p. 216-223.
43. I.D. Norris, M.M. Shaker, F.K. Ko, and A.G. MacDiarmid, "*Electrostatic fabrication of ultrafine conducting fibers: polyaniline/polyethylene oxide blends.*" *Synthetic Metals*, 2000. **114**(2): p. 109-114.
44. P. Fattahi, G. Yang, G. Kim, and M.R. Abidian, "*A Review of Organic and Inorganic Biomaterials for Neural Interfaces.*" *Advanced Materials*, 2014. **26**(12): p. 1846-1885.
45. E. Marg and J.E. Adams, "*Indwelling multiple micro-electrodes in the brain.*" *Electroencephalography and Clinical Neurophysiology*, 1967. **23**(3): p. 277-280.

46. A.L. Benabid, S. Chabardes, J. Mitrofanis, and P. Pollak, "*Deep brain stimulation of the subthalamic nucleus for the treatment of Parkinson's disease.*" *The Lancet Neurology*, 2009. **8**(1): p. 67-81.
47. N.G. Hatsopoulos and J.P. Donoghue, "*The Science of Neural Interface Systems.*" *Annual Review of Neuroscience*, 2009. **32**(1): p. 249-266.
48. L.R. Hochberg, D. Bacher, B. Jarosiewicz, N.Y. Masse, J.D. Simeral, J. Vogel, S. Haddadin, J. Liu, S.S. Cash, P. van der Smagt, and J.P. Donoghue, "*Reach and grasp by people with tetraplegia using a neurally controlled robotic arm.*" *Nature*, 2012. **485**(7398): p. 372-375.
49. G. Buzsáki, "*Large-scale recording of neuronal ensembles.*" *Nature Neuroscience*, 2004. **7**(5): p. 446-451.
50. V.S. Polikov, P.A. Tresco, and W.M. Reichert, "*Response of brain tissue to chronically implanted neural electrodes.*" *Journal of neuroscience methods*, 2005. **148**(1): p. 1-18.
51. M.A.L. Nicolelis, D. Dimitrov, J.M. Carmena, R. Crist, G. Lehew, J.D. Kralik, and S.P. Wise, "*Chronic, multisite, multielectrode recordings in macaque monkeys.*" *Proceedings of the National Academy of Sciences*, 2003. **100**(19): p. 11041-11046.
52. K.D. Wise, "*Silicon microsystems for neuroscience and neural prostheses.*" *IEEE Engineering in Medicine and Biology Magazine*, 2005. **24**(5): p. 22-29.

53. P.J. Rousche and R.A. Normann, "*Chronic recording capability of the Utah Intracortical Electrode Array in cat sensory cortex.*" *Journal of Neuroscience Methods*, 1998. **82**(1): p. 1-15.
54. J.P. Seymour and D.R. Kipke, "*Neural probe design for reduced tissue encapsulation in CNS.*" *Biomaterials*, 2007. **28**(25): p. 3594-3607.
55. X. Cui, V.A. Lee, Y. Raphael, J.A. Wiler, J.F. Hetke, D.J. Anderson, and D.C. Martin, "*Surface modification of neural recording electrodes with conducting polymer/biomolecule blends.*" *Journal of Biomedical Materials Research*, 2001. **56**(2): p. 261-272.
56. X. Cui and D.C. Martin, "*Fuzzy gold electrodes for lowering impedance and improving adhesion with electrodeposited conducting polymer films.*" *Sensors and Actuators A: Physical*, 2003. **103**(3): p. 384-394.
57. M.R. Abidian, K.A. Ludwig, T.C. Marzullo, D.C. Martin, and D.R. Kipke, "*Interfacing Conducting Polymer Nanotubes with the Central Nervous System: Chronic Neural Recording using Poly(3,4-ethylenedioxythiophene) Nanotubes.*" *Advanced Materials*, 2009. **21**(37): p. 3764-3770.
58. M.R. Abidian, J.M. Corey, D.R. Kipke, and D.C. Martin, "*Conducting-Polymer Nanotubes Improve Electrical Properties, Mechanical Adhesion, Neural Attachment, and Neurite Outgrowth of Neural Electrodes.*" *Small*, 2010. **6**(3): p. 421-429.
59. M.R. Abidian and D.C. Martin, "*Multifunctional Nanobiomaterials for Neural Interfaces.*" *Advanced Functional Materials*, 2009. **19**(4): p. 573-585.

60. J.D.W. Madden, N.A. Vandesteeg, P.A. Anquetil, P.G.A. Madden, A. Takshi, R.Z. Pytel, S.R. Lafontaine, P.A. Wieringa, and I.W. Hunter, "*Artificial muscle technology: physical principles and naval prospects.*" IEEE Journal of Oceanic Engineering, 2004. **29**(3): p. 706-728.
61. S. Shabalovskaya, "*Physicochemical and biological aspects of Nitinol as a biomaterial.*" International materials reviews, 2001. **46**(5): p. 233-250.
62. Y. Bar-Cohen, "*Electroactive polymer (EAP) actuators as artificial muscles: reality, potential, and challenges.*" Vol. 136. 2004: SPIE press.
63. R. Shankar, T.K. Ghosh, and R.J. Spontak, "*Dielectric elastomers as next-generation polymeric actuators.*" Soft Matter, 2007. **3**(9): p. 1116-1129.
64. R.H. Baughman, C. Cui, A.A. Zakhidov, Z. Iqbal, J.N. Barisci, G.M. Spinks, G.G. Wallace, A. Mazzoldi, D. De Rossi, and A.G. Rinzler, "*Carbon nanotube actuators.*" Science, 1999. **284**(5418): p. 1340-1344.
65. G.G. Wallace, P.R. Teasdale, G.M. Spinks, and L.A. Kane-Maguire, "*Conductive electroactive polymers: intelligent materials systems.*" 2002: CRC press.
66. T. Otero, E. Angulo, J. Rodriguez, and C. Santamaria, "*Electrochemomechanical properties from a bilayer: polypyrrole/non-conducting and flexible material—artificial muscle.*" Journal of Electroanalytical Chemistry, 1992. **341**(1-2): p. 369-375.
67. E. Smela, M. Kallenbach, and J. Holdenried, "*Electrochemically driven polypyrrole bilayers for moving and positioning bulk micromachined silicon plates.*" Journal of microelectromechanical systems, 1999. **8**(4): p. 373-383.

68. E.W. Jager, E. Smela, and O. Inganäs, "*Microfabricating conjugated polymer actuators.*" *Science*, 2000. **290**(5496): p. 1540-1545.
69. T. Otero, J. Martinez, and J. Arias-Pardilla, "*Biomimetic electrochemistry from conducting polymers. A review: artificial muscles, smart membranes, smart drug delivery and computer/neuron interfaces.*" *Electrochimica Acta*, 2012. **84**: p. 112-128.
70. E. Smela, O. Inganäs, and I. Lundström, "*Controlled folding of micrometer-size structures.*" *Science*, 1995. **268**(5218): p. 1735-1738.
71. E.W. Jager, O. Inganäs, and I. Lundström, "*Microrobots for micrometer-size objects in aqueous media: potential tools for single-cell manipulation.*" *Science*, 2000. **288**(5475): p. 2335-2338.
72. I.S. Romero, N.P. Bradshaw, J.D. Larson, S.Y. Severt, S.J. Roberts, M.L. Schiller, J.M. Leger, and A.R. Murphy, "*Biocompatible Electromechanical Actuators Composed of Silk-Conducting Polymer Composites.*" *Advanced Functional Materials*, 2014. **24**(25): p. 3866-3873.
73. A. Mazzoldi and D. De Rossi. "*Conductive-polymer-based structures for a steerable catheter.*" in *Smart Structures and Materials 2000: Electroactive Polymer Actuators and Devices (EAPAD)*. 2000. International Society for Optics and Photonics.
74. W. Lu, E. Smela, P. Adams, G. Zuccarello, and B.R. Mattes, "*Development of solid-in-hollow electrochemical linear actuators using highly conductive polyaniline.*" *Chemistry of materials*, 2004. **16**(9): p. 1615-1621.

75. B.K. Gu, Y.A. Ismail, G.M. Spinks, S.I. Kim, I. So, and S.J. Kim, "*A linear actuation of polymeric nanofibrous bundle for artificial muscles.*" *Chemistry of materials*, 2009. **21**(3): p. 511-515.
76. Y.A. Ismail, S.R. Shin, K.M. Shin, S.G. Yoon, K. Shon, S.I. Kim, and S.J. Kim, "*Electrochemical actuation in chitosan/polyaniline microfibers for artificial muscles fabricated using an in situ polymerization.*" *Sensors and Actuators B: Chemical*, 2008. **129**(2): p. 834-840.
77. L. Wang, Y. Wu, T. Hu, B. Guo, and P.X. Ma, "*Electrospun conductive nanofibrous scaffolds for engineering cardiac tissue and 3D bioactuators.*" *Acta biomaterialia*, 2017. **59**: p. 68-81.
78. D.J. Irvin, S.H. Goods, and L.L. Whinnery, "*Direct measurement of extension and force in conductive polymer gel actuators.*" *Chemistry of materials*, 2001. **13**(4): p. 1143-1145.
79. Q. Pei and O. Inganäs, "*Electroelastomers: Conjugated poly (3-octylthiophene) gels with controlled crosslinking.*" *Synthetic metals*, 1993. **57**(1): p. 3724-3729.
80. G. Han and G. Shi, "*Conducting polymer electrochemical actuator made of high-strength three-layered composite films of polythiophene and polypyrrole.*" *Sensors and Actuators B: Chemical*, 2004. **99**(2-3): p. 525-531.
81. F. Wang, J.-H. Jeon, S. Park, C.-D. Kee, S.-J. Kim, and I.-K. Oh, "*A soft biomolecule actuator based on a highly functionalized bacterial cellulose nano-fiber network with carboxylic acid groups.*" *Soft Matter*, 2016. **12**(1): p. 246-254.

82. T.H. Kim, C.H. Kwon, C. Lee, J. An, T.T.T. Phuong, S.H. Park, M.D. Lima, R.H. Baughman, T.M. Kang, and S.J. Kim, "*Bio-inspired hybrid carbon nanotube muscles.*" *Scientific reports*, 2016. **6**(1): p. 1-8.
83. B.C. Thompson, S.E. Moulton, J. Ding, R. Richardson, A. Cameron, S. O'Leary, G.G. Wallace, and G.M. Clark, "*Optimising the incorporation and release of a neurotrophic factor using conducting polypyrrole.*" *Journal of Controlled Release*, 2006. **116**(3): p. 285-294.
84. R. Wadhwa, C.F. Lagenaur, and X.T. Cui, "*Electrochemically controlled release of dexamethasone from conducting polymer polypyrrole coated electrode.*" *Journal of controlled release*, 2006. **110**(3): p. 531-541.
85. H. Xu, C. Wang, C. Wang, J. Zoval, and M. Madou, "*Polymer actuator valves toward controlled drug delivery application.*" *Biosensors and Bioelectronics*, 2006. **21**(11): p. 2094-2099.
86. M. Sharma, G.I. Waterhouse, S.W. Loader, S. Garg, and D. Svirskis, "*High surface area polypyrrole scaffolds for tunable drug delivery.*" *International journal of pharmaceutics*, 2013. **443**(1-2): p. 163-168.
87. B. Yan, B. Li, F. Kunecke, Z. Gu, and L. Guo, "*Polypyrrole-based implantable electroactive pump for controlled drug microinjection.*" *ACS applied materials & interfaces*, 2015. **7**(27): p. 14563-14568.
88. D. Li and Y.N. Xia, "*Electrospinning of nanofibers: Reinventing the wheel?*" *Advanced Materials*, 2004. **16**(14): p. 1151-1170.

89. D.H. Reneker and A.L. Yarin, "*Electrospinning jets and polymer nanofibers.*" *Polymer*, 2008. **49**(10): p. 2387-2425.
90. W.G. Cui, X.H. Li, S.B. Zhou, and J. Weng, "*Investigation on process parameters of electrospinning system through orthogonal experimental design.*" *Journal of Applied Polymer Science*, 2007. **103**(5): p. 3105-3112.
91. R. Inai, M. Kotaki, and S. Ramakrishna, "*Structure and properties of electrospun PLLA single nanofibres.*" *Nanotechnology*, 2005. **16**(2): p. 208-213.
92. A. Camposeo, F. Di Benedetto, R. Stabile, A.A.R. Neves, R. Cingolani, and D. Pisignano, "*Laser Emission from Electrospun Polymer Nanofibers.*" *Small*, 2009. **5**(5): p. 562-566.
93. J. Miao, M. Miyauchi, T.J. Simmons, J.S. Dordick, and R.J. Linhardt, "*Electrospinning of nanomaterials and applications in electronic components and devices.*" *Journal of nanoscience and nanotechnology*, 2010. **10**(9): p. 5507-5519.
94. J.M. Moran-Mirabal, J.D. Slinker, J.A. DeFranco, S.S. Verbridge, R. Ilic, S. Flores-Torres, H. Abruña, G.G. Malliaras, and H. Craighead, "*Electrospun light-emitting nanofibers.*" *Nano letters*, 2007. **7**(2): p. 458-463.
95. N.M. Bedford, M.B. Dickerson, L.F. Drummy, H. Koerner, K.M. Singh, M.C. Vasudev, M.F. Durstock, R.R. Naik, and A.J. Steckl, "*Nanofiber-Based Bulk-Heterojunction Organic Solar Cells Using Coaxial Electrospinning.*" *Advanced Energy Materials*, 2012. **2**(9): p. 1136-1144.

96. N. Pinto, A. Johnson Jr, A. MacDiarmid, C. Mueller, N. Theofylaktos, D. Robinson, and F. Miranda, "*Electrospun polyaniline/polyethylene oxide nanofiber field-effect transistor.*" Applied physics letters, 2003. **83**(20): p. 4244-4246.
97. W.J. Li, C.T. Laurencin, E.J. Caterson, R.S. Tuan, and F.K. Ko, "*Electrospun nanofibrous structure: a novel scaffold for tissue engineering.*" Journal of Biomedical Materials Research, 2002. **60**(4): p. 613-621.
98. X. Wang, B. Ding, and B. Li, "*Biomimetic electrospun nanofibrous structures for tissue engineering.*" Materials today, 2013. **16**(6): p. 229-241.
99. M.R. Abidian, L.G. Salas, A. Yazdan-Shahmorad, T.C. Marzullo, D.C. Martin, and D.R. Kipke, "*In-vivo evaluation of chronically implanted neural microelectrode arrays modified with poly (3, 4-ethylenedioxythiophene) nanotubes.*" 3rd International IEEE/EMBS Conference on Neural Engineering, 2007: p. 61-64.
100. K.N. Layton and M.R. Abidian, "*Conducting polymer nanofiber-based biosensor for detection of neurochemicals.*" 5th International IEEE/EMBS Conference on Neural Engineering, 2011: p. 298-301.
101. G. Yang, K.L. Kampstra, and M.R. Abidian, "*High performance conducting polymer nanofiber biosensors for detection of biomolecules.*" Advanced Materials, 2014. **26**(29): p. 4954-4960.
102. P. Sofokleous, E. Stride, and M. Edirisinghe, "*Preparation, Characterization, and Release of Amoxicillin from Electrospun Fibrous Wound Dressing Patches.*" Pharmaceutical Research, 2013. **30**(7): p. 1926-1938.

103. B.-G. Kim, M.-S. Kim, and J. Kim, "*Ultrasonic-assisted nanodimensional self-assembly of poly-3-hexylthiophene for organic photovoltaic cells.*" ACS nano, 2010. **4**(4): p. 2160-2166.
104. S.W. Lee, H.J. Lee, J.H. Choi, W.G. Koh, J.M. Myoung, J.H. Hur, J.J. Park, J.H. Cho, and U. Jeong, "*Periodic Array of Polyelectrolyte-Gated Organic Transistors from Electrospun Poly(3-hexylthiophene) Nanofibers.*" Nano Letters, 2010. **10**(1): p. 347-351.
105. N.J. Pinto, A.T.J. Jr., A.G. MacDiarmid, C.H. Mueller, N. Theofylaktos, D.C. Robinson, and F.A. Miranda, "*Electrospun polyaniline/polyethylene oxide nanofiber field-effect transistor.*" Applied Physics Letters, 2003. **83**(20): p. 4244-4246.
106. S. Agarwal, A. Greiner, and J.H. Wendorff, "*Functional materials by electrospinning of polymers.*" Progress in Polymer Science, 2013. **38**(6): p. 963-991.
107. J. Xue, J. Xie, W. Liu, and Y. Xia, "*Electrospun Nanofibers: New Concepts, Materials, and Applications.*" Accounts of Chemical Research, 2017. **50**(8): p. 1976-1987.
108. M.R. Abidian, D.H. Kim, and D.C. Martin, "*Conducting-Polymer Nanotubes for Controlled Drug Release.*" Adv Mater, 2006. **18**(4): p. 405-409.
109. A.K. Blakney, F.I. Simonovsky, I.T. Suydam, B.D. Ratner, and K.A. Woodrow, "*Rapidly Biodegrading PLGA-Polyurethane Fibers for Sustained Release of*

- Physicochemically Diverse Drugs.*" ACS biomaterials science & engineering, 2016. **2**(9): p. 1595-1607.
110. M. Antensteiner, M. Khorrami, F. Fallahianbijan, A. Borhan, and M.R. Abidian, "*Conducting polymer microcups for organic bioelectronics and drug delivery applications.*" Advanced Materials, 2017. **29**(39): p. 1702576.
111. S.S. Kim, M.S. Park, O. Jeon, C.Y. Choi, and B.S. Kim, "*Poly(lactide-co-glycolide)/hydroxyapatite composite scaffolds for bone tissue engineering.*" Biomaterials, 2006. **27**(8): p. 1399-1409.
112. J.M. Anderson and M.S. Shive, "*Biodegradation and biocompatibility of PLA and PLGA microspheres.*" Advanced Drug Delivery Reviews, 1997. **28**(1): p. 5-24.
113. H.K. Makadia and S.J. Siegel, "*Poly Lactic-co-Glycolic Acid (PLGA) as Biodegradable Controlled Drug Delivery Carrier.*" Polymers, 2011. **3**(3): p. 1377-1397.
114. A.C.R. Grayson, I.S. Choi, B.M. Tyler, P.P. Wang, H. Brem, M.J. Cima, and R. Langer, "*Multi-pulse drug delivery from a resorbable polymeric microchip device.*" Nature Materials, 2003. **2**(11): p. 767-772.
115. R.A. Jain, "*The manufacturing techniques of various drug loaded biodegradable poly(lactide-co-glycolide) (PLGA) devices.*" Biomaterials, 2000. **21**(23): p. 2475-2490.
116. D.H. Reneker, A.L. Yarin, H. Fong, and S. Koombhongse, "*Bending instability of electrically charged liquid jets of polymer solutions in electrospinning.*" Journal of Applied Physics, 2000. **87**(9): p. 4531-4547.

117. Z.X. Meng, Y.S. Wang, C. Ma, W. Zheng, L. Li, and Y.F. Zheng, "*Electrospinning of PLGA/gelatin randomly-oriented and aligned nanofibers as potential scaffold in tissue engineering.*" *Materials Science & Engineering C- Materials for Biological Applications*, 2010. **30**(8): p. 1204-1210.
118. J. Doshi and D.H. Reneker, "*Electrospinning Process and Applications of Electrospun Fibers.*" *Journal of Electrostatics*, 1995. **35**(2-3): p. 151-160.
119. A. Theron, E. Zussman, and A.L. Yarin, "*Electrostatic field-assisted alignment of electrospun nanofibres.*" *Nanotechnology*, 2001. **12**(3): p. 384-390.
120. D. Li, Y.L. Wang, and Y.N. Xia, "*Electrospinning of polymeric and ceramic nanofibers as uniaxially aligned arrays.*" *Nano Letters*, 2003. **3**(8): p. 1167-1171.
121. S.W. Lee, H.J. Lee, J.H. Choi, W.G. Koh, J.M. Myoung, J.H. Hur, J.J. Park, J.H. Cho, and U. Jeong, "*Periodic array of polyelectrolyte-gated organic transistors from electrospun poly (3-hexylthiophene) nanofibers.*" *Nano letters*, 2009. **10**(1): p. 347-351.
122. S. Sundarrajan, R. Murugan, A.S. Nair, and S. Ramakrishna, "*Fabrication of P3HT/PCBM solar cloth by electrospinning technique.*" *Materials Letters*, 2010. **64**(21): p. 2369-2372.
123. V. Beachley and X. Wen, "*Effect of electrospinning parameters on the nanofiber diameter and length.*" *Materials science & engineering. C, Materials for biological applications*, 2009. **29**(3): p. 663-668.
124. N. Bhardwaj and S.C. Kundu, "*Electrospinning: A fascinating fiber fabrication technique.*" *Biotechnology Advances*, 2010. **28**(3): p. 325-347.

125. T. Subbiah, G.S. Bhat, R.W. Tock, S. Pararneswaran, and S.S. Ramkumar, "*Electrospinning of nanofibers.*" *Journal of Applied Polymer Science*, 2005. **96**(2): p. 557-569.
126. P. Fattahi, A. Borhan, and M.R. Abidian, "*Microencapsulation of Chemotherapeutics into Monodisperse and Tunable Biodegradable Polymers via Electrified Liquid Jets: Control of Size, Shape, and Drug Release.*" *Advanced Materials*, 2013. **25**(33): p. 4555-4560.
127. P. Fattahi, A. Borhan, and M.R. Abidian, "*Characterization of the size, shape, and drug encapsulation efficiency of PLGA microcapsules produced via electrojetting for drug delivery to brain tumors.*" 6th International IEEE/EMBS Conference on Neural Engineering, 2013: p. 953-956.
128. H.J. Zhou, T.B. Green, and Y.L. Joo, "*The thermal effects on electrospinning of polylactic acid melts.*" *Polymer*, 2006. **47**(21): p. 7497-7505.
129. L. Zhao, C.G. He, Y.J. Gao, L. Cen, L. Cui, and Y.L. Cao, "*Preparation and cytocompatibility of PLGA scaffolds with controllable fiber morphology and diameter using electrospinning method.*" *Journal of Biomedical Materials Research Part B-Applied Biomaterials*, 2008. **87B**(1): p. 26-34.
130. D.S. Katti, K.W. Robinson, F.K. Ko, and C.T. Laurencin, "*Bioresorbable nanofiber-based systems for wound healing and drug delivery: Optimization of fabrication parameters.*" *Journal of Biomedical Materials Research Part B-Applied Biomaterials*, 2004. **70B**(2): p. 286-296.

131. A.M. Gañán-Calvo, J. Dávila, and A. Barrero, "*Current and droplet size in the electro spraying of liquids. Scaling laws.*" *Journal of Aerosol Science*, 1997. **28**(2): p. 249-275.
132. S. Tungprapa, I. Jangchud, and P. Supaphol, "*Release characteristics of four model drugs from drug-loaded electrospun cellulose acetate fiber mats.*" *Polymer*, 2007. **48**(17): p. 5030-5041.
133. Z.-G. Wang, L.-S. Wan, Z.-M. Liu, X.-J. Huang, and Z.-K. Xu, "*Enzyme immobilization on electrospun polymer nanofibers: An overview.*" *Journal of Molecular Catalysis B: Enzymatic*, 2009. **56**(4): p. 189-195.
134. J.I. Kim, T.I. Hwang, L.E. Aguilar, C.H. Park, and C.S. Kim, "*A Controlled Design of Aligned and Random Nanofibers for 3D Bi-functionalized Nerve Conduits Fabricated via a Novel Electrospinning Set-up.*" *Scientific Reports*, 2016. **6**: p. 23761.
135. J.M. Corey, D.Y. Lin, K.B. Mycek, Q. Chen, S. Samuel, E.L. Feldman, and D.C. Martin, "*Aligned electrospun nanofibers specify the direction of dorsal root ganglia neurite growth.*" *Journal of Biomedical Materials Research Part A*, 2007. **83A**(3): p. 636-645.
136. Y. You, S.J. Lee, B.M. Min, and W.H. Park, "*Effect of solution properties on nanofibrous structure of electrospun poly(lactic-co-glycolic acid).*" *Journal of Applied Polymer Science*, 2006. **99**(3): p. 1214-1221.

137. S.-Y. Gu and J. Ren, "*Process Optimization and Empirical Modeling for Electrospun Poly(D,L-lactide) Fibers using Response Surface Methodology.*" *Macromolecular Materials and Engineering*, 2005. **290**(11): p. 1097-1105.
138. S.V. Fridrikh, J.H. Yu, M.P. Brenner, and G.C. Rutledge, "*Controlling the fiber diameter during electrospinning.*" *Physical Review Letters*, 2003. **90**(14).
139. S. Takeuchi, P. Garstecki, D.B. Weibel, and G.M. Whitesides, "*An axisymmetric flow-focusing microfluidic device.*" *Advanced Materials*, 2005. **17**(8): p. 1067-+.
140. P. Fattahi, A. Borhan, and M.R. Abidian, "*Microencapsulation of chemotherapeutics into monodisperse and tunable biodegradable polymers via electrified liquid jets: control of size, shape, and drug release.*" *Adv Mater*, 2013. **25**(33): p. 4555-60.
141. J. Zhang, Y. Liu, R. Luo, S. Chen, X. Li, S. Yuan, J. Wang, and N. Huang, "*In vitro hemocompatibility and cytocompatibility of dexamethasone-eluting PLGA stent coatings.*" *Applied Surface Science*, 2015. **328**: p. 154-162.
142. C. D'Avila Carvalho Erbetta, "*Synthesis and Characterization of Poly(D,L-Lactide-co-Glycolide) Copolymer.*" *Journal of Biomaterials and Nanobiotechnology*, 2012. **03**(02): p. 208-225.
143. M. Portaccio, C. Menale, N. Diano, C. Serri, D.G. Mita, and M. Lepore, "*Monitoring production process of cisplatin-loaded PLGA nanoparticles by FT-IR microspectroscopy and univariate data analysis.*" *Journal of Applied Polymer Science*, 2015. **132**(3): p. n/a-n/a.

144. M. Norouzi, M. Soleimani, I. Shabani, F. Atyabi, H.H. Ahvaz, and A. Rashidi, "*Protein encapsulated in electrospun nanofibrous scaffolds for tissue engineering applications.*" *Polymer International*, 2013. **62**(8): p. 1250-1256.
145. M. Gazzano, C. Gualandi, A. Zucchelli, T. Sui, A. Korsunsky, C. Reinhard, and M. Focarete, "*Structure-morphology correlation in electrospun fibers of semicrystalline polymers by simultaneous synchrotron SAXS-WAXD.*" *Polymer*, 2015. **63**: p. 154-163.
146. A. Baji, Y.-W. Mai, S.-C. Wong, M. Abtahi, and P. Chen, "*Electrospinning of polymer nanofibers: effects on oriented morphology, structures and tensile properties.*" *Composites science and technology*, 2010. **70**(5): p. 703-718.
147. N. Butoescu, O. Jordan, P. Burdet, P. Stadelmann, A. Petri-Fink, H. Hofmann, and E. Doelker, "*Dexamethasone-containing biodegradable superparamagnetic microparticles for intra-articular administration: Physicochemical and magnetic properties, in vitro and in vivo drug release.*" *European Journal of Pharmaceutics and Biopharmaceutics*, 2009. **72**(3): p. 529-538.
148. A. Göpferich, "*Mechanisms of polymer degradation and erosion.*" *Biomaterials*, 1996. **17**(2): p. 103-114.
149. L. Smith and P. Ma, "*Nano-fibrous scaffolds for tissue engineering.*" *Colloids and surfaces B: biointerfaces*, 2004. **39**(3): p. 125-131.
150. I. Jun, H.-S. Han, J.R. Edwards, and H. Jeon, "*Electrospun fibrous scaffolds for tissue engineering: Viewpoints on architecture and fabrication.*" *International journal of molecular sciences*, 2018. **19**(3): p. 745.

151. M. Eslamian, M. Khorrami, N. Yi, S. Majd, and M.R. Abidian, "*Electrospinning of highly aligned fibers for drug delivery applications.*" *Journal of Materials Chemistry B*, 2019. **7**(2): p. 224-232.
152. R.L. Dahlin, F.K. Kasper, and A.G. Mikos, "*Polymeric nanofibers in tissue engineering.*" *Tissue Engineering Part B: Reviews*, 2011. **17**(5): p. 349-364.
153. S. Nemati, S.-j. Kim, Y.M. Shin, and H. Shin, "*Current progress in application of polymeric nanofibers to tissue engineering.*" *Nano convergence*, 2019. **6**(1): p. 1-16.
154. R. Sahay, P.S. Kumar, R. Sridhar, J. Sundaramurthy, J. Venugopal, S.G. Mhaisalkar, and S. Ramakrishna, "*Electrospun composite nanofibers and their multifaceted applications.*" *Journal of Materials Chemistry*, 2012. **22**(26): p. 12953-12971.
155. B. Li, F. Xiong, B. Yao, Q. Du, J. Cao, J. Qu, W. Feng, and H. Yuan, "*Preparation and characterization of antibacterial dopamine-functionalized reduced graphene oxide/PLLA composite nanofibers.*" *RSC Advances*, 2020. **10**(32): p. 18614-18623.
156. A.I. Rezk, H.M. Mousa, J. Lee, C.H. Park, and C.S. Kim, "*Composite PCL/HA/simvastatin electrospun nanofiber coating on biodegradable Mg alloy for orthopedic implant application.*" *Journal of Coatings Technology and Research*, 2019. **16**(2): p. 477-489.
157. D. Li, Y. Wang, and Y. Xia, "*Electrospinning of polymeric and ceramic nanofibers as uniaxially aligned arrays.*" *Nano letters*, 2003. **3**(8): p. 1167-1171.

158. W. Sigmund, J. Yuh, H. Park, V. Maneeratana, G. Pyrgiotakis, A. Daga, J. Taylor, and J.C. Nino, "*Processing and structure relationships in electrospinning of ceramic fiber systems.*" *Journal of the American Ceramic Society*, 2006. **89**(2): p. 395-407.
159. Y. Dai, W. Liu, E. Formo, Y. Sun, and Y. Xia, "*Ceramic nanofibers fabricated by electrospinning and their applications in catalysis, environmental science, and energy technology.*" *Polymers for Advanced Technologies*, 2011. **22**(3): p. 326-338.
160. M. Maleki, M. Latifi, M. Amani-Tehran, and S. Mathur, "*Electrospun core-shell nanofibers for drug encapsulation and sustained release.*" *Polymer Engineering & Science*, 2013. **53**(8): p. 1770-1779.
161. H. Jiang, L. Wang, and K. Zhu, "*Coaxial electrospinning for encapsulation and controlled release of fragile water-soluble bioactive agents.*" *J Control Release*, 2014. **193**: p. 296-303.
162. M. Rubert, J. Dehli, Y.-F. Li, M.B. Taskin, R. Xu, F. Besenbacher, and M. Chen, "*Electrospun PCL/PEO coaxial fibers for basic fibroblast growth factor delivery.*" *Journal of Materials Chemistry B*, 2014. **2**(48): p. 8538-8546.
163. A. Saraf, L.S. Baggett, R.M. Raphael, F.K. Kasper, and A.G. Mikos, "*Regulated non-viral gene delivery from coaxial electrospun fiber mesh scaffolds.*" *Journal of Controlled Release*, 2010. **143**(1): p. 95-103.

164. A. Townsend-Nicholson and S.N. Jayasinghe, "*Cell electrospinning: a unique biotechnique for encapsulating living organisms for generating active biological microthreads/scaffolds.*" *Biomacromolecules*, 2006. **7**(12): p. 3364-3369.
165. Y. Lu, J. Huang, G. Yu, R. Cardenas, S. Wei, E.K. Wujcik, and Z. Guo, "*Coaxial electrospun fibers: applications in drug delivery and tissue engineering.*" *Wiley Interdisciplinary Reviews: Nanomedicine and Nanobiotechnology*, 2016. **8**(5): p. 654-677.
166. N.K. Mohtaram, A. Montgomery, and S.M. Willerth, "*Biomaterial-based drug delivery systems for the controlled release of neurotrophic factors.*" *Biomed Mater*, 2013. **8**(2): p. 022001.
167. J.J. Liu, C.Y. Wang, J.G. Wang, H.J. Ruan, and C.Y. Fan, "*Peripheral nerve regeneration using composite poly(lactic acid-caprolactone)/nerve growth factor conduits prepared by coaxial electrospinning.*" *J Biomed Mater Res A*, 2011. **96**(1): p. 13-20.
168. C.-Y. Wang, K.-H. Zhang, C.-Y. Fan, X.-M. Mo, H.-J. Ruan, and F.-F. Li, "*Aligned natural–synthetic polyblend nanofibers for peripheral nerve regeneration.*" *Acta Biomaterialia*, 2011. **7**(2): p. 634-643.
169. C.-Y. Wang, J.-J. Liu, C.-Y. Fan, X.-M. Mo, H.-J. Ruan, and F.-F. Li, "*The effect of aligned core–shell nanofibres delivering NGF on the promotion of sciatic nerve regeneration.*" *Journal of Biomaterials Science, Polymer Edition*, 2012. **23**(1-4): p. 167-184.

170. H. Kerkhoff and F. Jennekens, "*Peripheral nerve lesions: the neuropharmacological outlook.*" *Clinical neurology and neurosurgery*, 1993. **95**: p. 103-108.
171. K. Shimoke and H. Chiba, "*Nerve growth factor prevents 1-methyl-4-phenyl-1, 2, 3, 6-tetrahydropyridine-induced cell death via the Akt pathway by suppressing caspase-3-like activity using PC12 cells: Relevance to therapeutical application for parkinson's disease.*" *Journal of neuroscience research*, 2001. **63**(5): p. 402-409.
172. S. Yan, L. Xiaoqiang, T. Lianjiang, H. Chen, and M. Xiumei, "*Poly (l-lactide-co- ϵ -caprolactone) electrospun nanofibers for encapsulating and sustained releasing proteins.*" *Polymer*, 2009. **50**(17): p. 4212-4219.
173. L. Tian, M.P. Prabhakaran, J. Hu, M. Chen, F. Besenbacher, and S. Ramakrishna, "*Coaxial electrospun poly(lactic acid)/silk fibroin nanofibers incorporated with nerve growth factor support the differentiation of neuronal stem cells.*" *RSC Advances*, 2015. **5**(62): p. 49838-49848.
174. E. Kijeńska-Gawrońska, T. Bolek, M. Bil, and W. Swieszkowski, "*Alignment and bioactive molecule enrichment of bio-composite scaffolds towards peripheral nerve tissue engineering.*" *Journal of Materials Chemistry B*, 2019. **7**(29): p. 4509-4519.
175. H. Zhou, Z. Shi, X. Wan, H. Fang, D.-G. Yu, X. Chen, and P. Liu, "*The relationships between process parameters and polymeric nanofibers fabricated using a modified coaxial electrospinning.*" *Nanomaterials*, 2019. **9**(6): p. 843.

176. S. Yu and N.V. Myung, "*Minimizing the diameter of electrospun polyacrylonitrile (PAN) nanofibers by design of experiments for electrochemical application.*" *Electroanalysis*, 2018. **30**(10): p. 2330-2338.
177. M. Wang, J.H. Yu, D.L. Kaplan, and G.C. Rutledge, "*Production of submicron diameter silk fibers under benign processing conditions by two-fluid electrospinning.*" *Macromolecules*, 2006. **39**(3): p. 1102-1107.
178. A. Moghe and B. Gupta, "*Co-axial electrospinning for nanofiber structures: preparation and applications.*" *Polymer Reviews*, 2008. **48**(2): p. 353-377.
179. Y. Zhang, X. Wang, Y. Feng, J. Li, C. Lim, and S. Ramakrishna, "*Coaxial electrospinning of (fluorescein isothiocyanate-conjugated bovine serum albumin)-encapsulated poly (ϵ -caprolactone) nanofibers for sustained release.*" *Biomacromolecules*, 2006. **7**(4): p. 1049-1057.
180. C. Wang, K.-W. Yan, Y.-D. Lin, and P.C.H. Hsieh, "*Biodegradable Core/Shell Fibers by Coaxial Electrospinning: Processing, Fiber Characterization, and Its Application in Sustained Drug Release.*" *Macromolecules*, 2010. **43**(15): p. 6389-6397.
181. S.A. Weissman and N.G. Anderson, "*Design of experiments (DoE) and process optimization. A review of recent publications.*" *Organic Process Research & Development*, 2015. **19**(11): p. 1605-1633.
182. T. Keskin Gundogdu, I. Deniz, G. Caliskan, E.S. Sahin, and N. Azbar, "*Experimental design methods for bioengineering applications.*" *Crit Rev Biotechnol*, 2016. **36**(2): p. 368-88.

183. M.I. Rodrigues and A.F. Iemma, "*Experimental design and process optimization.*" 2014: CRC Press.
184. Z. Sun, E. Zussman, A.L. Yarin, J.H. Wendorff, and A. Greiner, "*Compound Core–Shell Polymer Nanofibers by Co-Electrospinning.*" *Advanced Materials*, 2003. **15**(22): p. 1929-1932.
185. X. Xu, X. Zhuang, X. Chen, X. Wang, L. Yang, and X. Jing, "*Preparation of Core-Sheath Composite Nanofibers by Emulsion Electrospinning.*" *Macromolecular Rapid Communications*, 2006. **27**(19): p. 1637-1642.
186. S.K. Tiwari, R. Tzezana, E. Zussman, and S.S. Venkatraman, "*Optimizing partition-controlled drug release from electrospun core-shell fibers.*" *Int J Pharm*, 2010. **392**(1-2): p. 209-17.
187. T. Jiang, E.J. Carbone, K.W.H. Lo, and C.T. Laurencin, "*Electrospinning of polymer nanofibers for tissue regeneration.*" *Progress in Polymer Science*, 2015. **46**: p. 1-24.
188. S.L. Ferreira, R.E. Bruns, H.S. Ferreira, G.D. Matos, J.M. David, G.C. Brandao, E.G. da Silva, L.A. Portugal, P.S. dos Reis, A.S. Souza, and W.N. dos Santos, "*Box-Behnken design: an alternative for the optimization of analytical methods.*" *Anal Chim Acta*, 2007. **597**(2): p. 179-86.
189. X. Huang and C.S. Brazel, "*On the importance and mechanisms of burst release in matrix-controlled drug delivery systems.*" *Journal of Controlled Release*, 2001. **73**(2-3): p. 121–136.

190. A. Tzafriri, "Mathematical modeling of diffusion-mediated release from bulk degrading matrices." *Journal of controlled release*, 2000. **63**(1-2): p. 69-79.
191. M.M. Ba-Abbad, P.V. Chai, M.S. Takriff, A. Benamor, and A.W. Mohammad, "Optimization of nickel oxide nanoparticle synthesis through the sol–gel method using Box–Behnken design." *Materials & Design*, 2015. **86**: p. 948-956.
192. M.F. Elahi and W. Lu, "Core-shell Fibers for Biomedical Applications-A Review." *Journal of Bioengineering & Biomedical Science*, 2013. **03**(01).
193. Y. Hang, Y. Zhang, Y. Jin, H. Shao, and X. Hu, "Preparation of regenerated silk fibroin/silk sericin fibers by coaxial electrospinning." *International journal of biological macromolecules*, 2012. **51**(5): p. 980-986.
194. I.H. Pereira, E. Ayres, L. Averous, G. Schlatter, A. Hebraud, S.T.O. Mendes, and R.L. Oréface, "Elaboration and Characterization of Coaxial Electrospun Poly (ϵ -Caprolactone)/Gelatin Nanofibers for Biomedical Applications." *Advances in Polymer Technology*, 2014. **33**(S1).
195. Z.-C. Yao, J.-C. Wang, Z. Ahmad, J.-S. Li, and M.-W. Chang, "Fabrication of patterned three-dimensional micron scaled core-sheath architectures for drug patches." *Materials Science and Engineering: C*, 2019. **97**: p. 776-783.
196. G. Mathew, J. Hong, J. Rhee, D. Leo, and C. Nah, "Preparation and anisotropic mechanical behavior of highly-oriented electrospun poly (butylene terephthalate) fibers." *Journal of applied polymer science*, 2006. **101**(3): p. 2017-2021.
197. D. Sharma, D. Maheshwari, G. Philip, R. Rana, S. Bhatia, M. Singh, R. Gabrani, S.K. Sharma, J. Ali, R.K. Sharma, and S. Dang, "Formulation and optimization of

- polymeric nanoparticles for intranasal delivery of lorazepam using Box-Behnken design: in vitro and in vivo evaluation.*" Biomed Res Int, 2014. **2014**: p. 156010.
198. A. Alaoui, K. El Kacemi, K. El Ass, and S. Kitane, "*Application of Box-Behnken design to determine the optimal conditions of reductive leaching of MnO₂ from manganese mine tailings.*" Russian Journal of Non-Ferrous Metals, 2015. **56**(2): p. 134-141.
199. P.A. Netti, M. Biondi, and M. Frigione, "*Experimental Studies and Modeling of the Degradation Process of Poly (Lactic-co-Glycolic Acid) Microspheres for Sustained Protein Release.*" Polymers, 2020. **12**(9): p. 2042.
200. M.R. Prausnitz and R. Langer, "*Transdermal drug delivery.*" Nature biotechnology, 2008. **26**(11): p. 1261-1268.
201. S. Malvey, J.V. Rao, and K.M. Arumugam, "*Transdermal drug delivery system: A mini review.*" Pharma Innov. J, 2019. **8**: p. 181-197.
202. R. Sridhar, R. Lakshminarayanan, K. Madhaiyan, V.A. Barathi, K.H.C. Lim, and S. Ramakrishna, "*Electrosprayed nanoparticles and electrospun nanofibers based on natural materials: applications in tissue regeneration, drug delivery and pharmaceuticals.*" Chemical Society Reviews, 2015. **44**(3): p. 790-814.
203. M. Amjadi, B. Mostaghaci, and M. Sitti, "*Recent advances in skin penetration enhancers for transdermal gene and drug delivery.*" Current gene therapy, 2017. **17**(2): p. 139-146.

204. L. Naves, C. Dhand, L. Almeida, L. Rajamani, S. Ramakrishna, and G. Soares, "*Poly (lactic-co-glycolic) acid drug delivery systems through transdermal pathway: an overview.*" *Progress in biomaterials*, 2017. **6**(1-2): p. 1-11.
205. Y. Zhang, J. Yu, J. Wang, N.J. Hanne, Z. Cui, C. Qian, C. Wang, H. Xin, J.H. Cole, and C.M. Gallippi, "*Thrombin-responsive transcutaneous patch for auto-anticoagulant regulation.*" *Advanced materials*, 2017. **29**(4): p. 1604043.
206. J. Yu, Y. Zhang, Y. Ye, R. DiSanto, W. Sun, D. Ranson, F.S. Ligler, J.B. Buse, and Z. Gu, "*Microneedle-array patches loaded with hypoxia-sensitive vesicles provide fast glucose-responsive insulin delivery.*" *Proceedings of the National Academy of Sciences*, 2015. **112**(27): p. 8260-8265.
207. J. Di, S. Yao, Y. Ye, Z. Cui, J. Yu, T.K. Ghosh, Y. Zhu, and Z. Gu, "*Stretch-triggered drug delivery from wearable elastomer films containing therapeutic depots.*" *ACS nano*, 2015. **9**(9): p. 9407-9415.
208. A. Tamayol, A.H. Najafabadi, P. Mostafalu, A.K. Yetisen, M. Comotto, M. Aldhahri, M.S. Abdel-Wahab, Z.I. Najafabadi, S. Latifi, and M. Akbari, "*Biodegradable elastic nanofibrous platforms with integrated flexible heaters for on-demand drug delivery.*" *Scientific reports*, 2017. **7**(1): p. 1-10.
209. D. Son, J. Lee, S. Qiao, R. Ghaffari, J. Kim, J.E. Lee, C. Song, S.J. Kim, D.J. Lee, and S.W. Jun, "*Multifunctional wearable devices for diagnosis and therapy of movement disorders.*" *Nature nanotechnology*, 2014. **9**(5): p. 397.
210. H. Lee, T.K. Choi, Y.B. Lee, H.R. Cho, R. Ghaffari, L. Wang, H.J. Choi, T.D. Chung, N. Lu, and T. Hyeon, "*A graphene-based electrochemical device with*

- thermoreponsive microneedles for diabetes monitoring and therapy.*" *Nature nanotechnology*, 2016. **11**(6): p. 566-572.
211. Y. Deng, J. Chen, Y. Zhao, X. Yan, L. Zhang, K. Choy, J. Hu, H.J. Sant, B.K. Gale, and T. Tang, "*Transdermal delivery of siRNA through microneedle array.*" *Scientific reports*, 2016. **6**(1): p. 1-8.
212. M.N. Pastore and M.S. Roberts, *Selection of topically applied chemical candidates: transdermal drug delivery systems*, in *Skin Permeation and Disposition of Therapeutic and Cosmeceutical Compounds*. 2017, Springer. p. 251-262.
213. M. Amjadi, S. Sheykhansari, B.J. Nelson, and M. Sitti, "*Recent advances in wearable transdermal delivery systems.*" *Advanced Materials*, 2018. **30**(7): p. 1704530.
214. B. Azimi, H. Maleki, L. Zavagna, J.G. De la Ossa, S. Linari, A. Lazzeri, and S. Danti, "*Bio-based electrospun fibers for wound healing.*" *Journal of Functional Biomaterials*, 2020. **11**(3): p. 67.
215. S. Parham, A.Z. Kharazi, H.R. Bakhsheshi-Rad, H. Ghayour, A.F. Ismail, H. Nur, and F. Berto, "*Electrospun nano-fibers for biomedical and tissue engineering applications: A comprehensive review.*" *Materials*, 2020. **13**(9): p. 2153.
216. H.M. Ibrahim and A. Klingner, "*A review on electrospun polymeric nanofibers: Production parameters and potential applications.*" *Polymer Testing*, 2020: p. 106647.

217. V. Pillay, C. Dott, Y.E. Choonara, C. Tyagi, L. Tomar, P. Kumar, L.C. du Toit, and V.M. Ndesendo, "A review of the effect of processing variables on the fabrication of electrospun nanofibers for drug delivery applications." *Journal of Nanomaterials*, 2013. **2013**.
218. M. Rahmani, S. Arbabi Bidgoli, and S.M. Rezayat, "Electrospun polymeric nanofibers for transdermal drug delivery." *Nanomedicine Journal*, 2017. **4**(2): p. 61-70.
219. İ. Esentürk, M.S. Erdal, and S. Güngör, "Electrospinning method to produce drug-loaded nanofibers for topical/transdermal drug delivery applications." *İstanbul Üniversitesi Eczacılık Fakültesi Dergisi*, 2016. **46**(1): p. 49-69.
220. X. Shen, D. Yu, L. Zhu, C. Branford-White, K. White, and N.P. Chatterton, "Electrospun diclofenac sodium loaded Eudragit® L 100-55 nanofibers for colon-targeted drug delivery." *International journal of pharmaceutics*, 2011. **408**(1-2): p. 200-207.
221. K. Madhaiyan, R. Sridhar, S. Sundarrajan, J.R. Venugopal, and S. Ramakrishna, "Vitamin B12 loaded polycaprolactone nanofibers: A novel transdermal route for the water soluble energy supplement delivery." *International journal of pharmaceutics*, 2013. **444**(1-2): p. 70-76.
222. G. Singh, T. Kaur, R. Kaur, and A. Kaur, "Recent biomedical applications and patents on biodegradable polymer-PLGA." *Int J Pharmacol Pharm Sci*, 2014. **1**(2): p. 30-42.

223. G. Malliaras and M.R. Abidian, "*Organic bioelectronic materials and devices.*" Advanced materials (Deerfield Beach, Fla.), 2015. **27**(46): p. 7492.
224. S. Park, G. Yang, N. Madduri, M.R. Abidian, and S. Majd, "*Hydrogel-Mediated Direct Patterning of Conducting Polymer Films with Multiple Surface Chemistries.*" Advanced materials, 2014. **26**(18): p. 2782-2787.
225. L. Bay, T. Jacobsen, S. Skaarup, and K. West, "*Mechanism of actuation in conducting polymers: osmotic expansion.*" The Journal of Physical Chemistry B, 2001. **105**(36): p. 8492-8497.
226. E. Smela, "*Conjugated polymer actuators.*" MRS bulletin, 2008. **33**(3): p. 197-204.
227. C. Weidlich, K.-M. Mangold, and K. Jüttner, "*EQCM study of the ion exchange behaviour of polypyrrole with different counterions in different electrolytes.*" Electrochimica Acta, 2005. **50**(7-8): p. 1547-1552.
228. M. Antensteiner and M.R. Abidian. "*Tunable nanostructured conducting polymers for neural interface applications.*" in *2017 39th Annual International Conference of the IEEE Engineering in Medicine and Biology Society (EMBC)*. 2017. IEEE.
229. M.R. Abidian, L.G. Salas, A. Yazdan-Shahmorad, T.C. Marzullo, D.C. Martin, and D.R. Kipke. "*In-vivo Evaluation of Chronically Implanted Neural Microelectrode Arrays Modified with Poly (3,4-ethylenedioxythiophene) Nanotubes.*" in *2007 3rd International IEEE/EMBS Conference on Neural Engineering*. 2007.

230. R.M. Miriani, M.R. Abidian, and D.R. Kipke. "*Cytotoxic analysis of the conducting polymer PEDOT using myocytes.*" in *2008 30th Annual International Conference of the IEEE Engineering in Medicine and Biology Society*. 2008. IEEE.
231. K.A. Marx, "*Quartz crystal microbalance: a useful tool for studying thin polymer films and complex biomolecular systems at the solution– surface interface.*" *Biomacromolecules*, 2003. **4**(5): p. 1099-1120.
232. G. Sauerbrey, "*Verwendung von Schwingquarzen zur Wägung dünner Schichten und zur Mikrowägung.*" *Zeitschrift für physik*, 1959. **155**(2): p. 206-222.
233. S. Baek, R.A. Green, and L.A. Poole-Warren, "*Effects of dopants on the biomechanical properties of conducting polymer films on platinum electrodes.*" *Journal of Biomedical Materials Research Part A*, 2014. **102**(8): p. 2743-2754.
234. A. Gelmi, M.J. Higgins, and G.G. Wallace, "*Physical surface and electromechanical properties of doped polypyrrole biomaterials.*" *Biomaterials*, 2010. **31**(8): p. 1974-1983.
235. Y. Velmurugu and S. Skaarup, "*Ion and solvent transport in polypyrrole: experimental test of osmotic model.*" *Ionics*, 2005. **11**(5-6): p. 370-374.
236. C. Paulino, V. Kalienkova, A.K. Lam, Y. Neldner, and R. Dutzler, "*Activation mechanism of the calcium-activated chloride channel TMEM16A revealed by cryo-EM.*" *Nature*, 2017. **552**(7685): p. 421-425.

237. M. Shahinpoor, "*Conceptual design, kinematics and dynamics of swimming robotic structures using ionic polymeric gel muscles.*" *Smart Materials and Structures*, 1992. **1**(1): p. 91.
238. M. Shahinpoor, Y. Bar-Cohen, J. Simpson, and J. Smith, "*Ionic polymer-metal composites (IPMCs) as biomimetic sensors, actuators and artificial muscles-a review.*" *Smart materials and structures*, 1998. **7**(6): p. R15.
239. K.J. Kim and M. Shahinpoor, "*Ionic polymer-metal composites: II. Manufacturing techniques.*" *Smart materials and structures*, 2003. **12**(1): p. 65.
240. F. Carpi, R. Kornbluh, P. Sommer-Larsen, and G. Alici, "*Electroactive polymer actuators as artificial muscles: are they ready for bioinspired applications?*" *Bioinspiration & biomimetics*, 2011. **6**(4): p. 045006.
241. Y. Zhao, L. Song, Z. Zhang, and L. Qu, "*Stimulus-responsive graphene systems towards actuator applications.*" *Energy & Environmental Science*, 2013. **6**(12): p. 3520-3536.
242. F. Carpi and E. Smela, "*Biomedical applications of electroactive polymer actuators.*" 2009: John Wiley & Sons.
243. Y. Yan, T. Santaniello, L.G. Bettini, C. Minnai, A. Bellacicca, R. Porotti, I. Denti, G. Faraone, M. Merlini, and C. Lenardi, "*Electroactive ionic soft actuators with monolithically integrated gold nanocomposite electrodes.*" *Advanced Materials*, 2017. **29**(23): p. 1606109.

244. L. Lu, J. Liu, Y. Hu, Y. Zhang, and W. Chen, "*Graphene-stabilized silver nanoparticle electrochemical electrode for actuator design.*" *Advanced materials*, 2013. **25**(9): p. 1270-1274.
245. I. Takeuchi, K. Asaka, K. Kiyohara, T. Sugino, N. Terasawa, K. Mukai, T. Fukushima, and T. Aida, "*Electromechanical behavior of fully plastic actuators based on bucky gel containing various internal ionic liquids.*" *Electrochimica Acta*, 2009. **54**(6): p. 1762-1768.
246. J. Kim, J.-H. Jeon, H.-J. Kim, H. Lim, and I.-K. Oh, "*Durable and water-floatable ionic polymer actuator with hydrophobic and asymmetrically laser-scribed reduced graphene oxide paper electrodes.*" *Acs Nano*, 2014. **8**(3): p. 2986-2997.
247. C. Lu, Y. Yang, J. Wang, R. Fu, X. Zhao, L. Zhao, Y. Ming, Y. Hu, H. Lin, and X. Tao, "*High-performance graphdiyne-based electrochemical actuators.*" *Nature communications*, 2018. **9**(1): p. 1-11.
248. L. Kong and W. Chen, "*Carbon Nanotube and Graphene-based Bioinspired Electrochemical Actuators.*" *Advanced materials*, 2014. **26**(7): p. 1025-1043.
249. K. Kaneto, M. Kaneko, Y. Min, and A.G. MacDiarmid, " "*Artificial muscle*": *electromechanical actuators using polyaniline films.*" *Synthetic Metals*, 1995. **71**(1-3): p. 2211-2212.
250. J.M. Sansiñena, J. Gao, and H.L. Wang, "*High-Performance, Monolithic Polyaniline Electrochemical Actuators.*" *Advanced Functional Materials*, 2003. **13**(9): p. 703-709.

251. Y. Wu, G. Alici, G.M. Spinks, and G. Wallace, "*Fast trilayer polypyrrole bending actuators for high speed applications.*" *Synthetic Metals*, 2006. **156**(16-17): p. 1017-1022.
252. R.A. Green, N.H. Lovell, and L.A. Poole-Warren, "*Cell attachment functionality of bioactive conducting polymers for neural interfaces.*" *Biomaterials*, 2009. **30**(22): p. 3637-3644.
253. R.A. Green, R.T. Hassarati, J.A. Goding, S. Baek, N.H. Lovell, P.J. Martens, and L.A. Poole-Warren, "*Conductive hydrogels: mechanically robust hybrids for use as biomaterials.*" *Macromolecular bioscience*, 2012. **12**(4): p. 494-501.
254. Q. Pei and O. Inganaes, "*Electrochemical applications of the bending beam method. 1. Mass transport and volume changes in polypyrrole during redox.*" *The Journal of Physical Chemistry*, 1992. **96**(25): p. 10507-10514.
255. L. Bay, T. Jacobsen, S. Skaarup, and K. West, "*Mechanism of actuation in conducting polymers: osmotic expansion.*" *J. Phys. Chem. B*, 2001. **105**: p. 8492-8497.
256. M. Berggren and A. Richter-Dahlfors, "*Organic bioelectronics.*" *Advanced Materials*, 2007. **19**(20): p. 3201-3213.
257. J. Rivnay, S. Inal, A. Salleo, R.M. Owens, M. Berggren, and G.G. Malliaras, "*Organic electrochemical transistors.*" *Nature Reviews Materials*, 2018. **3**(2): p. 1-14.
258. M.R. Abidian, J.M. Corey, D.R. Kipke, and D.C. Martin, "*Conducting-polymer nanotubes improve electrical properties, mechanical adhesion, neural*

- attachment, and neurite outgrowth of neural electrodes.*" *small*, 2010. **6**(3): p. 421-429.
259. M.R. Abidian, K.A. Ludwig, T.C. Marzullo, D.C. Martin, and D.R. Kipke, "*Interfacing conducting polymer nanotubes with the central nervous system: chronic neural recording using poly (3, 4-ethylenedioxythiophene) nanotubes.*" *Advanced Materials*, 2009. **21**(37): p. 3764-3770.
260. M. Fahlman, S. Fabiano, V. Gueskine, D. Simon, M. Berggren, and X. Crispin, "*Interfaces in organic electronics.*" *Nature Reviews Materials*, 2019. **4**(10): p. 627-650.
261. J. Harding and I. Sneddon. "*The elastic stresses produced by the indentation of the plane surface of a semi-infinite elastic solid by a rigid punch.*" in *Mathematical Proceedings of the Cambridge Philosophical Society*. 1945. Cambridge University Press.
262. C.S. Kim and S.M. Oh, "*Spectroscopic and electrochemical studies of PMMA-based gel polymer electrolytes modified with interpenetrating networks.*" *Journal of power sources*, 2002. **109**(1): p. 98-104.
263. S. Liang, W. Yan, X. Wu, Y. Zhang, Y. Zhu, H. Wang, and Y. Wu, "*Gel polymer electrolytes for lithium ion batteries: Fabrication, characterization and performance.*" *Solid State Ionics*, 2018. **318**: p. 2-18.
264. S.-K. Lee, Y. Choi, W. Sim, S.S. Yang, H. An, and J.J. Pak. "*Fabrication of electroactive polymer actuator composed of polypyrrole and solid-polymer electrolyte and its application to micropump.*" in *Smart Structures and Materials*

2000: *Electroactive Polymer Actuators and Devices (EAPAD)*. 2000.

International Society for Optics and Photonics.

265. R. Pomfret, G. Miranpuri, and K. Sillay, "*The substitute brain and the potential of the gel model.*" *Annals of neurosciences*, 2013. **20**(3): p. 118.
266. T. Parupudi, R. Rahimi, M. Ammirati, R. Sundararajan, A.L. Garner, and B. Ziaie, "*Fabrication and characterization of implantable flushable electrodes for electric field-mediated drug delivery in a brain tissue-mimic agarose gel.*" *Electrophoresis*, 2018. **39**(17): p. 2262-2269.
267. K. Sillay, D. Schomberg, A. Hinchman, L. Kumbier, C. Ross, K. Kubota, E. Brodsky, and G. Miranpuri, "*Benchmarking the ERG valve tip and MRI Interventions Smart Flow neurocatheter convection-enhanced delivery system's performance in a gel model of the brain: employing infusion protocols proposed for gene therapy for Parkinson's disease.*" *Journal of neural engineering*, 2012. **9**(2): p. 026009.
268. E. Smela, "*Conjugated polymer actuators.*" *MRS Bulletin*, 2011. **33**(03): p. 197-204.
269. E. Stavrinidou, P. Leleux, H. Rajaona, D. Khodagholy, J. Rivnay, M. Lindau, S. Sanaur, and G.G. Malliaras, "*Direct measurement of ion mobility in a conducting polymer.*" *Advanced Materials*, 2013. **25**(32): p. 4488-4493.
270. M. Eslamian, M. Antensteiner, and M.R. Abidian. "*Direct Measurement of Mass Transport in Actuation of Conducting Polymers Nanotubes.*" in *2018 40th Annual*

International Conference of the IEEE Engineering in Medicine and Biology Society (EMBC). 2018. IEEE.

271. D. Wang, C. Lu, J. Zhao, S. Han, M. Wu, and W. Chen, "*High energy conversion efficiency conducting polymer actuators based on PEDOT: PSS/MWCNTs composite electrode.*" *RSC advances*, 2017. **7**(50): p. 31264-31271.
272. N. Terasawa and K. Asaka, "*High-performance PEDOT: PSS/single-walled carbon nanotube/ionic liquid actuators combining electrostatic double-layer and faradaic capacitors.*" *Langmuir*, 2016. **32**(28): p. 7210-7218.
273. Y. Li, R. Tanigawa, and H. Okuzaki, "*Soft and flexible PEDOT/PSS films for applications to soft actuators.*" *Smart Materials and Structures*, 2014. **23**(7): p. 074010.
274. H. Okuzaki, S. Takagi, F. Hishiki, and R. Tanigawa, "*Ionic liquid/polyurethane/PEDOT: PSS composites for electro-active polymer actuators.*" *Sensors and Actuators B: Chemical*, 2014. **194**: p. 59-63.
275. J.-P. Péraud, A.J. Nonaka, J.B. Bell, A. Donev, and A.L. Garcia, "*Fluctuation-enhanced electric conductivity in electrolyte solutions.*" *Proceedings of the National Academy of Sciences*, 2017. **114**(41): p. 10829-10833.
276. G. Wu, X. Wu, Y. Xu, H. Cheng, J. Meng, Q. Yu, X. Shi, K. Zhang, W. Chen, and S. Chen, "*High-Performance Hierarchical Black-Phosphorous-Based Soft Electrochemical Actuators in Bioinspired Applications.*" *Advanced Materials*, 2019. **31**(25): p. 1806492.

277. A. Della Santa, D. De Rossi, and A. Mazzoldi, "*Performance and work capacity of a polypyrrole conducting polymer linear actuator.*" *Synthetic metals*, 1997. **90**(2): p. 93-100.
278. M. Christophersen, B. Shapiro, and E. Smela, "*Characterization and modeling of PPy bilayer microactuators.*" *Sensors and Actuators B: Chemical*, 2006. **115**(2): p. 596-609.
279. B. Shapiro and E. Smela, "*Bending actuators with maximum curvature and force and zero interfacial stress.*" *Journal of intelligent material systems and structures*, 2007. **18**(2): p. 181-186.
280. J.M. Gere and S.P. Timoshenko, "*Mechanics of materials, PWS-KENT Pub.*" Comp., Boston, 1984.
281. S. Timoshenko, "*Analysis of bi-metal thermostats.*" *Josa*, 1925. **11**(3): p. 233-255.
282. V. Panwar, J.-H. Jeon, G. Anoop, H.J. Lee, I.-K. Oh, and J.Y. Jo, "*Low voltage actuator using ionic polymer metal nanocomposites based on a miscible polymer blend.*" *Journal of Materials Chemistry A*, 2015. **3**(39): p. 19718-19727.
283. J. Ding, D. Zhou, G. Spinks, G. Wallace, S. Forsyth, M. Forsyth, and D. MacFarlane, "*Use of ionic liquids as electrolytes in electromechanical actuator systems based on inherently conducting polymers.*" *Chemistry of materials*, 2003. **15**(12): p. 2392-2398.
284. R. Kiefer, J.G. Martinez, A. Kesküla, G. Anbarjafari, A. Aabloo, and T.F. Otero, "*Polymeric actuators: Solvents tune reaction-driven cation to reaction-driven anion actuation.*" *Sensors and Actuators B: Chemical*, 2016. **233**: p. 328-336.

285. O. Kim, H. Kim, U.H. Choi, and M.J. Park, "*One-volt-driven superfast polymer actuators based on single-ion conductors.*" *Nature communications*, 2016. **7**(1): p. 1-8.
286. N. Terasawa, N. Ono, K. Mukai, T. Koga, N. Higashi, and K. Asaka, "*A multi-walled carbon nanotube/polymer actuator that surpasses the performance of a single-walled carbon nanotube/polymer actuator.*" *Carbon*, 2012. **50**(1): p. 311-320.
287. K. Mukai, K. Asaka, T. Sugino, K. Kiyohara, I. Takeuchi, N. Terasawa, D.N. Futaba, K. Hata, T. Fukushima, and T. Aida, "*Highly conductive sheets from millimeter-long single-walled carbon nanotubes and ionic liquids: application to fast-moving, low-voltage electromechanical actuators operable in air.*" *Advanced materials*, 2009. **21**(16): p. 1582-1585.
288. L. Lu, J. Liu, Y. Hu, Y. Zhang, H. Randriamahazaka, and W. Chen, "*Highly stable air working bimorph actuator based on a graphene nanosheet/carbon nanotube hybrid electrode.*" *Advanced Materials*, 2012. **24**(31): p. 4317-4321.
289. J.-W. Lee, Y.-T. Yoo, and J.Y. Lee, "*Ionic polymer-metal composite actuators based on triple-layered polyelectrolytes composed of individually functionalized layers.*" *ACS applied materials & interfaces*, 2014. **6**(2): p. 1266-1271.
290. J. Li, W. Ma, L. Song, Z. Niu, L. Cai, Q. Zeng, X. Zhang, H. Dong, D. Zhao, and W. Zhou, "*Superfast-response and ultrahigh-power-density electromechanical actuators based on hierarchical carbon nanotube electrodes and chitosan.*" *Nano letters*, 2011. **11**(11): p. 4636-4641.

291. G. Wu, Y. Hu, J. Zhao, T. Lan, D. Wang, Y. Liu, and W. Chen, "*Ordered and Active Nanochannel Electrode Design for High-Performance Electrochemical Actuator.*" *Small*, 2016. **12**(36): p. 4986-4992.
292. B. Kim, C. Too, J. Kwon, J. Ko, and G. Wallace, "*A flexible capacitor based on conducting polymer electrodes.*" *Synthetic Metals*, 2011. **161**(11-12): p. 1130-1132.
293. K. Idla, O. Inganäs, and M. Strandberg, "*Good adhesion between chemically oxidised titanium and electrochemically deposited polypyrrole.*" *Electrochimica Acta*, 2000. **45**(13): p. 2121-2130.
294. W. Lu, A.G. Fadeev, B. Qi, E. Smela, B.R. Mattes, J. Ding, G.M. Spinks, J. Mazurkiewicz, D. Zhou, and G.G. Wallace, "*Use of ionic liquids for π -conjugated polymer electrochemical devices.*" *Science*, 2002. **297**(5583): p. 983-987.
295. Y.-R. Chang, V.K. Raghunathan, S.P. Garland, J.T. Morgan, P. Russell, and C.J. Murphy, "*Automated AFM force curve analysis for determining elastic modulus of biomaterials and biological samples.*" *Journal of the mechanical behavior of biomedical materials*, 2014. **37**: p. 209-218.
296. M. Salvadori, I. Brown, A. Vaz, L. Melo, and M. Cattani, "*Measurement of the elastic modulus of nanostructured gold and platinum thin films.*" *Physical Review B*, 2003. **67**(15): p. 153404.
297. E. Tan and C. Lim, "*Nanoindentation study of nanofibers.*" *Applied Physics Letters*, 2005. **87**(12): p. 123106.

298. D. Reifer, R. Windeit, R. Kumpf, A. Karbach, and H. Fuchs, "*AFM and TEM investigations of polypropylene/polyurethane blends.*" *Thin solid films*, 1995. **264**(2): p. 148-152.
299. C.B. Horner, G. Ico, J. Johnson, Y. Zhao, and J. Nam, "*Microstructure-dependent mechanical properties of electrospun core-shell scaffolds at multi-scale levels.*" *Journal of the mechanical behavior of biomedical materials*, 2016. **59**: p. 207-219.
300. A.M. Jones, "*Drag coefficients for flat plates, spheres, and cylinders moving at low Reynolds numbers in a viscous fluid.*" 1957.
301. G. Hong and C.M. Lieber, "*Novel electrode technologies for neural recordings.*" *Nature Reviews Neuroscience*, 2019. **20**(6): p. 330-345.
302. J.A. Frank, M.-J. Antonini, and P. Anikeeva, "*Next-generation interfaces for studying neural function.*" *Nature biotechnology*, 2019. **37**(9): p. 1013-1023.
303. B.S. Wilson, C.C. Finley, D.T. Lawson, R.D. Wolford, D.K. Eddington, and W.M. Rabinowitz, "*Better speech recognition with cochlear implants.*" *Nature*, 1991. **352**(6332): p. 236-238.
304. E. Zrenner, "*Will retinal implants restore vision?*" *Science*, 2002. **295**(5557): p. 1022-1025.
305. A. Jackson and J.B. Zimmermann, "*Neural interfaces for the brain and spinal cord—restoring motor function.*" *Nature Reviews Neurology*, 2012. **8**(12): p. 690.
306. S. Raspopovic, M. Capogrosso, F.M. Petrini, M. Bonizzato, J. Rigosa, G. Di Pino, J. Carpaneto, M. Controzzi, T. Boretius, and E. Fernandez, "*Restoring natural*

- sensory feedback in real-time bidirectional hand prostheses.*" *Science translational medicine*, 2014. **6**(222): p. 222ra19-222ra19.
307. W.C. Stacey and B. Litt, "*Technology insight: neuroengineering and epilepsy—designing devices for seizure control.*" *Nature clinical practice Neurology*, 2008. **4**(4): p. 190-201.
308. M.L. Kringelbach, N. Jenkinson, S.L. Owen, and T.Z. Aziz, "*Translational principles of deep brain stimulation.*" *Nature Reviews Neuroscience*, 2007. **8**(8): p. 623-635.
309. D.H. Hubel, "*Tungsten microelectrode for recording from single units.*" *Science*, 1957. **125**(3247): p. 549-550.
310. K.D. Wise, J.B. Angell, and A. Starr, "*An integrated-circuit approach to extracellular microelectrodes.*" *IEEE transactions on biomedical engineering*, 1970(3): p. 238-247.
311. K.D. Wise, D.J. Anderson, J.F. Hetke, D.R. Kipke, and K. Najafi, "*Wireless implantable microsystems: high-density electronic interfaces to the nervous system.*" *Proceedings of the IEEE*, 2004. **92**(1): p. 76-97.
312. P.K. Campbell, K.E. Jones, and R.A. Normann, "*A 100 electrode intracortical array: structural variability.*" *Biomed. Sci. Instrum*, 1990. **26**: p. 161-165.
313. J.J. Jun, N.A. Steinmetz, J.H. Siegle, D.J. Denman, M. Bauza, B. Barbarits, A.K. Lee, C.A. Anastassiou, A. Andrei, and Ç. Aydın, "*Fully integrated silicon probes for high-density recording of neural activity.*" *Nature*, 2017. **551**(7679): p. 232-236.

314. M. Lee, H.J. Shim, C. Choi, and D.-H. Kim, "*Soft high-resolution neural interfacing probes: Materials and design approaches.*" *Nano letters*, 2019. **19**(5): p. 2741-2749.
315. J. Kim, R. Ghaffari, and D.-H. Kim, "*The quest for miniaturized soft bioelectronic devices.*" *Nature Biomedical Engineering*, 2017. **1**(3): p. 1-4.
316. Z. Suo, E. Ma, H. Gleskova, and S. Wagner, "*Mechanics of rollable and foldable film-on-foil electronics.*" *Applied Physics Letters*, 1999. **74**(8): p. 1177-1179.
317. B.J. Kim and E. Meng, "*Review of polymer MEMS micromachining.*" *Journal of Micromechanics and Microengineering*, 2015. **26**(1): p. 013001.
318. A. Weltman, J. Yoo, and E. Meng, "*Flexible, penetrating brain probes enabled by advances in polymer microfabrication.*" *Micromachines*, 2016. **7**(10): p. 180.
319. Z.J. Du, C.L. Kolarcik, T.D. Kozai, S.D. Luebben, S.A. Sapp, X.S. Zheng, J.A. Nabity, and X.T. Cui, "*Ultrasoft microwire neural electrodes improve chronic tissue integration.*" *Acta biomaterialia*, 2017. **53**: p. 46-58.
320. T.-i. Kim, J.G. McCall, Y.H. Jung, X. Huang, E.R. Siuda, Y. Li, J. Song, Y.M. Song, H.A. Pao, and R.-H. Kim, "*Injectable, cellular-scale optoelectronics with applications for wireless optogenetics.*" *Science*, 2013. **340**(6129): p. 211-216.
321. L. Lu, X. Fu, Y. Liew, Y. Zhang, S. Zhao, Z. Xu, J. Zhao, D. Li, Q. Li, and G.B. Stanley, "*Soft and MRI compatible neural electrodes from carbon nanotube fibers.*" *Nano letters*, 2019. **19**(3): p. 1577-1586.
322. R.J. Vetter, J.C. Williams, J.F. Hetke, E.A. Nunamaker, and D.R. Kipke, "*Chronic neural recording using silicon-substrate microelectrode arrays*

- implanted in cerebral cortex.*" IEEE Transactions on Biomedical Engineering, 2004. **51**(6): p. 896-904.
323. A.K. Engel, C.K. Moll, I. Fried, and G.A. Ojemann, "*Invasive recordings from the human brain: clinical insights and beyond.*" Nature Reviews Neuroscience, 2005. **6**(1): p. 35-47.
324. J. Muthuswamy, S. Anand, and A. Sridharan, "*Adaptive movable neural interfaces for monitoring single neurons in the brain.*" Frontiers in neuroscience, 2011. **5**: p. 94.
325. J. Muthuswamy, M. Okandan, A. Gilletti, M.S. Baker, and T. Jain, "*An array of microactuated microelectrodes for monitoring single-neuronal activity in rodents.*" IEEE Transactions on Biomedical Engineering, 2005. **52**(8): p. 1470-1477.
326. J.G. Cham, E.A. Branchaud, Z. Nenadic, B. Greger, R.A. Andersen, and J.W. Burdick, "*Semi-chronic motorized microdrive and control algorithm for autonomously isolating and maintaining optimal extracellular action potentials.*" Journal of Neurophysiology, 2005. **93**(1): p. 570-579.
327. C. Pang, Y.-C. Tai, J.W. Burdick, and R.A. Andersen. "*Electrolysis-based parylene balloon actuators for movable neural probes.*" in *2007 2nd IEEE International Conference on Nano/Micro Engineered and Molecular Systems*. 2007. IEEE.
328. X. Cui, J.F. Hetke, J.A. Wiler, D.J. Anderson, and D.C. Martin, "*Electrochemical deposition and characterization of conducting polymer polypyrrole/PSS on*

- multichannel neural probes.*" Sensors and Actuators A: Physical, 2001. **93**(1): p. 8-18.
329. X. Cui, J. Wiler, M. Dzaman, R.A. Altschuler, and D.C. Martin, "*In vivo studies of polypyrrole/peptide coated neural probes.*" Biomaterials, 2003. **24**(5): p. 777-787.
330. M.R. Abidian, L.G. Salas, A. Yazdan-Shahmorad, T.C. Marzullo, D.C. Martin, and D.R. Kipke. "*In-vivo evaluation of chronically implanted neural microelectrode arrays modified with poly (3, 4-ethylenedioxythiophene) nanotubes.*" in *2007 3rd International IEEE/EMBS Conference on Neural Engineering*. 2007. IEEE.
331. R. Biran, D.C. Martin, and P.A. Tresco, "*Neuronal cell loss accompanies the brain tissue response to chronically implanted silicon microelectrode arrays.*" Experimental neurology, 2005. **195**(1): p. 115-126.
332. Y. Lei, B. Song, R.D. van der Weijden, M. Saakes, and C.J. Buisman, "*Electrochemical induced calcium phosphate precipitation: importance of local pH.*" Environmental science & technology, 2017. **51**(19): p. 11156-11164.
333. F. Pervin and W.W. Chen, *Mechanically similar gel simulants for brain tissues*, in *Dynamic Behavior of Materials, Volume 1*. 2011, Springer. p. 9-13.
334. Z.-J. Chen, G.T. Gillies, W.C. Broaddus, S.S. Prabhu, H. Fillmore, R.M. Mitchell, F.D. Corwin, and P.P. Fatouros, "*A realistic brain tissue phantom for intraparenchymal infusion studies.*" Journal of neurosurgery, 2004. **101**(2): p. 314-322.

335. W. Jensen, K. Yoshida, and U.G. Hofmann, "*In-vivo implant mechanics of flexible, silicon-based ACREO microelectrode arrays in rat cerebral cortex.*" IEEE Transactions on Biomedical Engineering, 2006. **53**(5): p. 934-940.
336. A.A. Sharp, A.M. Ortega, D. Restrepo, D. Curran-Everett, and K. Gall, "*In vivo penetration mechanics and mechanical properties of mouse brain tissue at micrometer scales.*" IEEE transactions on biomedical engineering, 2008. **56**(1): p. 45-53.
337. K.J. Paralikar and R.S. Clement, "*Collagenase-aided intracortical microelectrode array insertion: effects on insertion force and recording performance.*" IEEE Transactions on Biomedical Engineering, 2008. **55**(9): p. 2258-2267.

